



HAL
open science

Synthesis and high-temperature behavior of self-restoring coatings

Romain Troncy

► **To cite this version:**

Romain Troncy. Synthesis and high-temperature behavior of self-restoring coatings. Matériaux composites et construction. Université de La Rochelle, 2021. English. NNT : 2021LAROS034 . tel-03722119

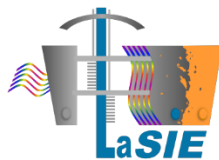
HAL Id: tel-03722119

<https://theses.hal.science/tel-03722119>

Submitted on 13 Jul 2022

HAL is a multi-disciplinary open access archive for the deposit and dissemination of scientific research documents, whether they are published or not. The documents may come from teaching and research institutions in France or abroad, or from public or private research centers.

L'archive ouverte pluridisciplinaire **HAL**, est destinée au dépôt et à la diffusion de documents scientifiques de niveau recherche, publiés ou non, émanant des établissements d'enseignement et de recherche français ou étrangers, des laboratoires publics ou privés.



ÉCOLE DOCTORALE EUCLIDE

La Rochelle Université

Laboratoire des Sciences de l'Ingénieur pour l'Environnement
LaSIE (UMR-CNRS 7356)

THÈSE DE DOCTORAT

présentée par :

Romain TRONCY

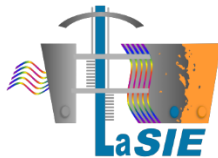
Soutenance prévue le 30 novembre 2021
pour l'obtention du grade de Docteur de l'Université de La Rochelle

Discipline : Sciences des Matériaux

Synthesis and high-temperature behavior of self-restoring coatings

Composition du jury :

<i>Mme. Cecilia Bartuli</i>	<i>Professeure des Universités, Sapienza Université de Rome</i>	<i>Rapporteure</i>
<i>M. Juan José de Damborenea</i>	<i>Directeur de Recherche, CSIC-CENIM de Madrid</i>	<i>Rapporteur</i>
<i>M. Henri Buscail</i>	<i>Professeur des Universités, Université Clermont-Auvergne</i>	<i>Examinateur</i>
<i>Mme. Véronique Gauthier-Brunet</i>	<i>Maîtresse de Conférences HDR, Université de Poitiers</i>	<i>Examinatrice</i>
<i>Mme. Céline Pascal</i>	<i>Maîtresse de Conférences HDR, Université de Grenoble Alpes</i>	<i>Examinatrice</i>
<i>M. Gilles Bonnet</i>	<i>Professeur des Universités, La Rochelle Université</i>	<i>Co-directeur</i>
<i>M. Fernando Pedraza</i>	<i>Professeur des Universités, La Rochelle Université</i>	<i>Co-directeur</i>



ÉCOLE DOCTORALE EUCLIDE

La Rochelle Université

Laboratoire des Sciences de l'Ingénieur pour l'Environnement
LaSIE (UMR-CNRS 7356)

THÈSE DE DOCTORAT

présentée par :

Romain TRONCY

Soutenance prévue le 30 novembre 2021
pour l'obtention du grade de Docteur de l'Université de La Rochelle

Discipline : Sciences des Matériaux

Synthèse et comportement à haute température de revêtements auto-régénérant

Composition du jury :

<i>Mme. Cecilia Bartuli</i>	<i>Professeure des Universités, Sapienza Université de Rome</i>	<i>Rapporteuse</i>
<i>M. Juan José de Damborenea</i>	<i>Directeur de Recherche, CSIC-CENIM de Madrid</i>	<i>Rapporteur</i>
<i>M. Henri Buscail</i>	<i>Professeur des Universités, Université Clermont-Auvergne</i>	<i>Examinateur</i>
<i>Mme. Véronique Gauthier-Brunet</i>	<i>Maîtresse de Conférences HDR, Université de Poitiers</i>	<i>Examinatrice</i>
<i>Mme. Céline Pascal</i>	<i>Maîtresse de Conférences HDR, Université de Grenoble Alpes</i>	<i>Examinatrice</i>
<i>M. Gilles Bonnet</i>	<i>Professeur des Universités, La Rochelle Université</i>	<i>Co-directeur</i>
<i>M. Fernando Pedraza</i>	<i>Professeur des Universités, La Rochelle Université</i>	<i>Co-directeur</i>

Table of contents

Introduction.....	7
Chapter I. State of the art.....	11
I-Gas turbines: generalities and selection of materials for high-temperature applications	12
II-Nickel based superalloys for gas turbines	13
II.A-Microstructure	13
II.B-Structure and solidification	14
II.C-Alloying elements	15
III-Degradation of metallic materials at high temperature	17
IV-High temperature protection of nickel-based superalloys	19
IV.A-Diffusion coatings	20
IV.B-Nickel aluminide coatings and Ni-Al binary phase diagram.....	20
IV.C-High-activity and low activity-activity diffusion coatings.....	21
V-High-temperature ageing of coated superalloys	23
V.A-Oxidation of nickel aluminide coatings	23
V.B-Factors and mechanisms responsible for spallation of the oxide layer.....	25
V.C-Formation and propagation of the interdiffusion zone of the coating.....	28
V.D-Phase transformation in additive layer of the coating.....	29
VI-Diffusion barriers.....	30
VI.A-Diffusion barrier based on an oxide layer.....	30
VI.B-Diffusion barriers enriched with refractory element	31
VII-Motivation of the present study	32
VII.A-Slurry coating	32
VII.B-Synthesis of a self-restoring coatings	33
References.....	36
Chapter II. Experimental methods.....	49
I-Materials of study	50
I.A-Electrodeposition of nickel	51
I.A.1-Electroplating bath assembly.....	52
I.A.2-Bath assembly.....	52
I.A.3: Electrolytes and protocols used	53
II-Characterization of metallic powders.....	55
III-Elaboration of the slurry coatings	61

III.A-Composition and preparation of the slurries	61
III.B-Deposition of the slurries on metallic substrate by air brush.....	61
III.C-Thermal treatments.....	62
IV-Degradation of the coatings	63
IV.A-Isothermal oxidation	63
V-Characterization methods	63
V.A-Calorimetry analyses	63
V.A-Crystallographic and structural analyses	63
V.C-Microscopic analyses	64
Reference.....	66
Chapter III. Study of the reactivity and microstructure of Al and preoxidized Ni powders by DSC.....	69
I-Article I: Reactivity and microstructural observation of Al+Niox and Niox/Al system by DSC ...	71
Abstract.....	71
I-Introduction	71
II-Experimental procedure	73
III-Results	74
III.A-Effect of the preoxidation time of the Ni powder	74
III.B-Reactivity of Al-Ni _{ox} microparticles	77
III.C-Reactivity of preoxidized Ni over pure Al.....	82
IV-Discussion	87
IV.A-Effect of the preoxidation time	87
IV.B-Layout 1- Mixture of preoxidized Ni and Al particles	88
IV.C-Layout 2- preoxidized Ni powders over the Al particles.....	89
V-Conclusion.....	91
References.....	93
II- Reactivity and microstructural observations of Al/Niox system by DSC	97
II.A-Results.....	97
I.A.1-Differential scanning calorimetry.....	97
I.B-Microstructural development	99
II.C-Discussion	102
II.D-Conclusion.....	104
III-Reactivity of the Al particles with pure preoxidized nickel substrate.....	105
III.A-layout A and B: Pure Ni and pure Ni with Al particles	105
III.A.1-Results	105

III.B-Layout C: Preoxidized pure Ni with Al particles	107
III.B.1-Results	107
III.C-Discussion	113
III.D-Conclusion.....	114
References.....	116
Chapter IV: Synthesis of self-regenerating composite coatings using aluminothermic reaction.....	
120	
I-Article II: Synthesis of self-regenerating NiAl-Al ₂ O ₃ composite coatings	122
Abstract.....	122
I.A-Introduction.....	122
I.B-Experimental procedure	123
I.C-Results	125
I.C.1-Pre-oxidation of bulk Ni	125
I.C.2-Influence of the annealing temperature	128
I.C.3-Influence of the pre-oxidation time of the nickel substrate	130
I.D-Discussion	134
I.D.1-Influence of the heat treatment on the formation mechanisms of coatings.....	134
I.D.2-Influence of the pre-oxidation time.....	136
I.E-Conclusions	138
References.....	139
II-Synthesis of self-regenerating NiAl-Al ₂ O ₃ composite coatings using Ni plating and aluminothermic reaction	143
II.A-Results.....	144
II.A.1-Microstructure of Ni plating.....	144
II.A.2-Texture	147
II.A.3-Preoxidation of Ni plates.....	149
II.A.4-Influence of the current density and preoxidation time on the aluminized layers ..	154
II.B-Discussion	158
II.B.1-Preoxidation of the Ni plating.....	158
II.B.2-Influence of the current density on the aluminothermic and aluminizing processes	159
II.B.3-Influence of the electrodeposit thickness on the aluminothermic reactions and the aluminizing processes.....	162
II.C-Conclusion.....	164
References.....	165

Chapter V: Synthesis of self-regenerating composite coating using electrocodeposition of Ni and preoxidized Al_3Ni_2 particles	168
I-Synthesis of intermetallic powders and preoxidation	169
II-Electro-codeposition of Ni and Al_3Ni_2 preoxidized particles.....	177
II.A-Surface morphology of the first layer.....	177
II.B-Electroplating and incorporation of $Al_3Ni_{2(ox)}$ particles in a metallic Ni matrix	181
II.B.1-Influence of current density.....	182
II.B.2-Influence of heat treatment temperature.	183
II.B.3-Influence of heat treatment time	186
III- Isothermal oxidation	189
III.A-Microstructure and composition	190
III.A.1-Aluminizing and isothermal oxidation of the coating carried out on the raw substrate	190
III.A.2-Aluminizing and isothermal oxidation of nickel plating	192
III.A.3-Aluminizing and isothermal oxidation of composite electrodeposits with “Ni flash”	193
III.A.4-Aluminizing and isothermal oxidation of composite electrodeposits without “Ni flash”	195
III.B-Oxidation kinetics.....	199
IV-Discussion	200
IV.A-Formation of the first layer of electrodeposited nickel (Ni flash)	200
IV.B-Effect of current density on the amount of preoxidized Al_3Ni_2 particles trapped in nickel electrodeposit matrix	200
IV.C-Effect of aluminizing temperature and time.....	201
IV.D-Isothermal oxidation	203
IV.D.1-Oxidation kinetics.....	203
IV.D.2-Evolution of the microstructure and compositions	204
V-Conclusions	207
References.....	208
Conclusion and perspectives	213
I-Summary and conclusion	213
II-Perspectives.....	216
Annexes	218
Annex 1	218

Introduction

The selection of structural materials for a given application is mostly based on their mechanical properties and then on their environmental resistance. By optimizing these two factors, it is therefore possible to increase the durability of the structural materials.

Ni-based superalloys are widely used in several domains, including aero and land-based turbine engines. For such applications, metallic components are carefully designed by adjusting their chemical composition and microstructure to respond to the demanding mechanical resistance. Placed at the exit of the combustion chambers, the turbine blades can be stressed at temperatures reaching 1150°C and their rotation speed is of the order of 10,000 revolutions/minute. Therefore, creep and fatigue linked to the cyclic use of turbines, erosion and oxidation at high temperature are the main modes of degradation of the blades.

All main gas turbine components (blades, vanes and disks) are also submitted to highly corrosive environments (O_2 , SO_2/SO_3 and H_2O species) with pressurized hot gases, combustion impurities and different types of erosive particles (salts, sand, volcanic ashes, concrete dust, etc.) leading to hot corrosion by CMAS (Calcium Magnesium Aluminosilicates). Under these conditions, the parts are usually coated with a platinum-modified nickel aluminide coating β -(Ni, Pt)Al or with an overlay MCrAlY (with M: Ni, Co) coating. These protective coatings on the surface are designed to limit the corrosion and oxidation of the substrates by forming an aluminum oxide and/or a chromium oxide layer. The application of protective coatings significantly increases the high-temperature surface stability of nickel-based superalloys and is essential to guarantee their integrity of the blades during their lifetime.

One of the main challenges in the aeronautical field is to increase the efficiency of the turbine engines, allowing to reduce the consumption of kerosene, hence the emissions of harmful gases into the atmosphere. The Brayton thermodynamic cycle demonstrates that the efficiency of gas turbine engines is a direct consequence of the turbine inlet temperature (TIT). The higher the TIT, the greater the thermodynamic efficiency of the engine. For example, increasing the turbine inlet temperature by 50°C enhances the specific thrust by 1% and reduces the fuel consumption by 5%. Therefore, aircraft manufacturers continuously increase the TIT of the turbine engines and the resistance of the materials must be thus increased. This is why in their latest developments, nickel-based superalloys are monocrystalline with a microstructure based on coherent γ - γ' precipitation and enriched in two refractory elements, rhenium and ruthenium. The developments have made it possible to increase the temperature of use of these alloys by around 100°C and to increase high creep and fatigue resistance compared to the first polycrystalline alloys. Increasing the temperature fosters the degradation of the blades by enhancing both oxidation and interdiffusion between Al (of the coating) and Ni (of the substrate) for instance. In addition, the usually less attacked components (low stages of turbine) become now extremely sensitive to the high-temperature oxidation and corrosion. These new corrosive conditions require the application of protective coatings to these stages and the improvement of state-of-the-art coatings for the upper stages.

For high-temperature oxidation resistance, industrial protective coatings are usually based on electrodeposition of platinum followed by CVD-related techniques to enrich the surface of nickel-based superalloys with Al. The nickel aluminide coatings, based on the β -NiAl phase, decrease

the oxidation kinetics of the underlying substrate by forming a dense and continuous $\alpha\text{-Al}_2\text{O}_3$ scales on the surface. The two main factors of degradation in cyclic oxidation are the spallation of the oxide layer upon thermal cycling conditions and the interdiffusion between Al and other elements in the nickel-based superalloys.

Indeed, under cyclic conditions, the damage of coated superalloys occurs by successive spallation of the aluminum oxide layer, which consumes the aluminum contained in the coating to form a new layer of alumina on the spalled areas. The ruin of coated superalloys occurs when the quantity of Al in the coating is not high enough to form a new layer of protective alumina. As a result, non-protective nickel-rich oxides, NiAl_2O_4 and NiO develop. The formation of these fast-growing and little adherent oxides accelerates the aging of the system. Thus, the content of the aluminum coating is a criterion characterizing the lifetime of a coated superalloy.

In addition, the differences in chemical compositions foster the interdiffusion between the elements of the superalloys substrates and their protective coatings at their temperature of use. This is particularly significant in the case of a $\beta\text{-NiAl}$ coating, because the difference in composition of the coating and of the superalloy is greater. The diffusion flow associated with this phenomenon leads to a premature depletion of the aluminum coating. The consequences related to the aluminum depletion mentioned above are thus increased.

The interdiffusion between the superalloy and its protective coating has other negative influences on the life of the coated superalloys. The diffusion of certain elements of the superalloys, such as titanium and tantalum, or certain impurities such as sulfur, decrease further the adhesion of the oxide layer. In addition, the premature depletion of the aluminum coating promotes phase transformation in the coating ($\beta\text{-NiAl} \rightarrow \gamma'\text{-Ni}_3\text{Al}$, martensitic transformation $\beta\text{-B2} \rightarrow \text{L}_{10}$). These transformations, by constraining the coating, also promote the spallation of the oxide layers. Finally, interdiffusion degrades the microstructure of the superalloys to a depth that increase with the time of exposure to high temperature. These modified zones reduce the “healthy” part of the superalloy, which carries the mechanical loading.

In order to limit the harmful consequences of interdiffusion and thus increase the lifespan of coated superalloys, studies focus on the development of diffusion barriers between the superalloy and its protective layer. These diffusion barriers consist of a dense layer of alumina or a rhenium based-alloy where the diffusion of aluminum, nickel and other elements of the superalloy and coating would be slowed down. Some of the last works of the group of Prof. T. Narita showed the development of chemically stable, effective diffusion barriers to limit interdiffusion for periods of at least 400 hours at 1100°C or 300 hours at 1150°C . However, the mechanical resistance and the resistance to thermal fatigue of a system with diffusion barriers can be reduced because of the differences in thermal expansion coefficients between the diffusion barrier, the coating and the superalloy. In addition, the initiation of cracks could be accentuated at the diffusion barrier level during mechanical fatigue stresses.

In contrast, these diffusion barriers are mostly applied for very high temperatures and not for the intermediate ones that the low-pressure turbine blades may undergo due to the increase of the TIT.

It is interesting to notice that the conventional industrial processes employed to generate a coating require technical resources, handle hazardous chemicals (halide activators, chromic acid, etc.) and can produce lots of waste in the particular case of pack-cementation. Therefore, to comply with environmental and safety regulations (e.g. Registration Evaluation Authorization and

Restriction of Chemicals), new approaches have been developed in the last decades for the high-temperature protective of metallic materials. One of this new approach started about a decade ago with the European project "PARTICOAT". The overall idea was based on the formation of a complete thermal barrier system (metallic bond coat, oxide scale and ceramic barrier coating) from water-based Al microparticles containing slurries. The complete thermal barrier system formed in a single-step process with a nickel aluminide bond coat and ceramic top coat expected to act as a cost-efficient and environmentally friendly manner to aluminize the turbine blades. These two aspects were explored in the thesis of B. Rannou and M. Mollard (nickel aluminide) and G. Boissonnet (ceramic top coat). In addition, B. Grégoire worked on the functionalization of coatings for hot corrosion applications.

These slurry synthesized coatings are found to be an economical and environmentally friendly alternative to the CVD synthesized diffusion coating. However, most of the aluminum contained in the coating is lost by interdiffusion with the substrate. Therefore, the main objectives of the present study are to form a self-regenerating nickel aluminide coating by slurry aluminizing process.

For this, two ways will be explored:

- The first way, consists in using the aluminothermic reaction between nickel oxide and aluminum. Preoxidation of the substrate or of a nickel electrodeposit followed by an aluminization treatment will allow the simultaneous formation of a diffusion coating and aluminum oxide
- The second way consists of the synthesis, preoxidation and incorporation of intermetallic microparticles in a nickel electrodeposit. Subsequently this composite electrodeposit will be aluminized by slurry route.

This manuscript has been divided in 5 main chapters:

Chapter I: Presents the state of the art and the industrial context for the high temperature oxidation and protection of metallic materials in gas turbine engines. A general overview focus on the diffusion barriers and nickel aluminide coating outcomes is given. The different modes of degradation encountered in gas turbines engines and their solution are also introduced.

Chapter II: Presents and describes the experimental methods of the present study, including the materials of study, elaboration of slurry coatings and the degradation tests performed. The characterization techniques carried out in this work are also presented.

Chapter III: Presents the study of the reactivity of the aluminum and preoxidized nickel particles. In this part, the influence of the sizes and the amount of NiO contained in the Ni particles, the heating rates and the arrangement of the different elements will be tested by DSC method. A better comprehension of the mechanisms of formation is needed before extrapolation to a pure Ni substrate and a nickel-based superalloy in chapter IV.

Chapter IV: Presents a preliminary study to obtaining a self-regenerating coating on pure nickel substrates. This part was subdivided into a first study on the influence of heat treatments and preoxidation time on raw nickel substrate and a second part on the influence of heat treatments and current density on preoxidized nickel electrodeposits.

Chapter V: Presents the synthesis of self-regenerating electrochemical coating and a preliminary study of oxidation behavior. Oxidation tests were performed to the effectiveness of the diffusion barrier and the protective behavior of the slurry coatings.

Chapter I. State of the art

Table of contents

<i>I-Gas turbines: generalities and selection of materials for high-temperature applications.....</i>	12
II-Nickel based superalloys for gas turbines	13
II.A-Microstructure	13
II.B-Structure and solidification	14
II.C-Alloying elements	15
III-Degradation of metallic materials at high temperature	17
IV-High temperature protection of nickel-based superalloys	19
IV.A-Diffusion coatings	20
IV.B-Nickel aluminide coatings and Ni-Al binary phase diagram.....	20
IV.C-High-activity and low activity-activity diffusion coatings.....	21
V-High-temperature ageing of coated superalloys	23
V.A-Oxidation of nickel aluminide coatings	23
V.B-Factors and mechanisms responsible for spallation of the oxide layer.....	25
V.C-Formation and propagation of the interdiffusion zone of the coating.....	28
V.D-Phase transformation in additive layer of the coating.....	29
VI-Diffusion barriers.....	30
VI.A-Diffusion barrier based on an oxide layer.....	30
VI.B-Diffusion barriers enriched with refractory element	31
VII-Motivation of the present study	32
VII.A-Slurry coating	32
VII.B-Synthesis of a self-restoring coatings	33
References.....	36

I-Gas turbines: generalities and selection of materials for high-temperature applications

Gas turbines have long been used in energy and aeronautical sectors. In an aircraft engine, the turbine is placed at the exit of the combustion chamber (Figure I-1.a) and consists of alternately fixed and rotating parts receiving the hot gases expelled from the combustion chamber. A turbine is divided into two sections, the high-pressure and the low-pressure turbines (HPT and LPT, respectively). By partial expansion of the combustion gases, the turbine transforms the thermal power of the gases passing through its rotating blades into mechanical power that in turn drive the compressor and the fan through the shaft. The blades are profiled obstacles immersed in the flow of fluids, serving to guide them. In contrast, in utility power plants, the heat produced by burning fossil (e.g. coal, gas, oil), or renewable (biomass) fuels or the heat stored in molten nitrates (thermosolar plants) is exchanged to heat and pressurize steam, which becomes the fluid that makes the blades rotate.

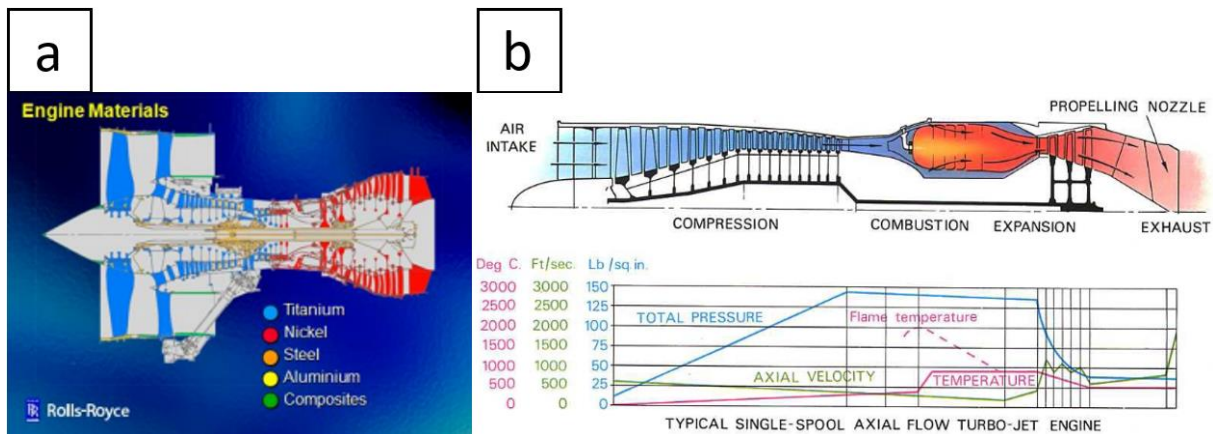


Figure I-1: (a) Schematic view in cross-section with the selected alloys for each section [1] and (b) evolution of the temperature, pressure and axe velocity through the engine [2].

According to aviation and environmental requirements, jet engines are expected to be more and more efficient. The thermodynamic efficacy of the gas turbine engine is ensured by the Turbine Inlet Temperature (Figure I-1.b) according to the Brayton cycle [3-4]. For example, increasing the turbine inlet temperature by 50°C enhances the specific thrust by 1% and reduces fuel consumption by 5%. The high-pressure turbine blades are located in the hottest part of the engine and operate in oxidizing (blade airfoil) and corrosive (blade root) atmospheres. The temperature at the tip and leading edge of the airfoils can reach nearly 1700°C [3-8]. In addition, they undergo strong mechanical stresses (about 10,000 revolutions/min). In this particularly harsh environments, nickel-based superalloys are used. Indeed, nickel-based superalloys have good mechanical properties at high temperatures, which have been optimized by modifying their composition and their microstructure. In particular, monocrystalline superalloys have excellent resistance to creep [5]. However, their use remains limited to surface temperatures of around 1100°C. To stay within this temperature range, sophisticated air film cooling have been designed [9]. The circulation of “cold” air (taken from the high-pressure compressor, at around 600°C) inside the blades, cools the superalloy. The internal cooling requires thinning of the walls of the blades, which in turn lower the overall mechanical resistance. Therefore, the internal cooling has currently

reached its maximum capacity and is thus combined with thermal barrier coatings to keep the metal temperature at around 1100°C [10] (Figure I-2).

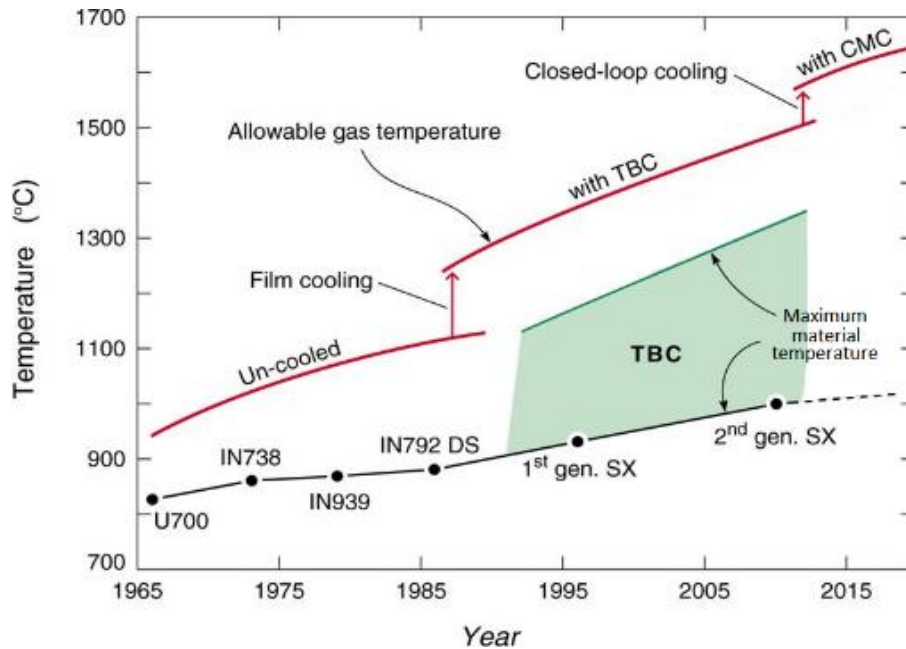


Figure I-2: Evolution of the high-pressure turbine blades over the past 50 years [5].

II-Nickel based superalloys for gas turbines

II.A-Microstructure

Nickel-based superalloys are a two-phase material with γ' -Ni₃Al phases in a γ -Ni matrix (Figure I-3) [5,11]. The γ -Ni matrix crystallizes in an A1 system and the γ' -Ni₃Al phases in an L₁₂ system. These two networks are semi-coherent, the crystallographic networks of the two phases having a very similar lattice parameter. The mechanical properties at high temperatures of the superalloys are due to two types of reinforcement that include the precipitation of the γ' -Ni₃Al hardening phase and the addition of hardening elements in solid solution in the γ -Ni matrix. In addition, the volume fraction of the γ' -Ni₃Al hardening phase can be as high as 70% at room temperature [12].

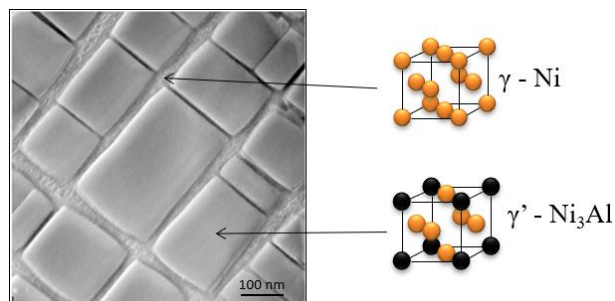


Figure I.3: Duplex γ - γ' microstructure of a nickel-based superalloy [5] and corresponding crystal structures.

II.B-Structure and solidification

The evolution of elaboration processes has made it possible to increase the mechanical properties of nickel-based superalloys at high-temperatures. After elaboration, nickel-based alloys have a dendritic structure (Figure I-4). The primary dendrite arms and their secondary ramification grow in the $\langle 100 \rangle$ direction. The dendrite arms have a fine γ/γ' microstructure, equivalent to one of Figure I-3, while the γ/γ' microstructure is coarser in the interdendritic spaces. Moreover, in these interdendritic spaces, massive γ' phases are formed, which do not contribute to the hardening of the alloy [5].

This dendritic structure comes from the rejection of certain elements from the solid phase to the liquid phase during the solidification of the alloy. Elements such as nickel, tungsten, rhenium and ruthenium for the most recent generation are not released into the liquid phase and are distributed preferably in the dendrite after solidification. The other elements, therefore, tend to segregate in the interdendritic spaces of the alloys [5]. Thus, a solution heat-treatment is required after the casting of the nickel-based superalloys to homogenize their microstructure. This treatment makes it possible to break the dendritic chemical inhomogeneity inherited from the solidification and to dissolve the γ/γ' eutectics pools. For this, the alloy is usually heated above the γ' solvus temperature and the closest possible to the incipient melting temperature (or solidus) to achieve the best chemical homogeneity in a reduced time. Thereafter, the alloy is quenched and two subsequent tempering (ageing) treatments are often performed to adjust the size and morphology of γ' precipitates, so as to achieve a regular array of cubical precipitates. During the first aging at 1080°C for 6h, followed by air quench, a very regular array of cubical precipitates is obtained. The last aging heat treatment is conducted at lower temperatures (typically between 750°C and 900°C) to relax residual stresses introduced during all processing steps (e.g. perforation of the cooling holes) and to make thinner γ matrix channels between the γ' allowing to limit dislocation mobility, hence to improve creep and fatigue resistance [13].

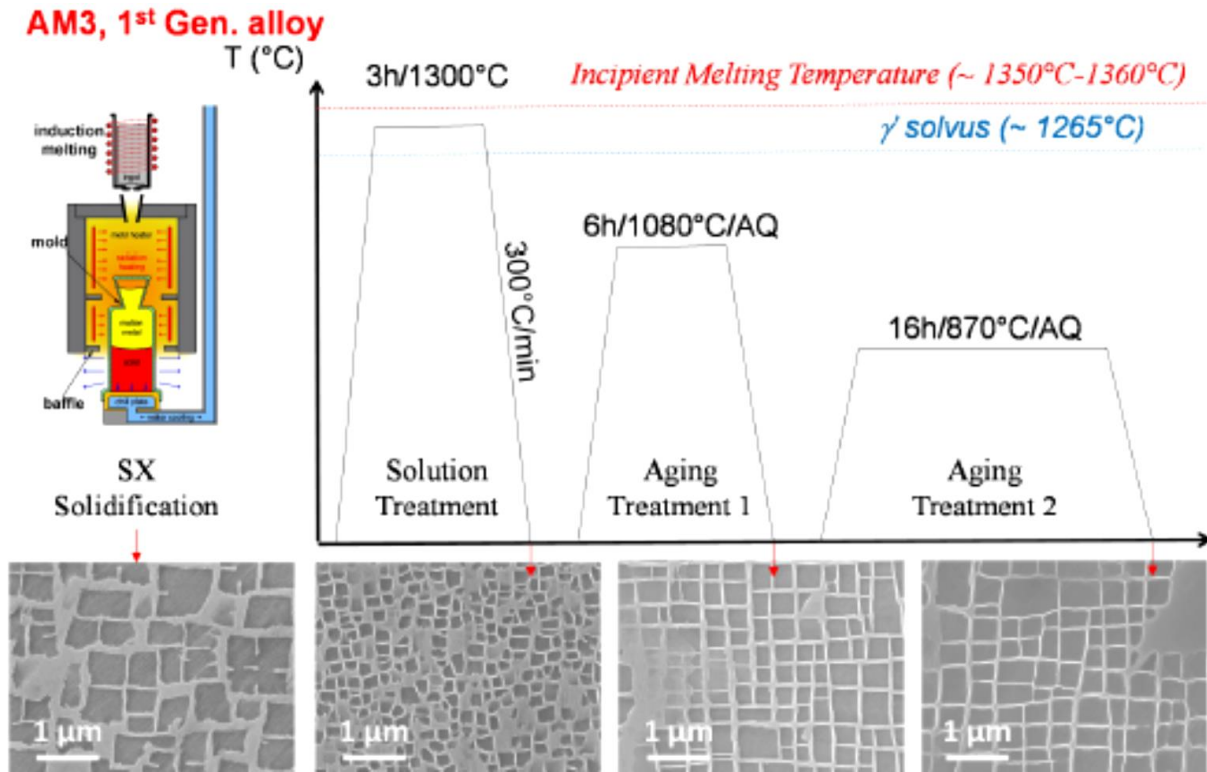


Figure I-4: γ' - γ microstructure evolution in primary dendrite arms of AM3 1st generation Ni-based SX superalloy from as cast to fully heat-treated state [13].

II.C-Alloying elements

The most advanced generation of single-crystal turbine blades operate at a temperature greater than 85% of their absolute melting temperature [10]. To increase resistance to creep and oxidation and corrosion resistance different elements can be added. The effect of the various alloying elements used in the nickel-based superalloys is summarized in Table I-1 and Figure I-5 [5, 13]. Ti and Ta are added to increase the proportion of hardening γ' phase, by substituting Al in γ' -Ni₃Al. Cr, Co, Mo and Re partition into the γ matrix and act mainly as solid solution strengthening elements to increase the creep properties [14]. Al and Cr play a fundamental role in promoting the formation of a stable alumina and chromia surface scales, which respectively promote the oxidation and corrosion resistance. The heavy refractory elements Mo, W, Re and Ta increase the creep properties by solid solution strengthening while the Ru added in the most advanced generation also improves fatigue properties. However, the contents of these elements shall be carefully controlled to avoid the formation of topologically close-packed (TCP) phases, such as σ , μ , P, etc., because they are brittle and lower ductility and creep strength [7,15-16]. These TCP phases also occur during the Al inward diffusion from aluminide coatings to the substrates.

III-Degradation of metallic materials at high temperature

The properties required to superalloys are high-temperature creep, high fatigue life, phase stability, as well as corrosion and oxidation resistance. Hot components of gas turbines operating in aggressive environments are subject to various modes of degradation that include high-temperature corrosion, oxidation and mechanical degradation (mainly erosion and foreign object damage). This thesis mainly focuses on the topic of oxidation resistance and therefore, the complex topic of hot corrosion will not be developed in this manuscript. Under normal conditions of use, the turbine blades are continuously under a pressurized flow of hot air. Oxidation is therefore inevitable and is the preponderant environmental degradation well above temperatures of 884°C (melting point of Na₂SO₄ considered as the “reference salt” of hot corrosion) (Figure I-6). Oxidation is a natural phenomenon where metal and oxygen will react together to form an oxide. The oxides have a negative Gibbs enthalpy of formation, which results in an exothermic reaction and therefore results in greater stability of the newly formed oxide. However, this phenomenon is not always harmful and protection against oxidation rely on the formation of protective oxides.

Indeed, when the oxide formed is compact, impermeable to the aggressive agent and adherent, it can offer protection against the environment. To characterize the protective aspect of the oxide, several parameters can be considered:

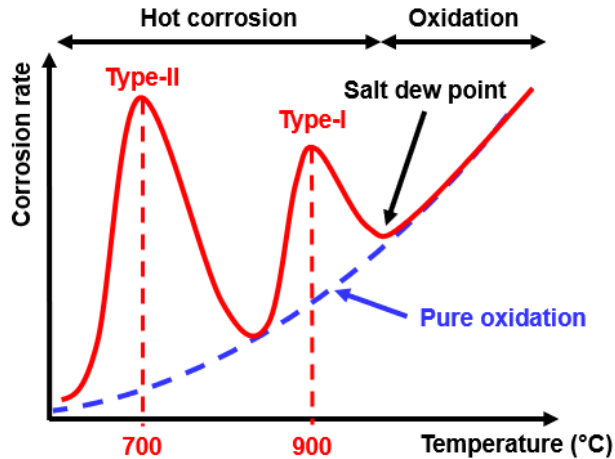


Figure I-6: Schematic illustration of the temperature dependence on the corrosion rate.

- The *Pilling and Bedworth ratio (PBR)* (eq. 1), which is the ratio between the volume of oxide formed and the volume of metal consumed or between masses [7]. If the PBR is lower than 1, the oxide layer is in compression and the oxide layer is in tension with PBR greater than 1. These stresses can induce cracks in the oxide layer or at the metal/oxide interface and ultimately spall off the oxide. The ideal case is when the PBR ratio is between 1 and 2, but this condition alone is not enough. Indeed, the RPB of HfO₂ or NiO is respectively 1.62 and 1.65, however, these oxides are harmful, unlike Al₂O₃ which is 1.28.

$$PBR = \frac{V_{oxide (formed)}}{V_{metal (consumed)}} = \frac{M_{oxide} \cdot \rho_{metal}}{n \cdot M_{metal} \cdot \rho_{oxide}} \quad (\text{eq. 1})$$

With:

M_{oxide} : molar mass of the oxide ($\text{g}\cdot\text{mol}^{-1}$)

M_{metal} : molar mas of the metal ($\text{g}\cdot\text{mol}^{-1}$)

N: number of metal atoms in the stoichiometry of the oxide

ρ_{oxide} : density of the oxide ($\text{g}\cdot\text{cm}^{-3}$)

ρ_{metal} : density of the metal ($\text{g}\cdot\text{cm}^{-3}$)

- The coefficient of thermal expansion (CTE), is the most important parameter under thermal-cycling conditions. If the differences of CTE between the superalloy and oxide are large (Figure I-7), the oxide layer will detach from the substrate, during the cooling part, thus causing a loss of mass and leaving a naked metal surface. Upon subsequent cycling, new layers of oxide may repeatedly detach and grow again, which consumes good metal thickness leading to the loss of mechanical properties.

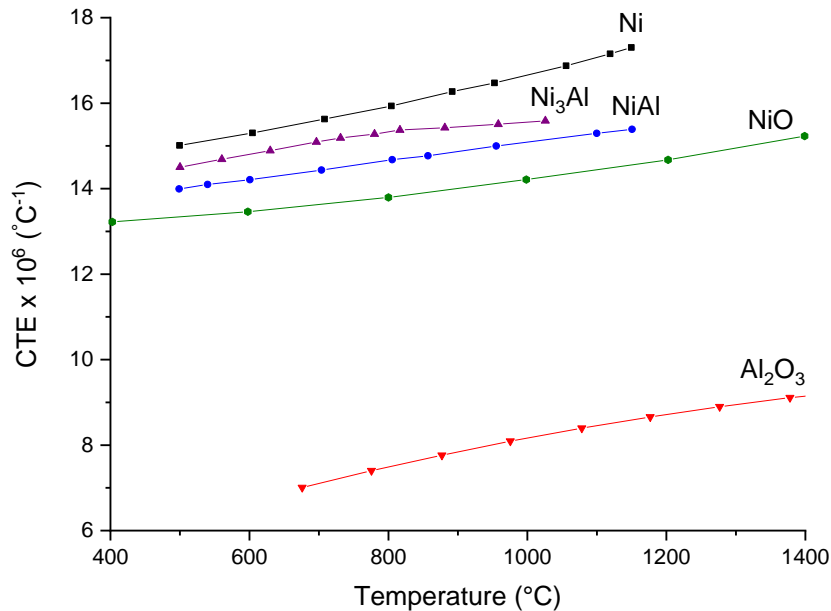


Figure I-7: The variation of CTE with temperature of $\alpha\text{-Al}_2\text{O}_3$ [17], pure Ni [18], NiAl [19], Ni₃Al [19] and NiO [20].

- The kinetic study is also an important element. These studies are carried out in most cases by measuring the variations of the mass of a sample in a chamber at high temperatures and under an aggressive atmosphere (thermogravimetric analyses). In an ideal case, a slow mass gain followed by a stagnation of mass, indicate that the oxide formed is impermeable to the aggressive

agent, but these behaviors never occur at high temperatures. It is therefore better to rely on oxide with slow parabolic growth, this will indicate that the growth of the oxide layer is rather anionic with a majority diffusion of oxygen towards the material. Anionic diffusion is preferred over the cationic diffusion because in the case of cationic diffusion the oxide forms outwardly, a vacancy flow is then formed in the other direction. These vacancies can segregate at the interface oxide/metal and pores are formed, which will weaken this interface (Kirkendall porosity). Thus, during thermal stress due to the CTE, the oxide layers can detach from the substrate.

One of the elements that have the best protective oxide for this temperature range is aluminum. Indeed, aluminum forms very quickly an oxide scale of alumina at 1100°C (α -Al₂O₃). The growth of this oxide follows a parabolic law and has a PBR of 1.28, one of the closest to an ideal value.

A comparative study of cyclic oxidation performance on 1st to the 4th generation of single crystal superalloys confirmed that in the latest generation, the mass loss by spallation of the oxide scale in cyclic oxidation conditions becomes larger (Figure I-8). Indeed, the latest generation of alloys has higher mechanical strength than the previous versions at the expense of their resistance to oxidation and corrosion. The latest generation of alloys has more interesting mechanical properties characteristics, due mostly to the addition of Re and Ru. However, mechanical resistance and oxidation resistance are incompatible properties. Indeed, the addition of Re and Ru induces oxidation of these two species in Re₂O₇ and RuO₄. Once these oxides have formed, they vaporize on the surface inducing significant spallation and consequently a reduction in the sound metal parts, which bear the mechanical loads [21]. To sum up, in nickel-based superalloys, Al plays a major role against oxidation resistance at high temperatures. However, it is kept below 6 wt.% to maximize the creep resistance and to avoid brittleness of the alloy. When such alloys are exposed to the environments encountered in gas turbines, they will rapidly degrade. Therefore, the current choice is to employ highly mechanical resistant superalloys and provide oxidation (and corrosion) protection through the application of coatings among which nickel aluminides are very popular in the turbine components [22].

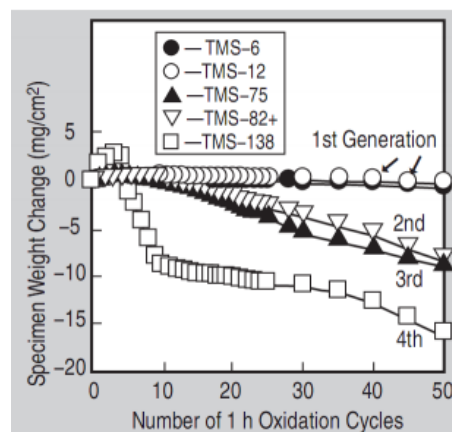


Figure I-8: Cyclic oxidation testing at 1100°C under air (1h hold at high temperature) for various generation of SC superalloys [21].

IV-High temperature protection of nickel-based superalloys

With the advent of turbojet engines and the increased gas flows and temperature, surface engineering has become an important area of research. To protect the parts from oxidizing or

corrosive environments, metallic coatings are most commonly used. These metallic coatings must be mechanically and chemically compatible with the substrate to maximize their effectiveness and service life. Coatings are often divided into two categories, overlay and diffusion coatings.

Overlay coatings, often refer to MCrAlY coating (with M= Ni in nickel-based superalloys). These Cr-rich coatings are mainly used when Type-I and Type-II hot corrosion are encountered [23-29]. These coatings are produced from metallic powders with selected chemical concentrations and sprayed at very high speed in the form of a molten droplet, by plasma spray or by high-velocity oxy-fuel (HVOF) [7].

Diffusion coatings are formed by enriching the surface layer of the superalloys with Al, Cr or Si. [8,23,29], and are generally produced by chemical vapor deposition (CVD) [29], like pack cementation [30-33] or other gas-phase processes [30,33-35]. To a lesser extent, slurry coatings are also used in repair stages to form a diffusion coating. Slurry coatings are characterized by their great flexibility. Indeed, it is an easy method to set up, easily adjustable, inexpensive and often environmentally friendly. In all cases, a donor compound that will deliver the element/s to the substrate to be coated shall be considered, for instance Ni/Al alloys or pure Al donors release Al to form the coating. The enrichment of the substrate with a protective element (Al, Cr or Si) allows the formation of a thin and adherent protective oxide scale, which decreases the kinetics oxidation [6-7,36]. Alumina oxide scales are particularly interesting since the oxide maintains good stability at elevated temperature and there is barely any points defect in the scale [7]. As a result, and under majority oxidation conditions, diffusion coatings developed for nickel-based superalloys are generally based on the unique formation of a layer of alumina.

In addition, for the very hot parts such as vanes and blades in the high-pressure turbines located at the outlet of the combustion chamber, thermal barriers are also added. Thermal barriers have a low thermal conductivity, which allows to thermally insulate the system and can, therefore, decrease the surface temperature by a hundred degrees provided the rear surface of the substrate is also cooled down [37-39].

IV.A-Diffusion coatings

To understand the processing and behavior of high-temperature coatings, background in thermodynamics, the kinetics of reactions, diffusion, crystal structure, phase equilibrium, and phase diagrams of alloys is necessary.

Diffusion is a process of the mass transport through matter. In solids, there are three main diffusion mechanisms. The first one is known as volume diffusion, atoms diffuse by migrating from atomic sites through vacancies. The second mechanism is a modification of the first, in which the atoms migrate through defect sites such as dislocations, surface and grain boundaries. The third mechanism involves the movement of atoms through interstitial atomic sites. The driving force of diffusion is the reduction of free energy. In many cases, this results from the existence of a concentration gradient occurring between higher and lower concentrations. The rate of diffusion is governed by Fick's laws.

IV.B-Nickel aluminide coatings and Ni-Al binary phase diagram

Nickel aluminide diffusion coatings are based on the β -NiAl intermetallic phase (Figure I-9). Even if we will focus on a Ni-based superalloy of complex chemical composition, the equilibrium binary phase diagram (Figure I-9) can give useful information on the typical phases in Al diffused coating of Ni-base superalloy.

The γ -Ni phase dissolves up to 4wt.% of Al below 400°C. The solubility increases as the temperature is raised. The γ' -Ni₃Al phases has a narrow phase field, which means that the composition does not vary significantly from Ni₃Al. The β -NiAl domain phase is much larger than that of the other phases and has a great concentration in Al. The β -NiAl intermetallic phase is particularly advantageous for reducing the harmful effect of oxidation at high temperatures. Indeed, this phase has a high melting point and a relatively low density (5.9 mg/cm² [40-42]). In addition, the coefficient of thermal expansion is close to the nickel-based superalloys (Figure I-7) [40-41]. At high temperatures, this phase develops a unique formation of alumina, which is characterized by slow growth and good resistance to spallation. The high Al concentration helps in providing a large reservoir of Al for oxidation protection through the formation and replenishment of the α -Al₂O₃ oxide scale [43-45]. These characteristics are very favorable in high-temperature coatings. Al₃Ni₂ and Al₃Ni phases contain a higher proportion of Al, which would make a reservoir with a larger capacity. However, these phases are less stable and brittle. In addition, a significant difference in concentration between the coating and the substrate induces a high interdiffusion rate. This will cause an accelerated depletion of the reservoir.

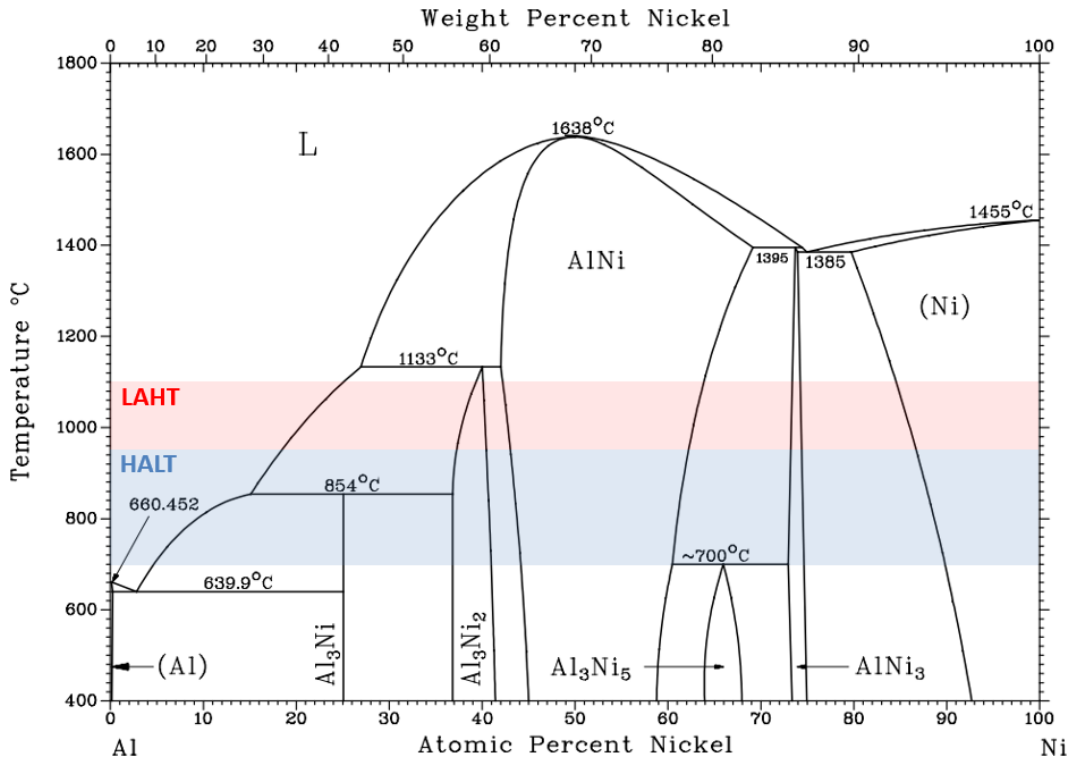


Figure I-9: Binary Al-Ni diagram phase [46].

To enrich the substrate with aluminum (aluminizing process), there are several methods such as high and low activities. These methods will be detailed in the following sections.

IV.C-High-activity and low activity-activity diffusion coatings

During the aluminizing process, one of the main factors that controls the microstructure of the coating is the activity of Al [28]. This activity is most often governed by the temperature of the process and/or by the Al donor source. Indeed, the high-activity coatings are produced between 700°C and 950°C and the low-activity coatings between 950°C and 1100°C (Figure I-9) [21,29,47].

The differences in microstructures are then linked to the mechanisms of formation of the coatings, and more particularly to the interdiffusion coefficient between Al and Ni [48].

- **HALT: High-Activity Low temperature (700 and 950°C)**

When the donor is rich in Al, the inward diffusion of Al in the substrate occurs at relatively low temperatures, and the mobility of Al is greater than Ni at low temperatures [48]. The fast Al diffusion leads to the formation of an Al-rich phases (i.e. NiAl_3 and Ni_2Al_3) in the substrate. When these phases are formed, the diffusion of Al is still preponderant and it keeps on diffusing into the substrate [31,48]. Simultaneously, the refractory elements such as W, Mo, and Ta segregate in the outer region of the coating (close to the interface coating/air) (Figure I-10.a). Carbides and other impurities can also be trapped in the coating. The phase often formed with this method is Ni_2Al_3 [31]. However, given its instability and brittleness, a subsequent annealing treatment is conducted between 1000 and 1100°C to form a β -NiAl phase [31,49]. As a result, an interdiffusion zone rich in precipitates forms under the initial surface (Figure I-10.a). This microstructure obtained is thus typical of the high-activity pack cementation (gas phase) [31,47,50-51] and simple aluminide slurry (liquid/solid) coatings [31,52]. One great advantage of this method is that the overall wall thickness is not increased, which is particularly interesting in components with very narrow dimensional tolerance as opposed to the coatings growing over the initial surface (LAHT).

- **LAHT: Low-Activity High-Temperature (950°C and 1100°C)**

The low activity coatings are carried out in a temperature range between 950 and 1100°C, where Ni preferentially diffuses compared to Al. The diffusion takes place outwardly from the initial surface of the substrate and a β -NiAl phase is directly formed [31]. The main outward diffusion of Ni above the substrate's surface brings about an "additive zone" free of precipitates (Figure I-10.b). However, the depletion of Ni under the initial surface brings about a concentration of the refractory elements in the "interdiffusion zone" and form numerous precipitates [31]. The interdiffusion zone is proportionally larger for the high-activity method than the low activity. Diffusion coatings by low-activity are often preferred to those produced by high-activity because they are precipitate-free, which gives better resistance to oxidation [53]. This coating microstructure is commonly observed with the out-of-pack process (gas phase) [34,47,51,54-55] and pack cementation using master alloys as Al donors [30]. Recently, low activity slurry coatings using powders of Cr/Al alloys, mixed Cr and Al powders and layers of Cr and Al powders have also been reported [56-59].

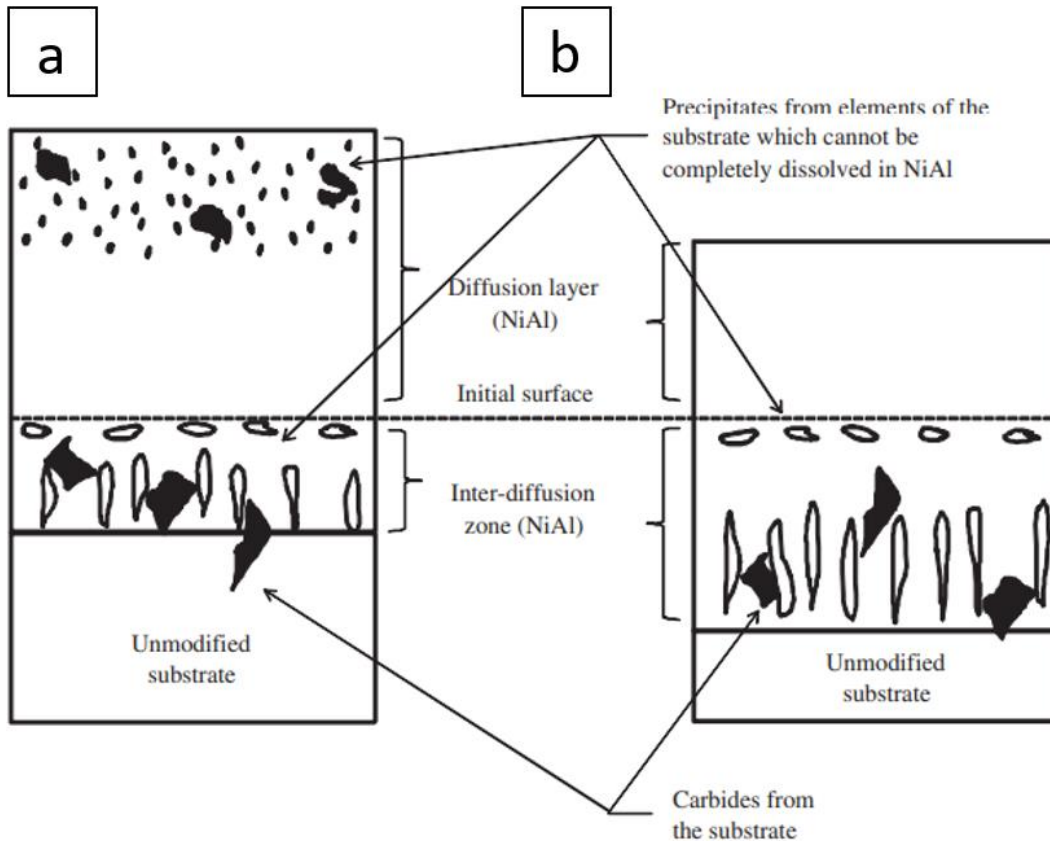


Figure I-10: Comparison between High-Activity Low-Temperature (HALT) and Low-Activity High-Temperature (LAHT) aluminide diffusion coatings [55].

V-High-temperature ageing of coated superalloys

V.A-Oxidation of nickel aluminide coatings

In service, the turbine blades are exposed to very hot gases coming out of the combustion chamber. At this temperature, the formation enthalpies of aluminum oxide and nickel oxide are -1689 and -469 kJ.mol⁻¹, respectively. Therefore, selective oxidation of Al from the β -NiAl coating occurs.

Several types of alumina can form with increasing temperature and exposure (Figure I-11.a). First, an amorphous alumina forms and crystallizes in a cubic structure to form γ -Al₂O₃. Then γ -alumina gradually turns into θ -Al₂O₃ of monoclinic structure and finally into α -Al₂O₃ of hexagonal structure. The allotropic α variety forms because of its hexagonal structure is the most among the different Al₂O₃ polymorphs [59] and is the one requested to protect the turbine blades.

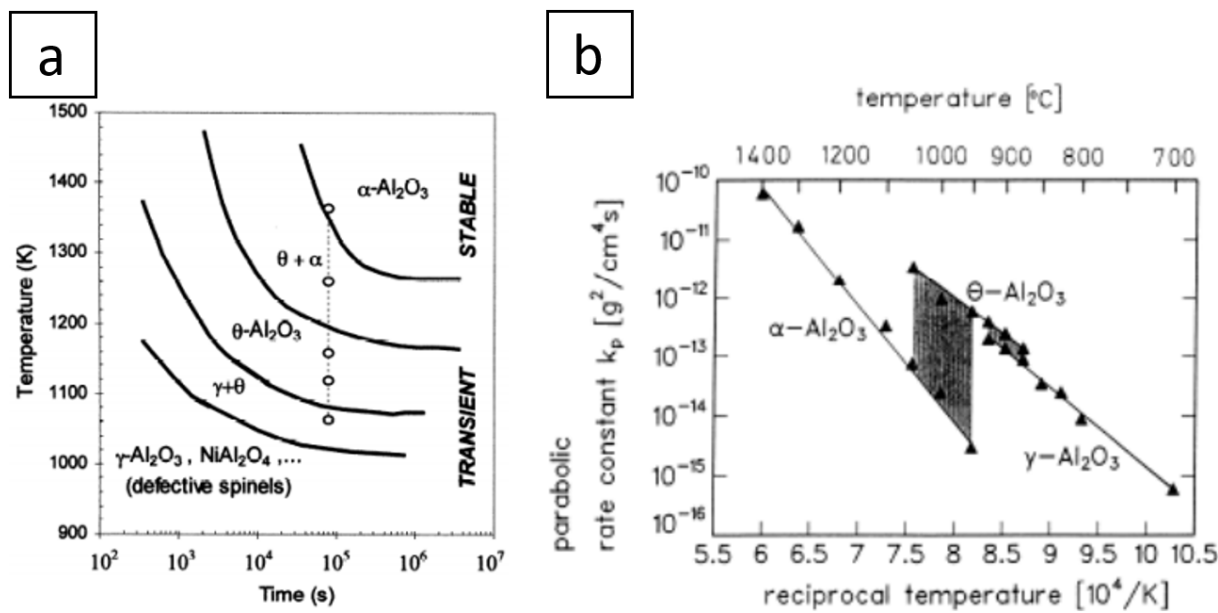


Figure I-11: (a) Schematic Temperature-Time-Transformation diagram for high-temperature oxidation of β -NiAl alloy [50] (b) Arrhenius diagram representing the kinetics of oxidation of aluminas [60].

Under the conditions encountered in the turbine blades (around 1100°C), the stable form α is obtained after the transformation of the transition alumina, mainly θ -Al₂O₃. It can be noted that the preferential formation of one or the other form of alumina, as well the rates of transformation depend on several parameters such as surface preparation or oxygen partial pressure [61].

θ -Al₂O₃ is a fast-growing oxide (Figure I-11.b and $k_p = 7.2 \cdot 10^{-6} \text{ mg}^2 \cdot \text{cm}^{-4} \cdot \text{s}^{-1}$ at 1100°C [60]) by major outward cation diffusion, which leads to an external growth of the oxide [44,60,62-64].

In the case of α -Al₂O₃, the formation mechanisms are not clearly defined. The diffusion coefficients of O²⁻ and Al³⁺ in alumina [65] do not explain the slow oxidations kinetics of α alumina (Figure I-11.a and $k_p = 1.62 \cdot 10^{-7} \text{ mg}^2 \cdot \text{cm}^{-4} \cdot \text{s}^{-1}$ at 1100°C [60]). Therefore, some authors [44,66-67] put forward two types of mechanisms whereby the growth of α -Al₂O₃ would be governed by a mixed anionic and cationic mechanism. First, oxygen (O²⁻) diffuses into the oxide layer mainly through the grain boundaries, which leads to oxidation of Al at the metal/oxide interface. In a second time, during the stationary phase the cations (Al³⁺) and anions (O²⁻) diffuse mainly through the grain boundaries and in opposite direction. The oxide can thus form at the grain boundaries [68], inducing an increased grain size and a slow decrease in the kinetics of oxidation of α -Al₂O₃ (Figure I-13.a).

For authors like Monceau et al. [69], the anionic transport of oxygen at the grain boundaries predominates over the cationic transport of aluminum. This may explain why an outer layer of equiaxed α -Al₂O₃ is observed above a layer of α -Al₂O₃ columnar structure (Figure I-12). The equiaxial grains would be composed of the alumina having germinated initially and the columnar grains are signs of an anionic growth. In addition, Al³⁺ and O²⁻ diffusing counter currently can also be trapped by defects, such as dislocations. Dislocations can climb outwards from the oxide/metal interface and climb inwards from the air/oxide interface and the new oxide molecule forms within the scale (Figure I-13.b) [68].

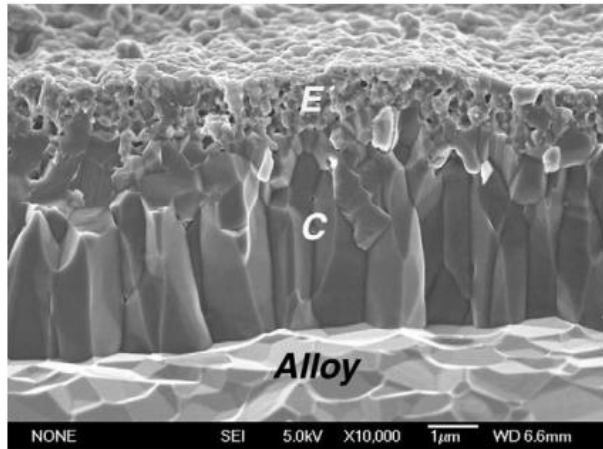


Figure I-12: Cross-section of an Al oxide formed by high-oxidation of a single crystal FeCrAlY alloy. In C the inner columnar oxide, whereas the outer portion E is equiaxial [68].

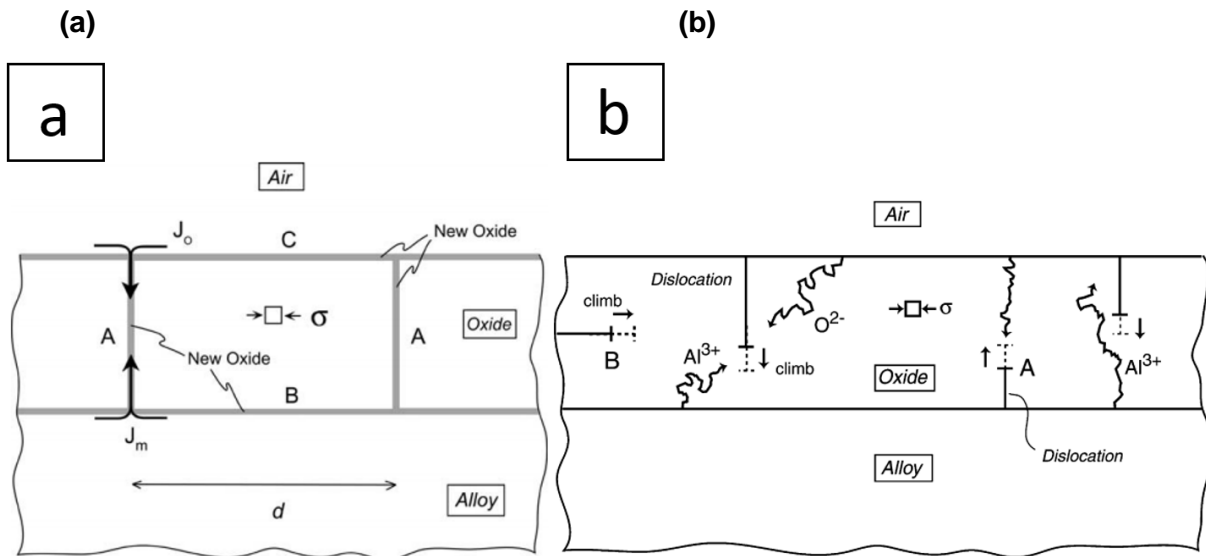


Figure I-13: (a) Schematic diagram of possible locations of new oxide formed as a result of the inward flux of oxygen, J_o and the outward flux of metal ions, J_m (b) and schematic diagram of possible edge dislocation climb due to the trapping of “unlucky” counter-diffusing Al and O ions at dislocation cores [68].

V.B-Factors and mechanisms responsible for spallation of the oxide layer

Spallation of the oxide layer is one of the main factors that determine the durability of a coating, and therefore of the system. The adhesion of the oxides partly depends on the internal stresses developed during their growth and the presence of defects at the metal/oxide interface.

- **Stress in oxide layers**

The stresses present in the oxide layers have two origins: stresses due to the growth of the oxide and stresses due to the thermal stress (especially in thermal cyclic conditions). The growth

constraints are essentially due to the variation in volume between the oxide formed and the metal consumed, characterized by the Pilling-Bedworth ratio (PBR). This ratio is 1.28 for α - Al_2O_3 formed on a β -NiAl alloy, which induces compressive stresses in the oxide layer and tensile stresses in the metal [70]. Furthermore, the allotropic transformations of alumina, which are accompanied by a change in volume, generate other types of stress. For example, the contraction in volume associated with the transformation of Θ - Al_2O_3 into α - Al_2O_3 is of about 5% and leads to constraints that decrease as the transformation takes place [71].

Thermal stresses are due to the differences in the coefficient of thermal expansion (CTE) between the substrate (Figure I-7) and the oxide layer. Thus, the oxide developed at high-temperature is subjected to compressive stresses and the substrate to tensile stresses during the cooling phases. These thermal stresses are the order of few GPa [72] and are much higher than the growth stresses of the order of hundreds of MPa [71]. Some of these stresses are relaxed by creep at high-temperature, and during cooling, cracking phenomena at the metal/oxide interface can occur, causing the spallation of the oxide layer.

- **Cavity formation at the metal/oxide interface**

The formation of interfacial cavities contributes to the reduction of the energy of adhesion of the oxide layer by reducing the contact surface between the oxide and the coating. Cavities also play the role of preferential crack initiation site during mechanical stresses, induced by the difference of CTE between the coating and the oxide layer (Figure I-7).

These cavities are empty spaces that develop and grow on the surface of the coating and under the oxide layer. Cavities can form at the start of oxidation of the coating, during the first heating ramp, or subsequently after the spallation of the oxide layer. Three major mechanisms are often proposed to explain the appearance of these cavities. The formation of the first layer of Θ - Al_2O_3 by cationic diffusion of Al^{3+} , would cause the formation of vacancies [73-74]. Indeed, the growth of the oxides induces a flow of Al coming from the coating and ending at the oxide/air interface. To fill this material departure, a flow of cationic vacancies would be created in the opposite directions. These vacancies can coalesce at the interface to form cavities [75]. A part of these cavities can either be removed when moving the oxide/metal interface with the formation of α - Al_2O_3 . Although the oxide layer is no longer in contact with the coating at the cavities, the oxide layer can continue to grow. For oxidation at 1100°C, the amount of aluminum evaporated from the surface of the cavities is greater than the amount of aluminum necessary to form an oxide [76]. For lower temperatures, the amount of Al is not sufficient and surface diffusion phenomena can fill up the cavities. The other factor that explains the formation of cavities is the Kirkendall effect [76]. The oxidation-induced Al-depleted zone on the external surface of the coatings leads to the diffusion of Ni from this zone towards the superalloy. The diffusion of Ni in the Al-poor NiAl is 3 times faster at 1000°C compared to that of Al in nickel aluminide alloys (Figure I-14) [77-78] and a countercurrent flow of Ni vacancies towards the metal/oxide interface would develop. Like in the previous case, the condensation of the nickel vacancies would thus result in the formation of cavities [79]. In contrast, the diffusion of Ni is greatly reduced (Figure I-14) in the Al-rich nickel aluminides, thereby reducing the formation of cavities associated with nickel [76]. In this situation, the formation of cavities would be thus linked to Al depletion is favored during the growth of Θ - Al_2O_3 .

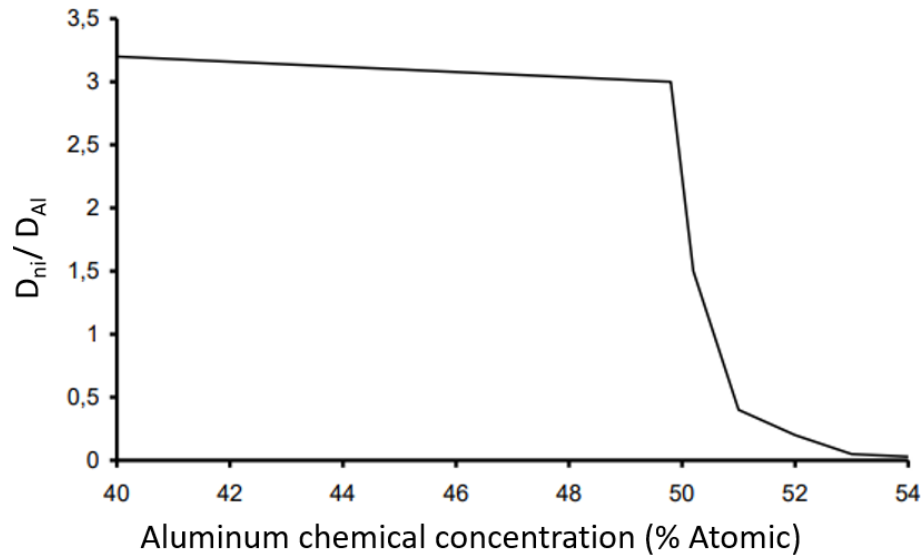


Figure I-14: Ratio of the diffusion coefficients of Ni and Al in the β -NiAl phase as function of the Al content [78].

For longer oxidation times at 1100°C, other authors [80] have observed the formation of another type of cavity related to the decohesion of the oxide layer. In thermal cycling, an undulation (roughness increase) of the interface between the coating and the oxide layer gradually takes place (Figure I-15). The stresses of thermal origin, applied in the oxide layer and coating due to the difference in CTE, therefore cause the appearance of cohesion constraints in the convex parts of this undulation. In these convex parts, the oxide layer can separate from the underlying coating, without necessarily causing spallation, and form interfacial cavities.

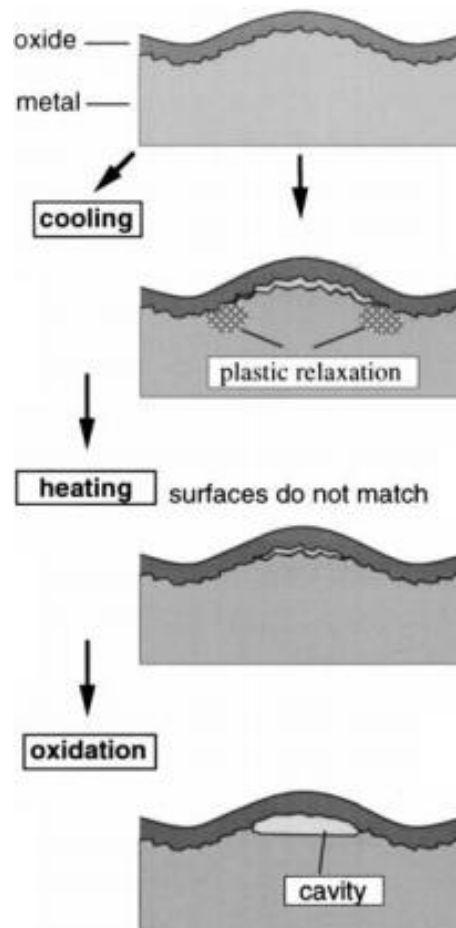


Figure I-15: Cavity formation during high-temperature oxidation [80].

V.C-Formation and propagation of the interdiffusion zone of the coating

The interdiffusion between the superalloy and its protective coating is due to the differences in chemical activities between the different elements composing the coating and the substrate. Diffusion flows of aluminum and nickel result from these large activities. Aluminum diffuses from the coating to the superalloy, while nickel and the elements contained in the superalloy diffuse in the opposite direction, towards the coating. These fluxes reduce the lifetime of the coated superalloys by modifying the oxidation behavior of the system.

The interdiffusion between the superalloy and the protective coating modifies the microstructure of the superalloy [81-91]. The enrichment of the aluminum superalloy and the departure of nickel towards the coating leads to a deterioration of the microstructure γ/γ' of the superalloy. Indeed, the γ/γ' microstructure transforms into the γ' -Ni₃Al phase and sometimes into β -NiAl. This transformation of the superalloy takes place from the aluminization stage where an interdiffusion layer is formed (Figure I-16). This area is made up of several thicknesses. First, the outermost layer in contact with the coating is composed of phases rich in γ -gene elements (Cr, Mo, W, etc.) or γ' -genes (Ta, Ti, etc.) in a matrix β -NiAl (Figure I-16.a) [47,92]. These phases appear because of the saturation of these elements during the phase transformation of the superalloy. The next layer is composed of phases rich in the γ -gene element and the β -NiAl phase trapped in the γ' -

Ni₃Al matrix. As for the previous layer, the formation of these phases is due to the saturation of the elements during phase transformation [47,92].

During high-temperature oxidation, the interdiffusion, especially between aluminum and nickel, causes the growth of this interdiffusion zone. The γ -Ni phase is transformed into the γ' -Ni₃Al phase and the thickness of the transformed zone depends directly on the time and temperature of the treatment. The γ/γ' structure of the superalloy is thus destabilized. The γ -gene elements that had saturated in the interdiffusion zone tend now to coalesce by continuous outward diffusion of nickel and inward Al diffusion. Their precipitation induce the appearance of a two-phase zone containing topologically-close packed (TCP) phases that propagate inside the superalloy (Figure I-16.b) [47].

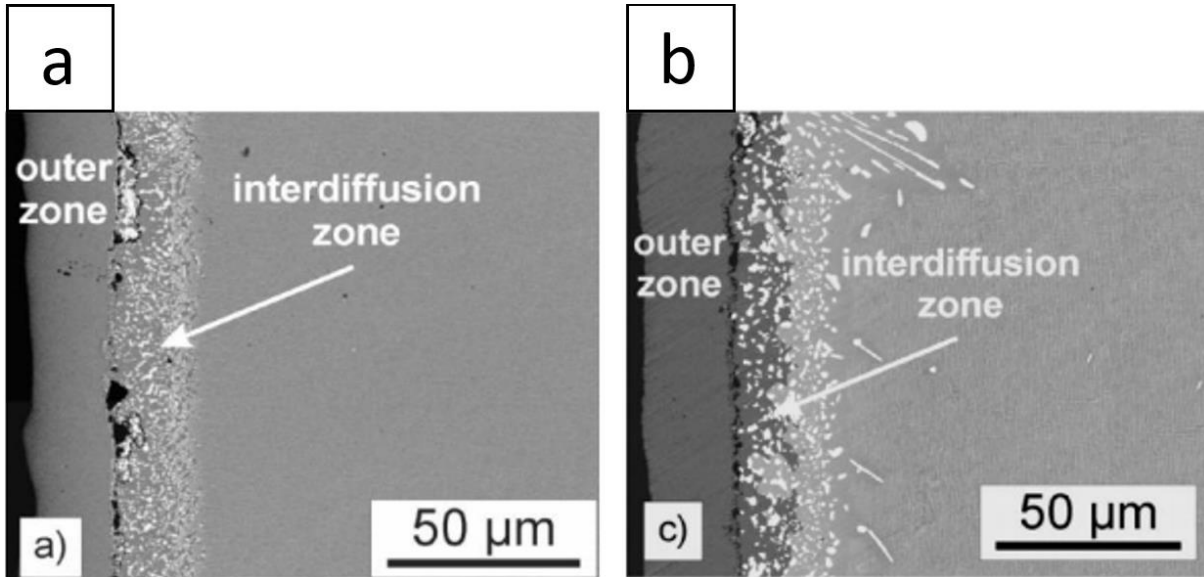


Figure I-16: (a) SEM cross section of a coated superalloy after the elaboration of coating, (b) SEM cross section of a coated superalloy after 500h at 1050 °C, under laboratory air [47].

V.D-Phase transformation in additive layer of the coating

The depletion of the aluminum coating and the enrichment in nickel leads to the transformation of the initial phase β -NiAl into γ' -Ni₃Al then γ -Ni.

Considering the loss of aluminum, the β -NiAl to γ' -Ni₃Al phase transformation is accompanied by a change in volume [93]. The reduction in volume induced by this phase transformation ($V_{\gamma'} = 0.62V_{\beta}$) causes tensile stresses within the coating. The increase in stresses due to this transformation induces an increase in the roughness of the metal/oxide interface [93].

These transformations and the depletion of Al lead above all to the loss of the oxidation resistant properties of the coating. Indeed, the low Al concentrations of the γ' -Ni₃Al and γ -Ni (Al) phases do not allow the formation of a protective oxide layer of α -Al₂O₃ [79,94-95]. During oxidation at 1100°C of the intermetallic compound γ' -Ni₃Al leads to the formation of nickel-rich oxides, such as spinel NiAl₂O₄ and the oxide NiO which coexists with alumina. The formation of several layers of non-protective oxide greatly increases spallation and drastically reduces the life of the system.

VI-Diffusion barriers

In the last paragraph, it has been shown that the interdiffusion between the substrate and the coating has harmful consequences on the life of the protective coatings. The main consequences are accelerated depletion in Al. N. Vialas [96] showed in a (Ni,Pt)Al coating exposed to 1050°C for 100 hours that the quantity of Al consumed by oxidation was of the order of 2 to 8% while the one lost by diffusion towards the superalloy reached 20 to 35% of the Al depending on the superalloy. For a very long period of oxidation (more than 15.000 hours), the tendency would be reversed, and oxidation would be a more important cause of loss of Al in the coating. Her results demonstrated that the increased performance of protective coatings cannot be solely achieved by the introduction of platinum in the coatings and therefore, the introduction of intermediate diffusion barriers have also been proposed [97-98]. Such diffusion barriers are placed between the coating and the superalloy to limit the diffusion of Al into the substrate, so as to increase the life of the coatings.

VI.A-Diffusion barrier based on an oxide layer

Some authors [99-102] have developed diffusion barriers based on Al oxide, such a γ -Al₂O₃, or compounds such as Ti-Al-O-N or even Al-O-N. Among these compounds, Al-O-N seems the most effective, due to this great stability at high-temperature. For diffusion barriers based on γ -Al₂O₃ [101], their efficiency is reduced due to transformation into α -Al₂O₃. This transformation induces a change of volume, crystallographic transformation and initiation of cracks favored the interdiffusion between the superalloys and the protective coating MCrAlY.

One of the oxides that can be considered for the development of diffusion barriers is α -Al₂O₃. With a compact hexagonal structure, few points of defects and high stability, α -Al₂O₃ is an oxide that has many interesting properties for a diffusion barrier application. Several studies [97,103] have therefore verified the possibility of depositing a layer of α -Al₂O₃ on a superalloy to quantify its effectiveness as a diffusion barrier between CMSX-4 and a coating of NiCoCrAlY type. Initially, Müller et al [97] showed that the CVD deposition methods it possible to deposit a dense and adherent layer of α -Al₂O₃ of approximately 3 μ m of thickness, however, a layer of a TiN with a thickness of 1 μ m is necessary for obtaining a compact layer of α -Al₂O₃. Subsequently, the effectiveness of this TiN/Al₂O₃ layer was tested between a CMSX-4 and a NiCoCrAlY coating. After 100h at 1100°C under an inert atmosphere, the samples with a diffusion barrier do not have an interdiffusion zone, while the system without diffusion barrier has an interdiffusion zone of 6 μ m for a duration of 10h (Figure I-17.a). For a period longer than 100h at 1100°C, the diffusion barrier layer remains intact and chemically stable (Figure I-17.b).

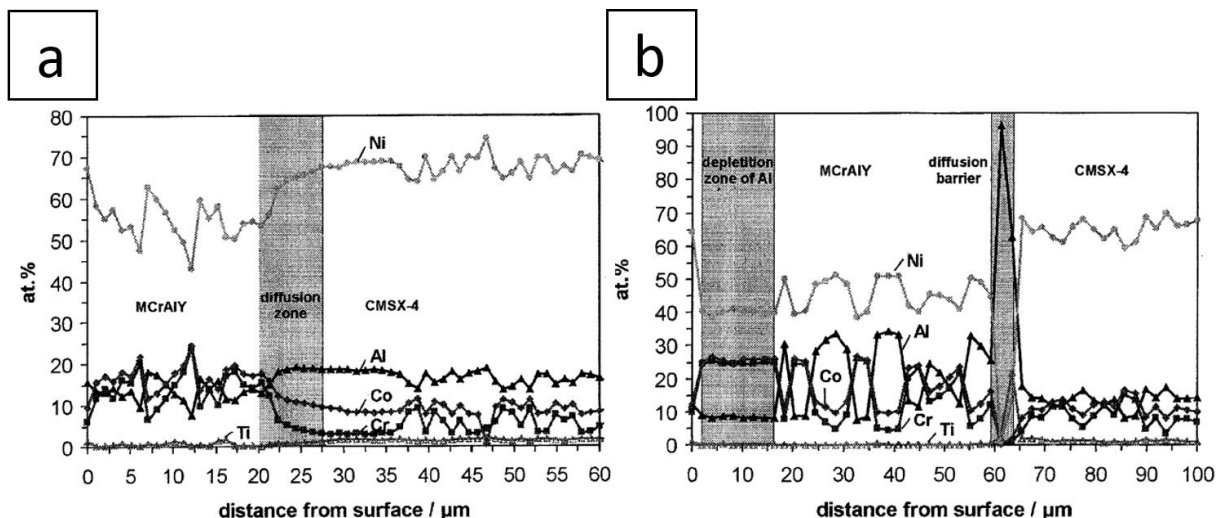


Figure I-17: (a) WDX linescan coated CMSX-4 sample without diffusion barrier annealed for 10h at 1100°C in Ar and (b) WDX linescan of a coated CMSX-4 with diffusion barrier sample annealed for 100h at 1100°C in Ar [103].

In a similar vein, other studies [104-105] developed a diffusion barrier using the EB-PVD method. By heating the substrate with an electron beam and under low oxygen pressure, an oxide layer composed of NiO, Cr₂O₃, and α-Al₂O₃ of thickness varying between 200 and 500 nm was grown. This diffusion barrier slows down the depletion of the coating in Al and Cr.

The main drawback of these oxide-based diffusion barriers is the difference in CTE. Indeed, the difference in CTE between the coating and the oxide layer and between the oxide layer and the substrate can induce stresses during cyclic oxidation, which in turn cause cracks, spallation and ultimately the ruin of the system.

VI.B-Diffusion barriers enriched with refractory element

The second type of diffusion barriers consists of refractory elements (high melting temperature) such as Re and W. The challenge of this approach is to form a dense layer composed of an intermetallic rich in refractory element between the coating and the superalloy [106-112]. The desired phase should be stable and an extremely high melting point (e.g. α(Re(W)-Cr-Ni with a T_f= 2284°C). High melting temperature is necessary to limit the diffusion to the intended applications.

A study [106] on diffusion couples between Re/Ni and Re(1-x)Ni-xAl (with x=0.12, 0.25 and 0.5) was realized at 1100°C to quantify the stability of a diffusion barrier between a superalloy and a protective coating of β-NiAl. The kinetics of diffusion of Re in γ-Ni phase is very low [113]. However, the solubility limit of Re in the γ-Ni phase is important, which can deteriorate the stability of the diffusion barrier for long periods of oxidation. The diffusion couples are very stable and show little interdiffusion after 100h at 1100°C. This agrees with the very low solubility limits of Re in γ'-Ni₃Al and β-NiAl intermetallics compounds.

The manufacturing process for these diffusion barriers enriched with refractory elements is however very complex and require a large amount of operations. In addition, the effectiveness of these barriers strongly depends on the experimental parameters used during the development of

the barriers and coating. Sumoyama et al. [111] studied electroplating of Re(Ni) and Ni(W) films, Al- and Cr- (high-Cr and low-Cr) pack cementations, and a combination of the two treatments. With the low-activity chromizing, the interdiffusion zones of 10 μm thick were observed. In contrast, the high-activity chromizing resulted in a dense zone of TCP phase precipitates present over a thickness of 100 μm (Figure I-18).

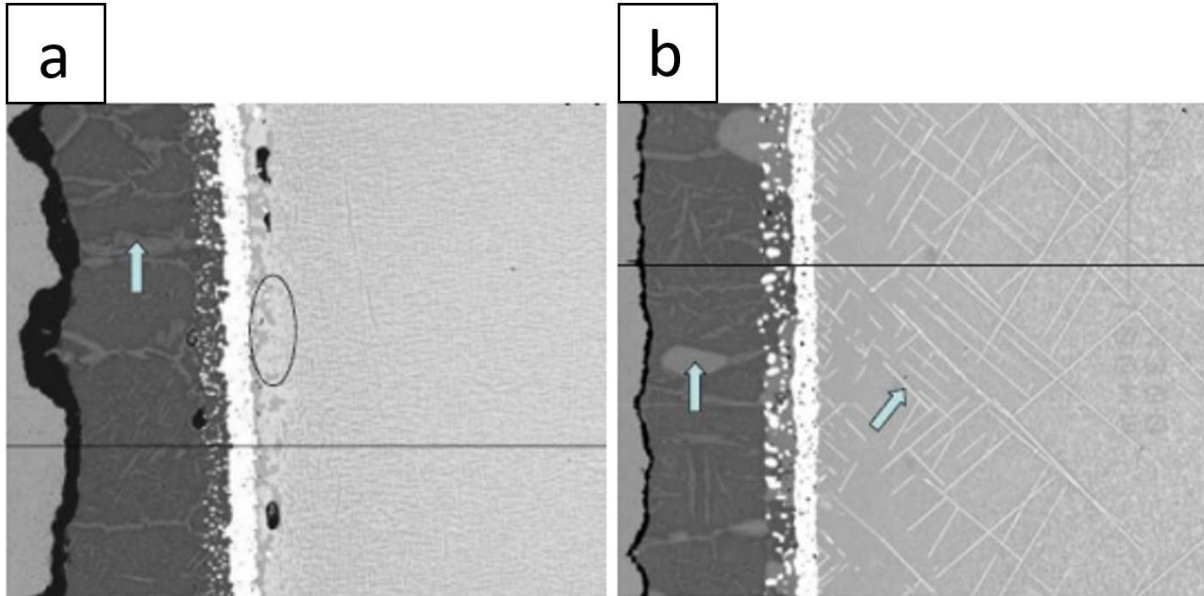


Figure I-18: Cross-section of a system with a diffusion barrier oxidized at 1150°C for 100h and having undergone a low-activity chromizing (a) or a high-activity chromizing (b) during their development [111].

VII-Motivation of the present study

VII.A-Slurry coating

Over the last decades, new approaches to produce protective coatings have been developed to comply with environmental and safety regulations [114-125]. In this sense, the slurry coating technique has been studied in several thesis at La Rochelle University. M. Mollard [119], B. Rannou [121], M. Brossard [122] and G. Grégoire [123] studied the slurry deposits on model Ni, Ni20Cr and on different superalloys and the resistance to isothermal and cyclic oxidation in air and in water vapour in addition to the Type II hot corrosion were assessed. C. Boulesteix [124] focused her investigations on the slurry aluminizing on different steels for to procure resistance to steam conditions. G. Boissonnet [125] employed the slurry approach to create thermal barrier coatings. The pioneer works of the slurry approach using water-based suspensions containing Al microparticles were proposed by Pedraza et al. by spraying the slurry on pure Ni [116]. After annealing in Ar atmosphere, a typical high-activity diffusion coating formed due to high Al contents in the donor [115,126]. Such microstructure resulted from the high exothermal synthesis [52,117,127]. A schematic representation of the different steps for the mechanisms of formation is given in Figure I-19. The diffusion layer increases rapidly due to the high exothermic reaction between the substrate and the Al particles. The synthesis reaction is mainly controlled by the molten Al, which dissolves the substrate and forms an intermetallic Al-rich Ni_xAl_y phase (Figure I-19.a). When all the Al particles have reacted, solid state diffusion occurs between the Al-rich phase

formed and the Ni-rich substrate forming a layer of Ni_2Al_3 (Figure I-19.b). The subsequent annealing treatment at high-temperature (i.e. 1000-1100°C) brings about major Ni outward diffusion and stabilizes the β -NiAl phase (Figure I-19.c). A foam of residual alumina shells (also called bisque or residue) remain on the surface at the end of the treatment. This foam can be removed by sandblasting or can be used, with a specific treatment under steam, as a thermal barrier [125]. Low-activity aluminide coatings have been also studied by making the Al powders react with Cr powders or with a Cr interlayer, which allows to increase the Type II hot corrosion [123]. The versatility of the slurry approach thus inspired me to evaluate the possibility of synthesizing self-restoring or self-healing coatings while considering the “diffusion barrier concepts” described above.

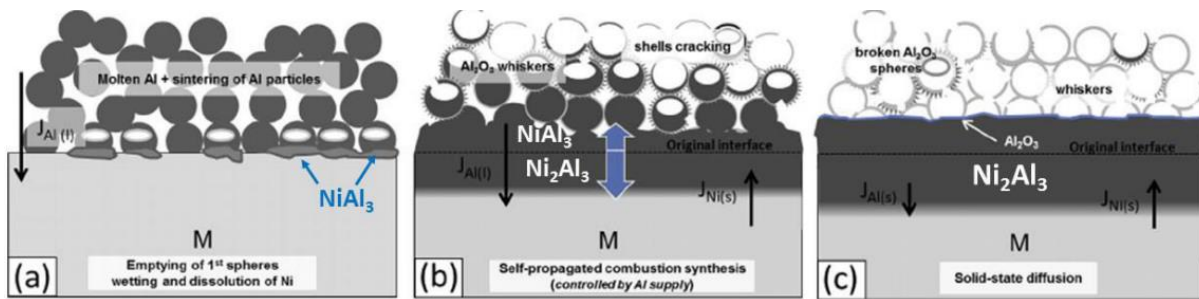


Figure I-19: Mechanisms of formation of the slurry coating [52].

VII.B-Synthesis of a self-restoring coatings

As seen in the previous parts, many turbine components are made of nickel-based superalloy and are protected against high-temperature oxidation by nickel aluminide diffusion coating, which permit to form a protective Al oxide of Al_2O_3 . However, the amount of Al decreases over time, due to the formation of the oxide layer and mainly by interdiffusion between the coating and the substrate. Below a critical content of Al content, the formation of a protective scale cannot be maintained and the protection is lost. To guarantee a sufficient quantity of Al diffusion barrier can be placed between the coating and the substrate. These barriers can be effective but are difficult to produce.

In this context, the main objective of this PhD is to elaborate a self-restoring coating, based on the slurry and aluminothermic approach, in a single step process.

The idea and the concept of self-healing or self-regenerating coatings are not new. In fact, in many fields, polymeric coatings are used as an environmental barrier to protect metallic structures, in particular from corrosion. When these barriers have a defect, scratches, or shock, the barrier action is no longer ensured and rapid corrosion of the metallic surface occurs. To prevent this, polymeric microcapsules or a vascular network can be incorporated into the polymeric coating (most often these capsules contain a resin and a hardener). When a shock or a scratch occurs, the capsules are broken and the elements contained in the capsules are released and reform a layer of polymers at the location of the defects thus preventing the degradation of the part to be protected [128].

More recently, the field of thermal barriers has benefited from the beneficial effect of self-regenerating coatings. This time, micro-capsules containing an Si-Mo alloy are trapped inside the

thermal barrier. When a crack occurs (caused by thermal or mechanical stresses), these capsules of Si-Mo alloy will oxidize in contact with hot air. A liquid glass then forms and fills the crack, thus preventing the propagation of the crack [129].

This concept of incorporating micro-capsules into coatings is therefore not new. All the originality of this study is to extrapolate these ideas to the metallic diffusion coatings for the very first time in the open literature. In the field of high-temperature oxidation and nickel-aluminide coatings, there are two main causes of coatings failures are Al depletion and the diffusion/oxidation of refractory elements to the surface. Thus, our idea is to incorporate alumina micro-capsules containing an Al-rich Ni_xAl_y alloys. Under operating conditions, a continuous flow of Al towards the superalloy has formed. When a critical level of Al is reached in the coating, a flow of Al from the micro-capsules will form between the capsules and the coatings passing through alumina shell. Also, these micro-particles will create obstacles for the diffusion of Al towards the substrate and harmful elements towards the coating (Ni, Ta, Ti, etc.). It is expected that these longer diffusion paths will delay the diffusion and oxidation of the harmful elements towards the surface.

Ideally these micro-particles should be composed of an $\alpha-Al_2O_3$ shell to avoid any phase transformation which will weaken the shells and of an intermetallic compound of Al_3Ni_2 or Al-rich NiAl which will be an important source of Al.

$\alpha-Al_2O_3$ has several advantages for constituting the shell of micro-particles. In fact, alumina has a great chemical and thermal stability and a very low wettability with Al. In addition, numerous studies have focused on the diffusion of Al^{3+} and O^{2-} ions through $\alpha-Al_2O_3$. One of these studies by Paladino and Kingery [130] measured a diffusion rate of the Al^{3+} ion between 10^{-13} and 10^{-15} m^2/s in the region from 1670 to 1905°C. For this region, the results can be described by the relation:

$$D = 28 \exp - \frac{114\,000 \pm 15\,000}{RT}$$

A comparison of the diffusion data of O^{2-} and Al^{3+} ions in $\alpha-Al_2O_3$ indicates that the mobility of Al ions is greater than the mobility of O ions (Figure I-20), which is highly desired in our case.

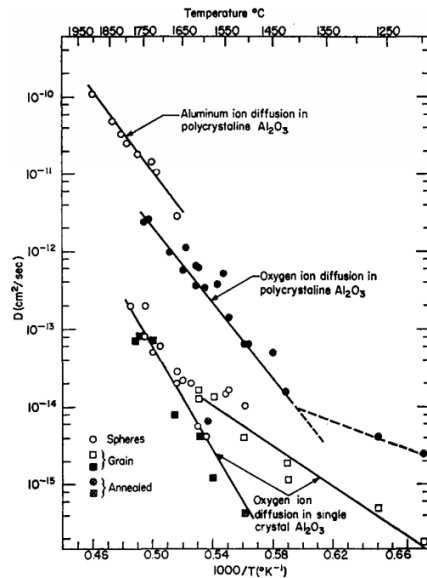


Figure I-20: Comparison of Al ions self-diffusion coefficients with O ion self-diffusion coefficients in $\alpha-Al_2O_3$ [130].

One of the uncertainties that awaits us is the possible reactions between $\alpha\text{-Al}_2\text{O}_3$ and Ni. In fact, during the depletion of the Al coating, the concentration of Ni increases. When a threshold in Ni concentration is reached, it is possible that an $\alpha\text{-Al}_2\text{O}_3 \rightarrow \text{NiAl}_2\text{O}_4$ transformation takes place (Figure I-21). This transformation is not desired for the resistance to cyclic oxidation at high-temperature [131]. In addition, this transformation can be accelerated by the internal diffusion of O^{2-} ions.

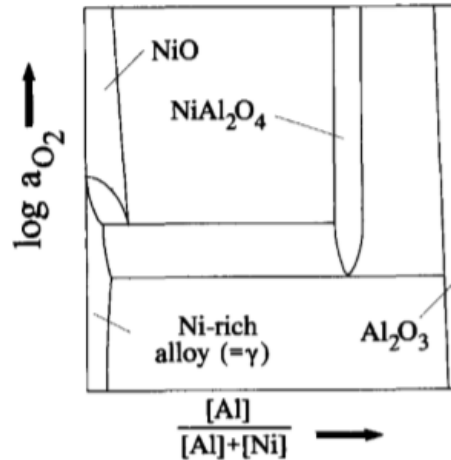


Figure I-21: Schematic $\log a_{\text{O}_2}$ vs composition phase diagram of the system Ni-Al-O at constant temperature [131].

To synthesize these coatings, two ways are envisaged. The first way consists of a Ni plating onto the surface of a superalloy, this layer of Ni will then be oxidized to form a thin coating of nickel oxide. Then an aluminum slurry will be sprayed onto the NiO and finally a heat treatment will be carried out.

The second way differs slightly from the first one. In this case, particles formed from an intermetallic core and an aluminum oxide shell will be synthesized first and they will be trapped them in the Ni plating before carrying out the slurry aluminization. Finally, these two types of coating will be chemically very similar but will have microstructural differences.

References

[1] <https://www.phase-trans.msm.cam.ac.uk/mphil/Trent1/sld024.htm>, Photo courtesy of Rolls Royce.

[2] <https://www.phase-trans.msm.cam.ac.uk/mphil/Trent1/sld009.htm>, Photo courtesy of Rolls Royce.

[3] D.R. Greatrix, *Powered Flight: The Engineering of Aerospace Propulsion*, Springer-Verlag London Limited (2012).

<https://doi.org/10.1007/978-1-4471-2485-6>

[4] P. Jansohn, *Modern gas turbine system: High efficiency, low emission, fuel flexible power generation*, Woodhead Publishing (2013).

ISBN: 9781845697280

[5]: R.C. Reed: *The Superalloys Fundamentals and Applications*, Cambridge University Press (2006)

<https://doi.org/10.1017/CBO9780511541285>

[6] M. Donachie, S. Donachie, *Superalloys: A Technical Guide 2nd edition*, ASM International (2002).

ISBN: 9780871707499

[7] S. Bose, *High Temperature Coatings*, Elsevier Science & Technology Books (2007).

ISBN: 9780750682527

[8] N. Eliaz, G. Shemesh, R.M. Latanision, Hot corrosion in gas turbine components, *Engineering Failure Analysis* 9 (2002) 31–43.

[https://doi.org/10.1016/S1350-6307\(00\)00035-2](https://doi.org/10.1016/S1350-6307(00)00035-2)

[9] X. Li, H. Sun Bo, L. Wange, Evolutions of Rolls-Royce air-cooled turbines blades and feature analysis, *Procedia Engineering* 99 (2015) 1482–1491.

<https://doi.org/10.1016/j.proeng.2014.12.689>

[10] D.R. Clarke, M. Oechsner, N.P. Padture, Thermal-barrier coatings for more efficient gas-turbine engines, *MRS Bulletin* 37 (2012) 891–898.

<https://doi.org/10.1557/mrs.2012.232>

[11] M. Durand-Charre, *The Microstructure of Superalloys*, Gordon and Breach Science Publisher (1997).

ISBN: 9789056990978

[12] P. Caron, T. Khan, Evolution of Ni-based superalloys for single crystal gas turbine blade applications, *Aerospace Science and Technology* 3 (1999) 513–523

[https://doi.org/10.1016/S1270-9638\(99\)00108-X](https://doi.org/10.1016/S1270-9638(99)00108-X)

[13] J. Cormier, C.A. Gandin, Processing of directionally cast nickel-based superalloys – Solidification and heat treatments in Nickel Base Superalloys across Length Scales, Ed. G. Cailletaud, Elsevier, Amsterdam 2020 (in preparation)

[14] F. Diologent, P. Caron, T. d’Almeida, S. Chambreland, A. Jacques, P. Bastie, Temperature dependence of lattice mismatch and γ' volume fraction of a fourth-generation monocrystalline nickel-based superalloy, International Journal of Materials Research 97 (2006) 8–14

<https://doi.org/10.3139/146.101350>

[15] Y. Koizumi, T. Kobayashi, T. Yokokawa, J. Zhang, m. Osawa, H. Harada, Y. Aoki, M. Arai, Development of next-generation Ni-base single crystal superalloys, Journal of the Japan Institute of Metals 67 (2004) 35–43.

https://doi.org/10.7449/2004/Superalloys_2004_35_43

[16] M. Pessah-Simonetti, P. Donnadieu, P. Caron, T.C.P. phase particles embedded in a superalloy matrix: Interpretation and prediction of the orientation relationships, Scripta Metallurgica et Materialia 30 (1994) 1553–1558.

[https://doi.org/10.1016/0956-716X\(94\)90307-7](https://doi.org/10.1016/0956-716X(94)90307-7)

[17] Y. Hirata, S. Itoh, T. Shimonosono, S. Sameshima, Theoretical and experimental analyses of Young’s modulus and thermal expansion coefficient of the alumina-mullite system, Ceramics International 42 (2016) 17067–17073.

<https://doi.org/10.1016/j.ceramint.2016.07.216>

[18] Y.S.Touloukian, R.K. Kirby, R.E. Taylor, P.D. Desai, Thermophysical properties of matter: the TPRC data series, A comprehensive compilation of data, vol. 12. IFI/Plenum, New York.

<https://apps.dtic.mil/dtic/tr/fulltext/u2/a129115.pdf>

[19] R.D. Noebe, R.R. bowman, M.V. Nathal, Physical and mechanical properties of the B2 compound NiAl, International Materials Review 39 (1993) 192–232.

<https://doi.org/10.1179/imr.1993.38.4.193>

[20] T.H. Nielson, M.H. Leipold, Thermal expansion of nickel oxide, Journal of the American Ceramic Society-Discussions and Notes 48 (1965), 164–164.

<https://doi.org/10.1111/j.1151-2916.1965.tb16057.x>

[21] K. Kawagishi, H. Harada, A. Sato, A. Sato, T. Kobayashi, The oxidation properties of fourth generation single-crystal nickel-based superalloys, The Journal of the Minerals, Metals & Material Society 58 (2006) 43–46.

<https://doi.org/10.1007/s11837-006-0067-z>

[22] F. Pedraza, Corrosion et Protection des Matériaux Haute Température, Tome 2, ed. Balbaud et al. Presses des Mines-TRANSVALOR (2018) 127–144.

[23] M.J. Pomeroy, Coatings for gas turbine materials and long-term stability issues, Materials and Design 26 (2005) 223–231.

<https://doi.org/10.1016/j.matdes.2004.02.005>

[24] J.S. Van Sluytman, T.M. Pollock, Optimal precipitate shapes in nickel-base γ - γ' alloys, *Acta Materialia* 60 (2012) 1771–1783.

<https://doi.org/10.1016/j.actamat.2011.12.008>

[25] R.A. MacKay, T.P. Gabb, A. Garg, R.B. Rogers, M.V. Nathal, Influence of composition on microstructural parameters of single crystal nickel-based superalloys, *Materials Characterization* 70 (2012) 83–100.

<https://doi.org/10.1016/j.matchar.2012.05.001>

[26] L.R. Liu, J. Jin, N.R. Zhao, X.F. Sun, H.R. Guan, Z.Q. Hu, Formation of carbides and their effects on stress rupture of a Ni-base single crystal superalloy, *Materials Science and Engineering A* 361 (2003) 191–197.

[https://doi.org/10.1016/S0921-5093\(03\)00517-3](https://doi.org/10.1016/S0921-5093(03)00517-3)

[27] B.P. Bewlay, S. Nag, A. Suzuki, M.J. Weimer, TiAl alloys in commercial aircraft engines, *Materials at High Temperatures* 33 (2016) 549–559.

<https://doi.org/10.1080/09603409.2016.1183068>

[28] J. Grüters, M.C. Galetz, Influence of thermodynamic activities of different masteralloys in pack powder mixtures to produce low activity aluminide coatings on TiAl alloys, *Intermetallics* 60 (2015) 19–27.

<https://doi.org/10.1016/j.intermet.2015.01.001>

[29] R. Rajendran, Gas turbine coatings- An overview, *Engineering Failure Analysis* 26 (2012) 355–369.

<https://doi.org/10.1016/j.engfailanal.2012.07.007>

[30] J.R. Nicholls, Designing oxidation-resistant coatings, *Journal of Minerals, Metals & Materials Society* 52 (2000) 28–35.

<https://doi.org/10.1007/s11837-000-0112-2>

[31] G.W. Goward, D.H. Boone, Mechanisms of formation of diffusion aluminide coatings on nickel-base superalloys, *Oxidation of Metals* 3 (1971) 475–495.

<https://doi.org/10.1007/BF00604047>

[32] C. Houngrinou, S. Chevalier, J.P. Larpin, Synthesis and characterization of pack cemented aluminide coatings on metals, *Applied Surface Science* 236 (2004) 256–269.

<https://doi.org/10.1016/j.apsusc.2004.04.026>

[33] B.M. Warnes, D.C. Punola, Clean diffusion coatings by chemical vapor deposition, *Surface and Coatings Technology* 94-95 (1997) 1–6.

[https://doi.org/10.1016/S0257-8972\(97\)00467-2](https://doi.org/10.1016/S0257-8972(97)00467-2)

[34] J. Benoist, K.F. Badawi, A. Malié, C. Ramade, Microstructure of Pt modified aluminide coatings on Ni-based superalloys without prior Pt diffusion, *Surface and Coatings Technology* 194 (2005) 48–57.

<https://doi.org/10.1016/j.surfcoat.2004.04.094>

[35] Y.Q. Wang, G. Sayre, Factors affecting the microstructure of platinum-modified aluminide coatings during vapor phase aluminizing process, *Surface and Coatings Technology* 203 (2009) 1264–1272.

<https://doi.org/10.1016/j.surfcoat.2008.10.031>

[36] F.H. Stott, G.C. Wood, J. Stringer, The influence of alloying elements on the development and maintenance of protective scales, *Oxidation of Metals* 44 (1995) 113–145.

<https://doi.org/10.1007/BF01046725>

[37] G.W. Goward, Progress in coatings for gas turbine airfoils, *Surface and Coatings Technology* 108-109 (1998) 73–79.

[https://doi.org/10.1016/S0257-8972\(98\)00667-7](https://doi.org/10.1016/S0257-8972(98)00667-7)

[38] Y. Wang, H. Liu, X. Ling, Y. Weng, Effect of pore microstructure on the effective thermal conductivity of thermal barrier coatings, *Applied Thermal Engineering* 102 (2016) 234–242.

<https://doi.org/10.1016/j.applthermaleng.2016.03.174>

[39] B. Gleeson, Thermal Barrier Coatings for Aeroengine Applications, *Journal of Propulsion and Power* 22 (2006) 375–383.

<https://doi.org/10.2514/1.20734>

[40] R. Darolia, W.S. Walston, M.V. Nathal, NiAl alloys for Turbine Airfoils, *Superalloy* (1996) 561–570.

https://doi.org/10.7449/1996/Superalloys_1996_561_570

[41] G. Frommeyer, R. Rablbauer, High temperature materials based on the intermetallic compound NiAl reinforced by refractory metals for advanced energy conversion technologies, *Steel Research International* 79 (2008) 507–512.

<https://doi.org/10.1002/srin.200806159>

[42] G.K. Dey, Physical metallurgy of nickel aluminides, *Sadhana* 28 (2003) 247–262.

<https://doi.org/10.1007/BF02717135>

[43] R. Prescott, M.J. Graham, The formation of aluminum oxide scales on high-temperature alloys, *Oxidation of Metals* 38 (1992) 233–254.

<https://doi.org/10.1007/BF00666913>

[44] H.J. Grabke, Oxidation of NiAl and FeAl, *Intermetallics* 7 (1999) 1153–1158.

[https://doi.org/10.1016/S0966-9795\(99\)00037-0](https://doi.org/10.1016/S0966-9795(99)00037-0)

[45] D.K. Das, Microstructure and high temperature oxidation behavior of Pt-modified aluminide bond coats on Ni-base superalloys, *Progress in Materials Science* 58 (2013) 151–182.

<https://doi.org/10.1016/j.pmatsci.2012.08.002>

[46] H. Okamoto, Al-Ni (aluminum-nickel), *Journal of Phase Equilibria and Diffusion* 25 (2004).

<https://doi.org/10.1007/s11669-004-0163-0>

[47] J. Angenete, K. Stiller, Comparison of inward and outward grown Pt modified aluminide diffusion coatings on a Ni based single crystal superalloy, *Surface and Coatings Technology* 150 (2002) 107–118.

[https://doi.org/10.1016/S0257-8972\(01\)01544-4](https://doi.org/10.1016/S0257-8972(01)01544-4)

[48] J.M. Brossard, B. Panicaud, J. Balmain, G. Bonnet, Modeling of aluminized coating growth on nickel, *Acta Materialia* 55 (2007) 6586–6595.

<https://doi.org/10.1016/j.actamat.2007.08.025>

[49] J. Angenete, Aluminide diffusion coatings for Ni-based superalloys, Doctoral thesis, Göteborg University (2002).

[50] K. Shivarni, S. Firouzi, A. Rashidghamat, Microstructures and cyclic oxidation behavior of Pt-free and low-Pt NiAl coatings on the Ni-base superalloy Rene-80, *Corrosion Science* 55 (2012) 378–384.

<https://doi.org/10.1016/j.corsci.2011.10.037>

[51] R.E. Malush, P. Deb, D.H. Boone, Structure and 900°C hot corrosion behavior of chromium-modified platinum aluminide coatings, *Surface and Coatings Technology* 36 (1988) 13–26.

[https://doi.org/10.1016/0257-8972\(88\)90132-6](https://doi.org/10.1016/0257-8972(88)90132-6)

[52] B. Bouchaud, B. Rannou, F. Pedraza, Slurry aluminizing mechanisms of Ni-based superalloys incorporating an electrosynthesized ceria diffusion barrier, *Materials Chemistry and Physics* 143 (2013) 416–424.

<https://doi.org/10.1016/j.matchemphys.2013.09.022>

[53] F. Pedraza, M. Mollard, B. Rannou, B. Bouchaud, J. Balmain, G. Bonnet, Oxidation resistance of thermal barrier coatings based on hollow alumina particles, *Oxidation of Metals* 85 (2016) 231–244.

<https://doi.org/10.1007/s11085-015-9570-3>

[54] J.A. Haynes, B.A. Pint, K.L. More, Y. Zhang, I.G. Wright, Influence of sulfur, platinum, and hafnium on the oxidation behavior of CVD NiAl bond coatings, *Oxidation of Metals* 58 (2002) 513–544.

<https://doi.org/10.1023/A:1020525123056>

[55] X. Montero, M.C. Galetz, M. Schütze, Low activity aluminide coatings for superalloys using a slurry process free of halide activators and chromates, *Surface & Coatings Technology* 222 (2013) 9–14.

<https://doi.org/10.1016/j.surfcoat.2013.01.033>

[56] B. Grégoire, G. Bonnet, F. Pedraza, Mechanisms of formation of slurry aluminide coatings from Al and Cr microparticles, *Surface & Coatings Technology* 359 (2019) 323–333.

<https://doi.org/10.1016/j.surfcoat.2018.11.077>

[57] B. Grégoire, G. Bonnet, F. Pedraza, Development of a new slurry coating design for the surface protection of gas turbine components, *Surface & Coatings Technology* 374 (2019) 521–530.

<https://doi.org/10.1016/j.surfcoat.2019.06.020>

[58] X. Montero, M.C. Galetz, M. Schütze, Low-activity aluminide coatings for superalloys using a slurry process free of halide activators and chromates, *Surface and Coatings Technology* 222 (2013) 9–14.

<https://doi.org/10.1016/j.surfcoat.2013.01.033>

[59] D.P. Garriga-Majo, B.A. Shollock, D.S. McPhail, R.J. Chater, J.F. Walker, Novel Strategies for Evaluating the Degradation of Protective Coatings on Superalloys, *International Journal of Inorganic Materials* 1 (1999) 325–336.

[https://doi.org/10.1016/S1466-6049\(99\)00047-1](https://doi.org/10.1016/S1466-6049(99)00047-1)

[60] M.W. Brumm, H.J. Grabke, The oxidation behaviour of NiAl – I. Phase transformations in the alumina scale during oxidation of NiAl and NiAl-Cr, *Alloys Corrosion Science* 33 (1992) 1677–1690.

[https://doi.org/10.1016/0010-938X\(92\)90002-K](https://doi.org/10.1016/0010-938X(92)90002-K)

[61] D. Monceau, A. Boudot-Miquet, K. Bouhanek, R. Peraldi, A. Malié, F. Crabos, B. Pieraggi, Oxydation et protection des matériaux pour sous-couches (NiAlPd, NiAlPt, NiCoCrAlYTa, CoNiCrAlY) de barrières thermiques, *Journal de Physique IV* 10 (2000) 167–171.

<https://doi.org/10.1051/jp4:2000423>

[62] G.C. Rybicki, J.L. Smialek, Effect of the θ/α -Al₂O₃ transformation on the oxidation behavior of β -NiAl + Zr, *Oxidation of Metals* 31 (1989) 275–304.

<https://doi.org/10.1007/BF00846690>

[63] J. Yang, E. Schumann, I. Levin, M. Ruhle, Transient oxidation of NiAl, *Acta Materialia* 46 (1998) 2195–2201.

[https://doi.org/10.1016/S1359-6454\(97\)00378-9](https://doi.org/10.1016/S1359-6454(97)00378-9)

[64] B.A. Pint, J.R. Martin, L.W. Hobbs, The oxidation mechanism of θ -Al₂O₃ scales, *Solid State Ionics* 78 (1995) 99–107.

[https://doi.org/10.1016/0167-2738\(95\)00013-V](https://doi.org/10.1016/0167-2738(95)00013-V)

[65] M. Le Gall, A.M. Huntz, B. Lesage, C. Monty, J. Bernardini, Self-diffusion in α -Al₂O₃ and growth rate of alumina scales formed by oxidation: effect of Y₂O₃ doping, *Journal of Materials Science* 30 (1995) 201–211.

<https://doi.org/10.1007/BF00352151>

[66] B.A. Pint, J.R. Martin, L.W. Hobbs, ^{18}O /SIMS characterization of the growth mechanism of doped and undoped $\alpha\text{-Al}_2\text{O}_3$, *Oxidation of Metals* 39 (1993) 167–174.

<https://doi.org/10.1007/BF00665610>

[67] V.K. Tolpygo, D.R. Clarke, Microstructural evidence for counter-diffusion of aluminum and oxygen during the growth of alumina scales, *Materials at high temperatures* 20 (2003) 261–271.

<https://doi.org/10.1179/mht.2003.030>

[68] D. R. Clarke, The lateral growth strain accompanying the formation of a thermally grown oxide, *Acta Materialia* 51 (2003) 1393–1407.

[https://doi.org/10.1016/S1359-6454\(02\)00532-3](https://doi.org/10.1016/S1359-6454(02)00532-3)

[69] D. Monceau, F. Crabos, A. Malié, B. Pieraggi, Effect of bond-coat preoxidation and surface finish on isothermal and cyclic oxidation, *Materials Science Forum*, 369-372 (2001) 607–614.

<https://doi.org/10.4028/www.scientific.net/MSF.369-372.607>

[70] L. Antoni, A. Galerie : Corrosion sèche des métaux, *Mécanismes Techniques de l'ingénieur* (2003)

[71] P.Y. Hou, A.P. Paulikas, B.W. Veal, Stress development and relaxation in Al_2O_3 during early stage oxidation of $\beta\text{-NiAl}$, *Materials at High Temperatures* 22 (2005) 535–543.

<https://doi.org/10.3184/096034005782744146>

[72] D.M. Lipkin, D.R. Clarke, M. Hollatz, M. Bobeth, W. Pompe, Stress Development in Alumina Scales Formed upon Oxidation of (111) NiAl Single Crystals, *Corrosion Science* 39 (1997) 231-242.

[https://doi.org/10.1016/S0010-938X\(97\)83344-6](https://doi.org/10.1016/S0010-938X(97)83344-6)

[73] L. Rivoaland, V. Maurice, P. Josso, M.-P. Bacos, P. Marcus, The Effect of Sulfur Segregation on the Adherence of the Thermally-Grown Oxide on NiAl II: The Oxidation Behavior at 900°C of Standard, Desulfurized or Sulfur-Doped NiAl (001) Single-Crystals, *Oxidation of Metals* 60 (2003) 159–178.

<https://doi.org/10.1023/A:1024625615544>

[74] H. Svensson, K. Stiller, J. Angenete, Investigation of oxide formation during short-term oxidation of model NiAl alloys, *Materials Science Forum* 461-464 (2004) 231–238.

<https://doi.org/10.4028/www.scientific.net/MSF.461-464.231>

[75] J. L. Smialek, Oxide morphology and spalling model for NiAl, *Metallurgical Transactions A* 9 (1978) 309-320.

<https://doi.org/10.1007/BF02646380>

[76] M.W. Brumm, H.J. Grabke, Oxidation behaviour of NiAl – II. cavity formation beneath the oxide scale on NiAl of different stoichiometries, *Corrosion Science* 34 (1993) 547–561.

[https://doi.org/10.1016/0010-938X\(93\)90271-H](https://doi.org/10.1016/0010-938X(93)90271-H)

[77] A. Paul, A.A. Kodentsov, F.J.J. Van Loo, On diffusion in the β -NiAl phase, *Journal of Alloys and Compounds* 403 (2005) 147-153.

<https://doi.org/10.1016/j.jallcom.2005.04.194>

[78] S. Shankar, L. L. Seigle, Interdiffusion and intrinsic diffusion in the NiAl (δ) phase of the Al-Ni system, *Metallurgical Transactions A* 9 (1978) 1467–1476.

<https://doi.org/10.1007/BF02661819>

[79] V.K. Tolpygo, D.R. Clarke, Wrinkling of α -Alumina Films Grown by Thermal Oxidation-II. Oxide Separation and Failure, *Acta Materialia* 46 (1998) 5167–5174.

[https://doi.org/10.1016/S1359-6454\(98\)00134-7](https://doi.org/10.1016/S1359-6454(98)00134-7)

[80] J. D. Kuenzly, D. L. Douglass, The oxidation mechanism of Ni₃Al containing yttrium, *Oxidation of Metals* 8 (1974) 139–178.

<https://doi.org/10.1007/BF00612170>

[81] J. Angenete, K. Stiller, V. Langer, Oxidation of simple and Pt-modified aluminide diffusion coatings on Ni-base superalloys. I. Oxide scale microstructure, *Oxidation of Metals* 60 (2003) 47–82.

<https://doi.org/10.1023/A:1024665229656>

[82] J. Angenete, K. Stiller, V. Langer, Oxidation of simple and Pt-modified aluminide diffusion coatings on Ni-base superalloys. II. Oxide scale failure, *Oxidation of Metals* 60 (2003) 83–101.

<https://doi.org/10.1023/A:1024617313726>

[83] J. Angenete, K. Stiller, A comparative study of two inward grown Pt modified Al diffusion coatings on a single crystal Ni base superalloy, *Materials Science and Engineering A* 316 (2001) 182–194.

[https://doi.org/10.1016/S0921-5093\(01\)01236-9](https://doi.org/10.1016/S0921-5093(01)01236-9)

[84] T.K. Redden, Ni-Al coating-base metal interactions in several nickel-base alloys, *Transactions of the Metallurgical Society of AIME* 242 (1968) 1695–1702.

[85] M. Göbel, A. Rahmel, M. Schütze, M. Schorr, W.T. Wu, Interdiffusion between the platinum-modified aluminide coating RT 22 and nickel-based single-crystal superalloys at 1000°C and 1200°C, *Materials at High Temperature* 12 (1994) 301–309.

<https://doi.org/10.1080/09603409.1994.11752534>

[86] M. Larnicol, C. Rio, Y. Renollet, Y. Pioche, R. Mevrel, Etude des phénomènes d'interdiffusion dans le système AM1/NiAl(Pt)/ZrO₂-Y₂O₃, *Journal de la Physique IV* 10(PR4) (2000) 155–161.

<https://doi.org/10.1051/jp4:2000422>

[87] E. Basuki, A. Crosky, B. Gleeson, Interdiffusion behaviour in aluminide-coated René6 80H at 1150°C, *Materials Science and Engineering A* 224 (1997) 27–32.

[https://doi.org/10.1016/S0921-5093\(96\)10556-6](https://doi.org/10.1016/S0921-5093(96)10556-6)

[88] J.H. Chen, J.A. Little, Degradation of platinum aluminide coating on CMSX-4 at 1100°C, *Surface and Coating Technology* 92 (1997) 69–77.

[https://doi.org/10.1016/S0257-8972\(96\)03117-9](https://doi.org/10.1016/S0257-8972(96)03117-9)

[89] I.M. Edmonds, H.E. Evans, C.N. Jones, Oxidation and coating evolution in aluminized fourth generation blade alloys, *Superalloys* (2008).

https://doi.org/10.7449/2008/Superalloys_2008_661_670

[90] M. Reid, M.J. Pomeroy, J.S. Robinson, Microstructural instability in coated single crystal superalloys, *Journal of Materials Processing Technology* 153–154 (2004) 660–665.

<https://doi.org/10.1016/j.jmatprotec.2004.04.132>

[91] C.M.F. Rae, M.S. Hook, R.C. Reed, The effect of TCP morphology on the development of aluminide coated superalloys, *Materials Science and Engineering A* 396 (2005) 231–239.

<https://doi.org/10.1016/j.msea.2005.01.005>

[92] C.C. Jia, K. Ishida, T. Nishizawa, Partition of alloying elements between γ (A1), γ' (L12) and β (B2) phases in Ni-Al base systems, *Metallurgical Transactions* 25 A (1994) 473–485.

<https://doi.org/10.1007/BF02651589>

[93] K. Tolpygo, D.R. Clarke, Surface rumpling of a (Ni, Pt)Al bond coat induced by cyclic oxidation, *Acta Materialia* 48 (2000) 3283–3293.

[https://doi.org/10.1016/S1359-6454\(00\)00156-7](https://doi.org/10.1016/S1359-6454(00)00156-7)

[94] E. Schumann, M. Ruhle, K.P. Trumble, M. Rühle, Microstructural observations on the oxidation of γ' -Ni₃Al at high oxygen partial pressure, *Acta Metallurgica et Materialia* 42 (1994) 1311–1319.

[https://doi.org/10.1016/0956-7151\(92\)90432-E](https://doi.org/10.1016/0956-7151(92)90432-E)

[95] S.H. Kim, M.H. Oh, K. Kishida, T. Hirano, D.M. Wee, Deposition of NiAl coating for improvement of oxidation resistance of cold-rolled Ni₃Al foils, *Intermetallics* 13 (2005) 129–136.

<https://doi.org/10.1016/j.intermet.2004.06.009>

[96] N. Vialas, Etude de la détérioration par oxydation haute température et interdiffusion de systèmes revêtement/superaliage à base de nickel. Prévion de durée de vie, PhD Thesis, Institut National Polytechnique de Toulouse (2004).

<http://ethesis.inp-toulouse.fr/archive/00001125/>

[97] J. Müller, M. Schierling, E. Zimmermann, D. Neuschütz, Chemical vapor deposition of smooth α -Al₂O₃ films on nickel base superalloys as diffusion barriers, *Surface and Coatings Technology* 120–121 (1999) 16–21.

[https://doi.org/10.1016/S0257-8972\(99\)00333-3](https://doi.org/10.1016/S0257-8972(99)00333-3)

[98] J.A. Haynes, Y. Zhang, K.M. Cooley, L. Walker, K.S. Reeves, B.A. Pint, High-temperature diffusion barriers for protective coatings, *Surface and Coatings Technology* 188–189 (2004) 153–157.

<https://doi.org/10.1016/j.surfcoat.2004.08.066>

[99] O. Knotek, F. Löffler, W. Beele, Diffusion barrier design against rapid interdiffusion of MCrAlY and Ni-base material, *Surface and Coating Technology* 61 (1993) 6–13.

[https://doi.org/10.1016/0257-8972\(93\)90194-S](https://doi.org/10.1016/0257-8972(93)90194-S)

[100] O. Knotek, E. Lugscheider, F. Löffler, W. Beele, Diffusion barrier coatings with active bonding designed for gas turbine blades, *Surface and Coatings Technology* 68-69 (1994) 22-26.

[https://doi.org/10.1016/0257-8972\(94\)90132-5](https://doi.org/10.1016/0257-8972(94)90132-5)

[101] R. Cremer, M. Witthaut, K. Reichert, M. Schierling, D. Neuschütz, Thermal stability of Al–O–N PVD diffusion barriers, *Surface and Coatings Technology* 108-109 (1998) 48–58.

[https://doi.org/10.1016/S0257-8972\(98\)00614-8](https://doi.org/10.1016/S0257-8972(98)00614-8)

[102] Q.M. Wang, Y.N. Wu, M.H. Guo, P.L. Ke, J. Gong, C. Sun, L.S. Wen, Ion-plated Al–O–N and Cr–O–N films on Ni-base superalloys as diffusion barriers, *Surface and Coatings Technology* 197 (2005) 68–76.

<https://doi.org/10.1016/j.surfcoat.2004.09.022>

[103] J. Müller, D. Neuschütz, Efficiency of α -alumina as diffusion barrier between bond coat and bulk material of gas turbine blades, *Vacuum* 71 (2003) 247–251.

[https://doi.org/10.1016/S0042-207X\(02\)00746-7](https://doi.org/10.1016/S0042-207X(02)00746-7)

[104] Z. Xu, L. He, R. Mu, X. Zhong, X. Cao, Formation of diffusion barrier on the Ni-based superalloy by low-pressure pre-oxidation, *Vacuum* 82 (2008) 1251–1258.

<https://doi.org/10.1016/j.vacuum.2008.03.057>

[105] Z. Xu, R. Mu, L. He, X. Cao, Effect of diffusion barrier on the high-temperature oxidation behavior of thermal barrier coatings, *Journal of Alloys and Compounds* 466 (2008) 471–478.

<https://doi.org/10.1016/j.jallcom.2007.11.083>

[106] T. Narita, K.Z. Thosin, L. Fengqun, S. Hayashi, H. Murakami, B. Gleeson, D. Young, Development of Re-based diffusion barrier coating on nickel-based superalloys, *Materials and Corrosion* 56 (2005) 923–929.

<https://doi.org/10.1002/maco.200503924>

[107] T. Narita, T. Izumi, T. Nishimoto, Y. Shibata, K.Z. Thosin, S. Hayashi, Advanced coatings on high-temperature applications, *Materials Science Forum* 522-523 (2006) 1–14.

<https://doi.org/10.4028/www.scientific.net/MSF.522-523.1>

[108] T. Narita, F. Lang, K.Z. Thosin, T. Yoshioka, T. Izumi, H. Yakuwa, S. Hayashi, Oxidation behavior of nickel-base single-crystal superalloy with rhenium-base diffusion barrier coating system at 1,423K in air, *Oxidation of Metals* 68 (2007) 346–363.

<https://doi.org/10.1007/s11085-007-9079-5>

[109] Y. Katsumata, T. Yoshioka, K.Z. Thosin, T. Nishimoto, T. Izumi, S. Hayashi, T. Narita, Formation and oxidation behavior of a diffusion-barrier-coating system on a Ni-Mo base alloy at 1,373K in air, *Oxidation of Metals* 68 (2007) 331–342.

<https://doi.org/10.1007/s11085-007-9078-6>

[110] F. Lang, T. Narita, Improvement in oxidation resistance of a Ni₃Al-based superalloy IC6 by rhenium-based diffusion barrier coatings, *Intermetallics* 15 (2007) 599–606.

<https://doi.org/10.1016/j.intermet.2006.10.042>

[111] D. Sumoyama, K.Z. Thosin, T. Nishimoto, T. Yoshioka, T. Izumi, S. Hayashi, T. Narita, Formation of a Rhenium-Base Diffusion-Barrier-Coating System on Ni-Base Single Crystal Superalloy and its Stability at 1,423K, *Oxidation of Metals* 68 (2007) 313–329.

<https://doi.org/10.1007/s11085-007-9077-7>

[112] T. Narita, S. Ford, T. Yoshioka, T. Nishimoto, T. Izumi, S. Hayashi, Formation of Pt-Modified γ' -Ni₃Al and Re-Based σ -Alloy Coating System and Cyclic Oxidation Behavior of Coated Superalloy, *Materials Science Forum* 595-598 (2008) 135–141.

<https://doi.org/10.4028/www.scientific.net/MSF.595-598.135>

[113] M.S.A. Karunaratne, P. Carter, R.C. Reed, Interdiffusion in the face-centred cubic phase of the Ni-Re, Ni-Ta and Ni-W systems between 900 and 1300°C, *Materials Science and Engineering A* 281 (2000) 229–233.

[https://doi.org/10.1016/S0921-5093\(99\)00705-4](https://doi.org/10.1016/S0921-5093(99)00705-4)

[114] <https://echa.europa.eu/regulations/reach/understanding-reach>

[115] F. Pedraza, M. Mollard, B. Rannou, J. Balmain, B. Bouchaud, G. Bonnet, Potential thermal barrier coating systems from Al microparticles. Mechanisms of coating formation on pure nickel, *Materials Chemistry and Physics* 134 (2012) 700–705.

<https://doi.org/10.1016/j.matchemphys.2012.03.053>

[116] X. Montero, M.C. Galetz, M. Schütze, A single step process to form in-situ an alumina foam/aluminide TBC system for alloys in extreme environments at high-temperatures, *Surface and coatings Technology* 206 (2011) 1586–1594.

<https://doi.org/10.1016/j.surfcoat.2011.05.052>

[117] M.C. Galetz, X. Montero, M. Mollard, M. Günthner, F. Pedraza, M. Schütze, The role of combustion synthesis in the formation of slurry aluminization, *Intermetallics* 44 (2014) 8–17.

<https://doi.org/10.1016/j.intermet.2013.08.002>

[118] V. Kolarik, R. Roussel, M. Juez Lorenzo, H. Fietzek, Factors influencing the formation of a diffusion zone and the adherence of the top coat of high-temperature coatings from micro-sized spherical aluminum particles, *Materials at High Temperatures* 29 (2012) 89-94.

<https://doi.org/10.3184/096034012X13316583881350>

[119] M. Mollard, Elaboration de systèmes barrière thermique par barbotine. Comportement du nickel et de ses superalliages revêtus en oxydation cyclique à haute température, PhD Thesis, Université de La Rochelle (2012).

<https://tel.archives-ouvertes.fr/tel-00839920>

[120] B. Rannou, Slurry coatings from aluminium microparticles on Ni-based superalloys for high temperature oxidation protection, PhD Thesis, Université de La Rochelle (2012).

<https://tel.archives-ouvertes.fr/tel-00839790>

[121] G. Boissonnet, B. Grégoire, G. Bonnet, F. Pedraza, Development of thermal barrier coating systems from Al microparticles. PartI: Influence of processing conditions on the mechanisms of formation, *Surface and Coatings Technology* 380 (2019) 125085.

<https://doi.org/10.1016/j.surfcoat.2019.125085>

[122] M. Brossard, Influence de l'eau (vapeur, liquide) et du régime d'oxydation sur la dégradation de revêtements aluminos-formeurs sur superalliage à base nickel, PhD Thesis, Université de La Rochelle (2014).

<https://tel.archives-ouvertes.fr/tel-01175472>

[123] B. Grégoire, Functionalization of aeronautical thermal barrier systems elaborated by slurry (FONBAT), PhD Thesis, Université de la Rochelle (2018).

<https://tel.archives-ouvertes.fr/tel-01939473>

[124] C. Boulesteix, Synthesis, environmental degradation and repairability of slurry aluminium coatings elaborated on steels employed in power plants, PhD Thesis, Université de La Rochelle (2017).

<https://tel.archives-ouvertes.fr/tel-01804936>

[125] G. Boissonnet, Factors influencing the thermal insulation potential of different thermal barrier coating systems, PhD Thesis, Université de La Rochelle (2019).

<https://tel.archives-ouvertes.fr/tel-02528825/>

[126] M. Mollard, B. Rannou, B. Bouchaud, J. Balmain, G. Bonnet, F. Pedraza, Comparative degradation of nickel aluminized by slurry and by pack cementation under isothermal conditions, *Corrosion Science* 66 (2013) 118–124.

<https://doi.org/10.1016/j.corsci.2012.09.009>

[127] P. Zhu, J.C.M. Li, C.T. Liu, Reaction mechanism of combustion synthesis of NiAl, *Materials Science and Engineering A* 329-331 (2002) 57–68.

[https://doi.org/10.1016/S0921-5093\(01\)01549-0](https://doi.org/10.1016/S0921-5093(01)01549-0)

[128] B.J. Blaiszik, S.L.B Kramer, S.C. Olugebefola, J.S. Moore, N.R. Sottos and S.R. White, Self-healing polymers and composites, *Annual Review of Materials Research* 40 (2010) 179–211.

<https://doi.org/10.1146/annurev-matsci-070909-104532>

[129] F. Nozahic, C. Estournès, A.L. Carabat, W.G. Sloof, S. Van Der Zwaag, D. Monceau, Self-healing thermal barrier coating system fabricated by spark plasma sintering, *Materials & Design* 143 (2018) 204–213.

<https://doi.org/10.1016/j.matdes.2018.02.001>

[130] A.E. Paladino, W.D. Kingery, Aluminum ion diffusion in aluminum oxide, *The Journal of Chemical Physics* 37 (1962) 957–962.

<https://doi.org/10.1063/1.1733252>

[131] K.P. Trumble, M. Rühle, The thermodynamics of spinel interphase formation at diffusion-bonded Ni/Al₂O₃ interfaces, *Acta Metallurgica et Materialia* 39 (1991) 1915–1924.

[https://doi.org/10.1016/0956-7151\(91\)90160-3](https://doi.org/10.1016/0956-7151(91)90160-3)

Chapter II. Experimental methods

Table of contents

I-Materials of study	50
I.A-Electrodeposition of nickel	51
I.A.1-Electroplating bath assembly.....	52
I.A.2-Bath assembly.....	52
I.A.3: Electrolytes and protocols used	53
II-Characterization of metallic powders.....	55
III-Elaboration of the slurry coatings	61
III.A-Composition and preparation of the slurries	61
III.B-Deposition of the slurries on metallic substrate by air brush.....	61
III.C-Thermal treatments.....	62
IV-Degradation of the coatings	63
IV.A-Isothermal oxidation	63
V-Characterization methods	63
V.A-Calorimetry analyses	63
V.A-Crystallographic and structural analyses	63
V.C-Microscopic analyses	64
Reference.....	66

I-Materials of study

Pure Ni was used as a model material to investigate the mechanisms of formation of the coatings whose nominal compositions and surface view after polishing are given in Table II-1 and Figure II-1.a. This material of study with pure composition makes it possible to carry out preliminary studies before extrapolation on more complex material such as superalloys. In addition, the aluminum diffuses extremely quickly in the nickel, which will highlight the self-regenerating nature of the coatings for short oxidation times.

The microstructures of pure Ni material were investigated by etching the 1 μm polished materials. The pure Ni substrate was chemically etched with a Kalling no. 2 solution (5g CuCl_2 + 100mL HCl + 100mL ethyl alcohol) (Figure II-1.b).

In addition, for all tests, the nickel coupons were hand-polished up to # 180 grade in order to decrease the preferential directions of the polishing scratches (Figure II-1.a).

Table II-1: Nominal composition (wt. %) of the investigated nickel-based materials.

Material	Ni	Co	Cr	C	S
Pure Ni (EQ)	99.98	<8 ppm	<8 ppm	<70 ppm	<10 ppm

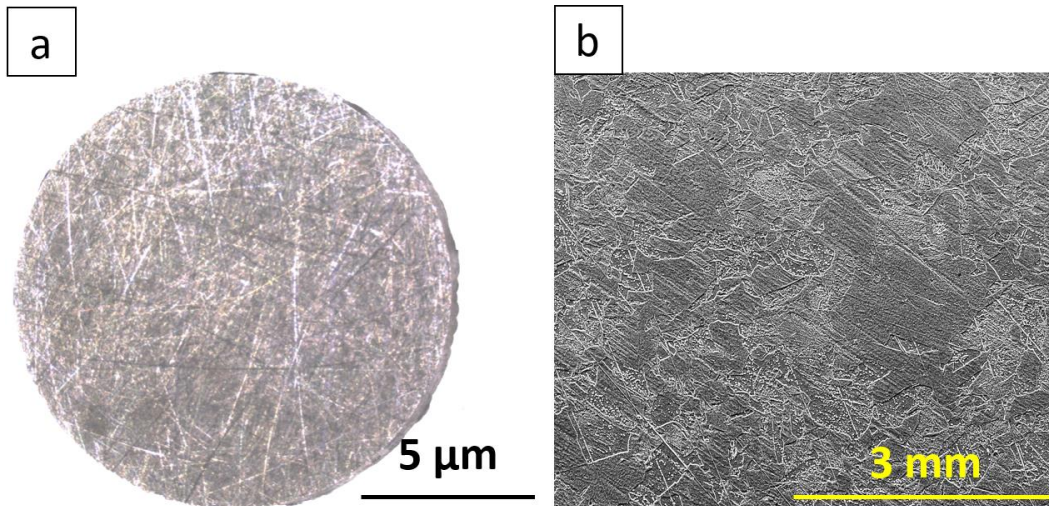


Figure II-1: (a) Surface view of pure Ni sample after polishing and (b) microstructure in SEM (SE mode) after chemical etch.

The XRD patterns of the different materials are presented in Figure II-2. The FCC structure of γ -(Ni) was identified for pure Ni material.

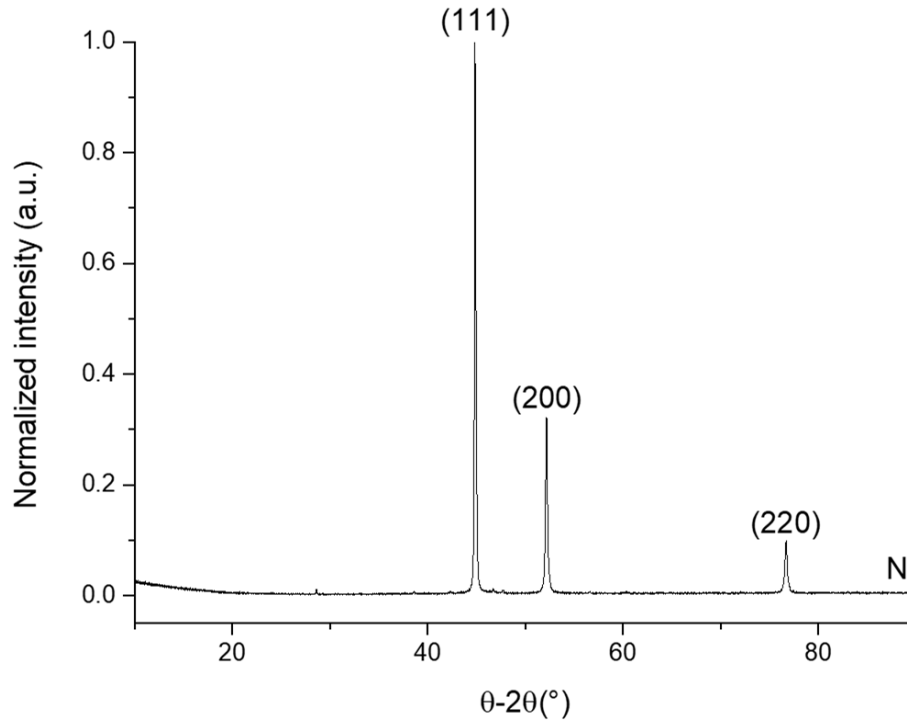


Figure II-2: XRD patterns of the pure Ni substrate of this study.

I.A-Electrodeposition of nickel

For the development of the Ni-plating, direct current and three baths were used to obtain two different coatings.

- the first coating (Figure II-3.a) consists of a simple Ni electroplating. This coating was carried out with a Watts bath and at a fairly high-current in order to obtain a porous coating,

- the second coating (Figure II-3.b) was carried out with two baths. The first bath of Ni sulfamate was carried out at low current density (5 mA/cm²) to obtain a first Ni plating with an average thickness of 10 μ m. This first step is expected to improve the adhesion of the second deposited coating. The second bath is composed of Ni sulfamate and Al₃Ni₂ preoxidized particles and aims at obtaining a composite coating where preoxidized Al₃Ni₂ particles will be homogeneously distributed in a Ni coating.

Subsequently, the first coating will be oxidized and aluminized using Al slurry and the second one will only be aluminized with the same slurry method.

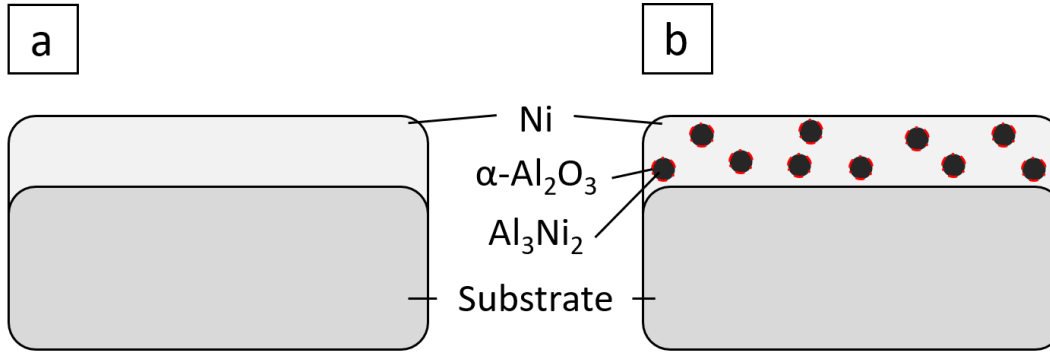


Figure II-3: Schematic drawing of sample after being coated with (a) a Ni deposit and (b) a Ni deposit with trapped Al_3Ni_2 micro-particles.

I.A.1-Electroplating bath assembly

Electroplating is a very popular technique because it has the advantages of being cheap and makes it possible to simply and effectively control the main parameters of the deposits (current density, temperature, composition of the baths, etc.).

The electrodeposition technique consists in imposing a current or a voltage between two electrodes (the working electrode and the counter electrode) immersed in a solution containing metal salts of the metal or alloy to be deposited. The coatings were produced in galvanostatic mode. This allows to record the potential as a function of time upon the application of a given current density. The plating is formed by reducing the metallic cations in solution at the active surface of the working electrode (the substrate).

In addition, it is possible, to determine the deposition time t so as to obtain a desired thickness e and it is defined by the following relation:

$$t = \frac{e \cdot F}{j_m \cdot \eta \left(\frac{x_{Ni} \cdot M_{Ni}}{z_{Ni} \cdot \rho_{Ni}} \right)} \quad (\text{eq. 1})$$



The parameters x_{Ni} , M_i , z_{Ni} et ρ_{Ni} are, respectively, the atomic fraction of Ni (=1), its molar mass ($\sim 58,693 \text{ g}\cdot\text{mol}^{-1}$, the number of electrons exchanged during the reduction reaction (eq. 2) and the density of Ni ($\sim 8.907 \text{ g}\cdot\text{cm}^{-3}$). The relation also depends on the electrical parameters such as the average current density j_m , the Faraday constant F ($\sim 96\,485 \text{ A}\cdot\text{mol}^{-1}$) and the faradic efficiency η defined by the ratio of mass measured vs. the theoretical mass. The thickness of the deposit is thus verified by measuring the weight gain.

I.A.2-Bath assembly

In this part, the development of the Ni coatings using the Watts and the sulfamate baths is presented. The device is an experimental set-up with two electrodes illustrated in Figure II-4. It is composed of a double-walled cell, a working electrode and a counter electrode. The cell is placed on a magnetic stirrer and is connected to a cryostat in order to obtain a homogenous temperature in the bath ($\sim 50^\circ\text{C}$). The counter electrode is a pure Ni plate of $60 \times 60 \text{ mm}^2$ in the case of Watts bath and a 20 mm diameter cylinder in the case of the sulfamate bath. Finally, the working

electrode is the substrate coated with masking tape to deposit the coating on one side only. The two electrodes are connected to a Keysight U8001 generator (30 V and 3 A max.).

The active surfaces of the pure Ni sample are 1.27 cm².

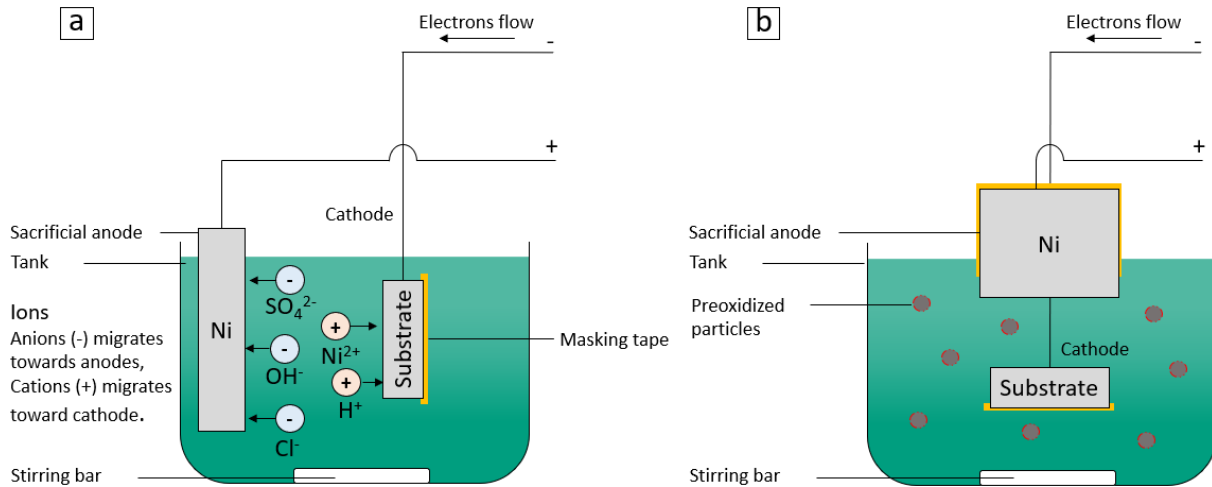


Figure II-4: Schematic representation of the bath assembly for (a) the simple Ni plating and (b) for the Ni plating with Al₂O₃ micro-particles.

I.A.3: Electrolytes and protocols used

- **Watts bath**

The Watts bath for Ni plating is traditionally used with additives such as coumarin, sodium lauryl sulfate, etc., to reduce internal stresses or simply to get an aesthetic aspect such as shine. In our case, none of these additives was added. The goal is to produce an electrodeposit with a large number of defects, which will allow, after oxidation, to have an oxide which also many defects to increase its permeability to aluminum.

The concentrations and the role of the different elements of the Watts bath are summarized in Table II-2. After the formulation of the bath and the dissolution of all the species, the pH value is comprised between 3.7 and 3.9. This pH is adjusted by adding nickel carbonate to obtain a pH between 4.2 and 4.3. For the tests, the temperature of the bath is set at 50°C. The bath is regularly renewed to allow good reproducibility of the tests (following excessively long times at 50°C), which represents approximately 4 hours.

Table II-2: Composition, utility and plating conditions of the nickel Watts bath.

Components	Quantity (g/L)	Function	Fixed parameters
Nickel sulfate tetrahydrate	280	Ni ²⁺ donor	pH= 4.2-4.3 Temperature=50°C
Nickel chloride hexahydrate	60	Reduce the passivation of the anode	
Boric acid	40	Acts as a pH buffer	
Nickel carbonate	---	Adjusts the pH (↗)	
Sulfuric acid	---	Adjusts the pH (↘)	

- **Ni sulfamate bath**

Ni sulfamate baths are well known and commonly used in industrial applications to obtain coatings without additives and with a low level of residual stress [1]. It is the reason why the sulfamate bath was chosen to make the codeposited coating. For these baths, different deposition protocols were used depending on the number of particles to be trapped and on the desired thickness of the deposit. The choice of the different protocols is based on several studies [2-11]. The concentrations and the role of the different elements for the sulfamate bath are summarized in Table II-3.

As with the Watt's bath, the sulfamate bath is regularly checked and renewed. For the sulfamate bath containing the microparticles, the procedure is different. The pH and the volume of the solution are checked and adjusted every 4 hours. But due to the reduced amount of preoxidized Al₃Ni₂ particles produced, the bath was renewed twice.

The first bath was used for preliminary tests such as the effect of current density, or the aluminization tests. During this period, the number of trapped particles in the coating decreased from 22% to 20% vol.. The second bath was used to synthesize the coatings tested in isothermal oxidation. In addition, approximately 0.4g of preoxydized particles are added to 1L of solution every 20 deposits.

Table II-3: Composition, role and plating conditions of the nickel sulfamate bath.

Components	Quantity (g/L)	Function	Fixed parameters
Nickel sulfamate tetrahydrate	300	Ni ²⁺ donor	pH= 4.2-4.3 Temperature=50°C
Nickel chloride hexahydrate	15	Reduce the passivation of the anode	
Boric acid	30	Acts as a pH buffer	
Nickel carbonate	---	Adjusts the pH (↗)	
Sulfuric acid	---	Adjusts the pH (↘)	

II-Characterization of metallic powders

Different metallic powders were selected and their reactivity was investigated (Table II-4). The Scanning Electron Microscopy (SEM) and Energy Dispersive Spectrometry (EDS) techniques (described later in §V.3) were employed to determine the morphology and the accurate composition of the powders. The SEM images and size dispersion are given in Figure II-5.

- **The Al metallic powders**

The Al powder supplied by Hermillon (France) is composed of spherical microparticles with a mean diameter of $4 \pm 3 \mu\text{m}$ (Figure II-5.a). The nanometric - and to a less extent the micrometric powders - are very dangerous because they are extremely flammable in contact with air (due to the energy released during the oxidation). Therefore, all these powders are passivated before transportation and subsequent use [12].

- **The Ni metallic powders**

Two different Ni powders (coarse and fine) supplied by GoodFellow and Alfa Aesar were selected in this study (Table II-4). The coarse Ni powder was composed of microparticles with a complex geometry and a mean diameter of $31 \pm 19 \mu\text{m}$ (Figure II-5.b). The fine Ni powder is approximately three times finer than the coarse one and also has a complex geometry (Figure II-5.c). Two different types of particles have been selected to study the influence of the size of the Ni powders on their reactivity with Al (Chapter III).

Table II-4: Main features of initial Ni and Al particles.

Powders	Supplier	Purity (wt.%)	Size (μm)	Geometry
Al	Hermillon	99.8	4 \pm 3	Spherical
Ni (coarse)	GoodFellow	99.95	31 \pm 19	Pseudo-spherical
Ni (fine)	Alfa Aesar	99.9	11 \pm 6	Pseudo-spherical

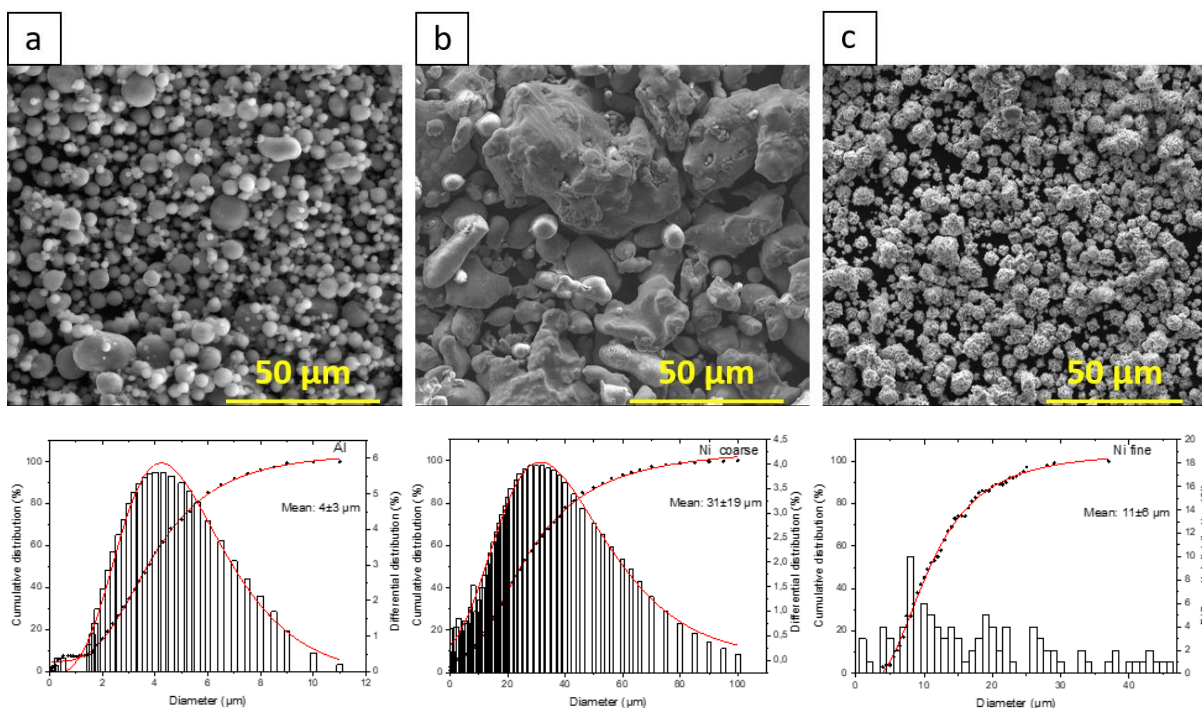


Figure II-5: SEM images and size dispersion of the three powders investigated in this study with (a) aluminum powder, (b) nickel coarse powder, and (c) nickel fine powder.

Furthermore, for the aluminothermic studies, the Ni coarse and fine powders were preoxidized to form a thin layer of NiO (Table II-5 and Figure II-6). The coarse particles were oxidized at 700°C for 1 h and 4 h in air (with intermediate crushing in a mortar every hour) and the small particles were oxidized for 15 and 40 min (with intermediate crushing in a mortar respectively every 5 and 10 min). The temperature of 700°C was chosen following the works of Peraldi et al. [13,14]. This part will be detailed in Chapter III.

Table II-5: Main features of the coarse and fine preoxidized Ni particles for different times at 700°C under atmospheric pressure of open air.

Powder	Ni coarse		Ni fine	
Size (μm)	10 \pm 9	17 \pm 14	7 \pm 4	5 \pm 3
Morphology	Pseudo-spherical	Pseudo-spherical	Pseudo-spherical	Pseudo-spherical
Oxidation time at 700°C	1 h	4 \times 1 h	3 \times 5 min	4 \times 10 min

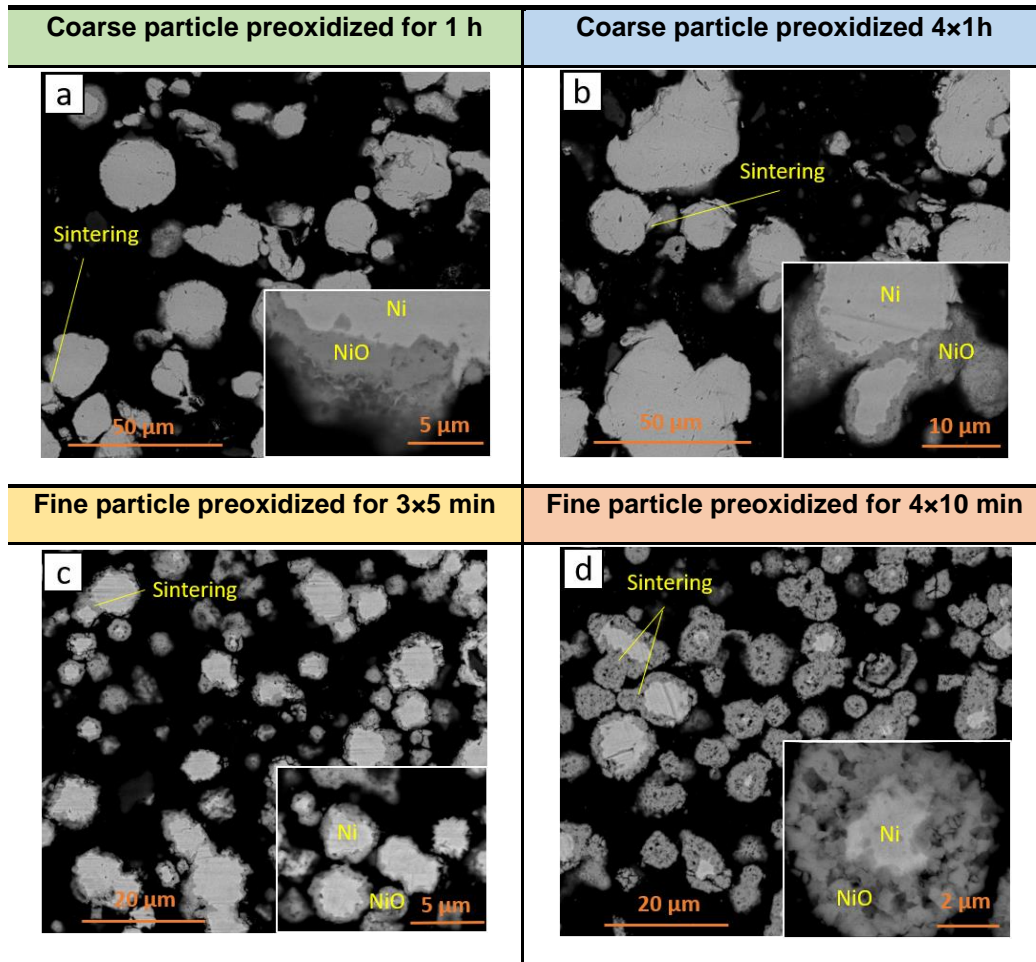


Figure II-6: SEM (BSE mode) cross-section images on the coarse and small preoxidized Ni particles at 700°C in air for different times.

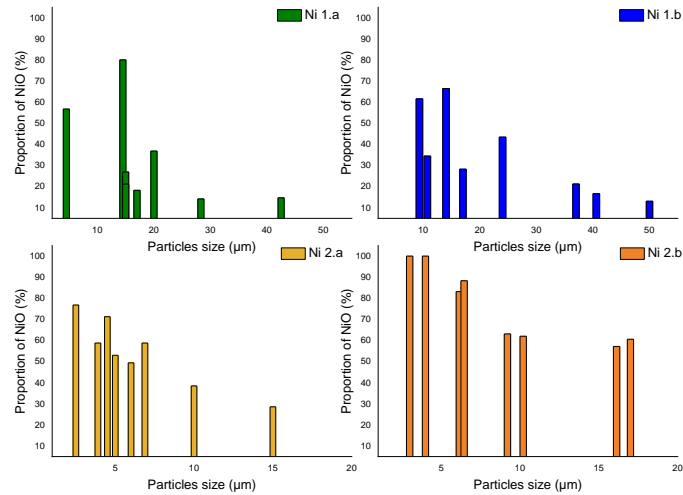


Figure II-7: Area proportion of NiO ($S_{NiO}/S_{Ni} \times 100$) as a function of particle size on the coarse (Ni-1.a & Ni-1.b) and small (Ni-2.a & Ni-2.b) preoxidized Ni particles.

- **Nickel aluminide powder**

The nickel aluminide particles were synthesized for the purpose of incorporating them into a nickel plating. For this, Ni sheets with a thickness of 250 μm and a purity of 99.98% (GoodFellow) were aluminized by pack cementation. Ten (10) sheets were cut into 10x10x0.25 mm² square-like coupons and rinsed with acetone and placed in an alumina crucible filled with 100 g of a powder mixture. The powders (56 g of Al₂O₃, 40 g Al and 4 g NH₄Cl) were mixed using a three-dimensional mixer (Turbula System Schatz type T2 F). The crucible was closed and heated at 800°C for 50h under Ar/5%H₂ atmosphere. The crucible temperature of 800°C was chosen to produce an LTHA coating (Low Temperature High-Activity), thus promoting the diffusion of aluminum and consequently the formation of the Al₃Ni₂ intermetallic phase.

Table II-6: Main features of powder mixture for pack-cementation.

Components	Quantity (wt.%)	Function	Fixed parameters
Al ₂ O ₃	56	Inert filler	50 h to 800°C
Al	40	Al ³⁺ donor	
NH ₄ Cl	4	Activator (allows the formation of AlCl ₃ (g))	

These samples were then ground into powder first with a jar milling to obtain coarse particles (Figure II-8). During this step, three aluminized nickel sheets were placed in the jar with two balls and a few drops of ethanol (ball and crucible in WC). The sheets were ground for 5 min at 30 Hz to obtain particles with a mean diameter of 4±9μm.

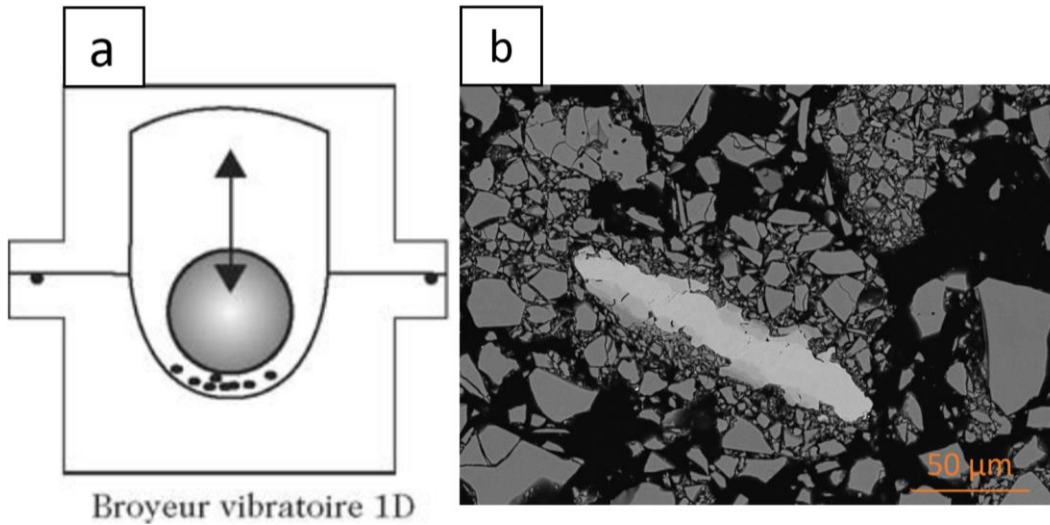


Figure II-8: (a) Schematic view of motion of the jar milling and (b) SEM cross-section images of the Al_3Ni_2 powder after the jar milling.

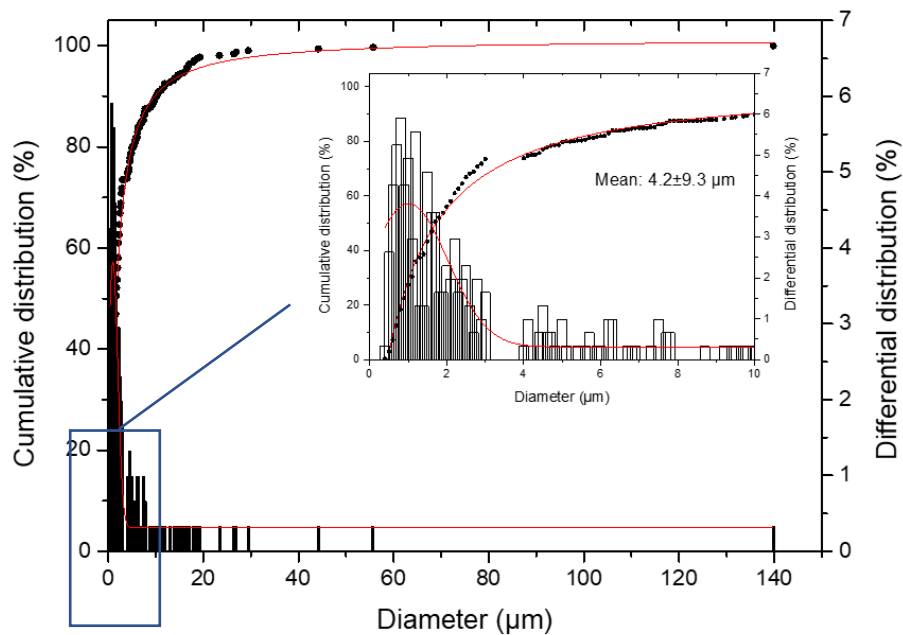


Figure II-9: Size dispersion of the particles after the jar milling (5 min at 100Hz).

To homogenize and further reduce the particle size, a planetary ball milling (P100 - Retsch) was used (Figure II-7). The powders previously obtained with the jar milling were placed at half of the volume of the crucible and filled with zirconia balls with a diameter of 2.15 mm. The free space between the particles was filled with 96% pure ethanol and the crucible was finally sealed. The crucible was then rotated at 500 rpm for 8 h. After the mechanical treatment, the particles and the balls were collected in a crystallizer and rinsed with ethanol. The crystallizer was then placed in an oven at 60°C for 12 hours to evaporate the whole ethanol.

Finally, the last step consisted of sorting the particles using several sieves positioned on a JEL 200 sieve machine. The sieves consisted of 5 assembly sieves made up of 630 μm , 250 μm , 160 μm , 100 μm and 25 μm mesh.

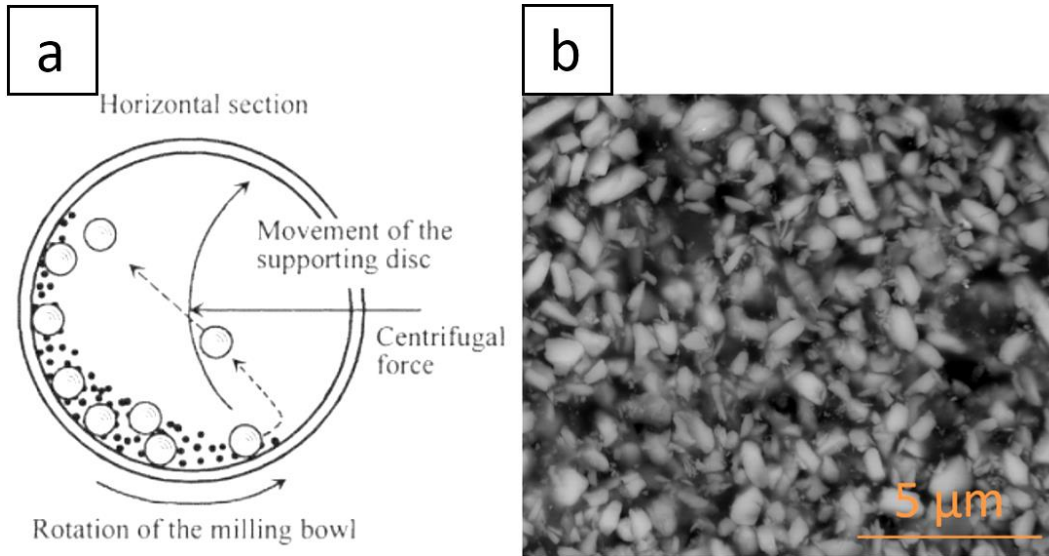


Figure II-10: (a) Schematic view of motion of the planetary ball milling and (b) SEM surface images of the Al_3Ni_2 powder after the planetary ball milling.

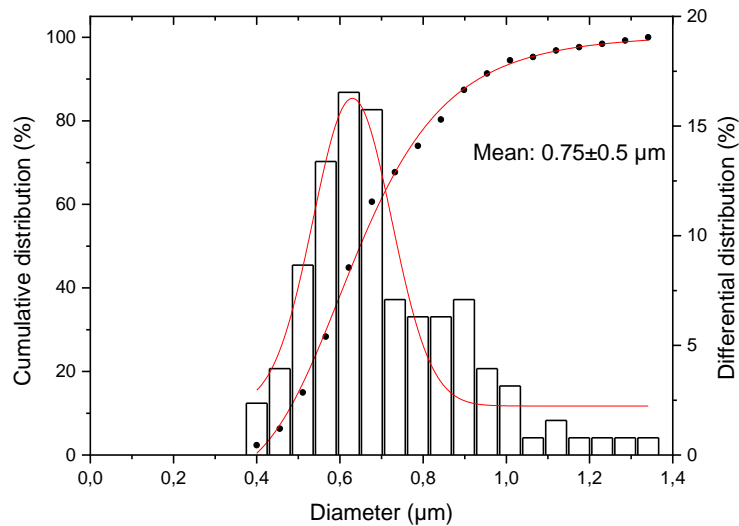


Figure II-11: Size dispersion of the particles after the planetary ball milling (8h at 500 rpm).

III-Elaboration of the slurry coatings

The coatings developed during this thesis were based on the use of a slurry with an environmentally-friendly composition. This composition is derived from the slurry initially developed and used for the European project PARTICOAT [15,16]. The elaboration of the slurry coatings follows the sequence:

1. Surface preparation of the metallic substrate (ground with #180 SiC paper)
2. Ni plating and/or a preoxidation
3. Preparation of the slurry (organic binder+ deionized water+ Al powder)
4. Deposition of the slurry by an air brush and drying of the slurry in an oven at 50°C during 30 min.
5. Heat treatment under Ar to form the self-regenerating coating

The following paragraph will detail the experimental procedure for the elaboration of the slurry coatings.

III.A-Composition and preparation of the slurries

The different slurries used in the present study were composed of:

- Metallic and pre-oxidized powders of Al and Ni_{ox}
- Polyvinyl alcohol (PVA) furnished by Sigma-Aldrich
- Milli-Q water as a solvent

The preparation of the slurries requires three stages. First, the PVA is weighed and dissolved in milli-Q water at around 40°C with a magnetic stirring (few drops of alcohol are added to the preparation to accelerate the dissolution of the PVA in water). The composition of the obtained binder follows a PVA/water ratio of 1/10. The work of B. Rannou et al. showed that below nine days no aging phenomenon was observed [15]. “Large” quantities of binder could so be prepared to save time and avoid raw material losses (over the entire study, no binder was used beyond one week after preparation).

The slurries were generally prepared the very day of depositing it on the samples. The metallic powders are accurately weighed and added to the binder in a pill box to get a slurry. For each composition, the proportions of the metallic powders were selected empirically after the deposition tests (it depends on several factors like the size, the morphology and the quantity of the particles). The slurry was then placed in a water bath at 40°C for a minimum time of 30 min. This step allowed to maintain slurry preparations always at the same temperature. Indeed, the viscosity of the slurries strongly depends on the temperature, which can fluctuate from one day to another.

III.B-Deposition of the slurries on metallic substrate by air brush

The slurry preparations were deposited on samples hand-polished up to #180 grade, followed by a Ni plating and/or a preoxidation. Polishing grade 180 was used to maintain continuity with the work done in previous years, where this grade was selected [17-20]. The purpose was to get a rough surface with no preferential direction of roughness to which the wet slurry adheres to [17]. After polishing, the samples were rinsed with milli-Q water and cleaned in an ethanol ultrasonic bath. The samples were then placed on a sample holder rotating at a constant speed ($5.25 \times 10^{-3} \text{ m.s}^{-1} = 1 \text{ rpm}$ [17]).

Slurry deposits were made using an airbrush (AZTEK A4709T model) and a nozzle (0.5 or 0.7 mm) placed at 10 cm from the samples (Figure II-12.a). The pressures used to spray slurries depend on each slurry composition and also on the quantity of slurry to be deposited. These pressures vary between 0.6 and 1.8 bars. To control the quantity of deposited slurry, the samples were weighed before and after deposition on each sample side (with a 10^{-4} g precision balance).

In addition, for a better reproducibility, no more than five samples were covered in a single pass (Figure II-12.b). Indeed, the deposited mass varied between the first and the last samples covered. For small series, this difference can vary between 0.2 and 1 $\text{mg}\cdot\text{cm}^{-2}$ and for larger series this variation can be larger and may exceed several mg/cm^{-2}

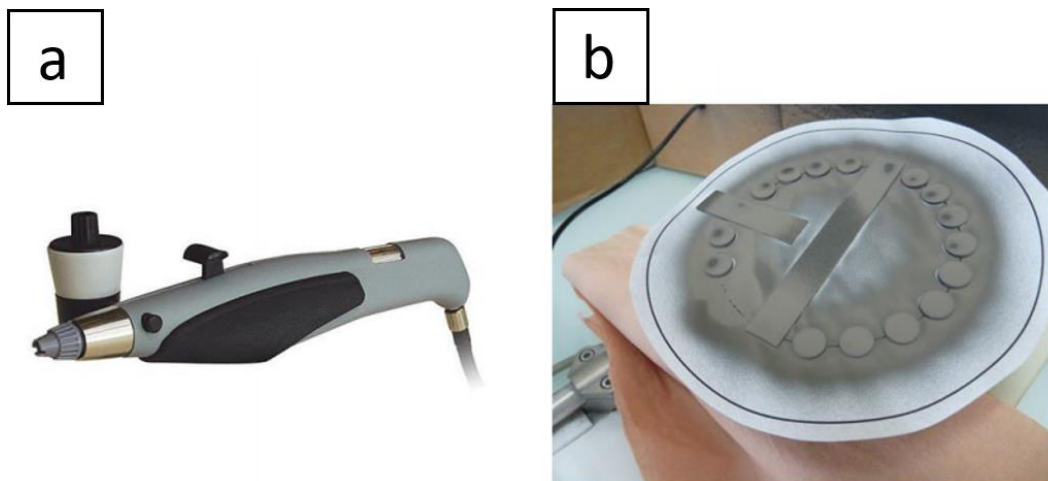


Figure II-12: (a) Picture of the airbrush and (b) view of the samples after deposition of the slurry by the airbrush.

III.C-Thermal treatments

- **Thermogravimetric analysis (TGA)**

A SETARAM TGA 92 thermobalance with a 10^{-6} g of accuracy was employed to study the evolution with high-temperature and time of the different slurry coatings on pure nickel and nickel plating. The different mass variations during the heat treatment help to detect the events that may occur during it, such as water evaporation, binder decomposition, oxidation, etc.

To reduce any uncontrolled oxidation, a partial vacuum is created in the combustion chamber (down to 4×10^{-2} mbar) before the heat treatment and an Ar flow (20mL/min) fills the space until reaching a pressure of 1.3 bars. The heating rate was fixed at $5^{\circ}\text{C}/\text{min}$ and at $25^{\circ}\text{C}/\text{min}$, and the cooling rate at 5°C or $50^{\circ}\text{C}/\text{min}$, to, respectively, reduce the thermal constraints or to keep the microstructure developed at the annealing temperature to room temperature and better comprehend the mechanisms of formation. The different heat treatments performed in the TGA will be detailed in the relevant chapters.

According to the supplier, small amounts of impurities are present in the gas bottle (5 vpm of H_2O and 2 vpm of O_2). Referring to the Ellingham diagram (thermodynamics considerations), the content in these oxidizing species is sufficient to cause the oxidation of Al at 600°C .

In addition, a SETARAM Setsys Evo 1750 (10^{-6} g accuracy) was used for the isothermal oxidation test.

IV-Degradation of the coatings

Once the coatings synthesized and characterized, it was essential to determine their stability and high-temperature behavior.

The samples were tested at high-temperature under an oxidizing gas to study oxidation resistance, the stability of the coating, and quantify the interdiffusion phenomena.

IV.A-Isothermal oxidation

Thermogravimetric analyses were conducted at 1000°C for periods of 48h in synthetic air (80 vol.% N₂ + 20 vol.% O₂) to study the oxidation kinetics. As previously described, the oxidation chamber was first purged with a vacuum pump and then filled with Ar. Once the dwell temperatures reached, the reaction chamber was emptied from Ar and synthetic air was then introduced. By measuring the mass variation of samples along oxidation time, by using a TGA92 (Setaram) thermobalance, it was possible to determine the growth kinetics of the oxide layer.

In order to get information from the isothermal oxidation kinetics, a complete parabolic law (eq. 1) was locally adjusted to the experimental curves that allowed to determine the parabolic oxidation coefficients, k_p [21]:

$$t = A + B. \Delta m/S + C. (\Delta m/S)^2 \text{ with } C = \frac{1}{k_p} \quad (\text{eq. 5})$$

With:

- t , the oxidation time at 1100°C, in s;
- $\Delta m/S$, the mass gain per surface area measured during the step at high-temperature, in mg.cm⁻²;
- k_p , the parabolic coefficient of oxidation in mg².cm⁻⁴.s⁻¹.

V-Characterization methods

V.A-Calorimetry analyses

Differential scanning calorimetry (DSC) is a technique able to detect thermal events occurring during heating and cooling periods. The DSC analyses were carried out using a SETARAM Labsys Evo 1600 thermal analysis. This type of DSC possesses two crucibles in parallel, which allow the simultaneous heating of the samples to be analyzed and of an inert sample. The measurements were performed in flowing Ar (20 mL/min) to limit oxidation phenomena and prevent secondary reactions in the system. For the different systems investigated, energy changes and temperatures of reaction or transformation were measured with the Calisto software coupled to the DSC instrument. The heat treatments were performed using alumina crucibles (90 μ L), depending on the system. The alumina crucibles were systematically cured at 1350°C. This technique was particularly helpful to analyze the reactivity between Al, Ni and NiO, with or without substrate.

V.A-Crystallographic and structural analyses

- **X-Ray Diffraction (XRD)**

X-ray diffraction is an analytical technique used to determine the crystallographic structure of compounds with a crystalline phase (such as metallic and oxide compounds). Coupled with the

Raman μ -spectrometry and the image and chemical analyses available thanks to the SEM, this technique is essential to differentiate products with the same chemical composition but with different crystalline structures. In addition, this technique is non-destructive and allows the underlying areas of the samples to be probed, unlike Raman and SEM. The surfaces of as-deposited, as-coated and degraded samples were analyzed by X-ray diffraction using a last generation Brüker D8 Advance diffractometer with Cu $K_{\alpha 1}$ radiation ($\lambda = 0.15406$ nm). The XRD patterns were acquired for a 2Θ range between 10° and 90° with a step size of 0.01° and an accumulation time fixed at 0.1s.

- **Raman micro-spectrometry**

Raman micro-spectrometry is a non-destructive technique which allows local analyses to characterize the molecular composition and the crystalline structure of the non-metallic compounds (such as oxides). A monochromatic radiation, with a known wavelength, is emitted by a laser and is directed onto a sample. The photons can then be reflected, absorbed or scattered, and some of these photons will be scattered in a non-elastic way. The nonelastic diffusion is characteristic of an energy exchange between the incident photon and the compound, corresponding to a transition between two vibrational energy levels [22]. Depending on the frequency (or energy) of the diffused photons compared to incident ones, the scattering can be qualified as Stokes or as anti-Stokes [22].

During this work, the oxides were analyzed using 2 micro-spectrometer Raman. A high-resolution micro-spectrometer Jobin Yvon Horiba (LabRAM HR8000 model) with a He-Ne laser ($\lambda = 632.817$ nm) and a LabRAM HR evolution model with a diode laser ($\lambda = 532$ nm). An Olympus confocal microscope is coupled to the micro-spectrometer to visualize the sample and focus the laser (10x, 50x and 100x magnifications).

V.C-Microscopic analyses

- **Optical microscopy**

Optical microscopy generally takes place after a first visual inspection to study the surface of the samples. This simple method comes before the more advanced techniques such as XRD, μ -Raman spectrometry and SEM. A LEICA DMRM microscope coupled to a LEICA MC170 HD camera was used to characterize the samples at the University of La Rochelle. The measurements were done with the LAS (Leica Application Suite) software associated with the microscope.

In DECHEMA- Forschungsinstitut (Germany), the samples were characterized with a LEICA DMRM microscope coupled to a LEICA DFC450 camera.

- **Scanning Electron Microscopy (SEM) and Energy Dispersive X-ray Spectroscopy (EDS)**

The SEM allows more detailed analyses of the samples. A focused electron beam scans the surface of the sample. The energy of the electrons is then transferred to the atoms of the matter increasing their potential energy. After being excited, the atoms then return to their ground state by de-excitation in the form of a secondary radiation. In the case of SEM, two types of radiation are used for the observation of the samples: secondary electrons, which permit to visualize a topographic contrast, and back-scattered electrons, which allow to visualize a chemical contrast.

-Secondary electrons imaging (SEI): secondary electrons are produced by the repulsion of incident electrons by atoms on the surface (inelastic interaction). The secondary electrons have a low energy and only those extracted from the surface can be detected. An excellent spatial resolution is then provided and therefore topographic image is obtained.

-Back-scattered electrons imaging (BSEI): the backscattered electrons are due to the elastic interactions between the atomic nuclei and the incident electrons. The energies emitted by this interaction directly depend on the atomic number of the atoms. As a result, this observation mode makes it possible to obtain a chemical contrast for the sample observed.

Surface and cross-section analyses were carried out with an environmental microscope FEI Quanta 200F equipped with a Schottky field emission gun (FEG). For cross-section observations, the samples were mounted in a polymeric resin and progressively ground with finer SiC papers up to grade #4000, then polished with a 1 μm water-based diamond suspension (Struers) to obtain a mirror polish surface. To finish, samples were cleaned with ultrasounds in successive baths of acetone and alcohol. The energy of the electron beam was fixed at 20 kV with a working distance of 10 mm and spot size between 3.4 and 3.7. To limit the charging effects of low-conductive samples (due to the ceramic part), the analyses were performed in low vacuum (0.9 mbar).

The SEM is coupled with an EDAX detector, for elemental analyses. Energy dispersive X-ray spectroscopy was carried out to analyze the chemical composition of the products by X-rays micro-diffraction.

Reference

[1] D.A. Fanner, R.A.F. Hammond, *The properties of nickel electrodeposited from a sulphamate bath*, The International Journal of Surface Engineering and Coatings 36 (1959) 32–4.2

<https://doi.org/10.1080/00202967.1959.11869768>

[2] J. Ross, J.P. Celis, J. Fransaer, C. Buelens, *The development of composite plating for advanced materials*, Journal of Metals 42 (1990) 60–63.

<https://doi.org/10.1007/BF03220440>

[3] P.M. Vereecken, I. Shao, P.C. Searson, *Particle codeposition in nanocomposite films*, Journal of Electrochemistry Society 147 (2000) 2572–2572.

<https://doi.org/10.1149/1.1393570>

[4] I. Shao, P.M. Vereecken, C.L. Chien, P.C. Searson, R.C. Cammarata, *Synthesis and characterization of particle-reinforced Ni/Al₂O₃ nanocomposites*, Journal of Materials Research 17 (2011) 1412–1418.

<https://doi.org/10.1557/JMR.2002.021>

[5] S.W. Banovic, K. Barmak, A.R. Marder, *Characterization of single and discretely-stepped electro-composite coatings of nickel-alumina*, Journal of Materials Science 34 (1999) 3203–3211.

<https://doi.org/10.1023/A:1004633923681>

[6] I. Shao, P.M. Vereecken, R.C. Cammarata, P.C. Searson, *Kinetics of particle codeposition of nanocomposites*, Journal of The Electrochemical Society 149 (2002) 610–614.

<https://doi.org/10.1149/1.1514672>

[7] N.S. Qu, K.C. Chan, D. Zhu, *Pulse co-electrodeposition of nano Al₂O₃ whiskers nickel composite coating*, Scripta Materialia 50 (2004) 11331–1134.

<https://doi.org/10.1016/j.scriptamat.2004.01.027>

[8] C.T.J. Low, R.G.A. Wills, F.C. Walsh, *Electrodeposition of composite coatings containing nanoparticles in a metal deposit*, Surface and Coatings Technology 201 (2006) 371–383.

<https://doi.org/10.1016/j.surfcoat.2005.11.123>

[9] S.L. Kuo, Y.C. Chen, M.D. Ger, W.H. Hwu, *Nano-particles dispersion effect of Ni/Al₂O₃ composite coatings*, Materials Chemistry and Physics 86 (2004) 5–10.

<https://doi.org/10.1016/j.matchemphys.2003.11.040>

[10] D.R. Grabe, F.C. Walsh, *The rotating cylinder electrode: a review of development*, Journal of Applied Electrochemistry 13 (1983) 3–21.

[11] C.F. Malfatti, J. Zoppas-Ferreira, C.B. Santos, B.V. Souza, E.P. Fallavena, S. Vaillant, J.P. Bonino, *Nip/SiC composite coatings: the effects of particles on the electrochemical behavior*, Corrosion Science 47 (2005) 567–580.

<https://hal.archives-ouvertes.fr/hal-00474900>

[12] A. Gromov, Y. Strokova, U. Teipel, *Stabilization of metal nanoparticles - A chemical approaches*, Chemical Engineering & Technology, 32 (2009) 1049–1060.

<https://doi.org/10.1002/ceat.200900022>

[13] R. Peraldi, D. Monceau, B. Pieraggi, *Correlations between growth kinetics and microstructure for scales formed by high-temperature oxidation of pure nickel. I. Morphologies and Microstructures*, Oxidation of Metals 58 (2002) 249–273.

<https://doi.org/10.1023/A:1020170320020>

[14] R. Peraldi, D. Monceau, B. Pieraggi, *Correlations between growth kinetics and microstructure for scales formed by high-temperature oxidation of pure nickel. II. Growth Kinetics*, Oxidation of Metals 58 (2002) 275–295.

<https://doi.org/10.1023/A:1020102604090>

[15] B. Rannou, F. Velasco, S. Guzman, V. Kolarik, F. Pedraza, *Aging and thermal behavior of a PVA/Al microspheres slurry for aluminizing purposes*, Materials Chemistry and Physics 134 (2012) 360–365.

<https://doi.org/10.1016/j.matchemphys.2012.03.002>

[16] X. Montero, M.C. Galetz, M. Schütze, *A single step process to form in-situ an alumina foam/aluminide TBC system for alloys in extreme environments at high temperature*, Surface and Coatings Technology 206 (2011) 1586–1594.

<https://doi.org/10.1016/j.surfcoat.2011.05.052>

[17] M. Mollard, *Elaboration de systèmes barrière thermique par barbotine. Comportement du nickel et de ses superalliages revêtus en oxydation cyclique à haute température*, PhD Thesis, Université de La Rochelle (2012).

<https://tel.archives-ouvertes.fr/tel-00839920>

[18] C. Boulesteix, *Synthesis, environmental degradation and repairability of slurry aluminum coatings elaborated on steels employed in power plants*, PhD Thesis, Université de La Rochelle (2017).

<https://tel.archives-ouvertes.fr/tel-01804936>

[19] B. Grégoire, *Functionalization of aeronautical thermal barrier systems elaborated by slurry (FONBAT)*, PhD Thesis, Université de La Rochelle (2017).

<https://tel.archives-ouvertes.fr/tel-01939473>

[20] G. Boissonnet, *Factors influencing the thermal insulation potential of different thermal barrier coating systems*, PhD Thesis, Université de La Rochelle (2019).

<https://tel.archives-ouvertes.fr/tel-02528825>

[21]: B. Pieraggi, *Calculations of parabolic reaction rate constants*, *Oxidation of Metals* 27 (1987) 177–185.

<https://doi.org/10.1007/BF00667057>

[22] I.R. Lewis, H.G.M. Edwards, L.A. Nafie, *Handbook of Raman Spectroscopy: From the research laboratory to the process line*, New-York Marcel Dekker Inc. (2001).

ISBN: 9780824705572

Chapter III. Study of the reactivity and microstructure of Al and preoxidized Ni powders by DSC.

Aluminothermic (or thermite) reactions are well known and have been used for centuries. The rise of this reaction is due to two unique characteristics. Indeed, aluminum has an extremely high affinity with oxygen, so it is able to reduce a large part of the metal oxides. In addition, this reaction is extremely exothermic and can reach temperatures above 2700°C [16-17]. For decades these two characteristics have been put into practice to weld railways. Indeed, when aluminum liquid ($T=660^{\circ}\text{C}$) is deposited on the junction of two rusty rails, the aluminum will reduce the iron oxide to form liquid iron ($T>1538^{\circ}\text{C}$) and alumina. The density of alumina being much lower (3.95 g/cm^3) than that of iron liquid, it naturally floats on the surface and can be easily removed.

In our case, the aluminothermic reactions take place between aluminum and nickel oxide to synthesize self-regenerating coatings. The goal of the thermite reaction is to provide additional exothermicity to the SHS reaction between aluminum and nickel, and essentially synthesize in-situ alumina. In this case, the presence of alumina is desired because it is often considered as a reinforcement element and moreover it blocks the diffusion of the species thus slowing down harmful phenomena such as interdiffusion.

For the study of these complex phenomena (aluminothermic process and SHS), the tests were divided into 2 parts. The first part treated in sub-chapters 1 and 2 concerns the study of the reactivity between the Al powders and preoxidized Ni powders. The second part addressed in sub-chapter 3, concerns the study of the reactivity between a model substrate (pure Ni) and Al powder.

In the first part, several parameters will be tested and the experiments will take place in 2 steps. The first step consists in oxidizing the Ni particles, weighing and mixing the powders to obtain the desired layout. Then, the crucibles are heated up in a DSC. This first step will give us an energetic analysis of the different reactions that will take place inside the alumina crucibles. The second step concerns the characterization of the microstructure and the analysis of the elements previously formed. This step consists of a slow and meticulous polishing in cross-section of the crucibles followed by SEM observation coupled with EDS analyses.

The reactivity between the powders has been studied by considering the size of Ni particles, the main oxide features of the preoxidized Ni powders, the arrangement of the particles (Al over Ni or vice versa and random mixtures) and the heating rates.

First, a scientific article [Troncy et al. *Materials Chemistry and Physics* (2020)] focuses on the powder mixture between Al and preoxidized Ni particles (Al + Ni_{ox}), and the second configuration is a bilayer system with Ni_{ox} on top of Al particles (Ni_{ox} / Al).

The Al over preoxidized Ni configuration (Al/Ni_{ox}) will be discussed separately.

Table of contents

I-Article I: Reactivity and microstructural observation of Al+Niox and Niox/Al system by DSC ...	71
Abstract.....	71
I-Introduction	71
II-Experimental procedure	73
III-Results	74
III.A-Effect of the preoxidation time of the Ni powder	74
III.B-Reactivity of Al-Ni _{ox} microparticles	77
III.C-Reactivity of preoxidized Ni over pure Al.....	82
IV-Discussion	87
IV.A-Effect of the preoxidation time	87
IV.B-Layout 1- Mixture of preoxidized Ni and Al particles	88
IV.C-Layout 2- preoxidized Ni powders over the Al particles.....	89
V-Conclusion	91
References.....	93
II- Reactivity and microstructural observations of Al/Niox system by DSC	97
II.A-Results.....	97
I.A.1-Differential scanning calorimetry.....	97
I.B-Microstructural development	99
II.C-Discussion	102
II.D-Conclusion.....	104
III-Reactivity of the Al particles with pure preoxidized nickel substrate.....	105
III.A-layout A and B: Pure Ni and pure Ni with Al particles	105
III.A.1-Results	105
III.B-Layout C: Preoxidized pure Ni with Al particles	107
III.B.1-Results	107
III.C-Discussion	113
III.D-Conclusion.....	114
References.....	116

I-Article I: Reactivity and microstructural observation of Al+NiOx and NiOx/Al system by DSC

Materials Chemistry & Physics 251 (2020) 123124.

Microstructural characterization of NiAl-Al₂O₃ composite materials obtained by in situ aluminothermic reduction of NiO for potential coating applications

R. Troncy^{1, a}, G. Bonnet^{1, b}, F. Pedraza^{1, c}

¹ La Rochelle Université. LaSIE, UMR-7356-CNRS. Avenue Michel Crépeau, 17042 La Rochelle Cedex 1, France

aromain.troncy1@univ-lr.fr, gbonnet@univ-lr.fr, fpedraza@univ-lr.fr

Abstract

Aluminothermic reactions between Al microparticles and preoxidized Ni particles were carried out to fabricate mixed compounds of Ni_xAl_y containing in situ generated Al₂O₃. The mixed composites were obtained by applying a thermal treatment to either a mixture of NiO and Al powders or to a stacking of powders. The effects of the particle size, thickness of oxide, heating ramp and temperature on the microstructure of the NiAl-Al₂O₃ coating are discussed. The results indicate that Ni₃Al forms first during the synthesis, followed by NiAl and Al₃Ni₂ while Al₃Ni forms on cooling. Moreover, the alumina was observed to form a continuous network surrounding Ni_xAl_y intermetallic compounds. It derives that these composites have a potential to form self-healing coatings.

I-Introduction

Nowadays, the demand for materials with high performances at elevated temperature is in constant increase. Nickel based superalloys possess excellent mechanical properties at high temperature due to their high melting point. However, their resistance to oxidation by hot gases and to so-called hot corrosion appears limited [1, 2]. To overcome these disadvantages, the use of intermetallic compounds was developed. NiAl is the most attractive due to capacity to develop a protective aluminum oxide layer through oxidation [3, 4]. The coating acts as an aluminum reservoir whereby aluminum is consumed by oxidation at the surface of the coating to form an alumina protective layer [1, 2, 5, 6]. Further, Al diffuses into the substrate, which lowers the overall Al content in the coating. Below a critical concentration, other non-protective oxides such as NiAl₂O₄ and NiO may form resulting in the rapid degradation of the material. For instance, during the oxidation of Ni(Pt)Al systems at high temperature (100 h at 1050°C), 2 to 8% of Al are consumed by the formation of the aluminum oxide while 20 to 35% of Al are “lost” by diffusion to the superalloy substrate [7]. Diffusion barriers can be employed to prevent diffusion of aluminum in the substrate. These diffusion barriers can be made of refractory elements or rare-earth ones whose effectiveness to slow down the diffusion of aluminum has been demonstrated [8-10]. However, such diffusion barriers mechanically weaken the coated components and increase the coating prices.

Our approach to maintain a sufficient amount of Al is to introduce aluminum micro-containers into the coating so that Al is released once a concentration gradient is established between the reservoir and the Al-impoverished coating matrix. The micro-containers are small volumes (tens of μm) of an Al-rich Ni_xAl_y intermetallics compound entrapped by aluminum oxide. The micro-containers shall thus have an Al-rich intermetallic core (Al_3Ni or Al_3Ni_2) encapsulated in an alumina shell. The intermetallic core can be synthesized by Self Propagating High-Temperature Synthesis (SHS). SHS is a complex thermally activated physicochemical process that takes place at elevated temperatures [11]. A great number of factors and process conditions can exert a significant influence on the results, in particular temperature, time, size of the particles, heating and cooling rates, pressure and atmosphere [12, 13]. The relationship between these different parameters and the reaction process between the three elements (Ni, Al and O) was reported by Levin & al. and results in multiphase (metal, liquid and oxide) components as shown in Figure III-1 [14].

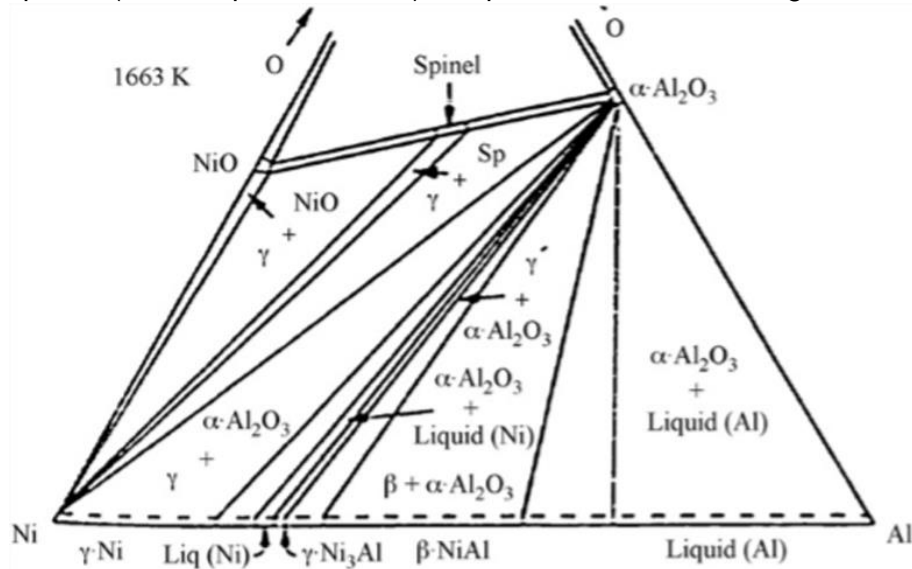
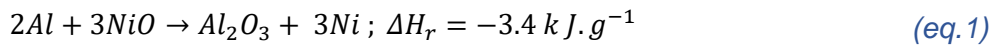


Figure III-1: Ternary phase diagram of Ni-Al-O at 1638 K (1365°C) [14].

The alumina shell can be produced in situ by an aluminothermic process following the thermite reaction (eq. 1) [15]:



The redox reaction between NiO and Al results in the release of a large amount of energy. The products of such a reaction are solid, liquid and sometimes gaseous, inducing an intense sputtering and destruction of the samples [16, 17]. However, the exothermic effect can be inhibited by the addition of an inert diluent, i.e. of a heat absorber. Vrel et al. studied the effects of the addition of alumina and of the limitation of one of the two reagents on the aluminothermic reaction [16, 17]. In addition, Biswas et al. [18] reported that the heating rate and the particle size could be modified to limit the amount of energy released and produce different intermetallic compounds. For instance, low heating rates and a large size of particles can cancel the explosion of the powders.

Based on the above, the Al-Ni SHS and the aluminothermic reactions will be combined in this work to synthesize $\text{Ni}_x\text{Al}_y\text{-Al}_2\text{O}_3$ phases that could serve as self-healing coatings. Different parameters

including particle size, heating rates, amount of nickel oxide and contact area between particles will be studied.

II-Experimental procedure

Commercially available Ni microparticles underwent a preoxidation treatment at 700°C in air for different times to form NiO oxide shells over the Ni powders. This oxidation temperature of 700°C was chosen following the works of Peraldi et al. [19, 20], who described the microstructure of the oxide scales grown on pure Ni as function of temperature and time. The porous NiO formed at 700°C for short times is expected to facilitate the Al flow during the SHS reactions. The particles size of the powders and the time of preoxidation are given in Table III-1.

Table III-1: Main features of initial Ni, Al and preoxidized Ni particles.

Powder	Aluminum	Nickel 1	Nickel 2	Nickel 1 preoxidized	Nickel 1 preoxidized	Nickel 2 preoxidized	Nickel 2 preoxidized
Symbol	Al	Ni-1	Ni-2	Ni-1.a	Ni-1.b	Ni-2.a	Ni-2.b
Purity (wt %)	99.8	99.95	99.9	---	---	---	---
Size (µm)	4±3	31±19	11±6	10±9	17±14	7±4	5±3
Morphology	Spherical	Spherical	Pseudo-spherical	Pseudo-spherical	Pseudo-spherical	Pseudo-spherical	Pseudo-spherical
Oxidation time at 700°C	0	0	0	1 h	4x1 h	3x5 min	4x10 min
Supplier	Hermillon	GoodFellow	Alfa Aesar	---	---	---	---

The coarse powder (Ni-1) was heated at 700°C for 1h (Ni-1.a) and 4h (Ni-1.b) in air (intermediate crushing in a mortar every hour). The small-sized powder (Ni-2) underwent the same preparation but the oxidation time was of 15 min (Ni-2.a) and 40 min (Ni-2.b) (intermediate crushing every 5 and 10 min, respectively). The intermediate crushing step was realized to increase the oxide thickness and avoid sintering. Such partial oxidation is assumed to present two simultaneous advantages, i.e. to reduce the energy release during the thermite reaction and to lower the content of one of the two reagents like in the works of Vrel et al. [16, 17]. Moreover, it allows to keep a metal core surrounded by a porous NiO to form the desired composite compounds [18-20].

A powder mixture containing the preoxidized nickel particles and aluminum particles was blended in the stoichiometric atomic ratio to form NiAl according to the Al-Ni binary diagram (Figure III-2.a). In addition, the preoxidized nickel particles were deposited over the Al microparticles (Figure III-2.b) to simulate the interfacial reactions of a potential coating. Both configurations (mixed and stacked powders) were placed in alumina crucibles for the DSC experiments (SETARAM Labsys Evo 1600 thermal analysis). The heating rates were fixed at 2 and 25°C/min with a maximum temperature of 1300°C; the cooling rate was fixed at 50°C/min (to keep the microstructures and crystal phases obtained at high temperature). Upon annealing, the reaction chamber was ventilated with a flow of Ar (20 mL/min) to limit oxidation phenomena and prevent secondary reactions in the system, although some air can be trapped between the powders when poured into the crucible. For each test, energy changes and reaction temperatures were determined using the Calisto software coupled to the DSC technique. To identify all the transformations, additional heat treatments were performed in the same conditions but the tests were interrupted at 750 and 1000°C.

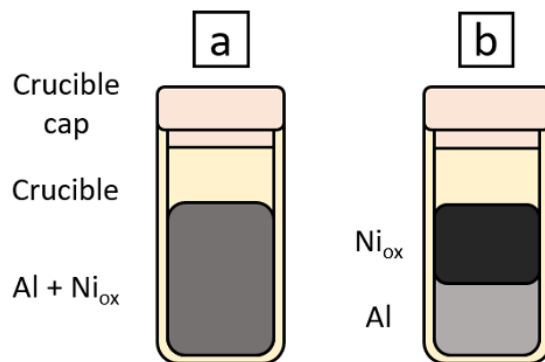


Figure III-2: Schematic drawings representing the two different layouts: (a) mixture of preoxidized Ni and of Al particles; (b) preoxidized Ni over the Al particles.

After the heat treatment, the crucibles were prepared for microscopy observation of the cross-sections. They were thus mounted in a phenolic resin, ground till SiC P4000 and finally polished with a 1 μm diamond suspension (Struers). The characterization of the cross-sections was performed with a SEM (FEI QUANTA 200F Field Emission Gun) coupled to an EDAX detector for chemical analysis at 20 kV in low vacuum (0.9 mbar). Raman micro-spectrometry (Jobin Yvon LabRam HR800, $\lambda=632.82$ nm) was also carried out to identify the different oxide phases.

III-Results

III.A-Effect of the preoxidation time of the Ni powder

Figure III-3 shows the cross-section of the preoxidized nickel particles. The Raman spectra of Figure III-4 clearly demonstrate the unique formation of NiO on all particles at different oxidation times at 700°C [21]. The smaller nickel particles (Ni-2) present thicker oxide scales on their surface although the oxidation time is shorter (15 and 40 min) than for the coarse particles (1 and 4 h). Some of the grain boundaries of the coarse particles (Ni-1) are also oxidized. At increased magnifications (see inset in Figure III-3), the surface of Ni-1 exhibits a duplex scale (platelet and compact) after 1 h but the oxide is thicker and porous after 4 h of oxidation. It thus appears that the oxides get thicker with increasing time and number of cycles of oxidation. However, the thickness of the oxide layer varies among the particles (0.3 to 3 μm for 1 h and 1 to 5 μm for 4x1 h). Additional characterization of the coverage with NiO as a function of particle size was performed with “Image J” software (Figure III-5). It can be observed that the smaller the particles, the greater the oxidation. Also, the dependence of oxidation with the particle size decreases with increasing the number of oxidation cycles. Moreover, sintering of the particles caused by oxide growth is observed for all the oxidation times and particle sizes, in particular for the smallest ones (Ni-2). This indicates that the crushing between oxidation cycles was effective in avoiding sintering. In addition, the large particles seem to break along the oxidized grain boundaries and thus form smaller particles upon the repetitive crushing.

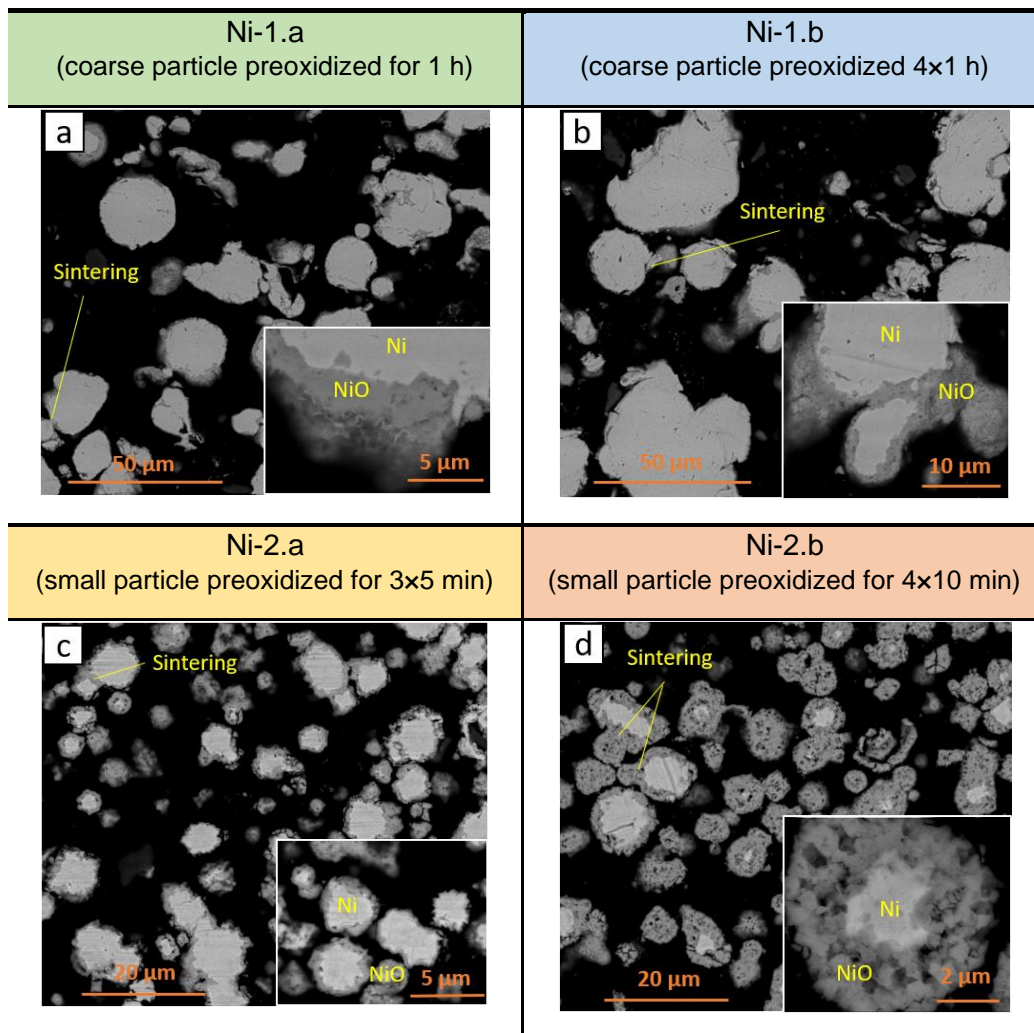


Figure III-3: SEM (BSE mode) cross-section images on the coarse (Ni-1.a & Ni-1.b) and small (Ni-2.a & Ni-2.b) preoxidized Ni particles at 700°C in air for different times.

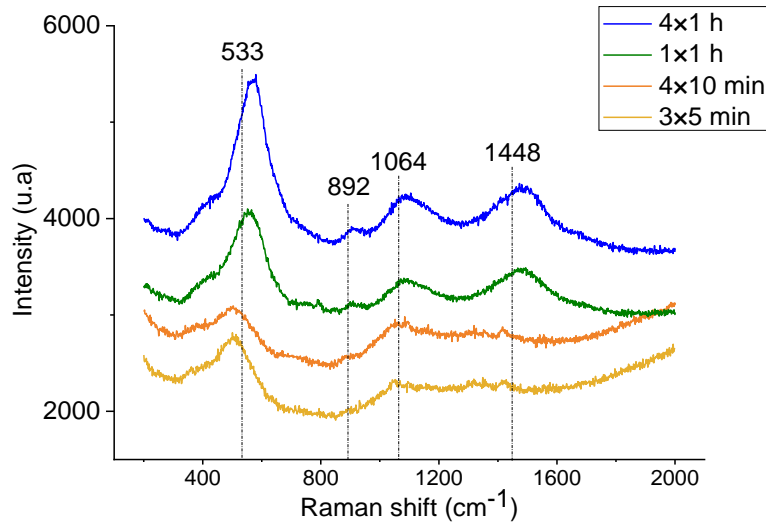


Figure III-4: Raman spectra of the oxides formed on the coarse (Ni-1) and small (Ni-2) particles after oxidation at 700°C in air for different times [21].

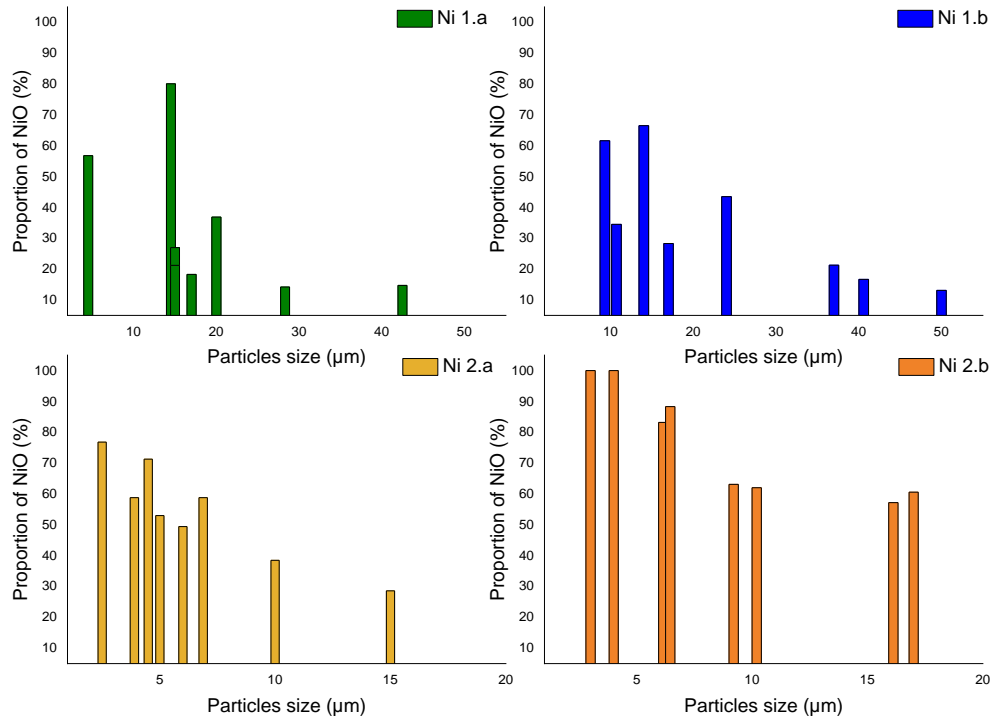


Figure III-5: Area proportion of NiO ($S_{NiO}/S_{Ni} \times 100$) as a function of particle size on the coarse (Ni-1.a & Ni-1.b) and small (Ni-2.a & Ni-2.b) preoxidized Ni particles.

III.B-Reactivity of Al-Ni_{ox} microparticles

- Differential scanning calorimetry

The DSC results of the reference powders (Al; metallic Ni-1 and Ni-2; preoxidized Ni-1 and Ni-2) heated at 25°C/min till 1300°C are shown in Figure III-6. The data are summarized in Table III-2. Coarse Ni (Ni-1) undergoes an event starting at 346°C that corresponds to the Curie temperature (358°C) [22]. In contrast, the same thermal event is more energetic and starts and finishes at a larger temperature interval when the particles are small (Ni-2). For Al, the onset and the maximum melting temperatures also differ (665 and 677°C for, respectively, the 2 and 25°C/min heating rates) but the overall endotherm is relatively similar. The differences with respect the theoretical melting temperature (660.5°C [23]) can be thus ascribed to the different heating rates [24] that change the manner heat is absorbed.

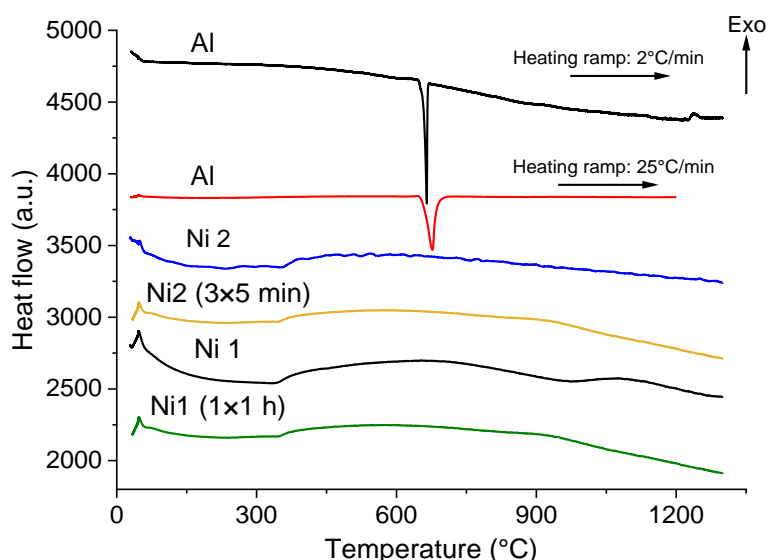


Figure III-6: DSC thermograms for the reference powders (Al, Ni and Ni oxidized) upon heating at 2 and 25°C/min till 1300°C in Ar.

Table III-2: Thermal data of the effects observed for the reference powders (Al, Ni and Ni oxidized) upon heating at 2 and 25°C/min till 1300°C in Ar.

Transformation	Ni-1 (coarse particles)			Ni-2 (small particles)		
	T _{max} (°C)	ΔT (°C)	ΔH (J g ⁻¹)	T _{max} (°C)	ΔT (°C)	ΔH (J g ⁻¹)
Curie temperature	654	346-950	-81	616	250-1300	-166
	Ni-1.a (coarse preoxidized particles: 1 h)			Ni-2.a (small preoxidized particles: 3x5 min)		
Curie temperature	593	352-901	-105	612	387-1300	-156
	Al-2°C/min			Al-25°C/min		
Melting point	665	645-671	362	677	658-686	385

In the mixed Al + Ni powders, the first exothermic peak at $620\pm 2^\circ\text{C}$ (label 1 in Figure III-7) is most likely related to a solid-state reaction between Al and NiO [25, 26]. This peak is followed by an endothermic one at $671\pm 6^\circ\text{C}$, which corresponds to the melting point of Al (label 2 in Figure III-7) [23]. For the coarse oxidized particles (Ni-1), the reaction between Al and Ni occurs at $852\pm 14^\circ\text{C}$ (label 3 in Figure III-7) and forms Ni_xAl_y intermetallic compounds [27]. Right after, a last exothermic peak (label 4 in Figure III-7) starting above 1000°C can be related to the stabilization of the NiAl intermetallic compound and to the transformation of metastable $\gamma\text{-Al}_2\text{O}_3$ into stable $\alpha\text{-Al}_2\text{O}_3$ [25, 27]. Interestingly, the maximum temperature for NiAl formation is lower in the least preoxidized coarse particles than the ones oxidized for longer times (4×1 h).

For the small preoxidized particles (Ni-2), the same reactions occur until 750°C (Figure III-7, Table III-3). However, a clear separation between NiAl and Al_2O_3 cannot be made at higher temperatures because the phenomena are now significantly exothermic. Further, the least oxidized particles (3×5 min) do not undergo a subsequent transformation of NiAl like the one observed in the preoxidized 4×10 min + Al mixtures.

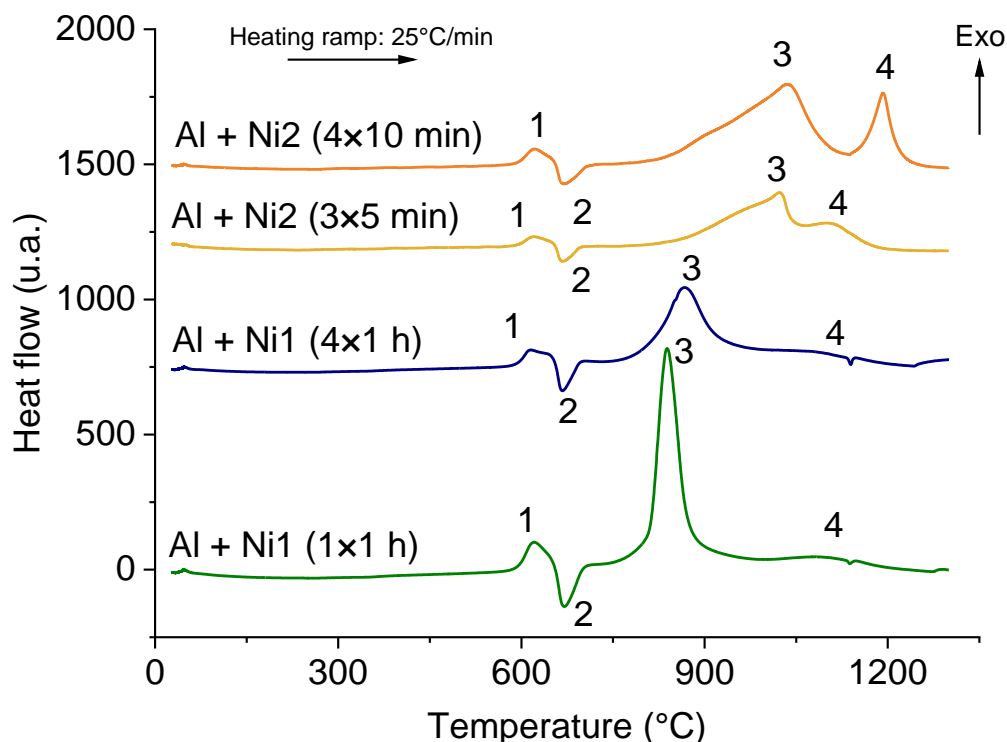


Figure III-7: DSC thermograms of the mixtures of Al with the different Ni particles upon heating $25^\circ\text{C}/\text{min}$ till 1300°C in Ar.

Table III-3: Thermal data and potential transformations in the mixtures of Al with the different Ni particles.

	T _{max} (°C)	ΔT (°C)	ΔH (J g ⁻¹)	T _{max} (°C)	ΔT (°C)	ΔH (J g ⁻¹)
Transformation	Al + Ni-1.a (coarse oxidized Ni particles: 1 h)			Al + Ni-1.b (coarse oxidized Ni particles: 4×1 h)		
NiO reduction	620	526-656	-73	618	540-656	-78
Al melting	671	656-712	63	669	656-711	69
NiAl formation	838	742-988	-596	867	740-1000	-576
γ-Al ₂ O ₃ → α-Al ₂ O ₃	1095	988-1252	-54	1080	993-1142	-52
	Al + Ni-2.a (small oxidized Ni particles: 3×5 min)			Al + Ni-2.b (small oxidized Ni particles: 4×10 min)		
NiO reduction	621	555-655	-66	621	551-655	-72
Al melting	668	655-724	61	670	655-727	81
NiAl formation and γ-Al ₂ O ₃ → α-Al ₂ O ₃	1023	754-1244	-1457	1036	742-1136	-1290
NiAl formation	---	---	---	1192	1136-1272	-314

- **Microstructural development**

The microstructures and the composition of the mixed powders obtained at 750, 1000 and 1300°C are shown in Figure III-8 and Figure III-9. These temperatures correspond to the main exothermic reactions observed in the DSC curves of Figure III-7 (peaks 1, 3 and 4).

In the coarse Ni particles (Ni-1.a and Ni-1.b), all the NiO formed by preoxidation is consumed by the aluminothermic reaction at 671±6°C. As a result, the particles present a homogeneous composition of about 30Al-70Ni (at %) (Figs. 8.a and 8.b). At 1000°C, quite similar concentration gradients of Al and Ni between the core and the external areas are observed in Ni1.a and Ni1.b (labels 1 to 4 in Figs. 8.c and 8.d). Concentrations of Al and Ni of 21-79; 37-63; 48-52 and 58-42 at % are respectively retrieved from the core to the surface. After the full treatment at 1300°C, all the particles show a fully homogenized NiAl phase with 46Al-54Ni (at %). Moreover, cracks and Kirkendall porosity appear.

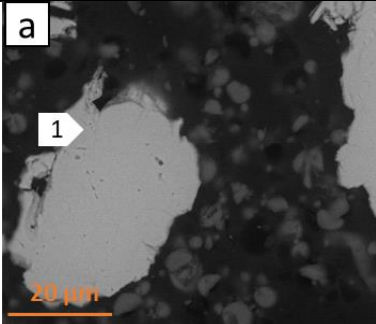
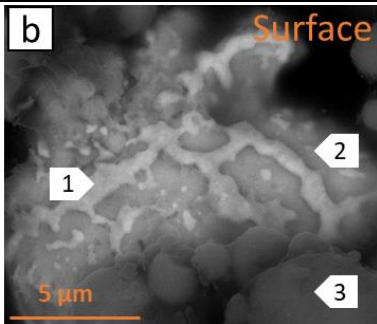
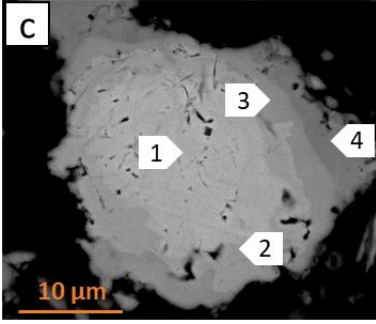
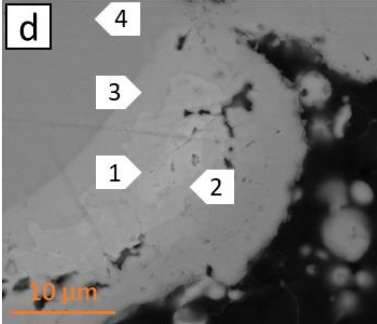
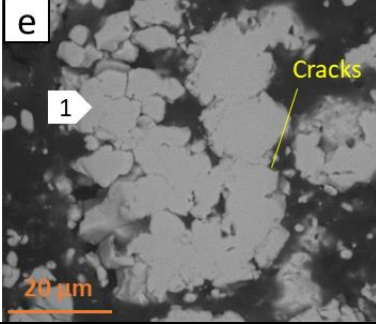
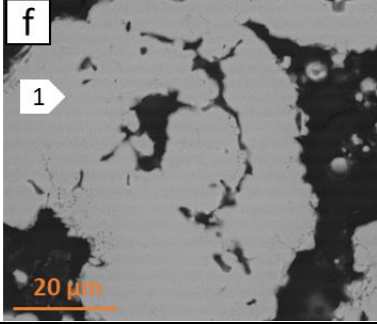
T(°C)	Al + Ni1.a (coarse oxidized Ni particles : 1 h)			Al + Ni1.b (coarse oxidized Ni particles : 4x1 h)				
	Spot	Al (at %)	Ni (at %)	Spot	Al (at %)	Ni (at %)		
750		1	30	70		1	33	67
						2	30	70
						3	94	6
1000		1	21	79		1	27	78
						2	37	63
						3	48	52
						4	58	42
1300		1	46	54		1	46	54

Figure III-8: SEM (BSE mode) of the mixture between Al and coarse Ni preoxidized particles (Ni1.a & Ni2.b) after DSC treatments at 25°C/min for different temperatures.

For the small Ni particles (Ni-2.a and Ni-2.b) preoxidized for 15 and 40 min, NiO is not fully consumed by the aluminothermic reaction before 750°C. The core of the particles presents a homogeneous phase with a composition of Al and Ni, respectively, of 16-84 and 39-61 at % (Figure III-9.a and 9.b). Moreover, a high content of Al is found in the oxide when the particles have been preoxidized for 40 min (label 2 in Figure III-9.b) but it was not possible to identify the precise nature of mixed Ni-Al oxide by XRD or Raman spectroscopy. A quasi-stoichiometric NiAl compound has been observed on the outer part of the particles (label 3 Figure III-9.b). For the treatment stopped at 1045°C for Ni-2.a (3x5 min), metallic and partially oxidized particles are observed. The metallic particles are composed of two different zones. One zone has a homogeneous composition of 15Al and 85Ni (at %) (label 1 in Figure III-9.c). Other areas show a gradient of concentration of Al and Ni respectively, 21-79; 32-68 and 38-62 (at %) from the core to the surface (labels 3 at 5 in Figure III-9.c). Concerning the partially oxidized particles (label 2 in Figure III-9.c), the core presents a

homogeneous phase with a composition of 63Al-37Ni (at %) while the periphery appears clearly oxidized with Al and Ni.

For the Ni-2.b (4x10 min), two types of partially oxidized particles can be observed. The first type is composed by a metal core with a composition of 11Al-89Ni at % (label 1 in Figure III-9.d), surrounded by an NiO layer which is itself surrounded by a metal layer identical to that of the particle core (view inset Figure III-9.d). The second type of particles is made of a homogeneous phase of 44Al and 56Ni (at %) (label 2 in Figure III-9.d) and interpenetrated alumina. After 1300°C, all the particles show a fully homogenized Ni₃Al phase with 31-68 and 27-73 at % of Al and Ni, respectively (labels 1 in Figure III-9.e and 9.f). Moreover, an aluminum oxide layer can be noticed at the periphery of the particles, as well as some aluminum oxide inclusions inside the particles.

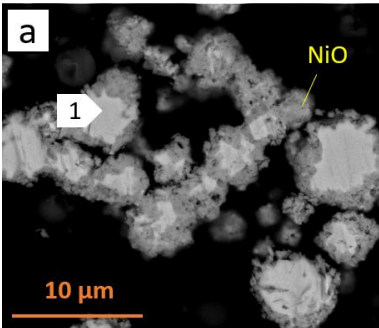
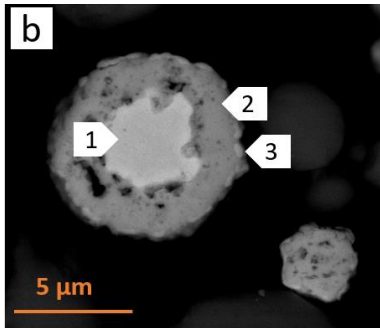
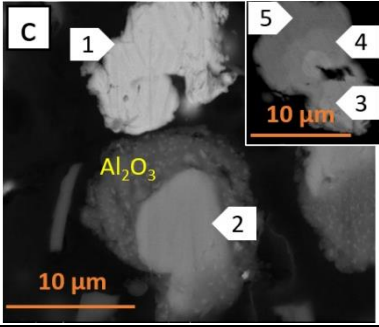
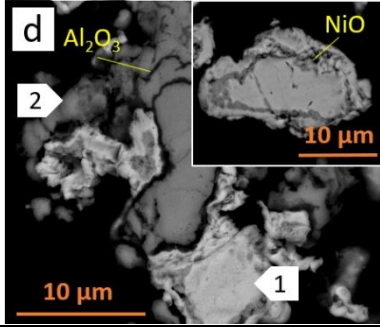
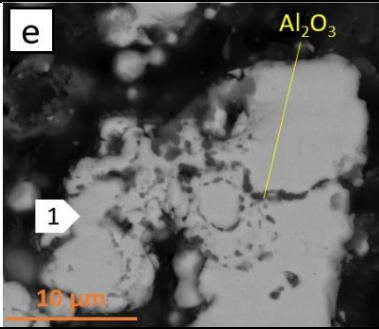
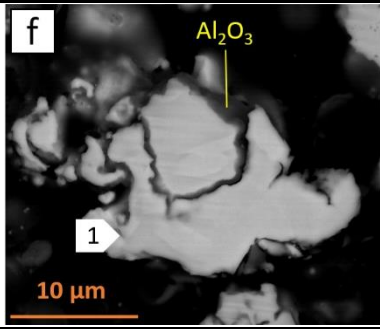
T(°C)	Al + Ni2.a (small oxidized Ni particles : 3x5 min)	Spot	Al (at %)	Ni (at %)	Al + Ni2.b (small oxidized Ni particles : 4x10 min)	Spot	Al (at %)	Ni (at %)
750		1	16	84		1	39	61
						2	43	57
						3	44	56
1045		1	15	85		1	11	89
						2	63	37
						3	21	79
						4	32	68
						5	38	62
1300		1	31	68		1	27	73

Figure III-9 SEM (BSE mode) of the mixture between Al and small Ni preoxidized particles (Ni-2.a & Ni-2.b) after DSC treatments at 25°C/min for different temperatures.

Therefore in the rest of the study, we will focus on the coarse particles oxidized 4×1 h (Ni-1.b) because the oxide layers are thicker and more homogeneous (Figs. 3 and 5), which should be favorable for the formation of micro-reservoirs. Concerning the small oxidized particles, the particles oxidized 4×10 min (Ni-2.b) will be discarded. Indeed, the oxide layers are conversely too important (Figs. 3 and 5), which would consume a large part of aluminum, likely impeding the formation of an Al-rich intermetallic core rich for the micro-reservoirs.

III.C-Reactivity of preoxidized Ni over pure Al

- Differential scanning calorimetry

The DSC results of the different preoxidized Ni particles obtained with two heating ramps (2 and 25°C/min) are shown in Figure III-10 and the thermal data are summarized in Table III-4. Reduction of NiO and melting of Al occur at respectively, $620\pm 2^\circ\text{C}$ and $670\pm 2^\circ\text{C}$. For the two heating rates applied to the coarse particles, and for the heating rate of 25°C/min applied to the small ones, many peaks (label 3 in Figure III-10) appear at temperatures ranging between 750 and 1300°C.

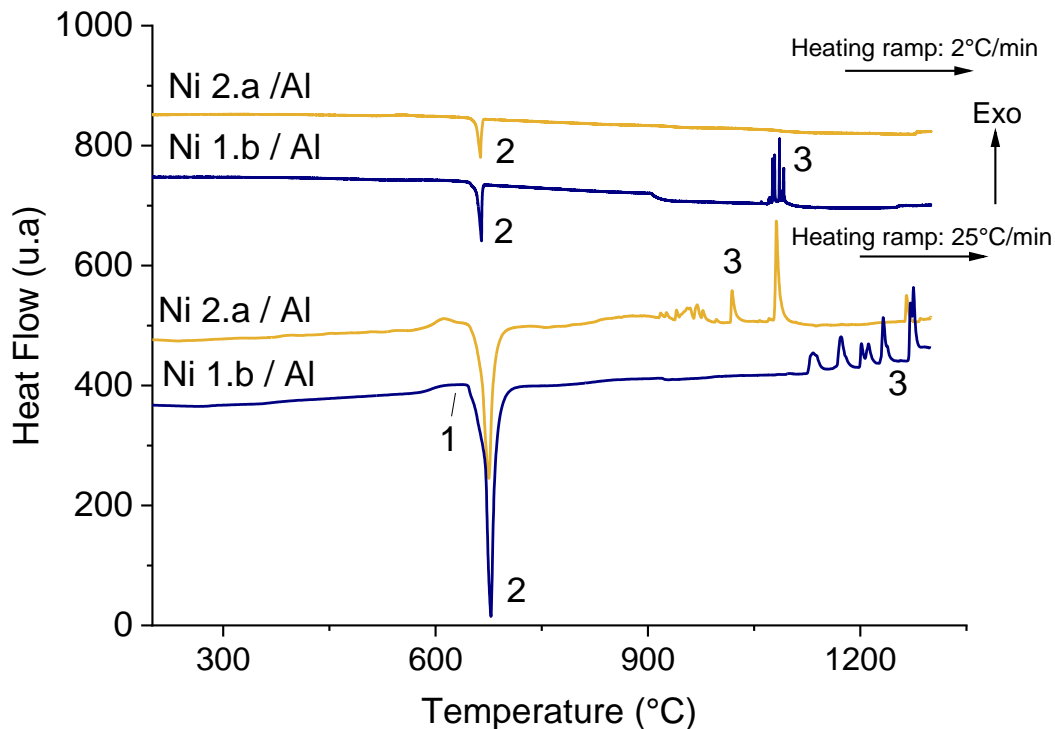


Figure III-10: DSC thermograms of the preoxidized Ni over Al upon heating (2 and 25°C/min) till 1300°C in Ar.

Table III-4: Thermal data and the potential transformations in the preoxidized Ni over Al layout

	T _{max} (°C)	ΔT (°C)	ΔH (J g ⁻¹)	T _{max} (°C)	ΔT (°C)	ΔH (J g ⁻¹)
Heating ramp	2°C/min			25°C/min		
Transformation	Ni-1.b / Al			Ni-1.b / Al		
NiO reduction	612	529-649	-50	622	577-648	-9
Al melting	665	649-671	99	678	648-732	104
NiAl formation	1086	1056-1124	-85	1275	1123-1292	-52
	Ni2.a / Al			Ni2.a / Al		
NiO reduction	556	511-549	-76	612	560-648	-14
Al melting	663	649-670	108	675	648-766	95
Ni ₃ Al and NiAl formation γ-Al ₂ O ₃ → α-Al ₂ O ₃	---	---	---	1081	757-1300	-137

- **Microstructural development**

The microstructure and composition of the layout “preoxidized Ni over Al” heated in Ar following different temperature ramps (2 and 25°C/min) till 1300°C are respectively shown in Figure III-11 and III-12. The crucible can be divided into three main sections from the top to the bottom. A summarized description of these different sections is given in Table III-5.

The top of the crucibles coincides with the area where the preoxidized Ni particles did not react with Al. No noticeable difference can be observed between the samples (Figure III-11.c and 11.d) except for the small oxidized particles for which the recrystallization of the NiO grains occurred forming compact faceted grains (Figure III-12.c and 12.d).

The central section of the crucible corresponds to the interface area between preoxidized Ni and Al particles. This zone is composed of different layers of nickel, intermetallic compounds and alumina. The coarse Ni particles form a compact Ni-rich NiAl phase when heated at 25°C/min (label 1, Figure III-11.e). Underneath, an Al-rich NiAl phase with Al₂O₃ segregated at the grain boundaries occurs (label 2 on Figure III-11.e). In between, many pores can be observed. The Al content increases further to the bottom (label 3 on Figure III-11.e). For a heating ramp of 2°C/min (Figure III-11.f), the NiAl compounds are also observed but the Al₂O₃ appears more segregated in the Ni-rich NiAl than in the Al-rich counterpart. Further, the interface is not homogeneous and displays cracks rather than pores. Ni/Al₂O₃/Ni-rich NiAl/Al-rich NiAl are distributed on one side and Ni/Al₂O₃ Al-rich NiAl on the other but this can be due to the evolution of the solid powders upon melting.

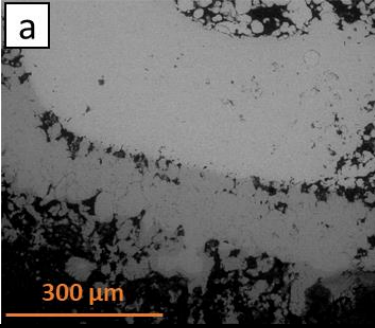
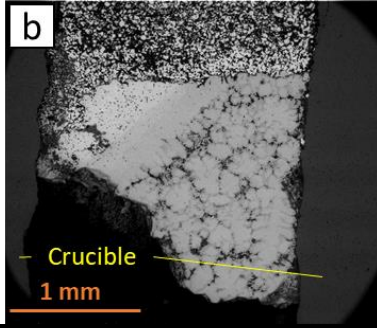
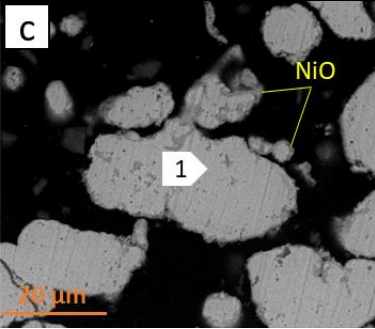
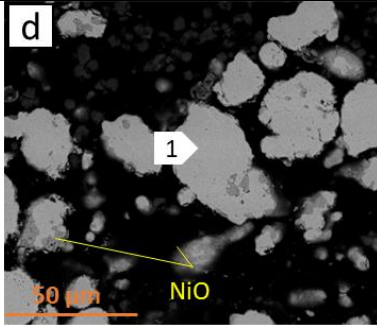
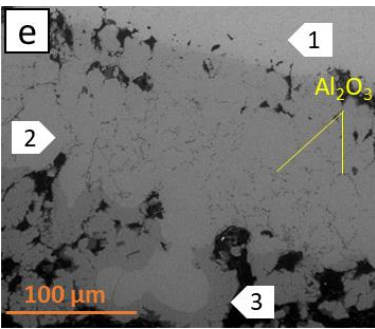
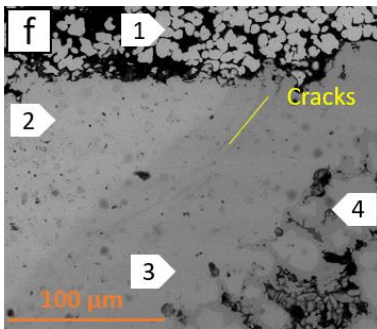
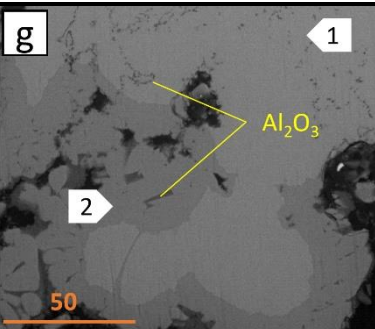
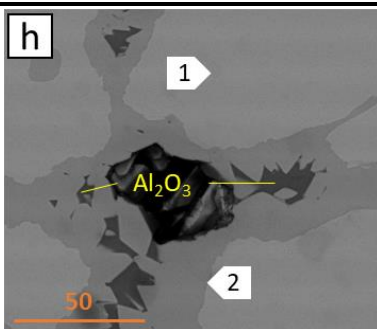
	Heating ramp: 25°C/min	Spot	Al (at %)	Ni (at %)	Heating ramp: 2°C/min	Spot	Al (at %)	Ni (at %)
Overview								
Top		1	9	91		1	3	97
Center (interface between Ni-1.b and Al)		1	33	67		1	8	92
		2	54	46		2	36	64
		3	62	38		3	56	46
						4	71	29
Bottom		1	54	46		1	60	40
		2	62	38		2	71	29

Figure III-11: SEM (BSE mode) cross-sections of the layout 2 with coarse preoxidized Ni particles (Ni-1.b over Al after DSC treatments at 25 and 2°C/min. (a) and (b) overview; (c) and (d) top; (e) and (f) center; (g) and (h) bottom of the crucible.

The small Ni particles form Ni_3Al (label 1 on Figure III-12.e) and Ni-rich NiAl (label 2 on Figure III-12.e) when heated at $25^\circ\text{C}/\text{min}$. The Ni-rich NiAl exhibits two different microstructures whereby one is compact and contains Al_2O_3 at the grain boundaries and the other is “porous” and contains Ni-rich NiAl grains trapped in Al_2O_3 . At the reduced heating ramp of $2^\circ\text{C}/\text{min}$, clusters of Ni grains (label 1 on Figure III-12.f) and Ni-rich NiAl (label 2 on Figure III-12.e) can be also observed. The interfaces between these clusters are composed by Al_2O_3 .

For the bottom of the crucibles, there is barely any significant difference between the heating ramps of 25 and $2^\circ\text{C}/\text{min}$. In contrast, the compounds formed differ between the coarse and small Ni particles. Indeed, Al-rich NiAl particles (label 1 in Figure III-11.g) surrounded by Al_3Ni_2 and simultaneous Al_2O_3 formation (label 2 in Figure III-11.g) are developed from the coarse particles. In contrast, the small Ni particles develop both the Ni-rich and the Al-rich NiAl compounds (labels 1 and 2, respectively in Figure III-12.g).

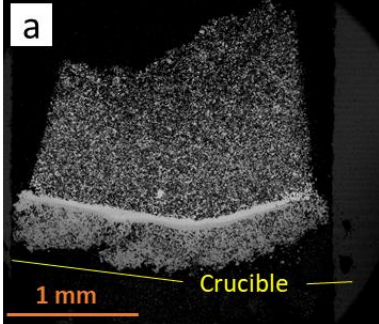
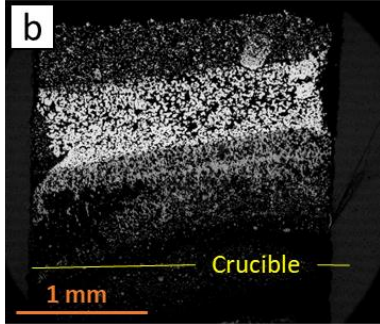
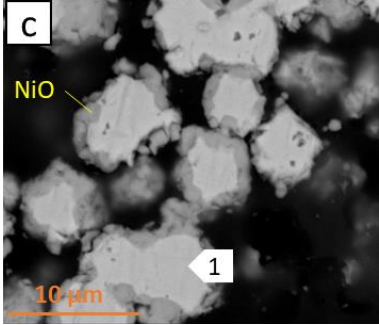
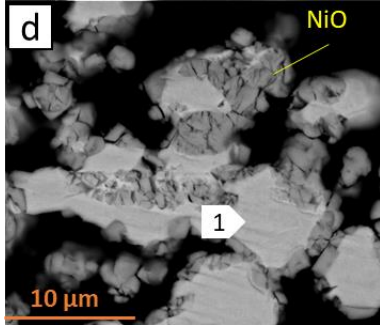
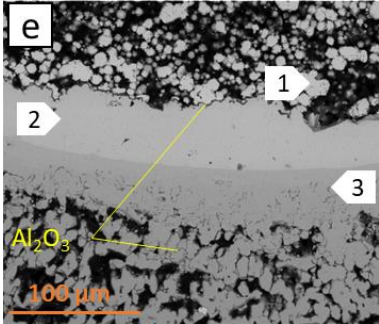
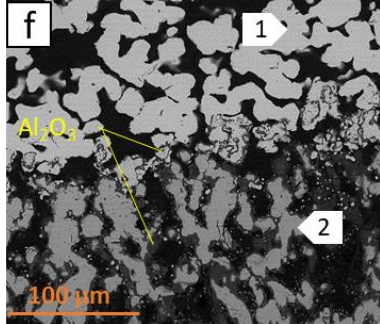
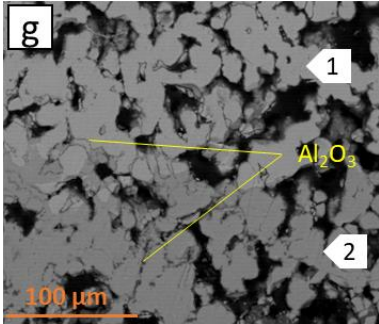
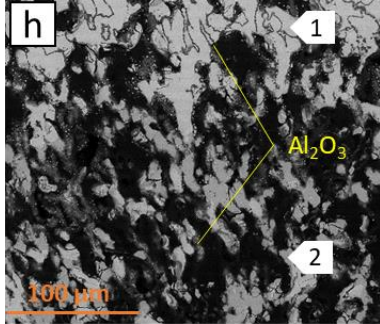
	Heating ramp: 25°C/min	Spot	Al (at %)	Ni (at %)	Heating ramp: 2°C/min	Spot	Al (at %)	Ni (at %)
Overview								
Top		1	1	99		1	1	99
Center (interface between Ni 2.a and Al)		1	6	94		1	4	96
		2	25	75		2	37	63
		3	41	59				
Bottom		1	46	54		1	60	40
		2	60	40		2	71	29

Figure III-12: SEM (BSE mode) cross-sections of the layout 2 with small preoxidized Ni particles (Ni-2.a over Al) after DSC treatments at 25 and 2°C/min. (a) and (b) overview; (c) and (d) top; (e) and (f) center; (g) and (h) bottom of the crucible. Heat treatment (cross-section)

Table III-5: Summary of the different zones observed metallographically

Heating ramp	25°C/min		2°C/min	
Particles	Ni-1.b / Al	Ni-2.a / Al	Ni-1.b / Al	Ni-2.a / Al
Zone 1 (top)	Ni particles with NiO	Ni particles with NiO recrystallized	Same as Ni 1.a at 25°C/min	Same as Ni 2.a at 25°C/min
Zone 2 (center)	-Ni particles (10 at % Al) -NiAl (Ni rich) -NiAl (Al rich) with Al ₂ O ₃ grain boundaries	- Ni particles with NiO Interface of Al ₂ O ₃ -Ni ₃ Al -NiAl (Ni rich) with grain boundaries of Al ₂ O ₃	Same as 25°C/min	- Ni particles with NiO -Interface of Al ₂ O ₃ -cluster of NiAl particles with grain boundaries of Al ₂ O ₃
Zone 3 (bottom)	-grains with a NiAl core and Al ₃ Ni ₂ at the edge + Al ₂ O ₃ in grain Al ₃ Ni ₂	- cluster of NiAl (Al rich) particles with grain boundaries of Al ₂ O ₃ -interface of Al ₂ O ₃ - cluster of Al ₃ Ni ₂ particles with grain boundaries of Al ₂ O ₃	Same as Ni 1.a zone 25°C/min but more developed	Same as Ni 2.a 25°C/min

IV-Discussion

IV.A-Effect of the preoxidation time

Two different Ni powders were oxidized at 700°C under air. The coarse particles (Ni-1) were crushed every hour to avoid the formation of different NiO morphologies and sintering of the oxidized powders. Indeed, porous equiaxial and duplex layer (equiaxial and columnar oxides) forms at the periphery of the Ni coarse particles during oxidation (Figure III-3.a). According to the works of Peraldi et al., a porous NiO scale forms at 700°C for short times [19, 20]. With increasing the oxidation time to 3 h, a duplex scale grows with the porous and equiaxed layer surmounted by columnar grains but the thickness remains almost constant (about 1 μm) [19, 20]. In our case, the formation of the duplex layer appears along the first hour of oxidation with oxide thicknesses ranging from 0.3 to 3 μm (Figure III-3.a and 5.a). The existence of these two types of oxide morphologies within the system may be due to the larger active surface of the Ni powders compared to the average grain size (2 mm) of the Ni studied by Peraldi et al. [19, 20]. When the exposure time is extended to 4 h with crushing of the powder every hour, the scale morphology is exclusively porous with thicknesses ranging from 1 to 5 μm (figure III-3.b and 5.b). This difference can be due to the stresses generated by the crushing of the particles, which in turn foster nickel and oxygen interdiffusion and/or provoke the spallation of the columnar grains [29]. In addition, the increase in oxidation time brings about the intergranular oxidation of the Ni particles. The action of crushing effectively disassembles the grains and causes the reduction of the grain sizes and the creation of new un-oxidized surfaces.

The greater reactivity of the smaller Ni particles (Ni-2) is due to their greater specific surface. Such a greater reactivity is demonstrated through the oxide thickness that ranges between 0.5 and 2 μm after just 15 min (i.e. 3×5 min) (Fig 5.c) and between 1.5 and 4 μm after 40 min (i.e. 4×10 min) (Fig 5.d) at 700°C. The oxidation of the small particles is so fast that some of them appear completely oxidized (Figure III-3.d). The small particles preoxidized for 40 min were thus consequently discarded as they would not allow the formation of Al-rich Ni_xAl_y cores in the particle by reaction with Al. Similarly, the coarse particles preoxidized for 1 h did not develop sufficiently

thick nickel oxide to results in Al_2O_3 shells upon the aluminothermic reaction. The coarse and small particles preoxidized for, respectively, 4 h (i.e. 4×1 h) and 15 min (i.e. 3×5 min) were then used to study the formation of the $\text{Ni}_x\text{Al}_y + \text{Al}_2\text{O}_3$ phases.

IV.B-Layout 1- Mixture of preoxidized Ni and Al particles

The DSC of the Al and preoxidized Ni powders show two peaks at temperatures corresponding to the melting of Al and to the Curie temperature of Ni. When these two powders are mixed together and heated, various additional phenomena appear. The first exothermic peak at $620 \pm 2^\circ\text{C}$ is most likely related to the solid-state aluminothermic reaction given in equation (1) [30]. The heat released upon this highly exothermic reaction causes the melting of Al and the stop of the solid-state aluminothermic reaction. Whereas by solid state or by molten Al, the whole NiO is consumed by Al to form Al_2O_3 and Ni (Figs. 13.b and 13.c). When the temperature exceeds the melting of Al, the dissolution of Ni can readily occur [31, 32]. Ni and Al are thus quickly consumed and form Ni_3Al (eq. 2) (Fig 13. c).



With increasing temperature between 740 and 1000°C , further Al inward diffusion occurs and the coarse Ni particles thus develop a concentration gradient between Ni at the core, the intermediate layer of Ni_3Al and the external layer of NiAl (Figure III-13.c). The formation of NiAl is accompanied of a strong exothermic peak shown in Figure III-7 following equation (3) [18]:



The residual Ni is fully transformed with the subsequent heating till 1300°C . The final microstructure is made of clusters of NiAl particles with many cracks (Figure III-13.d). In contrast, no alumina resulting from the aluminothermic reaction could be detected under the SEM, probably because it is either too thin and/or it came up to the surface given its much lower density than that of the Ni-Al intermetallic compounds.

For the small particles, the exothermic peak at 620°C associated with the NiO reduction is also observed but the energy released is lower than with the coarse particles. As a result, a large amount of the NiO grown on the small Ni particles has not reacted yet at about 656°C (Fig. 13.f). Between 750 and 1000°C , the exothermal reaction can be associated with the solid-liquid reduction reaction that brings about an exothermic reaction (Figure III-7). At this range of temperature three types of particles are formed: NiAl/ Al_2O_3 , Ni/ Ni_3Al /NiAl and Ni/NiO/Ni multi-layered microstructures (Fig. 13.g). For the first one, the Ni formed the periphery of the surface is the result of the aluminothermic reaction. These features would imply that the reaction is controlled by the solid-state diffusion of species through the products layers because of the incomplete dissolution of NiO. For the second and the third ones, all the NiO is consumed to form Ni and Al_2O_3 . Moreover, for the third case of Ni/NiO/Ni particles, the Al_2O_3 was expelled.

The full consumption of NiO, Ni and Al at 1050°C results in Ni_3Al and Al_2O_3 and the metastable γ - Al_2O_3 transforms into the stable α - Al_2O_3 that releases heat (Figure III-7) [24,33]. Moreover, isolated alumina particles can also be found inside the particles of Ni_3Al .

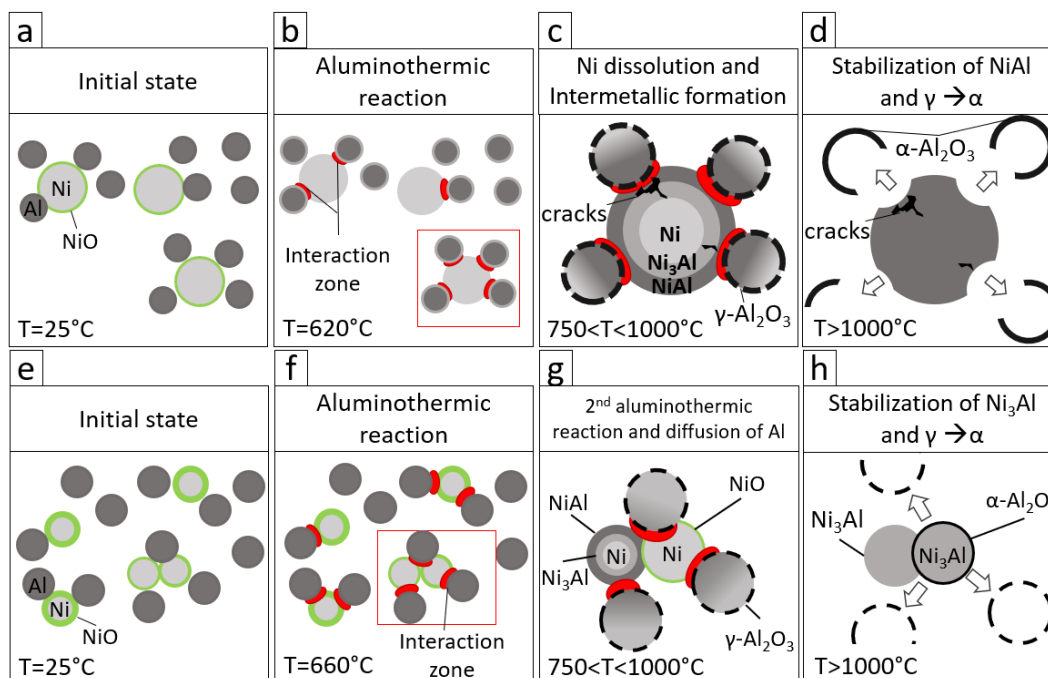


Fig. 13: Schematic model of NiO reduction and formation of intermetallic particles for a mixture of (a-d) coarse preoxidized Ni (4h) and Al and (e-h) small preoxidized (15 min) Ni and Al heated at f $25^{\circ}\text{C}/\text{min}$.

IV.C-Layout 2- preoxidized Ni powders over the Al particles

The comparison of the results obtained with the mixed particles with that for the layout “preoxidized Ni over Al” clearly points out the tremendous impact of the contact between the reactive particles. Indeed, for the same particle size, the melting enthalpy of Al is much lower with the mixed powders ($\sim 65 \text{ J g}^{-1}$) than with the double layer configuration ($\sim 100 \text{ J g}^{-1}$). Therefore, the greater contact area between Al and NiO results in the formation of more Al_2O_3 absorbing heat and hampering melting of Al. In contrast, when the preoxidized Ni powder is deposited over the Al particles, a front of reactions and of heat propagates from the interface, resulting in different compounds and microstructures.

In this latter configuration (Figs. 14.a and 15.a), the influence of the heating rate appears negligible. Indeed, the DSC curves present the same reaction peaks (within a couple of degrees of difference) and the SEM images exhibit similar zones. However, it has been noted that the extent of the Al-rich areas is greater than that of the Ni-rich area when a slow heating rate ($2^{\circ}\text{C}/\text{min}$) has been applied and vice-versa. This can be related to the fact that diffusion of aluminum is favored below 1000°C [34] (inward diffusion) while the outward diffusion of Ni is promoted above 1000°C [34]. The system therefore spends a longer time at low temperature with slow heating rates.

When the coarse preoxidized Ni particles are heated till 550°C , the solid/solid aluminothermic reaction begins [24]. The external NiO is reduced by Al, bringing about the formation of alumina and of nickel (Figure III-14.b). The resulting particles close to the interface (between Al and NiO particles) are then exposed to the flux of Al, which in turn allows the formation of intermetallic compounds (Ni₃Al and NiAl) successively towards the core (Figure III-14.b). This stage

progressively continues along the crucible until the onset of Al melting is reached ($645\pm 1^\circ\text{C}$). Part of this molten aluminum may be transported upwards by capillarity between the nickel particles. Therefore, the nickel particles get embedded in the molten aluminum (Figure III-14.c). Moreover, the melting of aluminum induces a preferential dissolution of Ni at the grain boundaries and the subsequent formation of cracks, either by shrinkage upon quenching or through the formation of denser phases. Beyond 750°C , aluminum keeps on diffusing through the Ni particles. Therefore, the Ni_xAl_y intermetallics get progressively richer in Al at the expense of Ni-rich Ni_xAl_y . In addition, the grains of the newly formed intermetallic phases grow during this stage causing the disappearance of porosity. The molten aluminum between these grains will be gradually “absorbed” by the Ni particles leaving behind alumina trapped between the grains (Figure III-14.c).

Between 1000 and 1300°C , the microstructure barely evolves while the composition slightly changes due to favored nickel diffusion. This results in Al-rich and Ni-rich NiAl compounds (Figure III-14.d). Quenching to room temperature provokes solidification of molten Al and the segregation of Al_3Ni_2 between the grains of Al-rich NiAl (Figure III-14.d).

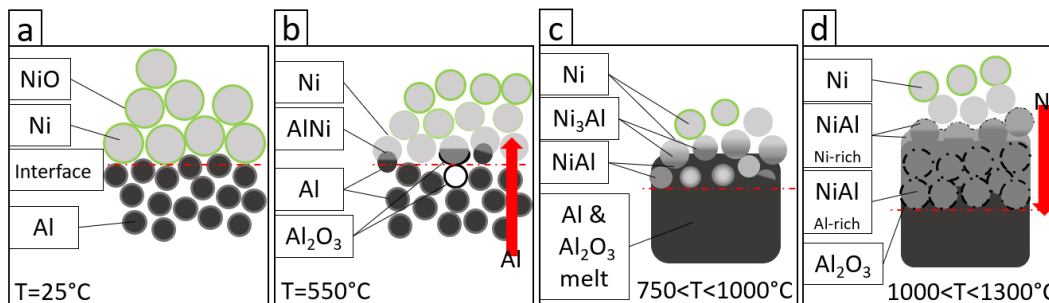


Figure III-14: Schematic drawings of the aluminothermic reduction and reactions between the coarse preoxidized Ni over Al particles (double layer configuration) heated at $25^\circ\text{C}/\text{min}$.

For the small particles the effect of the heating rate is very significant as demonstrated by the different DSC peaks (Figure III-10) and SEM microstructures at the center of the crucibles (Figure III-12). These differences can result from the preoxidation of the powders whereby the oxide growth at 700°C is ruled by the faster diffusion rate of the Ni^{2+} ions than that of the O^{2-} ions. As a consequence, pores and cavities are generated at the oxide/metal interface [35]. Further the particles are subjected to intermediate air quenching and crushing (3×15 min), which induce stress in the oxide and in the metallic Ni particle. These phenomena are enhanced on the small particles vs. the coarse ones because of their greater oxide thickness and less spherical morphology. Overall, the small particles become more reactive than the coarse ones.

When the temperature of 550°C is reached, the solid/solid aluminothermic reaction begins [27], NiO and Al react at the interface of the preoxidized Ni particles (Figure III-15.b). As opposed to the coarse particles, the thickness of the oxide layer is now quite significant and the aluminothermic reaction is thus momentarily superseded by the onset of the Al melting at $648\pm 1^\circ\text{C}$. Molten Al flows upwardly by capillarity between the Ni preoxidized particles NiO grains causing the entrapment of nickel particles in the molten Al and the enrichment of the NiO in Al (Figure III-15.c). Beyond 750°C , the second aluminothermic reaction (liquid/solid) begins. The remainder of the NiO near the interface is thus finally converted into an adherent Al_2O_3 (Figure III-15.c). Simultaneously, the NiO “barrier” over the Ni particles is transformed in Al_2O_3 creating cracks, the Ni core is directly exposed to the molten Al (Figure III-15.c). The greater amount of

alumina formed at this stage aggregates around the particles and prevents their sintering. As a result, clusters of intermetallic compounds with a lot of porosity are obtained (Figure III-15.c).

When the temperature reaches 950°C, a third exothermic peak appears when heating at 25°C/min (Figure III-10 peak labeled 3'). This peak results from the transformation of the Ni phase into Ni₃Al and NiAl but the reaction does not take place continuously. This reaction can be explained by the difference in the thermal expansion coefficient between Ni and NiO and the potential residual stress and cavities that cause cracking and spallation of the NiO layer. Therefore, Al becomes free to react with Ni and form Ni₃Al and NiAl. The NiO expelled continue its reduction in the molten Al to form Al₂O₃ that gets trapped between the grains of the intermetallic compounds as they grow. This step will be repeated until the intermetallic layer thickens enough to hamper the arrival of Al. The heat produced during this stage and the very low amount of trapped oxide do not prevent the sintering of the particles to each other to form a compact structure. The Ni₃Al layer will subsequently enrich with Al to form NiAl (Figure III-15.d).

In contrast, cracking and spallation of NiO do not occur when heating at 2°C/min. Therefore, when the temperature reaches 750°C, the solid/liquid aluminothermic reaction occurs and the remainder of the NiO near the interface is finally converted into an adherent Al₂O₃. Simultaneously, the NiO "barrier" over the Ni particles being reduced, the Ni core can now react directly with the molten Al (Figure III-15.c). The greater amount of alumina formed at this stage aggregates around the particles and prevent their sintering. As a result, clusters of intermetallic compounds with significant porosity are obtained (Figure III-15.c)

Deeper in the crucible and irrespective of the heating rate, clusters of Al₃Ni₂ and Al₃Ni are formed upon cooling (Figure III-15.d). At the surface of these clusters, almost no Al₂O₃ was observed, which suggests that Al₂O₃ either dissolves and/or that is transported to the surface of the melt given its lower density than the intermetallic compounds.

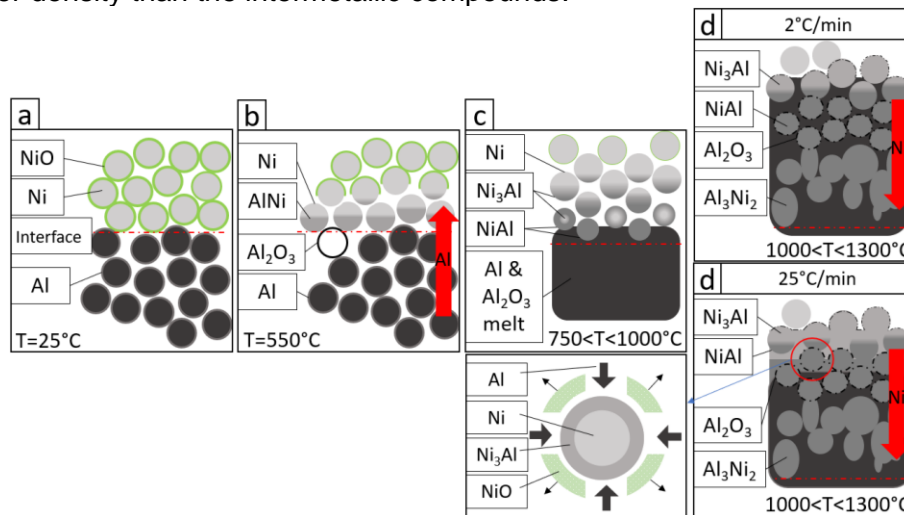


Figure III-15: Schematic drawings of the aluminothermic reduction and reactions between the small preoxidized Ni and Al (double layer configuration) heated at 2 and 25°C/min

V-Conclusion

The reaction process of a Ni_xAl_y-Al₂O₃ phases via thermite reaction of preoxidized Ni particles and aluminum particles was investigated by DSC and metallographic observations. It was found that different intermediate phases formed during heating of the powder mixtures. Metallic Ni formed

first at around 600°C, followed by the formation of Ni₃Al and NiAl and a temperature increase. After 1300°C, the coarse preoxidized Ni powders formed a cluster of NiAl particles while the small preoxidized Ni particles resulted in a cluster of interpenetrated Ni₃Al and Al₂O₃. The formation of Al₂O₃ is believed to result from a three-stage process. Initially, a small amount of Al₂O₃ was produced by the reduction of NiO with solid Al. Then, Al₂O₃ particles formed by the reduction of NiO with liquid Al. Finally, Al₂O₃ developed by the solid-state displacement reaction between NiO and nickel-aluminides (Al₃Ni, Al₃Ni₂, NiAl).

When the coarse preoxidized Ni particles lay over the Al ones, a dense structure composed by a Ni-rich NiAl above an Al-rich NiAl was formed. The Al₂O₃ formed by thermite reaction was trapped in the grain boundaries of the Al-rich NiAl. However, the small preoxidized Ni particles grew a dense structure with Ni₃Al above a Ni-rich NiAl and Al₂O₃ trapped in the grain boundaries in some areas and clusters of Al-rich NiAl and Al₃Ni₂ particles surrounded by a thin layer of Al₂O₃ in some other areas.

These results, therefore, suggest that the synthesis of self-regenerating coating could be obtained by e.g. spraying slurries containing mixtures of preoxidized Ni and metal Al or multilayering them onto a substrate. Subsequent heat treatments with relatively fast heating ramps (25°C) till moderate temperatures (~ 750°C) assisted by the aluminothermic reaction between NiO and Al could consolidate the formation of the micro-containers trapped in the coating.

References

[1] G.W. Goward, Current research on the surface protection of superalloys for gas turbine engines, JOM 22 (1970) 31–39.

<https://10.1007/BF03355665>

[2] J. Stringer, High-temperature corrosion of superalloys, Mater. Sci. Technol. 3 (1987) 482–493.

<https://10.1080/02670836.1987.11782259>

[3] M.W. Brumm, H.J. Grabke, The oxidation behaviour of NiAl – I. Phase transformations in the alumina scale during oxidation of NiAl and NiAl-Cr alloys, Corros. Sci. 33 (1992) 1677–1690.

[https://10.1016/0010-938X\(92\)90002-K](https://10.1016/0010-938X(92)90002-K)

[4] H.J. Choi, J. Jedlinski B. Yao, Y.H. Sohn, Transmission electron microscopy observations on the phase composition and microstructure of the oxidation scale grown on as-polished and yttrium-implanted β -NiAl, Surf. Coat. Technol. 205 (2010) 1206–1210.

<https://10.1016/j.surfcoat.2010.10.034>

[5] J.R. Nicholls, Designing oxidation-resistant coatings, JOM 52 (2000) 28–35.

<https://10.1007/s11837-000-0112-2>

[6] G.W. Goward, D.H. Boone, Mechanisms of formation of diffusion aluminide coatings on nickel-base superalloys, Oxid. Met. 3 (1971) 475–495.

<https://10.1007/BF00604047>

[7] N. Vialas, D. Monceau, Effect of Pt and Al content on the long-term high temperature oxidation behavior and interdiffusion of Pt-modified aluminide coating deposited on Ni-base superalloys, Surf. Coat. Technol. 201 (2006) 3846–3851.

<https://10.1016/j.surfcoat.2006.07.246>

[8] Y. Matsumura, M. Fukumoto, S. Hayashi, A. Kasama, I. Iwanaga, R. Tanaka, T. Narita, Oxidation behavior of a Re-base diffusion-barrier/NiAl coating on Nb–5Mo–15W at high temperatures, Oxid. Met. 61 (2004) 105–124.

<https://10.1023/B:OXID.0000016279.88052.d9>

[9] Y. Wang, H. Guo, H. Peng, L. Peng, S. Gong, Diffusion barrier behaviors of (Ru, Ni) Al/NiAl coatings on Ni-based superalloy substrate, Intermetallics 19 (2011) 191–195.

<https://10.1016/j.intermet.2010.08.016>

[10] T. Narita, Diffusion barrier coating system concept for high temperature applications, Canadian Metallurgical Quarterly 50 (2011) 278–290.

<https://10.1179/1879139511Y.0000000014>

[11] R.M. German, Sintering-Theory and Practice, Wiley Interscience, (1996).

[12] P. Nieroda, R. Zybała, K.T. Wojciechowski, Development of the method for the preparation of Mg₂Si by SPS technique, Am. Inst. Phys. Conf. Proc. 1449 (2012) 199–202.

<https://10.1063/1.4731531>

[13] M. Chmielewski, K. Pietrzak, Processing, microstructure and mechanical properties of Al₂O₃-Cr nanocomposites, J. Eur. Ceram. Soc. 27 (2007) 1273–1279.

<https://10.1016/j.jeurceramsoc.2006.05.093>

[14] E.M. Levin, C. R. Robbins, H.F. McMurdie, Phase diagrams for ceramists, American Ceramic Society (1990) 90.

[15] J.Z. When, S. Ringuette, G. Bohlouli-Zanjani, A. Hu, N.H. Nguyen, J. Persic, C.F. Petre, Y.N. Zhou, Characterization of thermochemical properties of Al nanoparticles and NiO nanowire composites, Nanoscale Res. Lett. 8 (2013) 184.

<https://10.1186/1556-276X-8-184>

[16] D. Vrel, P. Langlois, E.M. Heian, N. Karnatak, S. Dubois, M.F. Beaufort, Reactions kinetics and phase segregation in the 3NiO + 2Al → Al₂O₃ Thermite system, Int. J. Self-Propagating High-Temp. Synth. 12 (2004) 261–270.

[17] D. Vrel, A. Hendaoui, P. Langlois, S. Dubois, V. Gauthier, B. Cochevin, SHS reactions in the NiO-Al system: Influence of stoichiometry, Int. J. Self-Propagating High-Temp. Synth. 16 (2007) 62–69.

<https://10.3103/S1061386207020021>

[18] A. Biswas, S.K. Roy, K.R. Gurumurthy, N. Prabhu, S. Banerjee, A study of self-propagating high-temperature synthesis of NiAl in thermal explosion mode, Acta Mater. 50 (2002) 757–773.

[https://10.1016/S1359-6454\(01\)00387-1](https://10.1016/S1359-6454(01)00387-1)

[19] R. Peraldi, D. Monceau, B. Pieraggi, Correlations between growth kinetics and microstructure for scales formed by high-temperature oxidation of pure nickel, I. Morphologies and Microstructures, Oxid. Met. 58 (2002) 249–273.

<https://10.1023/A:1020170320020>

[20] R. Peraldi, D. Monceau, B. Pieraggi, Correlations between growth kinetics and microstructure for scales formed by high-temperature oxidation of pure nickel, II. Growth Kinetics, Oxid. Met. 58 (2002) 275–295.

<https://10.1023/A:1020102604090>

[21] N. Mironova-Ulmane, A. Kuzmin, I. Steins, J. Grabis, I. Sildos, M. Pärns, Raman scattering in nanosized nickel oxide NiO, J. Phys. Conf. Series 93 (2007).

<https://10.1088/1742-6596/93/1/012039>

[22] R. Serway, R. Beichner, W. John, Jr. Jewett, Physics for Scientists and Engineers, Forth Worth Saunders College Publishing 2 (2000) 1551

[23] H. Okamoto, Al-Cr (Aluminum-Chromium), J. Phase Equilibria Diffus. 29 (2008) 112–113.

<https://10.1007/s11669-007-9225-4>

[24] F. Pedraza, M. Mollard, B. Rannou, J. Balmain, B. Bouchaud, G. Bonnet, Potential thermal barrier coating systems from Al microparticles. Mechanisms of coating formation on pure nickel, *Materials Chemistry and Physics* 134 (2012) 700–705.

<https://10.1016/j.matchemphys.2012.03.053>

[25] V. Udhayabanu, N. Singh, B.S. Murty, Mechanical activation of aluminothermic reduction of NiO by high energy ball milling, *J. Alloys Compd.* 497 (2010) 142–146.

<https://10.1016/j.jallcom.2010.03.089>

[26] H.X. Zhu, R. Abbaschian, In-situ processing of NiAl-alumina composites by thermite reaction, *Mater. Sci. Eng.* 282 (2000) 1–7.

[https://10.1016/S0921-5093\(99\)00788-1](https://10.1016/S0921-5093(99)00788-1)

[27] D. Padmavardhani, A. Gomer, R. Abbaschian, Synthesis and microstructural characterization of NiAl-Al₂O₃ functionally gradient composites, *Intermetallics* 6 (1998) 229–241.

[https://10.1016/S0966-9795\(97\)00076-9](https://10.1016/S0966-9795(97)00076-9)

[28] R. Przeliorz, J. Piatkowsko, Application of DSC method in studies on phase transitions of Ni Superalloys, *Archives of Foundry Engineering* 17 (2017) 133–136.

<https://10.1515/afe-2017-0144>

[29] H.E. Evans, Stress effects in high temperature oxidation of metals, *International Materials Review* 40 (1995) 1–40.

<https://10.1179/imr.1995.40.1.1>

[30] A.M. Padhan, M. Sathish, P. Saravanan, Mechanical activation on aluminothermic reduction and magnetic properties of NiO powders, *J. Phys. Appl. Phys.* 50 (2017).

<https://10.1088/1361-6463/aa6cee>

[31] B. Bouchaud, B. Rannou, F. Pedraza, Slurry aluminizing mechanisms of Ni-based superalloys incorporating an electrosynthesized ceria diffusion barrier, *Materials Chemistry and Physics* 143 (2013) 416–424.

<https://10.1016/j.matchemphys.2013.09.022>

[32] M.C. Galetz, X. Montero, M. Mollard, M. Günthner, F. Pedraza, M. Schütze, The role of combustion synthesis in the formation of slurry aluminization, *Intermetallics* 44 (2014) 8–17.

<https://10.1016/j.intermet.2013.08.002>

[33] N. Eisenreich, H. Fietzek, M. del Mar Juez-Lorenzo, V. Kolarik, A. Koleczko, V. Weiser, On the mechanism of low temperature oxidation for aluminum particles down to the nano-scale, *Propellants, Explosives, Pyrotechnics* 29(2004) 137–145.

<https://10.1002/prop.200400045>

[34] J.M. Brossard, B. Panicaud, J. Balmain, G. Bonnet, Modelling of aluminized coating growth on nickel, *Acta Mater.* 55 (2007) 6586–6595.

<https://10.1016/j.actamat.2007.08.025>.

[35] Q. Jeangros, T.W. Hansen, J. B. Wagner, R. E. Dunin-Borkowski, C. Hébert, J. Van Herle, A. Hessler-Wyser, Oxidation mechanism of nickel particles studied in an environmental transmission electron microscope, *Acta Mat.* 67(2014) 362–372.

<https://10.1016/j.actamat.2013.12.035>

II- Reactivity and microstructural observations of Al/Ni_{ox} system by DSC

The preoxidized Ni particles were placed in an alumina crucible and covered with Al particles in an atomic stoichiometric ratio (size of particles in Table III-1, Figure III-16). The alumina crucibles were placed in the DSC (SETARAM Labsys Evo 1600 thermal analysis). Like with the previous configurations (Al+Ni_{ox} and Ni_{ox}/Al), the heating rates were fixed at 2 and 25°C/min with a maximum temperature of 1300°C and the cooling rate was fixed at 50°C/min.

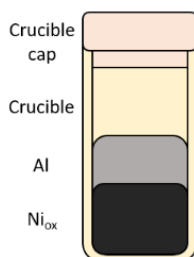


Figure III-16: Schematic drawings representing the layout: Al over preoxidized Ni particles.

II.A-Results

I.A.1-Differential scanning calorimetry

The DSC results of the different preoxidized Ni particles obtained with two heating ramps (2 and 25°C/min) are shown in Figure III-17 and the thermal data are summarized in Table III-6.

○ 2°C/min

For the coarse and small particles heated to 2°C/min, the first exothermic peaks at 549 and 557°C corresponds to a solid-state reaction between Al and NiO [1,2]. This exothermic reaction is directly followed by an endothermic reaction at 662 and 664°C which corresponds to the melting of Al [3].

For the coarse oxidized particles heated to 2°C/min, a third reaction takes place between 1307 and 1128°C, and many peaks appear. With the small oxidized particles heated to 25°C/min, two other exothermic reactions can be observed respectively between 767-1067°C and 1067-1224°C. These two exothermic reactions most probably correspond to the formation of Ni_xAl_y intermetallic compound and to the transformation of metastable γ -Al₂O₃ into stable α -Al₂O₃ [1,4-5].

○ 25°C/min

For the coarse and small particles heated to 25°C/min, the first and second peaks respectively correspond to the solid-state reaction [1,2] with a maximum at 608 and 621°C, and the melting of Al [3] 682 and 677°C.

The last exothermic phenomenon (more developed for small particles with a maximum at 1136±56°C) corresponds to the transformation of metastable γ -Al₂O₃ into stable α -Al₂O₃[1,4-5].

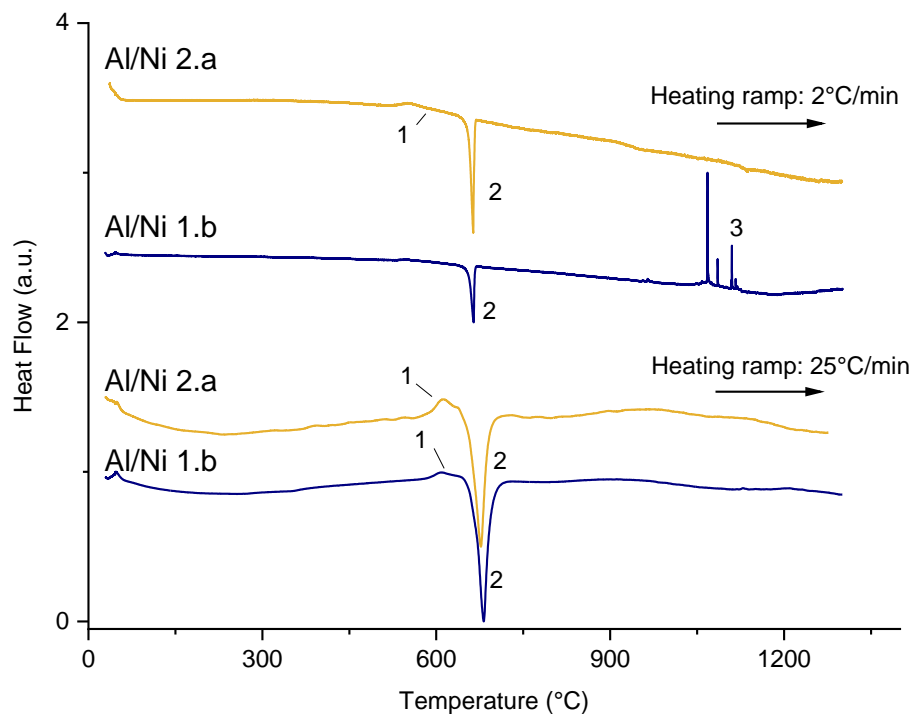


Figure III-17: DSC thermograms of the preoxidized Al particles over Ni preoxidized particles upon heating (2 and 25°C/min) till 1300°C in Ar.

Table III-6: Thermal data and the potential transformation in the Al particles over Ni preoxidized particles.

	T_{max} (°C)	ΔT (°C)	ΔH (J g ⁻¹)	T_{max} (°C)	ΔT (°C)	ΔH (J g ⁻¹)
Heating ramp	2°C/min			25°C/min		
Transformation	Al/Ni-1.b (coarse oxidized 4x1h)			Al/Ni-1.b (coarse oxidized 4x1h)		
NiO reduction	549	528-567	-4	608	568-643	-4
Al melting	662	567-670	56	682	643-734	78
NiAl formation	1105	996-1140	-85	---	---	---
	Al/Ni-2.a (small oxidized 3x10min)			Al/Ni-2.a (small oxidized 3x10 min)		
NiO reduction	557	507-634	-22	621	560-653	-23
Al melting	664	634-670	101	677	653-725	66

I.B-Microstructural development

The microstructure and the composition of the layout heated in Ar following different temperature ramps (2 and 25°C/min) till 1300°C are respectively shown in Figures III-18 and III-19. For a clearer description, the crucibles are divided into three parts, with a first part above the original interface, a second part at the interface level and a third part below the interface. A summarized description of these different sections is given in Table III-7.

For the coarse preoxidized particles (Figure III-18), the first part coincides with the area where the Al particles are initially placed (Figure III-18.c and Figure III-18.d). This area is defined by the formation of spherical particles with a size of $6\pm 4\ \mu\text{m}$. The largest particles are composed of Ni_3Al intermetallic compounds in the center and NiAl intermetallic compound on the outside of the particle. The smallest particles are mainly composed of NiAl. In addition, the periphery of the particles is particularly rich in Al_2O_3 , which is also sometimes trapped inside the particles.

The central section of the crucibles represents the interface of the parts rich in Al (top) and part rich in Ni (bottom) (Figure III-18.e and Figure III-18.f). The upper part of the interface is composed of NiAl particles sintered to each other, with alumina trapped between the particles. In addition, for rapid treatment (25°C/min), the NiAl particles appear more compact (Figure III-18.f) and consequently, the layer shrinks to $97 \pm 18\ \mu\text{m}$ compared to the one obtained with the slow heat treatment ($161 \pm 29\ \mu\text{m}$, Figure III-18.e). The bottom layer is made of Ni particles enriched in Al sintered to each other. As with the upper layers, a rapid heat treatment leads to greater compaction.

Deeper in the crucibles, a third zone can be observed (Figure III-18.g and Figure III-18.h). This area consists of unreacted preoxidized Ni particles.

In the case of small preoxidized Ni particles (Figure III-19), the first zone of the crucibles is very similar to the coarse counterparts (Figure III-19.c and Figure III-19.d). Indeed, we can observe the spherical particles of NiAl. However, unlike the coarse particles, a more compact area of NiAl particles sintered can be observed deeper. The microstructure of this area depends on the heating ramp. For 2°C/min, a compact Ni-rich NiAl area extends for about $70\ \mu\text{m}$. The grains are elongated with alumina segregated at the grain boundaries. Underneath the compact area, the clusters of Ni-rich NiAl particles appear separated by porosity (Figure III-19.c). In contrast, the heating ramp at 25°C/min results in clusters of Al-rich NiAl particles with a core of NiAl and alumina around (Figure III-19.d). This morphology extends to the centre of the crucible.

The center of the crucibles displays an Al gradient with cluster of Ni_3Al in the upper part of the interface and Ni in the lower part of the interface irrespective of the heating ramp. Alumina segregates between these two areas, in particular with the slowest heating rate of 2°C/min.

The third zone at the bottom is composed of un-reacted preoxidized Ni particles.

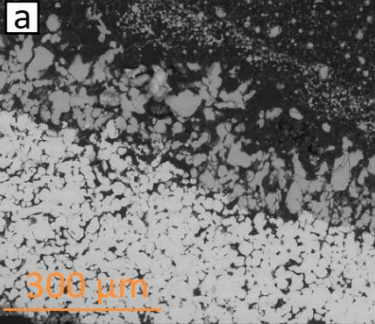
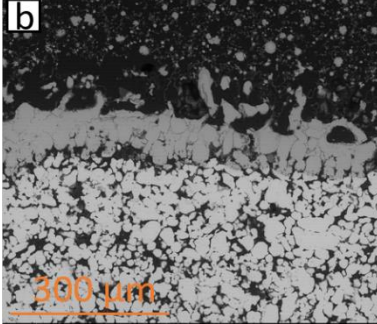
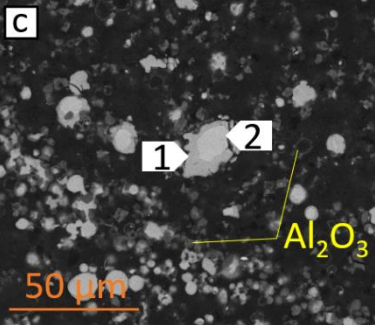
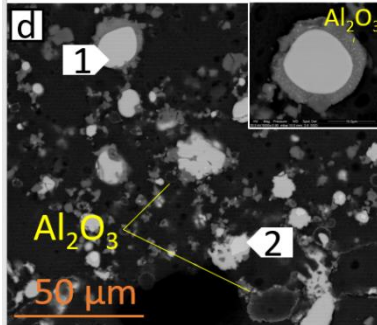
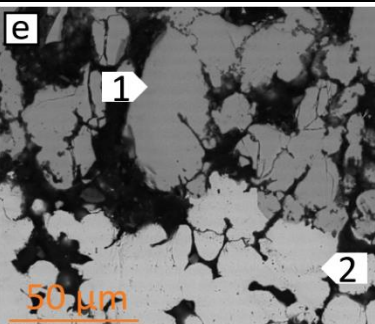
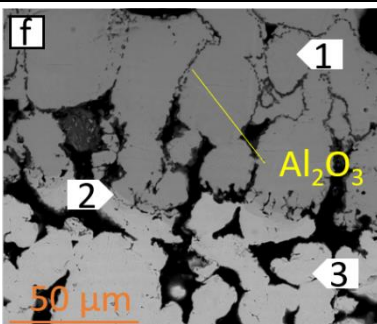
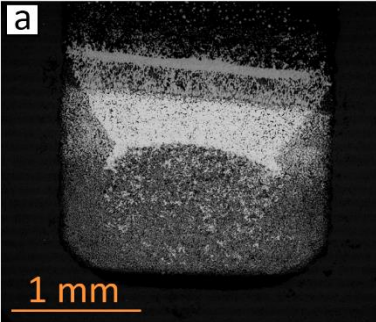
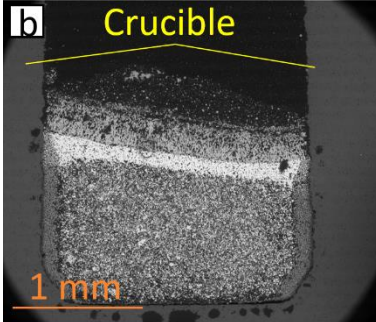
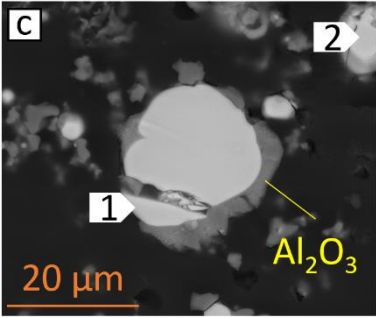
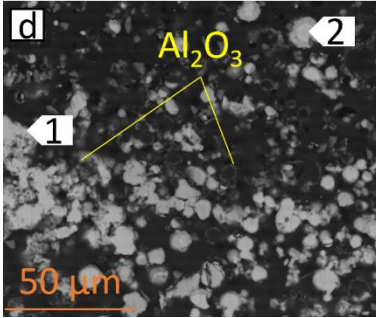
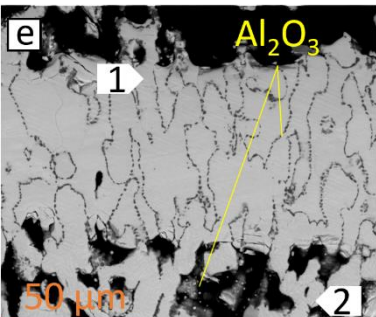
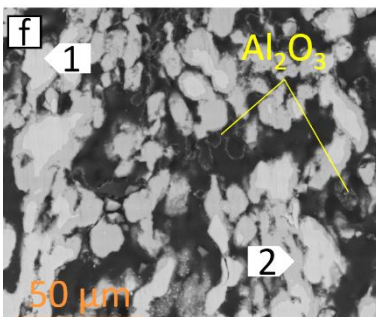
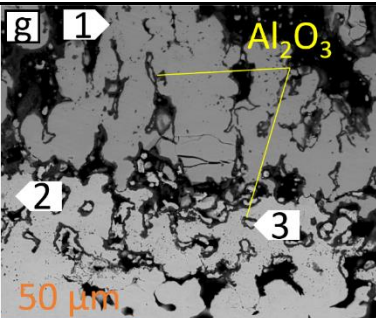
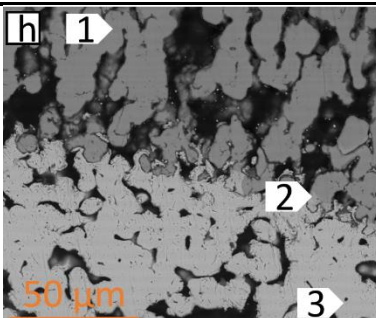
	Heating ramp: 2°C/min	Spot	Al (at %)	Ni (at %)	Heating ramp: 25°C/min	Spot	Al (at %)	Ni (at %)
Overview								
Top		1	71	29		1	66	34
		2	62	36		2	57	43
Center		1	56	44		1	46	54
		2	9	91		2	31	69
						3	14	86

Figure III-18: SEM (BSE mode) cross-sections of the layout with coarse preoxidized Ni particles (Ni-1.b over Al particles) after DSC treatment at 2 and 25°C/min. (a) and (b) overview; (c) and (d) top; (e) and (f) center of the crucible.

- III. Study of the reactivity and microstructure of Al and preoxidized Ni powders by -

	Heating ramp: 2°C/min	Spot	Al (at %)	Ni (at %)	Heating ramp: 25°C/min	Spot	Al (at %)	Ni (at %)
Overview								
Upper part of the top zone		1	62	38		1	51	49
		2	44	56		2	62	38
Inferior part of the top zone		1	45	55		1	48	52
		2	42	58		2	62	38
Center		1	38	62		1	43	57
		2	13	87		2	30	70
		3	10	90		3	10	90

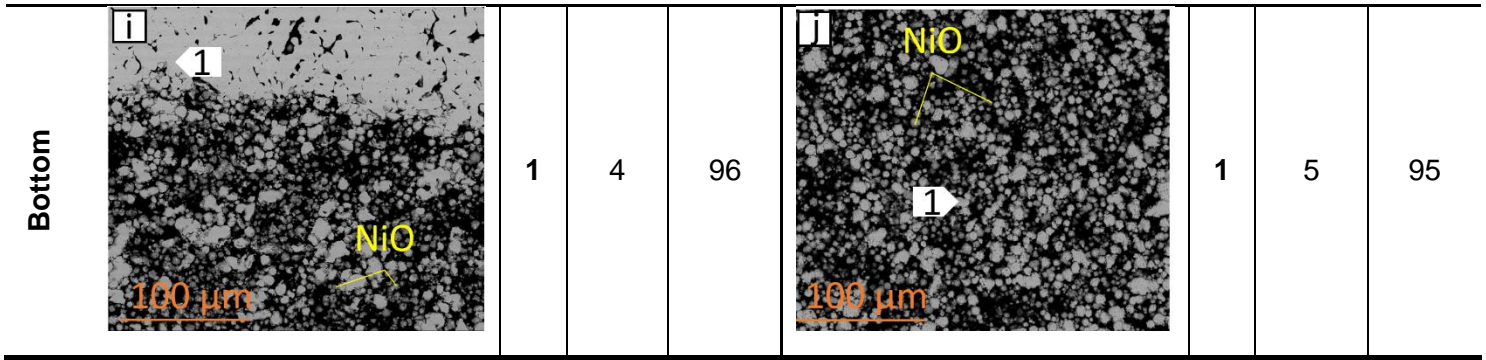


Figure III-19: (BSE mode) cross-sections of the layout with small preoxidized Ni particles (Ni-2.a over Al particles) after DSC treatment at 2 and 25°C/min. (a) and (b) overview; (c) and (d) top; (e) and (f) between top and center; (g) and (h) center; (i) and (j) the bottom of the crucible.

Table III-7: Summary of the different zones observed metallographically

Heating ramp	2°C/min		25°C/min	
Particles	Al / Ni-1.b	Al / Ni-2.a	Al / Ni-1.b	Al / Ni-2.a
Zone 1 (top)	Spheres of Ni ₃ Al and NiAl	Spheres of Ni ₃ Al and NiAl with a shell of Al ₂ O ₃	Spheres of Ni-rich NiAl and Al-rich-NiAl with a shell of Al ₂ O ₃	Spheres of Ni rich-NiAl and Al rich-NiAl
Zone 2 (center)	-Spheres of NiAl -Clusters of Al-rich NiAl particles sintered -Ni particles sintered (10 at % Al)	-Spheres of Al-rich NiAl -Compact clusters of Al-rich NiAl particles with grain boundaries of Al ₂ O ₃ interface in Al ₂ O ₃ -Ni particles sintered (10 at % Al)	-Compact clusters of Ni-rich NiAl particles with grain boundaries of Al ₂ O ₃ -Cluster of oxides particles	-Clusters of NiAl particles with Al ₂ O ₃ -Interface between Ni-rich NiAl and Ni clusters
Zone 3 (bottom)	-Ni particles sintered -Unreacted Ni preoxidized particles	-Same as Ni-1.b	-Same as Ni-1.b	-Same as Ni-1.b

II.C-Discussion

The DSC curves of the Al over Ni preoxidized particles show 2 main phenomena irrespective of the particle size and heating ramp. The first peak at 581±36°C (exothermic) is related to the solid-state aluminothermic reaction (Figure III-20, label 1) that reduces NiO into Ni by solid Al [5,6]. The heat released upon this exothermic reaction causes the melting of Al and stops the solid-state aluminothermic reaction [5,6]. The heat released during the aluminothermic reaction is relatively similar between the coarse (≈ 4 J.g⁻¹) and the small particles of Ni (≈ 22 J.g⁻¹) when considering the largest reactive surface of the latter. Yet, the enthalpy values are lower than the ones reported in the literature of 3,4 kJ.g⁻¹ [7] probably because of the low contact area between the particles of Al and NiO, and the small amount of NiO compared to the overall mass of Ni and Al.

The second peak at 669±9°C (endothermic) (Figure III-17, label 2) corresponds to the melting of Al [3]. Above the melting temperature of Al, no additional thermal event can be observed except

for the coarse particles and low heating rates. Indeed, a cluster of fine peaks appears above 1050°C that can be related to the formation of intermetallic compounds (Al_3Ni , NiAl , Ni_3Al ,) towards the Ni core [4]. In contrast, the thermal events cannot be detected in the other conditions because either the overall heat release is too small (low amount of compound formed) or the heating rate is too rapid to follow the event or both.

In spite of this, the SEM cross-sections of Figures III-18 & III-19 clearly show that the mechanisms of reaction are more dependent on the particle size than on the heating ramp. Indeed, the smallest particles are relatively more preoxidized than the coarse ones and are therefore less reduced into Ni by reaction with Al. Yet, when Al melts, the aluminothermically formed Al_2O_3 can be trapped and then segregate at the surface of the Ni_xAl_y intermetallic compound formed given that Al and Al_2O_3 do not wet each other [7]. The heat released by the aluminothermic reaction [8] and by the dissolution of Ni in the molten Al [9] then provokes a heat gradient in the crucible that explains the different degrees of reaction from the top to the bottom. The enrichment of the Ni_xAl_y in Al also allows the growth of the grains following the heat flow (elongated shape) and subsequent sintering. Therefore, only the milder conditions (2°C/min) do not allow the Ni_xAl_y particles to sinter since their periphery appears more oxidized (Figure III-18.e).

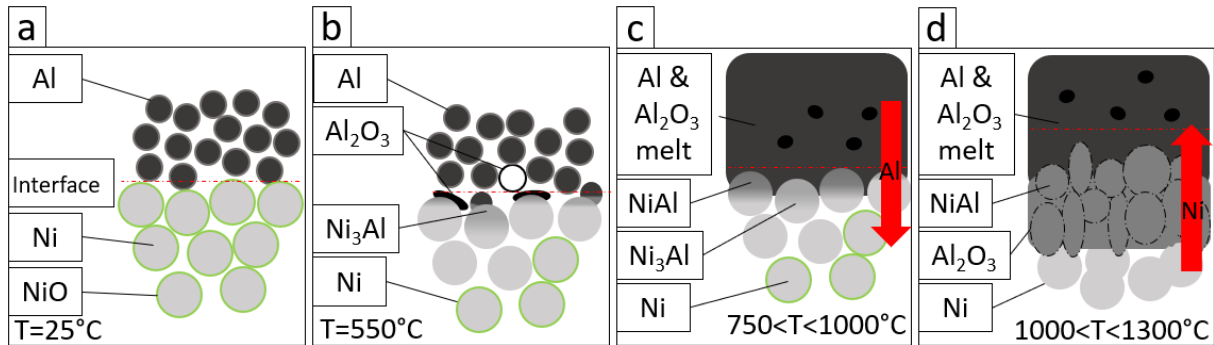


Figure III-20: Schematic drawing of the aluminothermic reduction reaction between the coarse or the small preoxidized above Al particles (double layer configuration) heated at 25°C/min.

II.D-Conclusion

The reaction process of a $Ni_xAl_y-Al_2O_3$ phase via thermite reaction of preoxidized Ni particles and aluminum particles was investigated by DSC and metallographic observations. A total of 3 particle arrangements, two heating rates, 2 Ni particle sizes and 4 preoxidation times were studied (Scientific article on $Al+Ni_{ox}$ and Ni_{ox}/Al and last section on Al/Ni_{ox}).

It was found that different intermediate phases formed during the heating of powder mixtures. The metallic nickel resulting from the aluminothermic reaction between the aluminum particles and the oxidized shells of the nickel particles formed at about $620 \pm 2^\circ C$, followed by the formation of Ni_3Al and $NiAl$ at about $\sim 980 \pm 164^\circ C$, after the aluminum melting temperature ($\sim 669 \pm 2^\circ C$). Finally, the transformation of $\gamma-Al_2O_3$ to $\alpha-Al_2O_3$ occurs at $\sim 1059 \pm 35^\circ C$.

Concerning the microstructure, after $1300^\circ C$ and cooling, the powder mixtures ($Al+Ni_{ox}$) form clusters, a cluster of $NiAl$ for the coarse preoxidized Ni particles and a cluster of interpenetrating Ni_3Al and Al_2O_3 for the small preoxidized nickel particles.

When the preoxidized Ni particles lay over the Al ones, a dense structure of Ni-rich $NiAl$ on top of Al-rich $NiAl$ for the Ni coarse particles occurs while a dense structure of Ni_3Al on top of Ni-rich $NiAl$ develops with the small preoxidized Ni particles. The Al_2O_3 formed during the aluminothermic reaction is found trapped at the grain boundaries of the Al-rich $NiAl$ structure for the coarse particles and of the Ni-rich $NiAl$ structure for the small particles. In addition, for the small particles, a cluster structure composed of Al-rich $NiAl$ and Al_3Ni_2 particles is surrounded by Al_2O_3 .

Finally, for the third configuration (Al over preoxidized nickel particles), two zones can be distinguished in the case of coarse Ni particles. The first zone consists of a cluster of Al-rich $NiAl$ particles when heated slowly ($2^\circ C/min$), which become Ni-rich $NiAl$ when rapidly heated ($25^\circ C/min$). Below, one can observe the Ni particles slightly enriched in aluminum sintered to each other.

As for fine particles, a first layer of a dense cluster of Ni-rich $NiAl$ particles with alumina grain boundaries can be observed for the heat treatment of $2^\circ C/min$ and this layer become porous for a treatment of $25^\circ C/min$. The second layer consists of elongated grains of Ni-rich $NiAl$, and finally below, the $Ni(Al)$ particles sintered to each other can be observed.

III-Reactivity of the Al particles with pure preoxidized nickel substrate

In part I and II, simplified powder systems of Al/NiO/Ni have been studied, but to understand the mechanisms of the formation of self-regenerating coatings on a metallic substrate, it is necessary to identify the reactions that take place between the slurry Al, the nickel oxide and the substrate. For this purpose, a pure nickel substrate is used as model material. The reactivity of the Al particles and the Ni and the preoxidized Ni substrate were studied by DSC. Three different layouts were tested to try to separate the contribution of the different elements.

For these tests, coupons of approximately 1x3.5 mm were prepared from a rod a pure Ni of 4 mm diameter (99.98% purity). For consistency with the TGA experiments (Chap. IV), the Ni samples were ground with SiC #180 paper then rinsed in distilled water and cleaned with acetone and ethanol under ultrasonic agitation before any further step.

Three different configurations were tested. The pure Ni substrate was first measured as a reference to identify the intrinsic transformations occurring in the substrate upon heating (Figure III-21.A). The second system employed as reference consists of a coupon of Ni placed at the bottom of the crucible onto which $\sim 20 \text{ mg.cm}^{-2}$ of Al microparticles were deposited (Figure III-21.B). The third system studied is very similar to the previous one. However, this time the Ni coupon was preoxidized beforehand at 1100°C for 2 hours (Figure III-21.C).

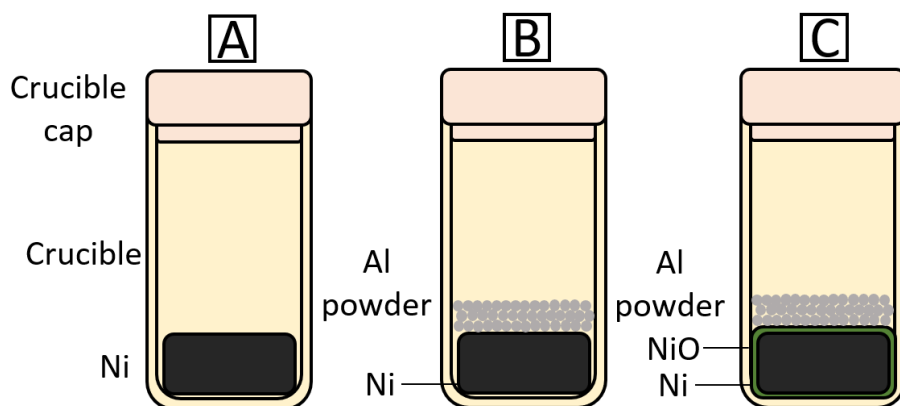


Figure III-21: Schematic drawing representing the three different layouts for the DSC tests between (A) pure Ni substrate, (B) with Al powder and (C) preoxidized Ni substrate with Al powder.

III.A-layout A and B: Pure Ni and pure Ni with Al particles

III.A.1-Results

- **Differential scanning calorimetry**

Like with the Ni particles, the peak associated with the Curie temperature $\sim 352^\circ\text{C}$ can be observed in the Ni substrate (Figure III-23) [10]. In addition, at higher temperature, an exothermic peak can be observed. This peak was attributed to the oxidation of nickel by the residual air remaining in the alumina crucible.

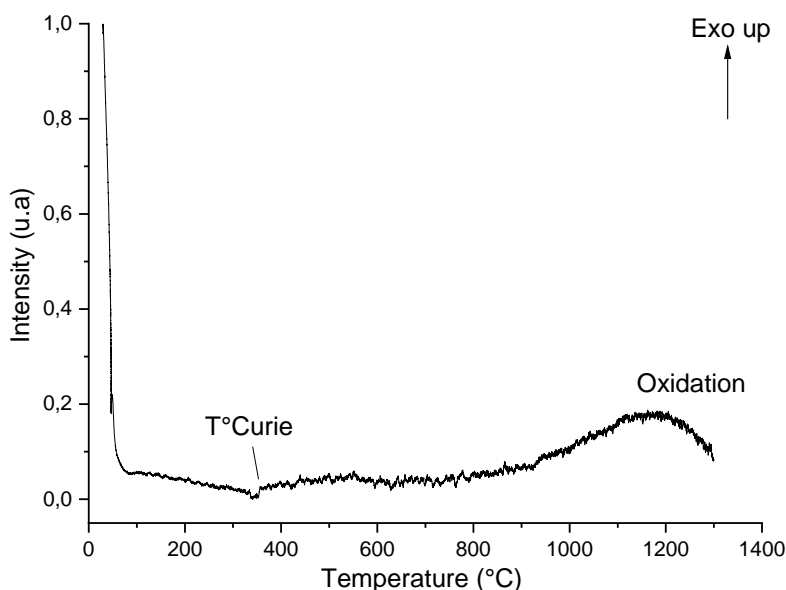


Figure III-22: DSC thermograms of a pure nickel sample (heating at 5 °C/min) till 1300°C in Ar.

As a reference test for self-regenerating coatings, the reactivity between pure Ni and Al powder (without slurry binder) was first investigated. The DSC thermograms for the heating rate of 5°C are given in Figure III-23 and the data are summarized in Table III-8.

A strong endothermic peak referring to the Al melting was observed at 659°C (Figure III-23). The heat exchanged for this reaction was lower than the one for the pure Al powder, which suggests that a small quantity of Al reacts with the substrate [11] and/or with the oxygen present in the combustion chamber. Nevertheless, the exothermic signal of this reaction between Al and Ni and/or Al and O₂ was not identified on the thermograms. Two other endothermic peaks induced by the melting of an element can be identified for this system, the melting of Ni₃Al takes place at 863°C and the melting of Ni₂Al₃ at 1242°C.

Finally, an exothermic peak can be observed over a large temperature range with a maximum of 1081°C. This peak most likely corresponds to the formation of the compound NiAl (possibly added with the oxidation of aluminum at higher temperature). In addition, this reaction and the melting of the Al₃Ni₂ compound take place at similar temperatures. This may explain the temperature shift observed for the melting of the intermetallic compounds.

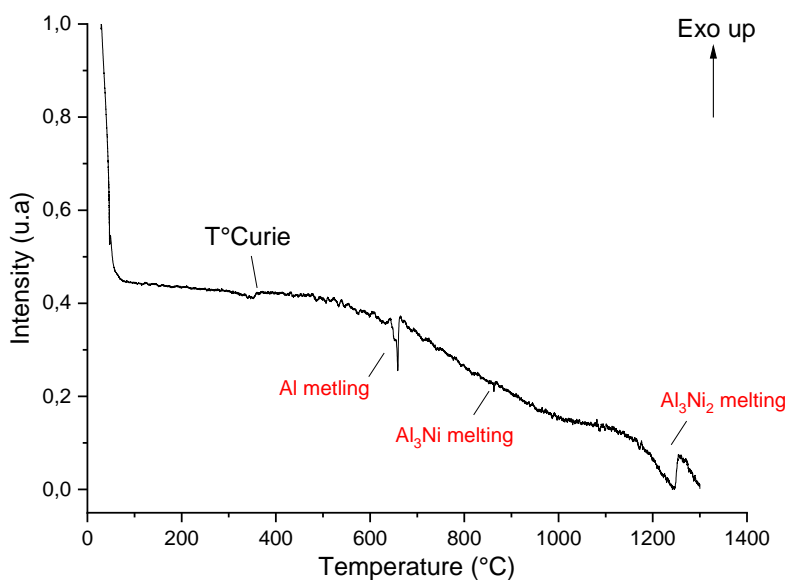


Figure III-23: DSC thermograms of the Ni samples with Al particles over upon heating (5°C/min) till 1300°C in Ar.

Table III-8: Thermal data and the potential transformation in the Al particles over Ni preoxidized particles.

	T_{\max} (°C)	ΔT (°C)	ΔH (J g ⁻¹)
Heating ramp	5°C/min		
T_{Curie}	352	---	---
Al melting	659	643-664	27
Al₃Ni melting	863	861-866	1
NiAl formation	1081	986-1289	-89
Al₃Ni₂ melting	1242	1177-1254	101

III.B-Layout C: Preoxidized pure Ni with Al particles

III.B.1-Results

- **Differential scanning calorimetry**

For the third system, where the preoxidized Ni substrate is made to react with the Al powder, the thermograms are given in Figure III-24. Considering the reactivity between the pure Ni and Al powder, two reactions occur for the heating rate at 2°C/min while four thermal events were identified for the heating rate at 25°C/min. The data are summarized in Table III-9.

○ **Heating rate of 2°C/min**

For the heating rate at 2°C / min, the endothermic peak at 660°C (Figure III-24, label 2) corresponds to the fusion of Al. As for the second and last peak could correspond to the fusion of the intermetallic compounds Al_3Ni_2 at 1133°C [12,13]. Finally, between 981 and 1246°C the strong exothermic formation of the β -NiAl phase occurs. Between 700 and 900°C, the diffusion of aluminum is favored and promotes the formation of phases rich in aluminum such as Al_3Ni and Al_3Ni_2 . Thereafter, from 900°C, the diffusion of Ni is favored. This makes it possible to enrich these phases previously synthesized to form β -NiAl, which is the most thermodynamically phase of the Al-Ni system [30,32,48-chapter I].

○ **Heating rate of 25°C/min**

For the heating rate of 25°C/min, the first exothermic reaction starts after the Curie's temperature of Ni (352°C) and refers to the solid/solid aluminothermic reaction between Al and NiO. This reaction occurs until the melting of Al. In addition, contrary to what is expected considering the reactivity between the powders (I and II), the peak has a "saw-tooth" shape. An endothermic reaction also takes place during the exothermic reaction. This endothermic reaction is probably caused by the heat released during the exothermic reaction. Indeed, when a sufficient amount of heat is emitted and the local temperature exceeds 660°C, the Al particles near the surface begin to melt, causing these endothermic peaks that can be seen on the thermogram (Figure III-24, label 2).

The third peak between 668 and 885°C is exothermic (Figure III-24, label 3) and most likely corresponds to the end of the reduction of NiO (S/L), as well as to the formation of the first intermetallic component, Al_3Ni in the bath of molten aluminum, γ '- Ni_3Al in the substrate and then quickly β -NiAl. In addition, in this temperature range a second endothermic phenomenon occurs. This phenomenon has been attributed to the melting of the Al_3Ni compound between 676 and 845°C [12,13].

Finally, the last exothermic peak (Figure III-24, label 4) corresponds to the transformation of alumina, during this exothermic reaction the melting of Al_3Ni_2 also occurs at 1136°C [12,13].

○ **Heating rate of 5°C/min**

The last heat treatment carried out at 5°C/min. This heating rate was selected because it corresponds to an industrial heating rate for larger installations. Moreover, this temperature seems to be a good compromise between the heating rate of 2°C/min and 25°C/min from a thermodynamic point of view. Indeed, the strong exothermicity observed for the temperature ramp of 25°C (Figure III-24, label 3) can be controlled, which should avoid any projections of molten material or significant deformation of the coating caused by excessive temperatures [14].

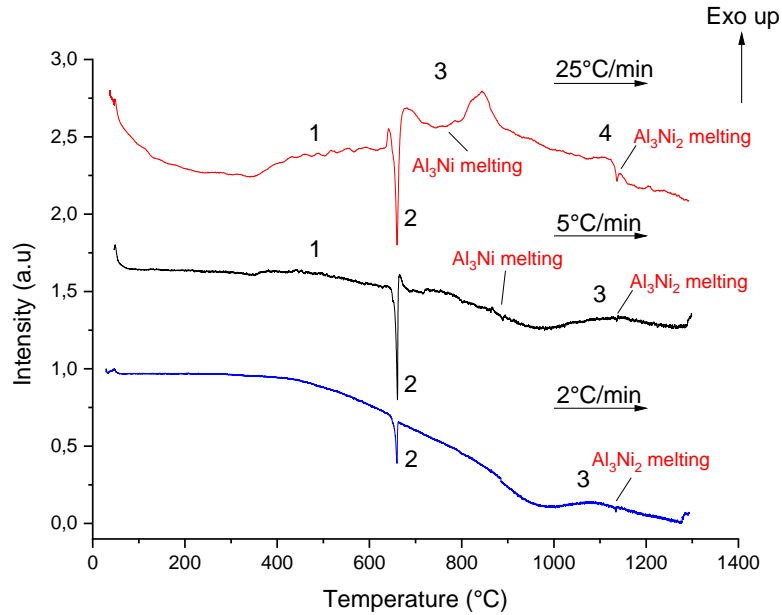


Figure III-24: DSC thermograms of a preoxidized pure nickel samples in contact with the Al metallic powders upon heating (2, 5 and 25°C/min) till 1300°C in Ar.

Table III-9: Thermal data and the potential transformation in the Al particles over Ni preoxidized particles upon heating (2, 5 and 25°C/min) till 1300°C in Ar.

	T_{\max} (°C)	ΔT (°C)	ΔH (J g ⁻¹)	T_{\max} (°C)	ΔT (°C)	ΔH (J g ⁻¹)	T_{\max} (°C)	ΔT (°C)	ΔH (J g ⁻¹)
Heating ramp	2°C/min			5°C/min			25°C/min		
NiO reduction	---	---	---	---	---	---	642	352-649	-13
Al melting	660	645-663	28	661	655-662	37	660	649-672	6
NiO reduction (S/L) + Ni _x Al _y formation	---	---	---	---	---	---	~756	668-886	-19
Al ₃ Ni melting	---	---	---	889	884-891	3	745	681-844	19
NiAl formation	1090	981-1246	-177	867	865-868	-1	1123	1068-1159	-5
Al ₃ Ni ₂ melting	1134	1134-1136	1	1136	1135-1138	1	1137	1123-1145	1

Subsequently, a DSC heat treatment comprising different stages depending on the thermal event of the aluminothermic reaction between nickel oxide and solid aluminum (620°C), nickel oxide with melting aluminum (700°C) and the formation of the intermetallic β -NiAl was deduced from the above results and applied to a preoxidized nickel substrate topped with aluminum particles (Figure III-25) so as to simulate the formation of a coating.

During the rise in temperature, the thermal event corresponding to the Curie temperature can be observed. When the first heating ramp is over and the dwell of 620°C is reached, a first exothermic event appears. It most likely corresponds to the solid aluminothermic reaction between aluminum particles and nickel oxide. This solid-state reaction generates significant energy during the first minute of the dwell (Figure III-25 label 1) and tends to fade with time.

During the second heating ramp to reach the temperature of 700°C, the aluminum melts and an endothermic peak is observed at 656°C (Figure III-25 label 2).

For the stage of 700°C, only one exothermic event can be observed after the aluminum melting. This one corresponds most certainly to the second step of the liquid aluminothermic reaction and to the formation of an Al₃Ni intermetallic. As in the previous case, most of the energy is released during the first moments of the dwell and then tends to fade away (Figure III-25 label 3). In addition, two endothermic peaks are detected, but with very low intensities. It thus appears difficult to unambiguously ascribe these peaks to noise or to a proof of fusion.

Finally, the last temperature rise occurs after 6 hours and 45 minutes of treatment, upon the heating ramp to 1080°C, where four exothermic peaks are noted. The first two at 715°C and 816°C could correspond to the aluminothermic reaction between molten aluminum and nickel oxide (Figure III-25 label 4). The third at 865°C could correspond to the formation of the intermetallic β-NiAl (Figure III-25 label 4) and finally the last at 1045°C would correspond to the transformation of aluminum oxide to its more stable form α-alumina (Figure III-25 label 5).

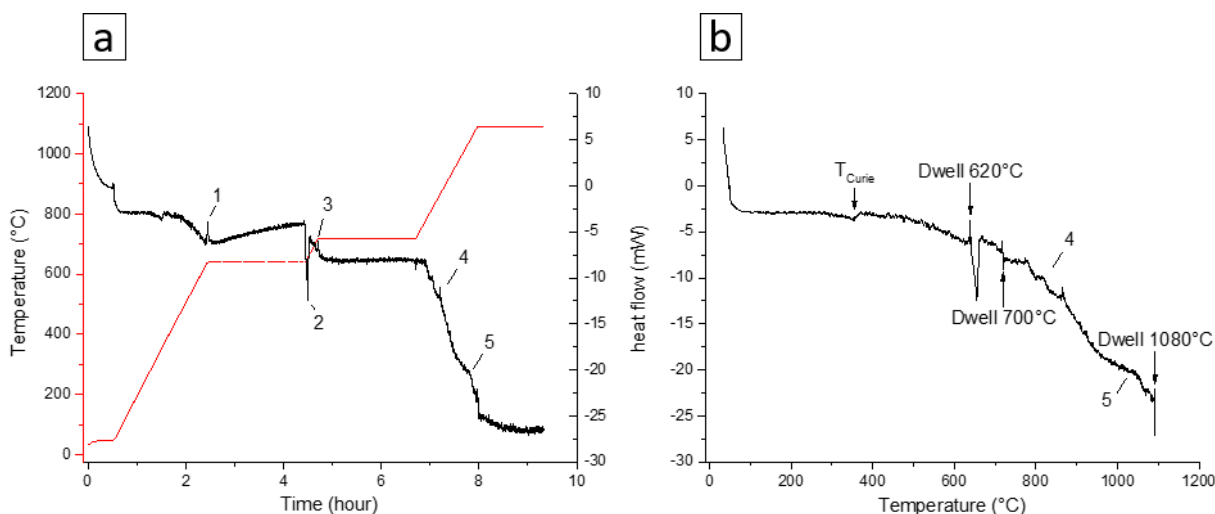


Figure III-25: DSC thermograms of a preoxidized pure nickel sample in contact with the Al metallic powders upon heating with a heating ramp of 5°C/min and dwells of 2h at 620°C, 700°C and 1080°C, in (a) curve as a function of the total duration of the heat treatment, and in (b) curve as a function of temperature (= dwell represented at 1 point).

Table III-10: Thermal data and the potential transformation in the Al particles over Ni preoxidized particles upon heating (5°C/min) till 1300°C in Ar.

	T_{\max} (°C)	ΔT (°C)	ΔH (J g ⁻¹)
Heating ramp		5°C/min	
NiO reduction	-92	627-640	-92
Al melting	655	639-663	8
Al₃Ni melting	---	---	---
NiAl formation	---	---	---
Al₂O₃ transformation	1042	959-1084	-14

- **Microstructural development**

The samples were analyzed in cross-section to observe the exothermic reactions and the different layers after the annealing DSC treatment. The SEM images (Figure III-26) and EDS spot measurements (Figure III-27) allowed to identify the phases formed after the heat treatment. The thicknesses of the different layers are summarized in Table III-11.

For the samples heated at 5°C/min up to 1300°C, 3 distinct zones can be observed (Figure III-26.a). The first and thickest layer (225±16µm) consists of an Al-rich β-NiAl intermetallic compound (Figure III-27). This layer can be divided into 2 parts, with a first part containing pores and alumina close to the surface, and a second part without pores and alumina close to the interface. The second layer of 31±6 µm consists of a Ni-rich β-NiAl intermetallic compound (Figure III-27). Finally, the last layer between the coating and the substrate is mainly composed of pores (Figure III-26.a).

For the second samples heated with 2 dwells of 620 and 700°C/2h, a first layer of Al₃Ni intermetallic is observed at the surface of the sample (Figure III-37). Below, a dense alumina layer can be observed which itself overcomes the residual NiO layer. It is interesting to observe that liquid aluminum did not evenly flow/percolate through the nickel oxide layer (Figure III-26.b). Finally, Al₃Ni₂ diffusion islands formed at the top of the substrate (Figure III-27)

The third heat treatment with an additional stage of 2 hours at 1080°C results in a coating very similar to those observed for a continuous heating rate of 5°C/min until 1300°C. At the top of the sample, the first layer of β-NiAl intermetallic and alumina clusters can be observed (Figure III-26.c). The cluster of alumina seems to adhere to the coating. A significant thickness of Al-rich β-NiAl of 341± µm is then observed which can be split into two main sublayers (Figure III-27). A first part close to the surface containing pores and a second part close to the substrate without pores, with a higher proportion/size of pores for the coating with a heat treatment of 5°C/1300°C. A second layer of 12±4 µm consist of a Ni-rich β-NiAl intermetallic compounds and along the interface a discontinuous layer of pores can be observed (Figure III-26.c)

In the case of heat treatments with stages at 620°C, 700°C, and 1080°C deduced from the different thermal events, the observations are in line with the previous results. Indeed, for the shortest heat treatment with a heating ramp of 2°C/min and two two-hour stages at 620°C and 700°C, the first layer of Al₃Ni intermetallic is observed at the surface of the sample. Below, a dense alumina layer

can be observed which itself overcomes the residual NiO layer. It is interesting to observe that liquid aluminum did not evenly flow/percolate through the nickel oxide layer. Areas with a higher concentration of defects allowed the liquid Al to fully pass through the NiO layer. Liquid Al was then able to reach the substrate and aluminize it, thus forming diffusion islands of Al_3Ni_2 (Figure III-26.b). For the heat treatment with the additional dwell of $1080^\circ\text{C}/2\text{h}$, the results of the end of the solid/liquid reduction of NiO, and the formation of NiAl intermetallics can be observed (Figure III-26.c).

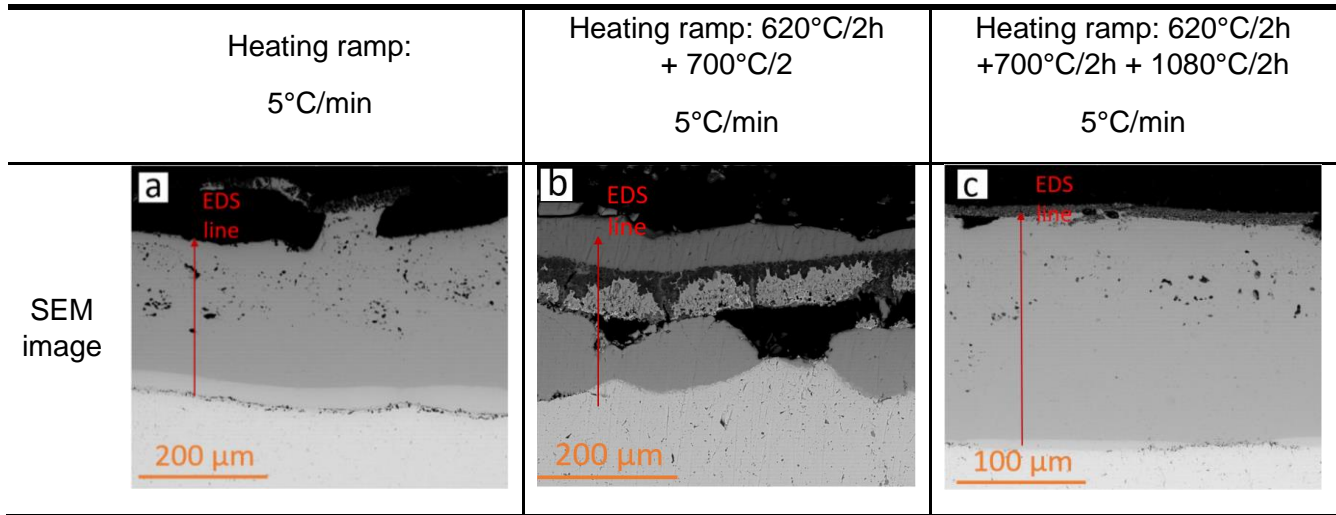


Figure III-26: SEM (BSE mode) cross-section of the preoxidized pure nickel sample in contact with the Al metallic powders upon heating with a heating ramp of 5°C/min until 1300°C (a) and dwells of 2h at (a) 620°C, (b) 700°C and (c) 1080°C.

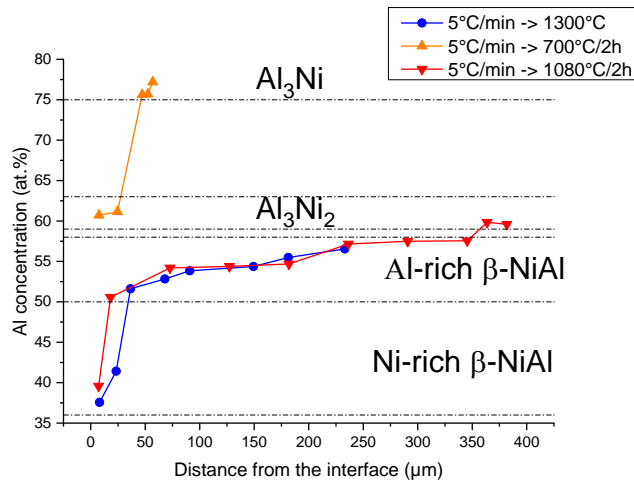


Figure III-27: EDS concentration profiles of Al in the coatings for preoxidized pure nickel sample in contact with the Al metallic powders upon heating with a heating ramp of 5°C/min until 1300°C (blue) and dwells of 2h at 620°C, 700°C (orange) and 1080°C (red).

Table III-11: Summary table of the different compounds and thicknesses of the samples after the heat treatments.

Heating ramp		5°C/min			
Layer	1	2	3	4	
Compounds	---	Al rich-NiAl	Ni rich-NiAl	Cavities	
Thickness (µm)	---	225±16	31±6.3	14±4	
Heat treatment		700°C/2h			
Compounds	Al ₃ Ni	Al ₂ O ₃	NiO	Al ₃ Ni ₂	
Thickness (µm)	15±1	3±1	2±1	9±1	
Heat treatment		1080°C/2h			
Compounds	Cluster of Al ₂ O ₃	Al rich-NiAl	Ni rich-NiAl	Cavities	
Thickness (µm)	16±3	341±9	11±4	7±4	

III.C-Discussion

As in the case of the heat treatment between the powders, during the first stage of 620°C, the Al particles reduce the surface of the NiO thus forming a thin Ni layer with inclusions of Al₂O₃ (Figure III-28.a). When the first dwell of 620°C is over, the temperature increases until reaching the second dwell of 700°C. During this temperature rise, the melting of the aluminum particles takes place and stops the solid aluminothermic reaction. When the second dwell of 700°C is reached, the solid/liquid aluminothermic reaction between the NiO and aluminum begins. As observed in the SEM images, this reaction is homogeneous at first, but then when the alumina layer becomes too thick and compact the molten aluminum penetrates through specific grain boundaries of the NiO. Molten Al reacts with the NiO to form metallic Ni and Al₂O₃ (Figure III-26.b). The Ni is immediately dissolved by the molten aluminum. This makes it possible to widen the cracks and to consolidate them (Figure III-28.b). When the liquid Al passes through the entire layer of NiO, it comes into contact with the Ni substrate and causes the aluminization of the substrate, resulting in the formation of an Al₃Ni₂ intermetallic diffusion islands. These islands form inwards and outwards the substrate, causing the NiO to lift out. At this temperature, the coating formed is so-called high-activity, which is characterized by a preferential diffusion of Al and the formation of an intermetallic rich Al coating (Figure III-28.c).

After the second dwell at 700°C, the temperature increases to reach 1080°C. During the heating ramp, Al becomes more fluid, accelerating the flow of it through the NiO cracks, consuming it and replacing it with Al₂O₃. The Al still available diffuses through the substrate to form a thick layer of intermetallic β-NiAl compound (Figure III-28.d).

The aluminization of the substrate can be separated in two steps, at a temperature below of 950°C, the coating formation mechanism is so-called by high-activity [15,16], resulting in the majority diffusion of Al in the coating and substrate [17]. In this case, this leads to the formation of a β -NiAl compound without pores. Subsequently, when the temperatures reach 1000°C, the coating formation mechanisms evolve into a low-activity coating [15,16,18], resulting in a decrease in the Al activity and the increase in the diffusion rate of Ni. During this step, the Ni will diffuse mainly in direction of the molten phase rich in Al. This diffusion causes a rapid enrichment of the liquid leading to its solidification. This rapid solidification will trap the air bubbles, that are present causing the formation of pores. It may be noted that the higher the heating, the bigger the size of trapped air bubbles as opposed to a slow heating rate. This significant diffusion of Ni also leads to a deficit of atoms in the substrate, which results in the formation of Kirkendall porosity at the coating/substrate interface [19].

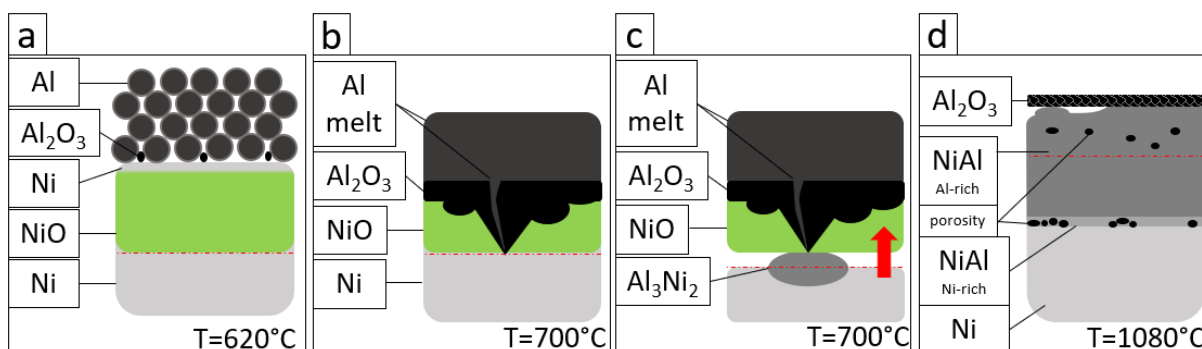


Figure III-28: Schematic drawing of the aluminothermic reduction reaction between a preoxidized Ni substrate and Al particles heated under DSC at 5°C/min with three dwells of 2h at 620°C, 700°C and 1080°C.

III.D-Conclusion

During this chapter III, the activity of Al powders with preoxidized Ni powders and preoxidized Ni substrate with Al powder were explored.

It has been revealed that the size, the preoxidation time of the Ni particles, and the heating rate are predominant parameters in the case of powder mixtures. Indeed, it has been demonstrated that when small particles of preoxidized nickel were used during the thermite reaction, a composite of complex structure between various Ni_xAl_y intermetallic and alumina is formed. This composite consists of particles with a metallic core is an alumina shell. As for the rate, it induces a difference in porosity between the different composites formed with the opposite effect in the case of layouts 2 (Ni_{ox} above Al) and 3 (Al above Ni_{ox}). In fact, in the case of layout 2, the faster the heating rate, the greater the compactness of the composite formed. On the contrary in layout 3, the composite formed is more compact during the slow heating rate. In addition, a larger area is affected by the diffusion of aluminum when heating slowly.

For these two configurations, the structures of the composite are promising for obtaining a coating with a self-regenerating character. An extrapolation of these preliminary results was then carried out on a raw preoxidized substrate.

The configuration of these tests is similar to the layout 3, where the aluminum particles lay on the nickel preoxidized particles. From the calorimetric point of view, the difference between the tests on the particles and on the preoxidized substrate is negligible for the low heating rates of 2 and

5°C / min. For a heating rate of 25°C/min, the energy exchanges observed are greater. Very likely, this corresponds to a difference in the amount of raw material available in the crucible and due to the difference in porosity between the powder mixtures and the substrate.

In addition, different temperature ramps were tested for these tests to highlight the different exothermic reactions such as the aluminothermic reaction between nickel oxide and aluminum. When the crucible is heated up to 700°C /2h, the various stages of the aluminothermic reaction take place on the surface of the preoxidized nickel, consequently forming a thick layer of alumina blocking the diffusion of aluminum. However, aluminum flows into defects of NiO to aluminize the substrate. This leads to the formation of diffusion islands and the lifting of the oxide layer. When the samples are heated to 1080°C, the entire NiO layer is reduced and the thickness of the aluminized substrate is several hundreds of microns.

The results obtained for the stage of 700°C /2h appear interesting for the continuation of this study, because the coating that forms on the surface consists of a Ni_xAl_y intermetallic coating and an alumina diffusion barrier. Subsequently, it will be necessary to reduce the entire nickel oxide layer during the aluminothermic reaction and to suppress the detachment effects.

One of the possible methods, is to reduce the thickness of the oxide layer and therefore control the oxidation time and/or the temperature.

References

[1] V. Udhayabanu, N. Singh, B.S. Murty, Mechanical activation of aluminothermic reduction of NiO by high energy ball milling, *Journal of Alloys and Compounds* 497 (2010) 142–146.

<https://doi.org/10.1016/j.jallcom.2010.03.089>

[2] H.X. Zhu, R. Abbaschian, In-situ processing of NiAl-alumina composites by thermite reaction, *Materials Science and Engineering A* 282 (2000) 1–7.

[https://doi.org/10.1016/S0921-5093\(99\)00788-1](https://doi.org/10.1016/S0921-5093(99)00788-1)

[3] H. Okamoto, Al-Cr (Aluminum-Chromium), *Journal of Phase Equilibria and Diffusion* 29 (2008) 112–113.

<https://doi.org/10.1007/s11669-007-9225-4>

[4] D. Padmavardhani, A. Gomer, R. Abbaschian, Synthesis and microstructural characterization of NiAl-Al₂O₃ functionally gradient composites, *Intermetallics* 6 (1998) 229–241.

[https://doi.org/10.1016/S0966-9795\(97\)00076-9](https://doi.org/10.1016/S0966-9795(97)00076-9)

[5] R. Troncy, G. Bonnet, F. Pedraza, Microstructural characterization of NiAl-Al₂O₃ composite materials obtained by in situ aluminothermic reduction of NiO for potential coating applications, *Materials Chemistry and Physics* 251 (2020) 123124.

<https://doi.org/10.1016/j.matchemphys.2020.123124>

[6] D. Oleszak, NiAl-Al₂O₃ intermetallic matrix composite prepared by reactive milling and consolidation of powders, *Journal of Materials Science* 39 (2004) 5169–5174.

<https://doi.org/10.1023/B:JMASC.0000039204.08971.26>

[7] S. Bao, K. Tang, A. Kvithyld, M. Tangstad, T.A. Enhg, Wettability of aluminium on alumina, *Metallurgical and Materials Transactions B* 45 (2011) 1358–1366.

<https://doi.org/10.1007/s11663-011-9544-z>

[8] J.Z. When, S. Ringuette, G. Bohlouli-Zanjani, A. Hu, N.H. Nguyen, J. Persic, C.F. Petre, Y.N. Zhou, Characterization of thermochemical properties of Al nanoparticles and NiO nanowire composites, *Nanoscale Research Letters* 8 (2013) 184.

<https://doi.org/10.1186/1556-276X-8-184>

[9] E. Ma, E. Nicolet, M. Nathan, Ni₃Al formation in Al/Ni thin-film bilayers with and without contamination, *Journal of Applied Physics* 65 (1989) 2703–2710.

<https://doi.org/10.1063/1.342756>

[10] A. Bolokang, M. Phasha, Thermal analysis on the curie temperature of nanocrystalline Ni produced by ball milling, *Advanced Powder Technology* 22 (2011) 518–521.

<https://doi.org/10.1016/j.apt.2010.07.005>

[11] M.C. Galetz, X. Montero, M. Mollard, M. Günthner, F. Pedraza, M. Schütze, The role of combustion synthesis in the formation of slurry aluminization, *Intermetallics* 44 (2014) 8–17.

<https://doi.org/10.1016/j.intermet.2013.08.002>

[12] P. Zhu, J.C.M Li, C.T. Liu, Reaction mechanism of combustion synthesis of NiAl, *Materials Science and Engineering A* 239-331 (2002) 57–68.

[https://doi.org/10.1016/S0921-5093\(01\)01549-0](https://doi.org/10.1016/S0921-5093(01)01549-0)

[13] A. Biswas, S.K. Roy, Comparison between the microstructural evolutions of two modes of SHS of NiAl: key to a common reaction mechanism, *Acta Materialia* 52 (2004) 257–270.

<https://doi.org/10.1016/j.actamat.2003.08.018>

[14] K. Wool, J.D. Gibbins, K. Slusarski, A.H. Kinsey, T. P. Weihs, The utilization of metal/metal oxide core-shell powders to enhance the reactivity of diluted thermite mixtures, *Combustion and Flame* 167 (2016) 259–267.

<https://doi.org/10.1016/j.combustflame.2016.02.006>

[15] G.W. Goward, D.H. Boone, Mechanisms of formation of diffusion aluminide coatings on nickel-base superalloys, *Oxidation of Metals* 3 (1971) 475–495.

<https://doi.org/10.1007/BF00604047>

[16] J. Angenete, K. Stiller, Comparison of inward and outward grown Pt modified aluminide diffusion coatings on a Ni based single crystal superalloy, *Surface and Coatings Technology* 150 (2002) 107–118.

[https://doi.org/10.1016/S0257-8972\(01\)01544-4](https://doi.org/10.1016/S0257-8972(01)01544-4)

[17] J.M. Brossard, B. Panicaud, J. Balmain, G. Bonnet, Modeling of aluminized coating growth on nickel, *Acta Materialia* 55 (2007) 6586–6595.

<https://doi.org/10.1016/j.actamat.2007.08.025>

[18] R. Rajendran: Gas turbine coatings- An overview, *Engineering Failure Analysis* 26 (2012) 355–369.

<https://doi.org/10.1016/j.engfailanal.2012.07.007>

[19] D.F. Susan, A.R. Marder, Ni-Al composite coatings: Diffusion analysis and coating lifetime estimation, *Acta Materialia* 49 (2011) 1153–1163.

<https://doi.org/10.2172/788093>

Chapter IV: Synthesis of self-regenerating composite coatings using aluminothermic reaction

The previous chapter dealt with the reactivity of aluminum and preoxidized nickel in two configurations: the mixture of aluminum and preoxidized nickel particles and the deposition of aluminum particles onto a preoxidized nickel substrate. It has been demonstrated that the high exothermicity of the aluminothermic reaction as well as the formation of Al-Ni intermetallics and aluminum oxide leads to a complex composite structure. Part of this composite is made up of an alumina shell and an intermetallic core of NiAl or Al_3Ni_2 .

Based on the results of Chapter III, Chapter IV now investigates the aluminizing of preoxidized Ni substrate via a slurry route in order to synthesize a nickel aluminide coating containing micro-reservoirs.

Table of contents

I-Article II: Synthesis of self-regenerating NiAl-Al ₂ O ₃ composite coatings	122
Abstract.....	122
I.A-Introduction.....	122
I.B-Experimental procedure.....	123
I.C-Results	125
I.C.1-Pre-oxidation of bulk Ni	125
I.C.2-Influence of the annealing temperature	128
I.C.3-Influence of the pre-oxidation time of the nickel substrate	130
I.D-Discussion	134
I.D.1-Influence of the heat treatment on the formation mechanisms of coatings.....	134
I.D.2-Influence of the pre-oxidation time.....	136
I.E-Conclusions	138
References.....	139
II-Synthesis of self-regenerating NiAl-Al ₂ O ₃ composite coatings using Ni plating and aluminothermic reaction	143
II.A-Results.....	144
II.A.1-Microstructure of Ni plating.....	144
II.A.2-Texture.....	147
II.A.3-Preoxidation of Ni plates.....	149
II.A.4-Influence of the current density and preoxidation time on the aluminized layers ..	154
II.B-Discussion	158
II.B.1-Preoxidation of the Ni plating.....	158
II.B.2-Influence of the current density on the aluminothermic and aluminizing processes	159
II.B.3-Influence of the electrodeposit thickness on the aluminothermic reactions and the aluminizing processes.....	162
II.C-Conclusion.....	164
References.....	165

I-Article II: Synthesis of self-regenerating NiAl-Al₂O₃ composite coatings

Submitted to Materials Chemistry & Physics (2021)

Synthesis of self-regenerating NiAl-Al₂O₃ composite coatings

R. Troncy^{1, a}, G. Bonnet^{1, b}, F. Pedraza^{1, c}

¹ LaSIE, La Rochelle Université, UMR CNRS 7356, Avenue Michel Crépeau, 17042 La Rochelle Cedex 1, France

^aromain.troncy1@univ-lr.fr, ^bgbonnet@univ-lr.fr, ^cfpedraza@univ-lr.fr

Keywords: Coating, Aluminothermic reaction; NiAl-Al₂O₃; Microstructure; Self-regenerating coating

Abstract

The aluminothermic reactions involved either in the mixtures or the stack of NiO and Al powders were elucidated in a previous work [1]. The present work now investigates the formation of potential self-regenerating coatings using the aluminothermic reaction between nickel oxide and aluminum. The use of this exothermic reaction allows the simultaneous formation of both alumina and nickel aluminides. The coatings were obtained by first pre-oxidizing the nickel substrate, then spraying an aluminum slurry before applying an adequate heat treatment. The most promising self-regenerating coatings display a first composite layer, made of an intermetallic compound (Al₃Ni or NiAl) and alumina, and a second layer with a higher concentration of oxide. The first layer is expected to play the role of an Al reservoir coating and the second one that of a diffusion barrier to slow down the Al flux to maintain the Al reservoir in the coating. The effects of preoxidation time and of temperature on the resulting coating microstructures are discussed as a function of time.

1.A-Introduction

Aluminum diffusion coatings manufactured by CVD-related techniques have long and widely been used for the protection of turbine blades made of Ni-based superalloys exposed to oxidative and corrosive conditions [2,3]. Some recent studies focused on slurry aluminizing via aqueous routes due to their milder ecological impact and much lower cost. The oxidation resistance of the slurry aluminide coatings was similar the one observed with traditional ones [4,5]. Pedraza et al. described the mechanisms of formation of such aluminide coatings on pure Ni [6] and Galetz and collab. [7] revealed the high exothermicity associated during the reaction of molten Al and Ni, which allowed the impressively quick formation of the coatings on different Ni-based superalloys [7,8].

However, irrespective of the fabrication mode (CVD or slurry), the Al from the diffusion coatings is mostly lost by diffusion into the substrate and diluted by the upward flow of the alloying elements upon exposure to high temperatures [9]. As a result, the Al reservoir of the coatings is depleted in particular with high activity coatings because of the significant Al gradient between the coating and the substrate [5]. While different approaches to slow down the Al inward diffusion have been proposed in the open literature, they all rely on placing diffusion barriers between the coating and the substrate mostly by using CVD [10], PVD [11], electrodeposition [12-14], and even by

explosive welding, forming and heat treatment [15]. Such diffusion barriers can result in different coating compositions, microstructures and thicknesses that can be tailored as a function of the final application. Yet, none of these studies investigated the simultaneous formation of a hybrid coating like the ones derived from the well-known aluminothermic exothermic reactions that result in composite coatings made of nickel aluminides and alumina. For instance, Padmavardhani et al. sintered functionally graded NiAl-Al₂O₃ composite compounds by reactive hot compaction of powders [16]. Hot-pressing of pre-oxidized NiAl powder was also employed to form NiAl-Al₂O₃ bulk samples with adequate bending strength and toughness [17]. One of our previous works highlighted the different reactive processes when mixing pre-oxidized Ni and metal Al vs. stacking metal Al onto pre-oxidized Ni. It was concluded that the particle size and preoxidation time governed the growth of the multilayered bulk samples made of nickel aluminides of different stoichiometries with various dispersions of the Al₂O₃ issued from the aluminothermic reaction [1]. Therefore, the goal of this paper is to extrapolate our previous findings to bulk samples to form potential self-regenerating coatings. The idea is to exploit the in situ exothermicity (with no external compaction) between the powders deposited from water-based slurries onto a pure Ni substrate to sinter the composite Ni_xAl_y-Al₂O₃ coatings. In addition, the high heat released during the aluminothermic reaction will be absorbed by the high thickness of the nickel, which will avoid the emission of gas or the projection of molten metal, as the work of K. Woll et al. as shown [18]. The mechanisms of formation of these original coatings are discussed for the first time in the literature.

1.B-Experimental procedure

Bulk Ni samples (99.98 wt. %, Goodfellow) were cut from 12.7 mm diameter cylindrical rods into coupons of about 1.5 mm thickness, polished with SiC P180 papers and then rinsed with deionized water and cleaned in ethanol before pre-oxidation at 1100°C for 2 h in air. After this pre-oxidation step, an Al-based slurry was sprayed on the coupons. The slurry formulation is based on a 1/10 PolyVinyl Alcohol (PVA)/deionized water solution to which 45 wt. % of spherical Al powders (4±3 μm, Hermillon Poudres, France) were added [12]. After blending, the slurries were deposited by airbrush on the pre-oxidized coupon samples. After each deposit, the samples were systematically dried in a stove at 50 °C for 30 min. The samples were weighed before and after slurry deposition with a 10⁻⁴g precision balance to control the deposited slurry quantity.

The dry coatings were then annealed in a TGA apparatus to form the diffusion coating, under a flow of argon (20 mL/min) to prevent any significant oxidation of the substrate and of the Al particles [7]. The heat treatment was adapted to consider the thermal events observed in the differential scanning calorimetry (DSC, SETARAM Labsys Evo 1600) measurements [1]. This gave us three steps: at 620°C for 2 h to foster the solid/solid reduction between Al and NiO; 700°C for 2h to promote the liquid/solid aluminothermic reduction and the Al inward diffusion and a final step at 1080°C to terminate the aluminothermic reduction and foster the outward diffusion of Ni [6].

Two series of short (2 h) and long (12 and 24 h) heat treatment times were investigated (Figure IV-1). In all of them, the heating and cooling rates were set at 5°C/min. In the short annealing series (Figure IV-1a), temperature increments from 620 to 700 and finally to 1080°C were also investigated. In the long annealing series (Figure IV-1b), the same temperatures were employed but the dwell times were longer (24h at 620 and at 700 °C and 12 h at 1080 °C). In the following, each heat treatment will be named through the last applied stage, for example: 620°C/2 h, 700°C/2 h or 1080°C/2 h, or 620°C/24 h.

Following these six different tests, the most promising heat treatments (700°C/24 h and 1080°C/2 h) were performed on the nickel substrate pre-oxidized for different times (30 min, 1 h, 1.5 h, 2 h), with a fixed quantity of deposited slurry (10±2 mg/cm²) to examine the influence of the effects of the nickel oxide layer.

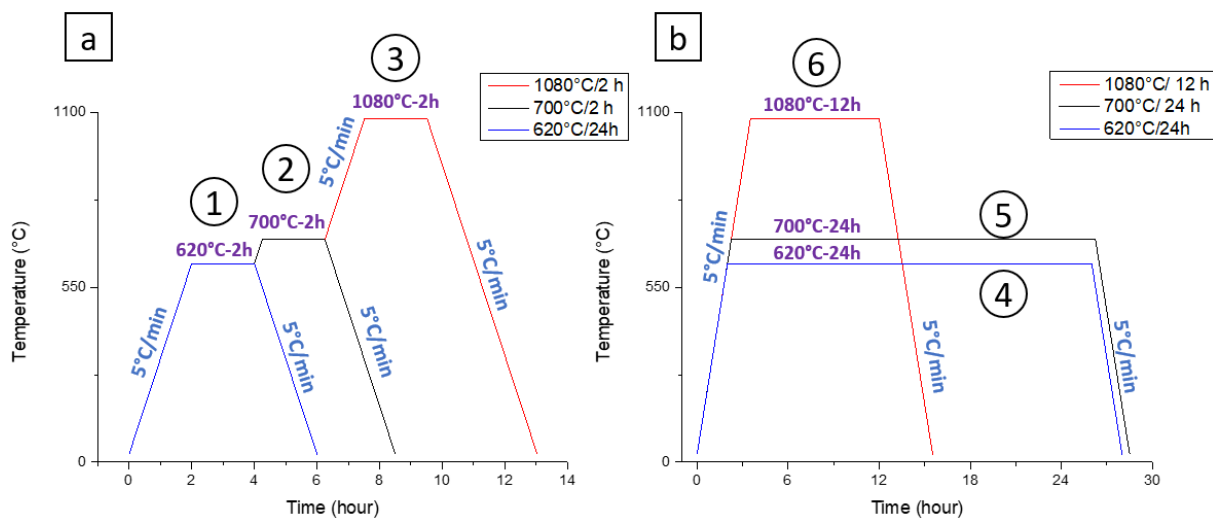


Figure IV-1: Schematic drawing of the annealing treatments (a) short (dwell of 2h) and (b) long (dwells of 12 and 24 h) times of treatment.

The analyses and observations were done with a SEM (FEI QUANTA 200F) coupled to an EDAX detector for chemical analysis, at 20 kV under low vacuum (0.9 mbar). Raman micro-spectrometry (Jobin Yvon LabRam HR800, $\lambda=632.82$ nm) was also carried out to identify the different oxide phases. In addition, the crystal structure was characterized by X-ray diffraction (XRD) in a Bruker AXS D8 Advance with Cu $k_{\alpha 1}$ radiation ($\lambda=0.15406$ nm). The cross-sections were polished down to 1 μm water-based diamond suspension (Struers).

In addition, the SEM surface images of the pre-oxidized samples were processed with Photoshop to remove the oxide ridges. This step was required to reduce noise in the Image J treatment for the calculation of the areas and grain sizes of the oxides.

I.C-Results

I.C.1-Pre-oxidation of bulk Ni

The Ni substrates were pre-oxidized for 30 min, 1, 1.5 and 2 h at 1100 °C in air. The SEM micrographs taken on the surface and in the cross-section are shown in Figure IV-2 in the secondary electron (SE) and backscattered electron (BSE) modes. The main results retrieved from image analysis are summarized in Table IV-1. Two morphologies of NiO (ridge-like and compact grains) can be observed at the surface of the samples for pre-oxidation times shorter than 1.5 h. Two mechanisms can be proposed to explain the formation of the ridge-like morphology. First, the growth of the oxide is enhanced in the regions close to the grain boundaries due to a greater cationic external diffusion. The ridges were also suggested to form over the grain boundaries due to a greater local stress resulting from the internal oxide formation [19,20]. In this mechanism, the oxide layer is supposed to relax stresses by plastic deformation forcing the oxide to move vertically, which leads to the creation of the ridges. In our case, the amount of ridges decreases with increasing the pre-oxidation time (Table IV-1). Increasing the pre-oxidation times allows the oxide to expand from the grain boundaries towards the grain surface, which thus lowers the outward cation diffusion and decreases the growth stresses. In a similar vein, the size of the compact oxide grains increases with the exposure time (Figure IV-3). Their growth is well reported in the literature to occur by outward lattice diffusion of Ni via singly or doubly charged Ni vacancies that leads to the columnar morphology [21] also observed in our study.

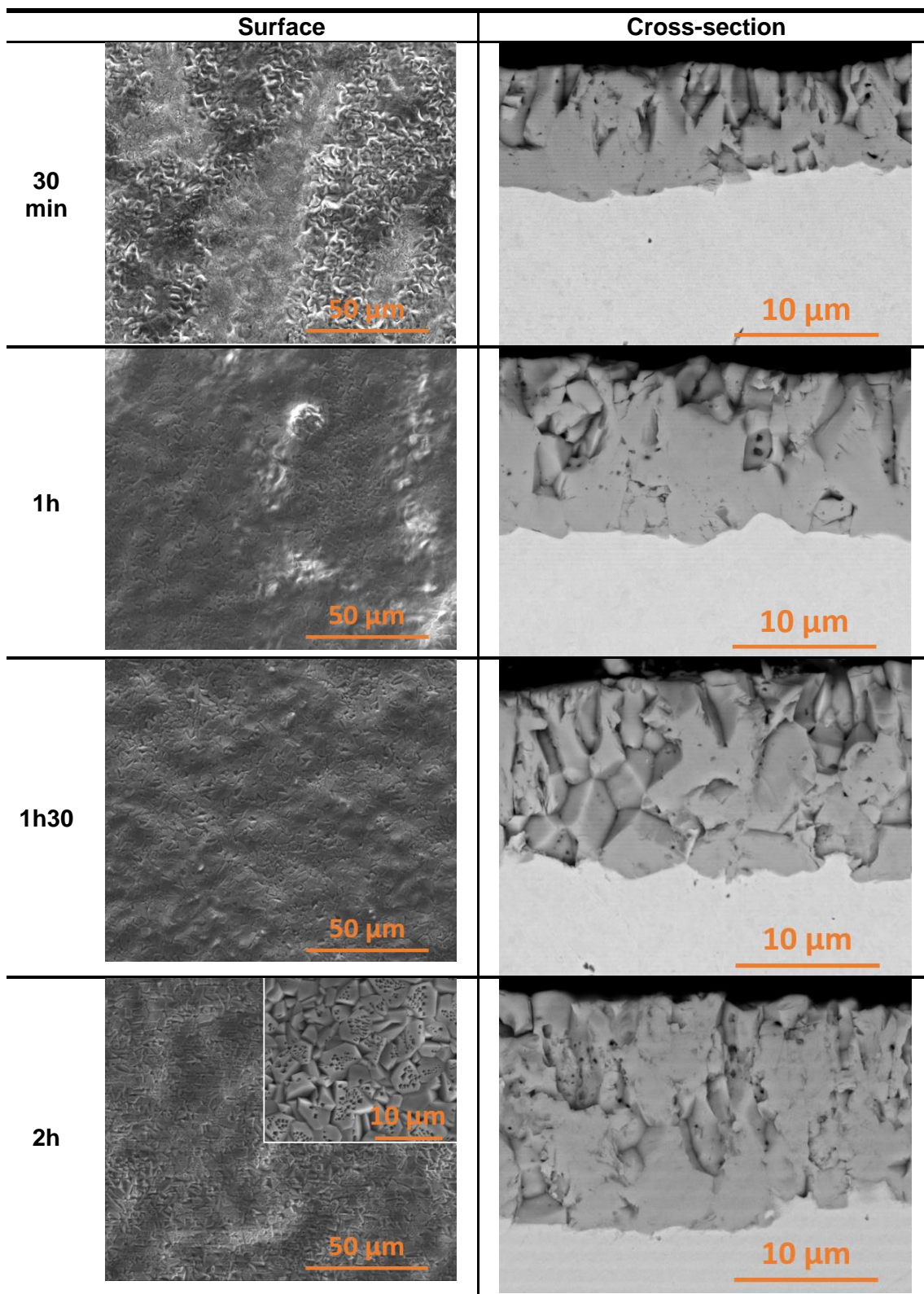


Figure IV-2: SEM (SE and BSE mode) of surface and cross-section images on Ni samples pre-oxidized at 1100 °C under air for 30 min, 1, 1.5 and 2 h.

Table IV-1: Summary table of the ratio, thickness and size of the grains for different times of pre-oxidation.

Time	Compact grain area ratio (%)	Size of the compact grains (μm)	Thickness of the oxide layer (μm)
30 min	40.6	2 ± 1	8 ± 1.1
1h	72.8	2 ± 1	12 ± 1
1.5h	100	2 ± 1	14 ± 2
2h	100	3 ± 1	15 ± 2

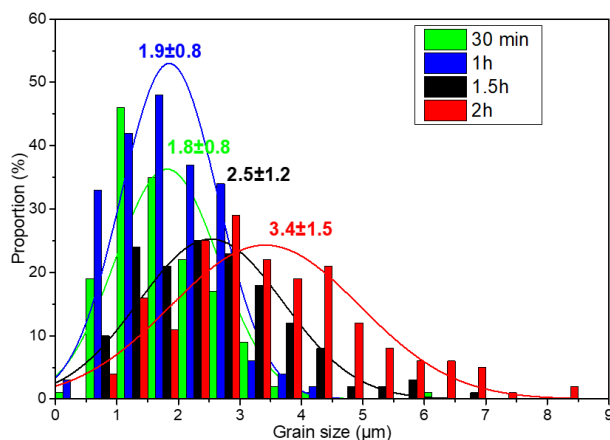


Figure IV-3: Size and dispersion of the NiO compact grain sizes for the different pre-oxidation times at 1100 °C.

The 10 mg/cm² slurries deposited on the pre-oxidized samples are shown in Figure IV-4. The top layer is 55 ± 4 μm thick and contains the bright Al microparticles (label 1 on Figure IV-4). Below, the nickel oxide layer formed by oxidation at 1100 °C for 2 hours of the underlying nickel substrate is observed (label 2 on Figure IV-4).

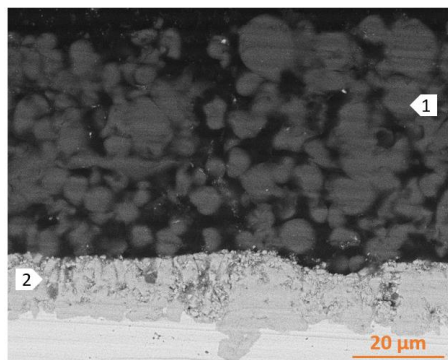


Figure IV-4: Cross-section of the sample after application of the slurry on the pre-oxidized Ni substrate (1100 °C for 2 h).

I.C.2-Influence of the annealing temperature

The microstructures of the pre-oxidized (2 h) bulk Ni samples after reaction with Al at 620, 700 and 1080°C for 2 and 24 h are shown in Figure IV-5. The compositions of the metallic elements in the observed layers are also given. The compounds formed and the thicknesses of the different layers are summarized in Table IV-2. They have been assessed by XRD, EDS and the Raman spectroscopy (Figure IV-6).

- **Heat treatment at 620°C for 2 h and 24 h**

After 2 h at 620°C (Fig. 5.a), only the outermost layer of NiO has reacted with Al to result in a porous Ni-rich layer of about $2.0 \pm 0.9 \mu\text{m}$ that also contains some oxide inclusions (Figure IV-5.a, layer 1). The layer below corresponds to the part of NiO that did not react during the heat treatment (Figure IV-5.a, layer 2). Indeed, the EDS analyses indicate that very little aluminum has diffused into this layer (Al-Ni 1-99 at. %). Increasing the time to 24 h results in a similar microstructure than after 2 h but now Al has diffused markedly (Figure IV-5.b).

- **Heat treatment at 700°C for 2 h and 24h**

The additional treatment at 700°C for 2 h brings about significant changes of the layers and of the microstructure (Figure IV-5.c). Indeed, a large part of the reduced Ni layer has reacted with Al to form an Al_3Ni intermetallic compound (Figure IV-5.c, layer 1). However, a thin layer of metallic Ni still remains below the Al_3Ni layer (Figure IV-5.c, layer 2). Then, the layer of NiO and the substrate are observed (Figure IV-5.c, layer 3). As opposed to 620°C/2h, a significant amount of Al has now diffused all across the layer of NiO (13 at. % Al) towards the substrate (9 at. % Al).

By increasing the reaction time to 24 h (Figure IV-5.d), three layers can be distinguished over the substrate. The thickest ($16 \pm 3 \mu\text{m}$) most external layer is composed of an intermetallic/oxide composite, with an Al_3Ni intermetallic matrix and Al oxide shells surrounding the original Al particles ($3.8 \pm 1.5 \mu\text{m}$) (Figure IV-5.d, layer 1). The central layer (thickness $8.7 \pm 1.8 \mu\text{m}$) is composed of a cluster of oxides (Figure IV-5.d, layer 2). This layer is separated from a $7.5 \pm 1.7 \mu\text{m}$ layer of unreacted NiO by a very thin layer of metallic Ni (Figure IV-5.d, layers 3 and 4). In addition, the EDS analyses indicate that a significant Al has diffused through NiO to the substrate, with Al amounts of 23 and 16 at. % respectively.

- **Heat treatment at 1080°C for 2 and 12h**

With the additional last heat treatments at 1080°C, the morphologies of the coatings are dramatically different from what was observed at lower temperatures. After 2 h, the first layer consists of NiAl intermetallic compound with Al_2O_3 inclusions (Figure IV-5.e, layer 1) and surmounts a thin and compact layer of Al_2O_3 (Figure IV-5.e, layer 2). Then, the fine layer of Ni appears above the layer of NiO and the substrate (Figure IV-5.e, layers 3 and 4).

After 12 h, the coating is mainly composed of NiAl but three inhomogeneous sub-layers can be observed (Figure IV-5.f). The first sub-layer is characterized by the presence of numerous pores (Figure IV-5.f, layer 1). The second one is quite similar to the one observed after 24 h at 620 and 700 °C, with the presence of Al_2O_3 clusters (Figure IV-5.f, layer 2). The third layer is very uneven and contains large oxidized cavities extending into the 4th layer that is composed of NiAl (Figure IV-5.f, layer 4). One can also note the delamination between the coating and the substrate probably due to a difference of their thermal expansion coefficients.

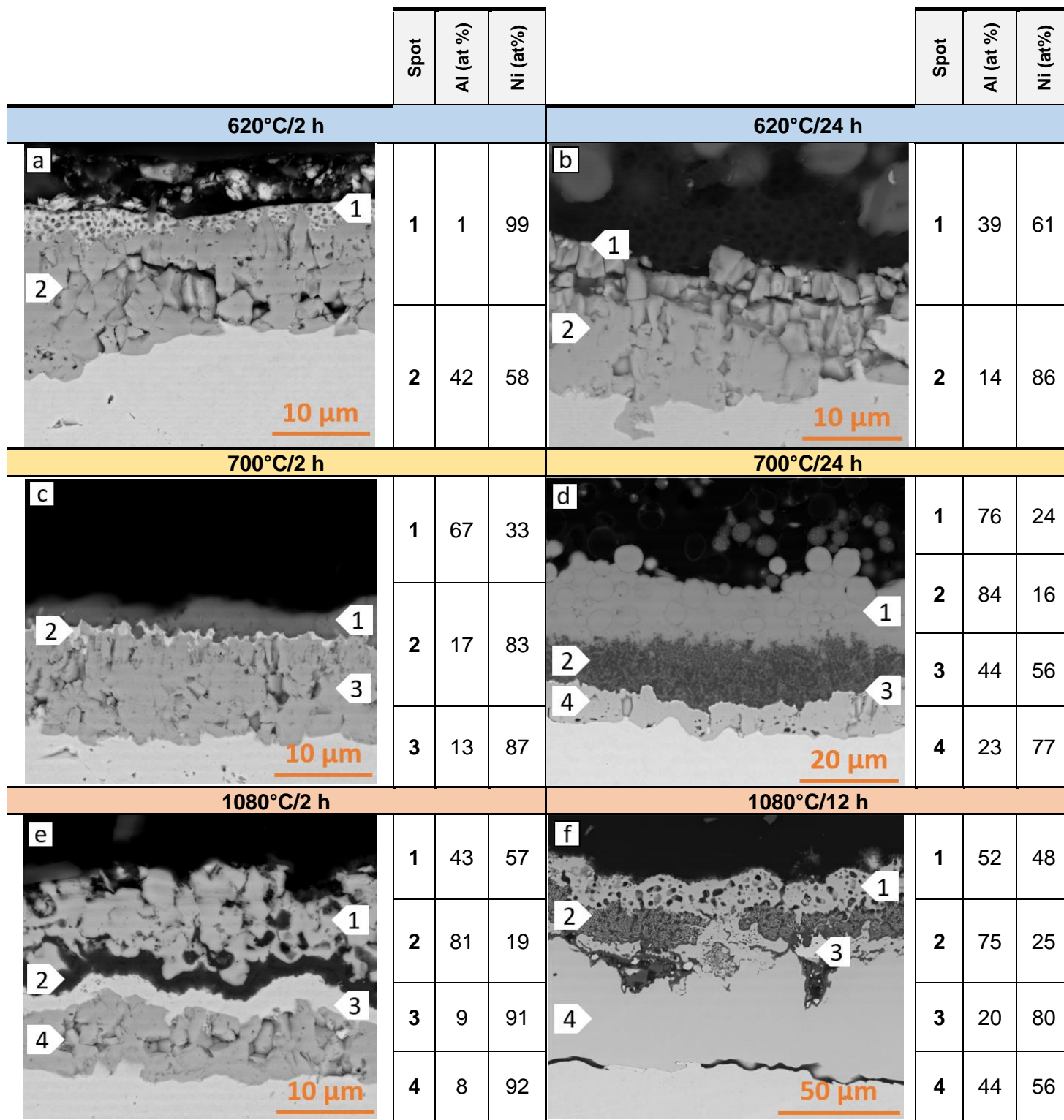


Figure IV-5: SEM (BSE mode) cross-sections of the samples pre-oxidized at 2h for 1100°C and subsequent annealing of the Al-slurry coating at 620°C (a and b), 700°C (c and d) and 1080°C (e and f) for 2, 12 or 24 h.

Table IV-2: Summary table of the different compounds and thicknesses of the samples after the heat treatment.

Figure	5.a				5.b			
Layer	1	2	3	4	1	2	3	4
Compounds	Ni + pores	NiO	Substrate	---	Ni	NiO	Substrate	---
Thickness (μm)	2.9 ± 1	1.8 ± 1.8	---	---	1 ± 0.2	13.2 ± 1.8	---	---
Figure	5.c				5.d			
Compounds	Al_3Ni	Ni	NiO	Substrate	Al_3Ni	Cluster of Al_2O_3	Ni	NiO
Thickness (μm)	3.1 ± 0.9	0.6 ± 0.5	10.2 ± 0.6	---	15.5 ± 3	8.7 ± 2	0.2 ± 0.1	7.5 ± 2
Figure	5.e				5.f			
Compounds	NiAl + $\alpha\text{-Al}_2\text{O}_3$	$\alpha\text{-Al}_2\text{O}_3$	Ni	NiO	NiAl + pores	Cluster of $\alpha\text{-Al}_2\text{O}_3$	Oxidized cavities	NiAl
Thickness (μm)	9.8 ± 1.5	2.4 ± 0.6	2.4 ± 0.7	6.9 ± 0.7	14.4 ± 2	12.3 ± 4	8.1 ± 6	52.7 ± 4

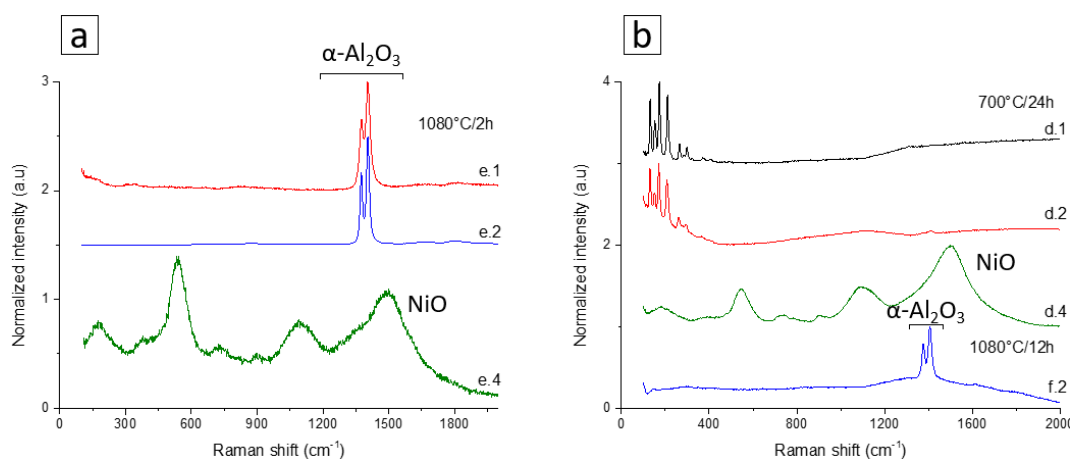


Figure IV-6: Raman spectra on the cross-sections of 2 h pre-oxidized samples after the heat treatments 1080°C/2h (a), 700°C/24 h and 1080°C/12 h (b).

1.C.3-Influence of the pre-oxidation time of the nickel substrate

Following the results presented in section 2.2, the most promising heat treatments for a possible self-regenerating coating application appear to be 1080°C/2 h and 700°C/24 h. Therefore, the study of the influence of the pre-oxidation of the nickel substrate was exclusively conducted with such heat treatments. The pre-oxidation times were thus set at 30 min, 1 h and 1.5 h. The microstructures and metal contents in the coatings after the heat treatments are given in Figure IV-7. Table IV-3 summarizes the crystallographic compounds assessed by XRD, EDS and Raman spectroscopy (Figure IV-8), and the thicknesses of the different layers (from SEM images).

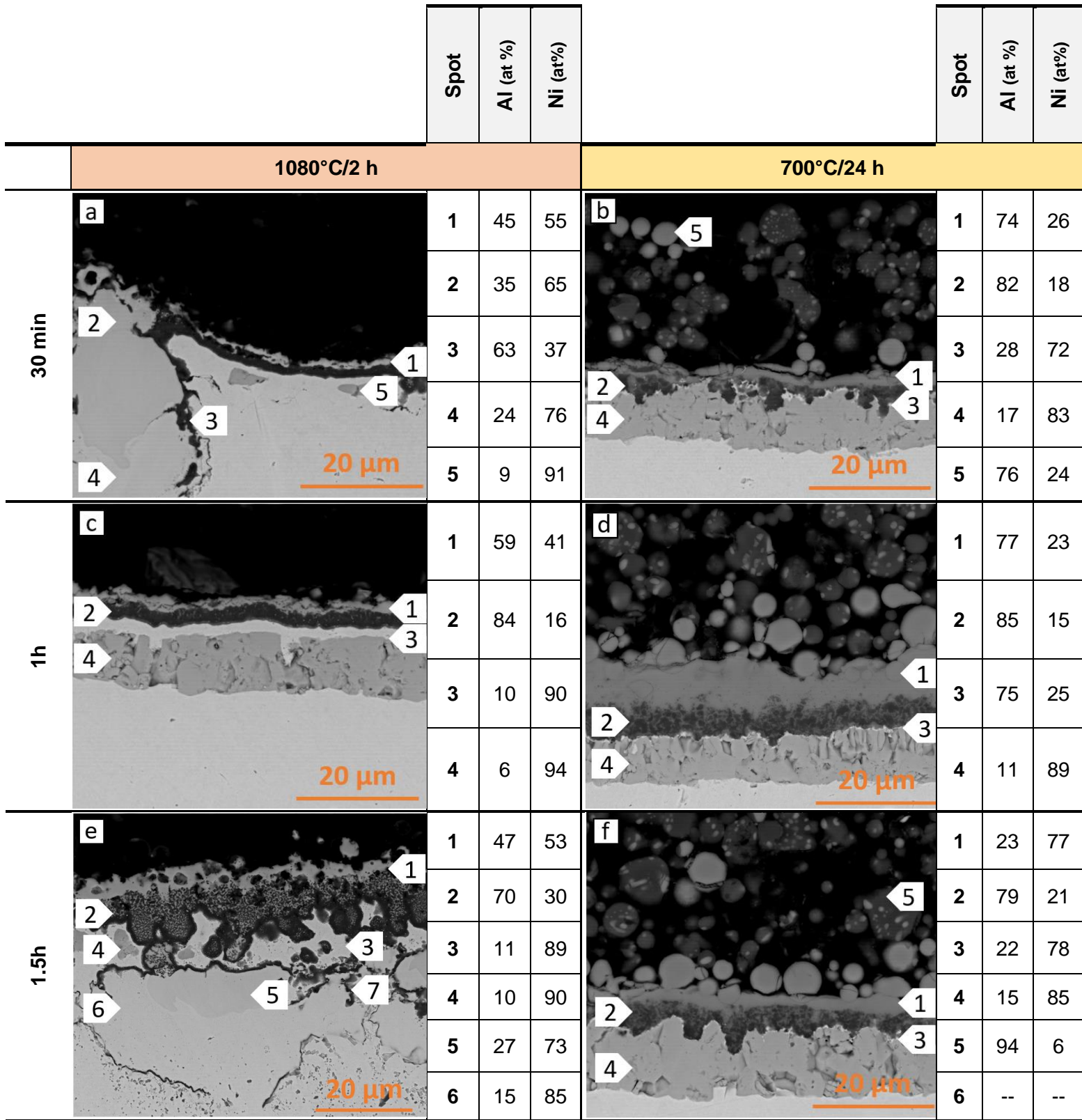


Figure IV-7: SEM (BSE mode) cross-sections of the pre-oxidized samples at 30 min, 1 h and 1.5 h for 1100 °C after TGA treatment at 1080°C/2h and 700°C/24 h.

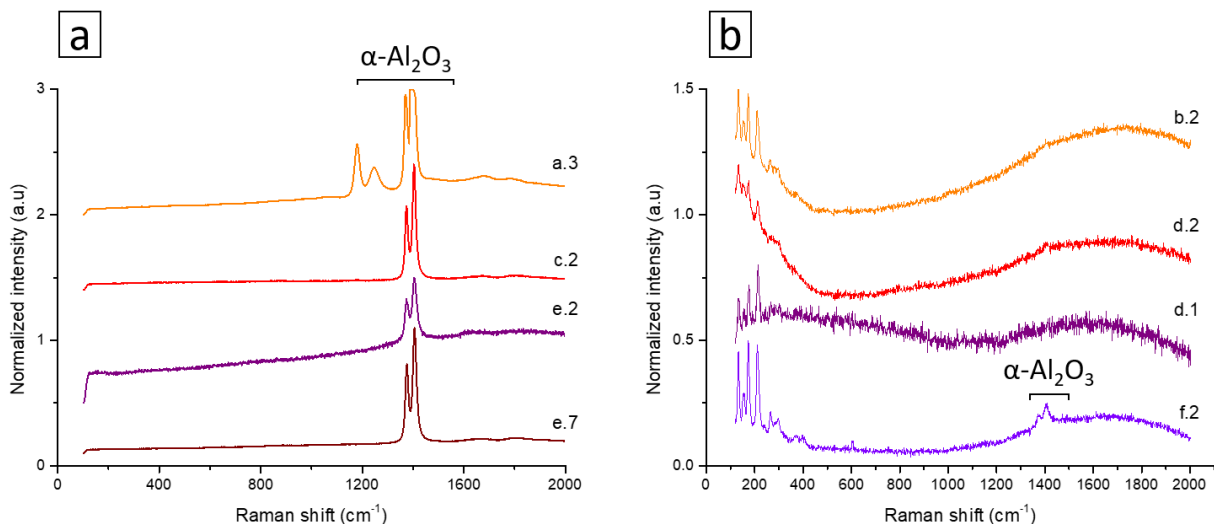


Figure IV-8: Raman spectra on the cross-sections of samples pre-oxidized for 30 min, 1 and 1.5 h made after the heat treatments 1080°C/2 h (a) and 700°C/24 h (b).

- **Heat treatment of 1080°C/2h**

For the heat treatment 1080°C/2 h applied on a Ni sample pre-oxidized for 30 min, the coating presents a non-homogeneous structure because the areas made of “diffusion islands” alternate with more homogeneous zones. The diffusion islands are composed of a NiAl (Figure IV-7.a label 1) and Ni₃Al core (Figure IV-7.a label 1) surrounded by aluminum oxide (Figure IV-7.a label 3). The more homogeneous area is made up of a first layer of NiAl, embedding alumina particles that surmounts a thick layer of aluminum oxide, nickel and NiO. It can be noted that only a few discontinuous areas of NiO remain (Figure IV-7.a label 5), i.e. most of the NiO has been consumed.

With 1 h of pre-oxidation, the diffusion islands can no longer be observed and the coating exhibits a more homogeneous aspect. Like with the 30 min of pre-oxidation, the first layer consists of an intermetallic compound (Figure IV-7.c label 1) that surmounts an alumina layer (Figure IV-7.c label 2) whose thickness is similar to the previous one. Finally, Ni resulting from NiO reduction (Figure IV-7.c label 3) and the remaining NiO can be observed closer to the substrate (Figure IV-7.c label 4).

For a pre-oxidation time of 1.5 h, the coating shows a very different structure, except for the first layer (Figure IV-7.e label 1) (NiAl embedding alumina particles). Below, a composite structure comprising Al₂O₃ and NiAl is found whose thickness is uneven and delimited by a dense layer of alumina (Figure IV-7.e label 2). Underneath, a Ni layer (Figure IV-7.e label 3) with NiO islands (Figure IV-7.e label 4) appears over the Ni substrate (Figure IV-7.e label 6) containing aluminized areas (Figure IV-7.e label 5) and alumina particles (Figure IV-7.e label 7).

- **Heat treatment of 700°C/24h**

For the heat treatment 700°C/24 h, the coatings appear rather similar to the one shown in Figure IV-5.d (section C.2) irrespective of the pre-oxidation time. Four different layers can again be observed. The top layer made of the intermetallic compound Al₃Ni (Figure IV-7.b,d,f label 1) surmounts an aluminum oxide cluster (Figure IV-7.b,d,f label 2), then a thin layer of Ni resulting

from the NiO reduction (Figure IV-7.b,d,f label 3) and finally, the remaining NiO (Figure IV-7.b,d,f label 4). Their thicknesses and compositions are however somewhat different (see Table IV-3). In addition, the coating contains no trapped particles when the pre-oxidation is conducted for just 30 min (Figure IV-7.b label 1).

Table IV-3: Summary table of the different compounds and thicknesses of the coating layers resulting from the heat treatments of the slurry after TGA treatment (1080°C/2 h and 700°C/24 h).

	1080°C/2 h				700°C/24 h			
Figure	7.a				7.b			
Layer	1	2	3	4	1	2	3	4
Compounds	NiAl	Al ₂ O ₃	Ni	NiO	Al ₃ Ni	Cluster of Al ₂ O ₃	Ni	NiO
Thickness (µm)	1.1±0.5	1.6±0.3	1±0.2	1.1±0.5	2.1±0.5	3±1.3	0.4±0.3	7.8±1.4
Figure	7.c				7.d			
Compounds	NiAl	Al ₂ O ₃	Ni	NiO	Al ₃ Ni	Cluster of Al ₂ O ₃	Ni	NiO
Thickness (µm)	1.7±0.7	2.6±0.3	1.7±0.3	9±0.8	5±1.5	2.4±1.2	0.4±0.3	9.5±1.8
Figure	7.e				7.f			
Compounds	NiAl	Cluster of Al ₂ O ₃	Ni	NiO	Al ₃ Ni	Cluster of Al ₂ O ₃	Ni	NiO
Thickness (µm)	3.4±1.3	9.6±3.4	2.3±3.5	2.8±1.8	3.7±1.9	3.9±1.4	0.3±0.2	10±2

I.D-Discussion

I.D.1-Influence of the heat treatment on the formation mechanisms of coatings

Concerning the heat treatment at 620°C, the observed phenomena are identical when the heat treatment is of 2 or 24 h and barely any aluminothermic reaction occurred. In contrast, significant differences appear when the temperature is raised to 1080°C (short times) or the times are extended (24 h) at intermediate temperature (700°C).

For the short times (2 h at 620 and at 700°C) till 1080°C/2 h, a sequence for the mechanisms of formation of the coatings is schematically depicted in Fig. 9. When the temperature reaches 517±15°C [1], an aluminothermic reaction between the Al microparticles and NiO starts at their interface (eq. 1). This solid/solid reaction of reduction results in the formation of a thin layer (2.9±1 µm) of metallic Ni after 2 h at 620°C (Fig. 9.a).



Then, at a temperature of about 660°C, Al melts and begins to dissolve the Ni product near the interface and provokes a competition reaction between the formation and the dissolution of the eutectic Al₃Ni [7]. During this step, no aluminothermic reaction takes place [1,14].

When the temperature increases and approaches 700°C, the formation of the Al₃Ni intermetallic is assumed to be sufficiently fast (eq. 2) to overcome its dissolution (3 µm after 2 h (Fig. 9.b)).



At higher temperature (1080°C), the Ni content locally increases and causes the transformation of Al₃Ni into solid Al₃Ni₂ (eq. 3) and then into NiAl (eq. 4) (Figure IV-9.c). The alumina formed during this step gets stuck at the grain boundaries of the NiO, depicting the pattern of nickel oxide shown in Figure IV-5.e and 5.f.



One shall note that these reactions are assumed to be fostered by the local temperature increase related to the high exothermicity involved in the dissolution of Ni in molten Al [7,8]. Therefore, the alumina formed by aluminothermic reaction (eq. 5) rapidly segregates at the interface between the intermetallic and the NiO, further reducing matter exchange, which stops the aluminothermic reaction (Figure IV-9.d). The combined thickening of alumina and the increased Ni content of the intermetallic slow down the solid-state diffusion and the overall activity of the system [18,22-23].

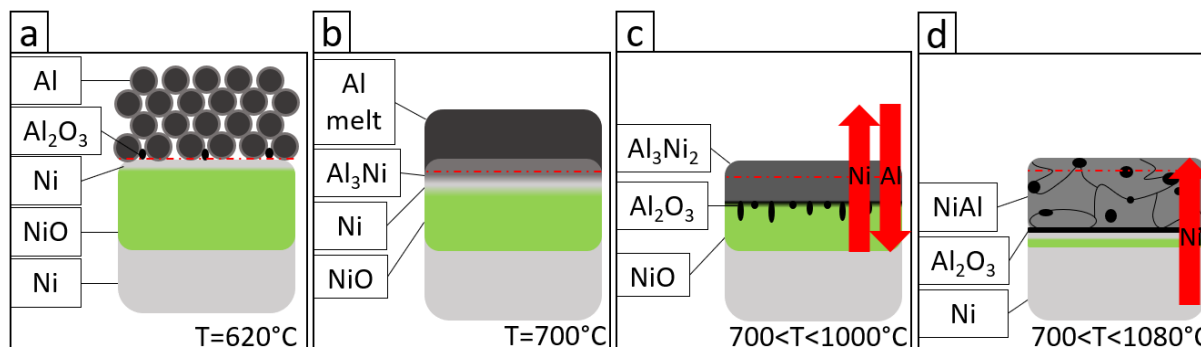


Figure IV-9: Schematic drawing of the aluminothermic reduction and reaction between a pre-oxidized Ni substrate and Al particles heated by stages till 1080°C.

In contrast, the evolution of the coating is quite significant at 700°C/24 h (Figure IV-10.a). Initially, the solid/solid aluminothermic reactions followed by melting of Al and the formation/dissolution of the eutectic Al_3Ni occur (Figure IV-10.b). However, two different microstructures of the coatings have been observed.

A first microstructure (Figure IV-10.c) results from the aluminothermic reaction between molten Al and NiO (eq. 5). This reaction brings about the formation of Al_2O_3 that segregates at the Al/NiO interface. While compact, the alumina layer is relatively discontinuous and therefore restricts the diffusion phenomena between the species without blocking them fully. As a result, the thickness of alumina increases till a threshold value ($\sim 5 \mu\text{m}$) over which interdiffusion is arrested and the remaining NiO cannot be reduced.

In the second coating microstructure (Figure IV-10.d), the initial development is assumed to be quite similar. However, the Al_2O_3 grains issued from the aluminothermic reactions form clusters that do not slow down sufficiently direct contact of molten Al with the newly formed Al_3Ni . This exothermic reaction brings about the dissolution of the intermetallic component and the Al_2O_3 clusters to float over the melt. The subsequent aluminothermic reaction will keep on producing the Al_2O_3 clusters dispersed in the intermetallic layer. The end of the reactions can occur by either an insufficient amount of Al that would stop the aluminothermic reaction, but this does not seem to be the case, or by the increased amount of Al_2O_3 in the coating, which appears in line with the experimental observations because Al_2O_3 both blocks interdiffusion of the species and lowers the local temperature given the fact that Al_2O_3 is an inert heat absorber [23].

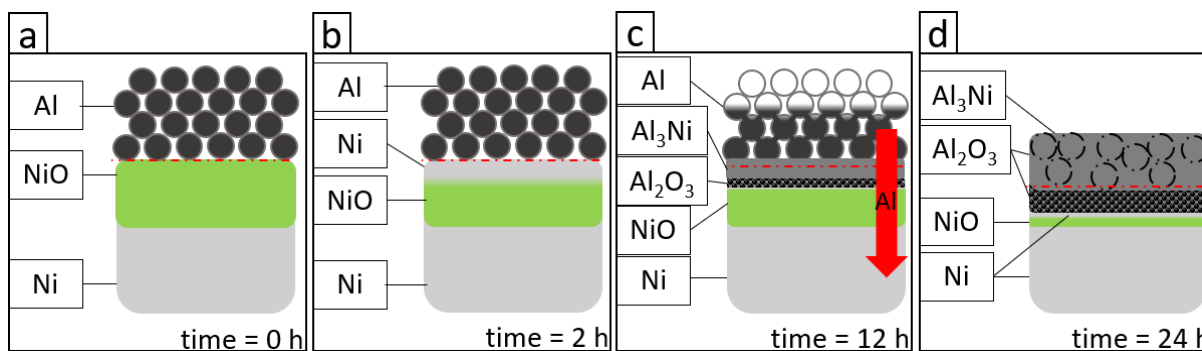


Figure IV-10: Schematic drawing of the aluminothermic reduction and reactions between a preoxidized Ni substrate and Al particles heated at 700°C during 24 h

I.D.2-Influence of the pre-oxidation time

• 700°C/24 h

The coating microstructures obtained after 24 h at 700°C on the substrate pre-oxidized for different times do not differ markedly. In particular, the thin NiO scale formed after just 30 min of pre-oxidation remains almost identical (Figure IV-11). In contrast, a greater permeability of Al through the NiO layer to form Al₃Ni is obtained with longer pre-oxidation times (Figure IV-11.a). This can be interpreted on the basis of the vacancy concentration in the oxide. Indeed, NiO is a p-type semiconductor, which implies that thickening of the oxide takes place by outward cation diffusion hence leading to a porous scale (Figure IV-12.a). In addition, different studies reported that the NiO oxide scale develop a continuous network of pores and cracks that reach the substrate [21,24-29] due to many different reasons including the dissociation of the oxide along the defects (grain boundaries, porosity, etc.) [30-33], cracking induced by the internal stresses [24, 34-37] and opening of the microcracks related to different diffusion rates within the oxide scale (Figure IV-12.b) [37]. In this study, we hypothesize that the molten Al and Al₃Ni can pass through these channels by capillarity. This is supported by the fact that the 1.5 h pre-oxidized nickel does not form homogeneous clusters of Al₂O₃ after annealing the coatings till 1080°C/2 h and 700°C/24 h (Figure IV-12.c). In contrast, the Al₂O₃ seems to segregate at the channels and grain boundaries of NiO (Figure IV-12.c). Furthermore, the Al-rich flux does not reach the Ni/NiO interface because (i) the defects in the oxide are too discontinuous to allow a regular flow of Al and/or diffusion of Ni to form the Al₃Ni, (ii) the Al activity lowers significantly, hence limiting the aluminothermic reaction and the interdiffusion of the species and (iii) the Al₂O₃ layer grows over the critical threshold and blocks the direct contact of Al with Ni. Very likely, a combination of the three phenomena occurs but (iii) appears more plausible and is coherent with the significant amounts of Al₂O₃ shown in the coatings and with the fact that Al particles get trapped by outward diffusion of Ni (Figure IV-12.d).

• 1080°C/2 h

As opposed to 700°C/24 h, the pre-oxidation time exerts a great influence on the aluminothermic reaction and on the aluminizing of the nickel substrate. Indeed, for the samples pre-oxidized 30 min and 1 h, the Al₂O₃ resulting from the aluminothermic reaction blocks the reaction between Al and Ni. As a result, the reaction is stopped and the substrate cannot be aluminized. For longer pre-oxidation times (1.5 h), the Al₂O₃ mimics the shape of the former NiO grains. This suggests that molten Al and/or Al₃Ni permeates through the defects of NiO and that reduction of half of the NiO thickness has occurred (Figure IV-11.b).

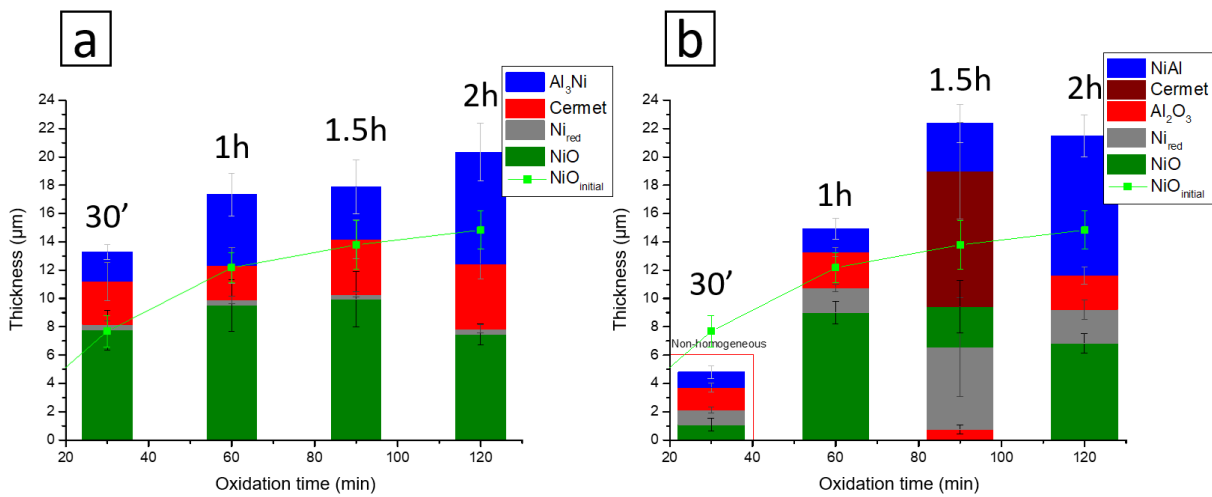


Figure IV-11: Histogram of the thicknesses of the different formed layers for a heat treatment 700°C/24 h (a) and 1080°C/2 h (b) applied after different Ni substrate pre-oxidation times.

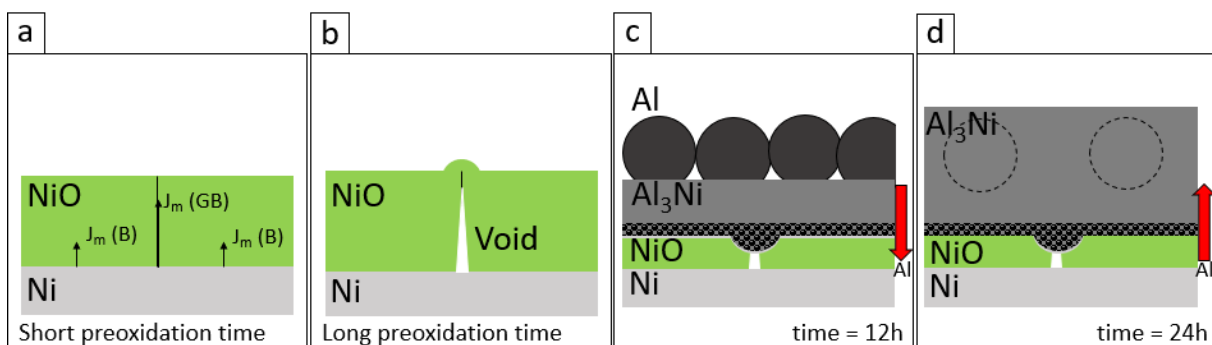


Figure IV-12: Schematic drawing of the aluminothermic reduction and reactions between pre-oxidized Ni substrate and Al particles heated at 700°C during 24 h, emphasizing on the role of the NiO grains boundaries.

1.E-Conclusions

The formation of potential self-regenerating coatings with Al-rich Ni_xAl_y phases and Al_2O_3 dispersion has been investigated using aluminothermic reactions on pre-oxidized nickel substrate. It has been found that one key parameter to achieve even coatings is the duration of the preoxidation of the substrate. The short pre-oxidation times (< 1 h) grow a “ridge-like” morphology of NiO that impedes the homogeneous aluminization of the substrate. The longer pre-oxidation times ($1 < t < 2$ h) leads to the growth of compact grains that allows the aluminothermic reaction to occur, hence to obtain even aluminized layers. It is believed that the increase in the permeability of NiO to Al is due to the many defects present in the oxide layer caused by the major diffusion of Ni^{2+} cations to the oxide surface.

One of the promising coatings was sintered by pre-oxidizing the Ni substrate for 2 h followed by a slurry aluminizing at $700^\circ C$ for 24 h. The coating consists of a first layer of Al_3Ni and alumina microspheres and a second layer with a composite microstructure between the alumina and the intermetallic compound. However, an unreacted NiO layer remained over the substrate even after 24 h of aluminizing. It thus appears that the control of the thickness of the NiO oxide needed for the reduction could be achieved by electroplating nickel layers onto the substrates to be coated, which shall be investigated. Similarly, the interdiffusion behavior should be studied to assess the regenerating effect of the coatings $Al_3Ni + Al_2O_3$.

References

[1]: R. Troncy, G. Bonnet, F. Pedraza, Microstructural characterization of NiAl–Al₂O₃ composite materials obtained by in situ aluminothermic reduction of NiO for potential coating applications, *Materials Chemistry and Physics* 251 (2020) 123-124.

<https://doi.org/10.1016/j.matchemphys.2020.123124>

[2]: G.W. Goward, Current research on the surface protection of superalloys for gas turbine engines, *JOM* 22 (1970) 31-39.

<https://10.1007/BF03355665>

[3]: J. Stringer, High-temperature corrosion of superalloys, *Material Science and Technology* 3(7) (1987) 482-493.

<https://doi.org/10.1080/02670836.1987.11782259>

[4]: B.G. Mc Mordie, Oxidation resistance of slurry aluminides on high temperature titanium alloys, *Surface and Coating Technology* 49 (1991) 18-23.

[https://doi.org/10.1016/0257-8972\(91\)90025-R](https://doi.org/10.1016/0257-8972(91)90025-R)

[5]: B. Rannou, B. Bouchaud, J. Balmain, G. Bonnet, F. Pedraza, Comparative isothermal oxidation behavior of new aluminide coatings from slurries coating Al particles and conventional out-of-pack aluminide coatings, *Oxidation of Metals* 81 (2014) 139-149.

<https://doi.org/10.1007/s11085-013-9427-6>

[6]: F. Pedraza, M. Mollard, B. Rannou, J. Balmain, B. Bouchaud, G. Bonnet, Potential thermal barrier coating systems from Al microparticles. Mechanisms of coating formation on pure nickel, *Materials Chemistry and Physics* 134 (2012) 700–705.

<https://doi.org/10.1016/j.matchemphys.2012.03.053>

[7]: M.C. Galetz, X. Montero, M. Mollard, M. Günthner, F. Pedraza, M. Schütze, The role of combustion synthesis in the formation of slurry aluminization, *Intermetallics* 44 (2014) 8–17.

<https://doi.org/10.1016/j.intermet.2013.08.002>

[8]: A. Biswas, S.K. Roy, K.R. Gurumurthy, N. Prabhu, S. Banerjee, A study of self-propagating high-temperature synthesis of NiAl in thermal explosion mode, *Acta Materialia* 50 (2002) 757-773.

[https://doi.org/10.1016/S1359-6454\(01\)00387-1](https://doi.org/10.1016/S1359-6454(01)00387-1)

[9]: E. Perez, T. Patterson, Y. Sohn, Interdiffusion analysis for NiAl versus superalloys diffusion couples, *Journal Phase Equilibria and Diffusion*, 27(6) (2006) 659-664.

<https://doi.org/10.1007/bf02736569>

[10]: J. Müller, M. Schierling, E. Zimmermann, D. Neuschütz, Chemical vapor deposition of smooth α -Al₂O₃ films on nickel base superalloys as diffusion barriers, *Surface and Coatings Technology* 120-121 (1999) 16-21.

[https://doi.org/10.1016/S0257-8972\(99\)00333-3](https://doi.org/10.1016/S0257-8972(99)00333-3)

[11]: C. Guo, W. Wang, Y. Cheng, S. Zhu, F. Wang, Yttria partially stabilized zirconia as diffusion barrier between NiCrAlY and Ni-base single crystal René N5 superalloy, *Corrosion Science* 94 (2015) 122-128.

<https://doi.org/10.1016/j.corsci.2015.01.048>

[12]: B. Bouchaud, B. Rannou, F. Pedraza, Slurry aluminizing mechanisms of Ni-based superalloys incorporating an electrosynthesized ceria diffusion barrier, *Materials Chemistry and Physics* 143 (2013) 416-424.

<https://doi.org/10.1016/j.matchemphys.2013.09.022>

[13]: H. Liu, M.M. Xu, S. Li, Z.B. Bao, S.L. Zhu, F.H. Wang, Improving cyclic oxidation resistance of Ni₃Al-based single crystal superalloy with low-diffusion platinum-modified aluminide coating, *Journal of Materials Science & Technology* 54 (2020) 132-143.

<https://doi.org/10.1016/j.jmst.2020.05.007>

[14]: Y.F. Yang, P. Ren, Z.B. Bao, S.L. Zhu, F.H. Wang, W. Li, Microstructure and cyclic oxidation of a Hf-doped (Ni,Pt)Al coating for single-crystal superalloys, *Journal Materials of Science* 55 (2020) 11687-11700.

<https://doi.org/10.1007/s10853-020-04782-5>

[15]: V.G. Shmorgun, L.D. Iskhakova, A.I. Bogdanov, A.O. Taube, Phase composition of heat-resistance layered coatings of the Al-Cr-Ni system, *Metallurgist* 60 (9-10) (2017) 1113-1119.

<https://doi.org/10.1007/s11015-017-0414-z>

[16]: D. Padmavardhani, A. Gomer, R. Abbaschian, Synthesis and microstructural characterization of NiAl-Al₂O₃ functionally gradient composites, *Intermetallics* 6 (1998) 229-241.

[https://10.1016/S0966-9795\(97\)00076-9](https://10.1016/S0966-9795(97)00076-9)

[17]: C.S. Hwang, T.J. Liu, Microstructure and mechanical properties of NiAl/Al₂O₃ composites, *Journal of Materials research* 14(01) (1999) 75-82.

<https://doi.org/10.1557/JMR.1999.0013>

[18]: K. Woll, J. David Gibbins, K. Slusarski, A.H. Kinsey, T.P. Weihs, The utilization of metal/metal oxide core shell-powders to enhance the reactivity of diluted thermite mixtures, *Combustion and Flame* 167 (2016) 259-267.

<https://10.1016/j.combustflame.2016.02.006>

[19]: R. Peraldi, D. Monceau, B. Pieraggi, Correlations between growth kinetics and microstructure for scales formed by high-temperature oxidation of pure nickel, I. Morphologies and Microstructures, *Oxidation of Metals* 58 (2002) 249-273.

<https://10.1023/A:1020170320020>

[20]: R. Peraldi, D. Monceau, B. Pieraggi, Correlations between growth kinetics and microstructure for scales formed by high-temperature oxidation of pure nickel, II. Growth Kinetics, *Oxid. Metals* 58 (2002) 275-295.

<https://10.1023/A:1020102604090>

[21]: R. Haugrud, On the high-temperature oxidation of nickel, *Corrosion Science* 45 (2003) 211-235.

[https://doi.org/10.1016/S0010-938X\(02\)00085-9](https://doi.org/10.1016/S0010-938X(02)00085-9)

[22]: D. Vrel, P. Langlois, E.M. Heian, N. Karnatak, S. Dubois, M.F. Beaufort, Reaction kinetics and phase segregation in the $3\text{NiO} + 2\text{Al} \rightarrow 3\text{Ni} + \text{Al}_2\text{O}_3$ Thermite system, *International Journal of High-Temperature Synthesis* 12 (2004) 261-270.

[23]: D. Vrel, A. Hendaoui, P. Langlois, S. Dubois, V. Gauthier, B. Cochevin, SHS reactions in the NiO-Al system: influence of stoichiometry, *International Journal of High-Temperature Synthesis* 16 (2007) 62-69.

<https://10.3103/S1061386207020021>

[24]: A. Atkinson, R.I. Taylor, P.D. Goode, Transport processes in the oxidation of Ni studied using tracers in growing NiO scales, *Oxidation of Metals* 13 (1979) 519-543.

<https://doi.org/10.1007/BF00812776>

[25]: N.N. Khoi, W.W. Smeltzer, J.D. Embury, Growth and structure of nickel oxide on nickel crystal faces, *Journal of The Electrochemical Society* 122 (1975) 11.

[26]: A. Atkinson, F.C.W. Pummery, C. Monty, Diffusion of ^{18}O tracer in NiO grain boundaries, *Transport in Nonstoichiometric Compounds* 129, 359–370, Plenum Press, New York 1985.

https://doi.org/10.1007/978-1-4613-2519-2_27

[27]: R.A. Rapp, The high temperature oxidation of metals forming cation-diffusing scales, *Metallurgical Transactions A*, 15 (1984) 765-782.

<https://doi.org/10.1007/BF02644552>

[28]: C.K. Kim, L.W. Hobbs, Microstructural evidence for short-circuit oxygen diffusion paths in the oxidation of a dilute Ni-Cr alloy, *Oxidation of Metals* 45 (1996) 247-265.

<https://doi.org/10.1007/BF01046984>

[29]: S.K. Verma, G.M. Raynaud, R.A. Rapp, *Chemical metallurgy: a tribute to Carl Wagner*, The Metallurgical Society of AIME 419–40, New-York 1981.

[30]: A. Brückman, R. Emmerich, S. Mrowec, Investigation of the high-temperature oxidation Fe-Cr alloys by means of the isotope ^{18}O , *Oxidation of Metals* 5 (1972) 137-147.

<https://doi.org/10.1007/BF00610841>

[31]: A. Brückman, The mechanism of transport of matter through the scales during oxidation of metals and alloys, *Corrosion Science* 7 (1967) 51-54.

[https://doi.org/10.1016/S0010-938X\(67\)80069-6](https://doi.org/10.1016/S0010-938X(67)80069-6)

[32]: S. Mrowec, On the mechanism of high-temperature oxidation of metals and alloys, *Corrosion Science* 7 (1967) 563-578.

[https://doi.org/10.1016/0010-938X\(67\)80033-7](https://doi.org/10.1016/0010-938X(67)80033-7)

[33]: G.J. Yurek, H. Schmaltzried, Deviation from local thermodynamic equilibrium during interdiffusion of CoO–MgO and CoO–NiO, *Berichte Der Bunsengesellschaft Für Physikalische Chemie*, 79(3) (1975) 255-262.

<https://doi.org/10.1002/bbpc.19750790304>

[34]: A. Atkinson, D.W. Smart, Transport of nickel and oxygen during the oxidation of nickel and dilute nickel/chromium alloy, *Journal of The Electrochemical Society* 135 (1988) 11.

<https://doi.org/10.1149/1.2095454>

[35]: J. Robertson, M.I. Manning, Criteria for formation of single layer, duplex, and breakaway scales on steels, *Materials Science and Technology* 4 (1988) 12.

<https://doi.org/10.1179/mst.1988.4.12.1064>

[36]: A.G. Evans, D. Rajdev, D.L. Douglass, The mechanical properties of nickel oxide and their relationship to the morphology of thick scales formed on nickel, *Oxidation of Metals* 4 (1972) 151-170.

<https://doi.org/10.1007/BF00613090>

[37]: P. Kofstad, On the formation of porosity and microchannels in growing scales, *Oxidation of Metals* 24 (1985) 265-276.

<https://doi.org/10.1007/BF00657061>

II-Synthesis of self-regenerating NiAl-Al₂O₃ composite coatings using Ni plating and aluminothermic reaction

In the previous part, it was demonstrated that the use of an aluminothermic reaction allows the synthesis of a self-regenerating coating. The most promising combination was obtained with a preoxidation treatment of 2 hours at 1100°C followed by an aluminizing treatment of 24 hours at 700°C. However, despite the aluminizing treatment, a thin layer of nickel oxide from the preoxidation treatment remained located between the coating and the substrate. It was also shown that the longer the preoxidation time, the greater the permeability of the nickel oxide layer by Al.

In this second part, the aim was to increase the permeability of the oxide layer to transform it entirely during the aluminizing step.

For this, a nickel layer was electroplated on a Ni sample. It was then preoxidized before aluminizing. This method presents two major advantages: the electrodeposit results in the unique formation of nickel oxide during the preoxidation step and therefore impedes the formation of any other -less reducible- oxide from the underlying alloy or superalloy substrate. Moreover, by adjusting the current density, it is possible to manage the porosity and grain size of the Ni electrodeposit [39-40], which in turns should increase the porosity of nickel oxide, hence its permeability to aluminum.

The challenge is here to achieve a nickel deposit that is porous enough to allow its full oxidation and the subsequent permeation of Al resulting in the formation of the expected composite structure (micro-reservoirs of Al-rich intermetallic phase and alumina shells). The nickel electrodeposits were elaborated from a nickel sulfate solution (Watt's bath). The influence of the electroplating current density, of the thickness of the deposit and of the preoxidation time on the resulting aluminide coating have been investigated.

The Ni electrodeposits were carried out on Ni substrates polished by successive SiC papers down to P180 grade. A first layer of Ni (= Ni *flash*) of 5 ± 1 μm was previously deposited at 50 mA/cm² to increase the adhesion of the Ni electrodeposit. Indeed, stresses can be generated during electrodeposition. These stresses appear greater for high current densities and can cause decohesion at the interface between the coating and the substrate. The application of a first flash electrodeposited layer is reported to reduce these interfacial constraints [40-42]. The electrodeposits were then carried out with higher current densities of 90, 270 and 530 mA/cm², i.e. an applied intensity of 0.1, 0.3 and 0.6 A.

The targeted thickness of electrodeposits was of 40 ± 10 μm for current densities of 90, 270 and 530 mA/cm². Moreover, thinner (20 μm) electrodeposits synthesized with a current density of 530 mA/cm² have also been studied. Since the nickel electrodeposits made from nickel sulfate induce strong internal stresses [43], annealing of 4 hours at 150°C under argon was conducted after the electrodepositions [44] to reduce such stresses and the risk of spallation.

II.A-Results

II.A.1-Microstructure of Ni plating

The SEM cross-section micrographs of the electrodeposited Ni layer are shown in Figure IV-13. The mean thicknesses of Ni deposits retrieved from image analysis are summarized in Table IV-4.

All electrodeposits exhibit a columnar grain morphology irrespective the applied current density, which is in line with the results of literature [38,40,45-47]. Columnar structures are indeed frequently observed in the case of electrodeposited films. According to Thompson et al., the formed grains tend to grow perpendicularly to the substrate when the grain growth takes place without coalescence [47]. In addition, several studies report that the grain size and the microstructure of deposits are directly affected by the adsorption of species that inhibit film growth.

Winand et al. [38] developed a diagram (Figure IV-15) showing the different microstructures as a function of two parameters [48-51]. The first parameters are linked to the crystallization overvoltage. However, this measurement is difficult to obtain, therefore Winand et al. chose to express J/J_{lim} ou $J/C_{Me^{z+}}$ (= the apparent cathodic current density to the bulk concentration in metallic ions to be discharged). The second parameter is related to the inhibition intensity and depends on the adsorption affinity at the surface of the samples. Winand et al. have shown that nickel electrodeposits are highly sensitive to these inhibitory phenomena [38]. In the case of the Watt's bath, the inhibitors are electrolyte anions such as Cl^- and SO_4^{2-} (Figure IV-15).

In the considered range of current density, it seems that the grain growth can be described by the model proposed by Fischer, based upon a basis-orientated reproduction type (BR) (Figure IV-15) [38]. This type of growth has been observed for moderate current densities and moderate degrees of inhibition. The growth begins with a 2D nucleation mechanism with the formation of polyatomic species leading to the formation of BR type deposits (Figure IV-15). In addition, for long electroplating times, the crystal size can become large enough to trap electrolyte in the deposit, which then inhibits growth.

Furthermore, one can observe a decohesion between the first electrodeposit made at 50 mA/cm² and the substrate (Figure IV-14). We suppose that this decohesion takes place during the shrinkage of the polymeric resin due to its change in volume, or during polishing. After polishing, fragments of nickel were embedded in the gap (Figure IV-13.a). The decohesion between the plate and the substrate nevertheless indicates a weak interface between the plate and the substrate and not between the flash and the electrodeposit (Figure IV-13).

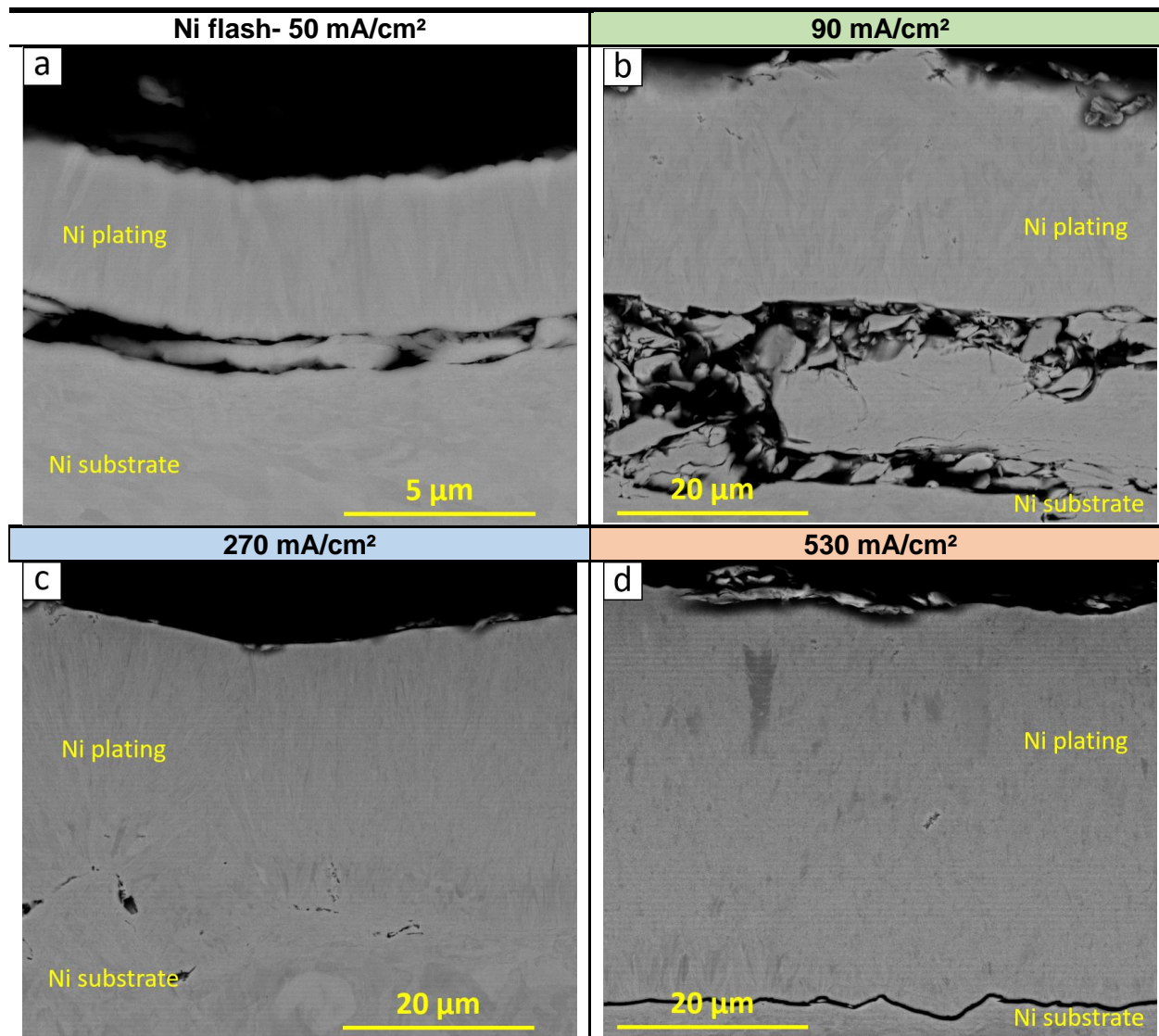


Figure IV-13: SEM (BSE mode) cross-section images on the Ni plates for (a) the Ni flash 50 mA/cm² and the Ni electrodeposits at (b) 90 (c) 270 and (d) 530 mA/cm².

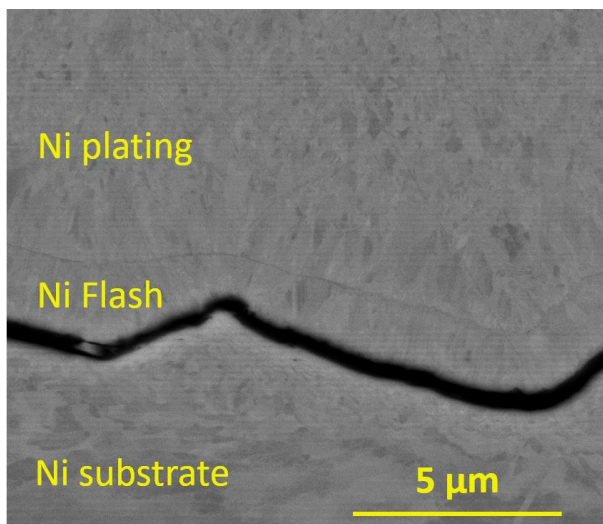


Figure IV-14: SEM (BSE mode) cross-section images zoom on the Ni plating sample of 530 mA/cm².

Table IV-4: Summary table of the thicknesses of Ni plating for different current densities and times.

Current density (mA/cm ²)	50	90	270	530 _{40μm}	530 _{20μm}
Time (min)	10	60	23	10	5'30
Ni thickness (μm)	5±1	39±2	45±2	42±3	22±2

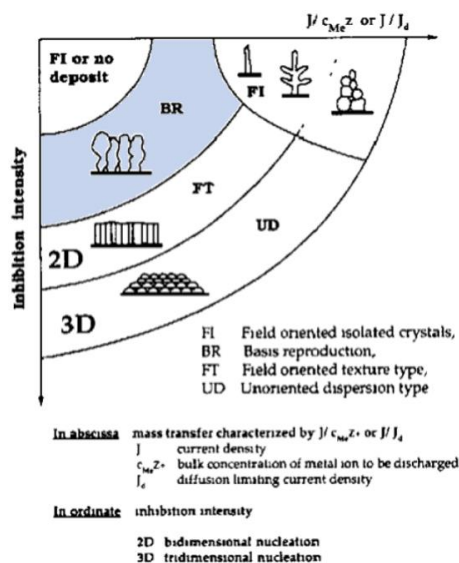


Figure IV-15: Simplified diagram showing different possible types of polycrystalline electrodeposits as function of $J/C_{Me^{z+}}$ and inhibition intensity [38].

II.A.2-Texture

Figure IV-16 shows the diffractograms obtained from the ~40 μm thick electrodeposits and Table IV-5 gathers their normalized intensity. First, the calculated thickness probed by the X beam using is 10.1 μm for the plane (111), 11.7 μm for the plane (200) and 16.5 μm for the plane (220), well below the total thickness (~40 μm) of the electrodeposit (detailed method in annex 1). It can be observed that the three main peaks of the substrate (111), (200) and (220) are also observed in all the electrodeposits irrespective the applied current density. They appear respectively at 44.5, 51.8 and 76.4°. However, the direct comparison of the relative intensity with the ones of the pure polycrystalline Ni substrate (JCPDS #01-087-0712) indicates that the <111> orientation becomes preponderant with respect the <200> and <220>. This clearly suggests some texturing of the electrodeposits in line with the literature [52-53] and with the columnar microstructure observed under the SEM (Figure IV.13). After annealing, the XRD peaks observed are at ~44.5° and corresponds to the crystallographic plane (111), the second peak at 51.8° corresponds to the plane (200) and the third peak at 76.4° corresponds to the plane (220). In a polycrystalline material without preferential grain orientation (as in the substrate Figure IV-16.a) the relative intensity of the peaks corresponds respectively to 1, 0.42 and 0.21 for the planes (111), (200) and (220) (JCPDS #01-087-0712).

Concerning the electrodeposits, texturing of the grains at (111) can be observed for the three current densities. These values are in line with those of literature [52-53]. Additionally, textured coatings show a mixture of fine and coarse grains. The coarse grains are oriented and have few defects and the fine grains are randomly oriented and appear to have a high concentration of defects [39,53-54].

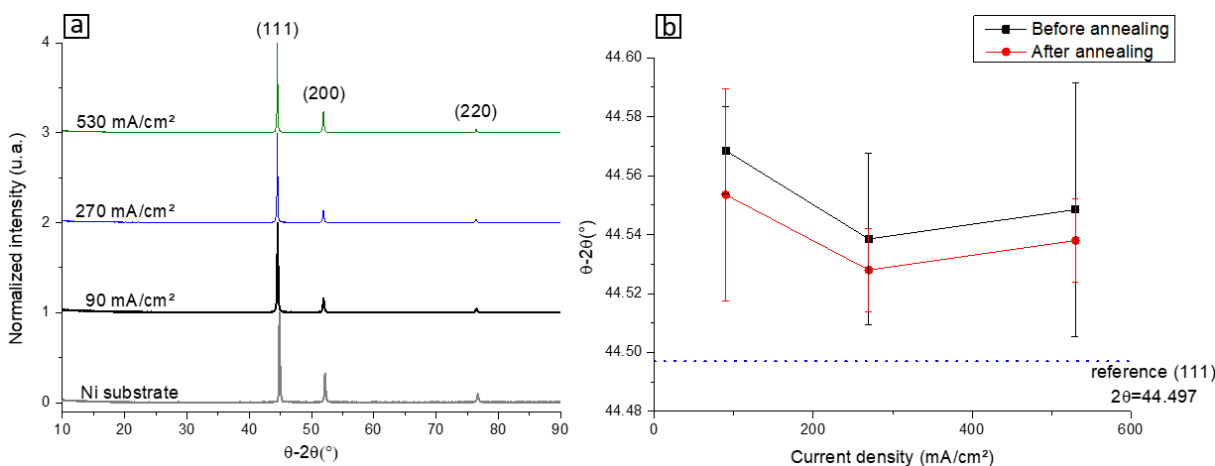


Figure IV-16: XRD patterns of the surface of the samples (a) before and (b) after annealing.

Nickel electrodeposits made from nickel sulfate bath are known to sustain significant internal stresses [40-42,55] which can induce cracking or interfacial detachment. To avoid these phenomena during oxidation, annealing treatments are carried out at 150°C for 4 hours. Following these annealing treatments, a slight deviation of the peaks positions can be observed (Figure IV-16.b). This deviation sees a decrease in the 2θ value of the peaks and a move towards the nickel reference values. This could suggest a widening of the mesh and a reduction in the compressive stresses [56]. In addition, the thickness calculated from the X beam is 10.1 μm for the plane (111),

11.7 μm for the plane (200) and 16.5 μm for the plane (220), which means that only the Ni electrodeposit is probed (Figure V-17).

Table IV-5: Summary table of the normalized intensity and texturing of Ni plating for different current densities.

Reference			Current density (mA/cm ²)	Ni plating			After annealing		
<111>	<200>	<220>		<111>	<200>	<220>	<111>	<200>	<220>
1	0.42	0.1	90	1	0.16	0.04	1	0.16	0.04
			270	1	0.14	0.04	1	0.14	0.04
			530	1	0.24	0.04	1	0.26	0.04

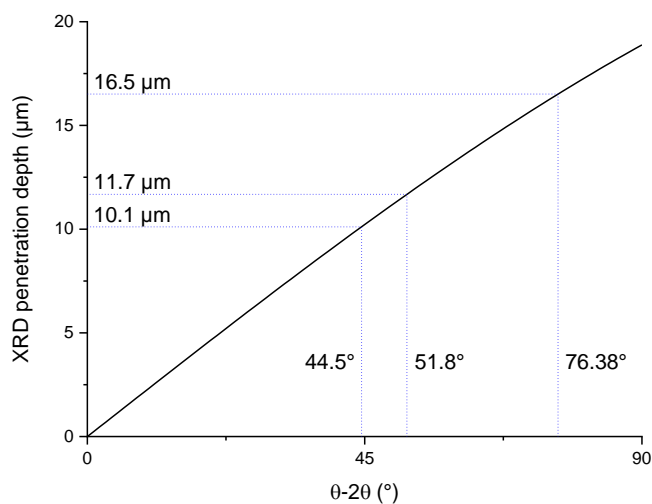


Figure IV-17: Nickel penetration depth for the $K_{\alpha 1}$ copper for symmetrical mounting

II.A.3-Preoxidation of Ni plates

The optical microscope and SEM cross-section micrographs of Ni-plated samples after 1h or 2h of preoxidation are shown in Figure IV-18 and IV-20 for optical images and Figure IV-19 and Figure IV-21 for SEM images. The mean thicknesses for remaining Ni plating and formed NiO extracted from image analysis are summarized in Table IV-6.

The microstructure of electrodeposits preoxidized for 1 and 2h at 1100°C are quite similar. Indeed, in both cases, a relatively thick layer of nickel oxide has formed on the surface. The average thickness of the oxide grown on the electrodeposits increase from $10 \pm 2 \mu\text{m}$ to $13 \pm 2 \mu\text{m}$ when extending the preoxidation time from 1 to 2 hours and are of about the same magnitude than for the oxide layers developed on raw ("reference") substrates (Table IV-6). In addition, it appears that the oxide layer consists of two or three grains of nickel oxide, with a columnar structure close to the surface, and of equiaxial grains close to the oxide/electrodeposit interface.

The microstructure of the electrodeposit also evolves, since the size of the nickel grains becomes larger and pores form across the thicknesses of the electrodeposit and at the interface with the substrate.

The microstructures of the Ni plating produced at 90 mA/cm^2 have similar structure between 1 and 2 hours of oxidation. In fact, pores have formed mainly at the electrodeposits/substrate interface (Figure IV-19.a and IV-21.a). In addition, depressions proven to be caused by bubbles during electroplating can be observed at the top of the samples. (Figure IV-18.a and 20.a)

The $40 \mu\text{m}$ Ni plating produced at 530 mA/cm^2 are also similar to those produced at 90 mA/cm^2 . The interface between the substrate and the electrodeposits consists of numerous pores (Figure IV-19.c and 21.c). These pores are larger and decohesion can be observed. Similar observations can also be made for $20 \mu\text{m}$ Ni plating (Figure IV-19.d and 21.d).

Finally, a particularity can be observed for the electrodeposits made at 270 mA/cm^2 . The pores formed during the heat treatment are no longer localized at the interface but are also present throughout the entire electrodeposit layer (Figure IV-18.b, 19.b, 20.b and 21.b). Two types of pores can be observed, pores of a few micrometers (grey/black spot on the SEM) and larger pores (about ten micrometers). In addition, some larger pores have their inner walls coated with nickel oxide (Figure IV-19.b and 21.b).

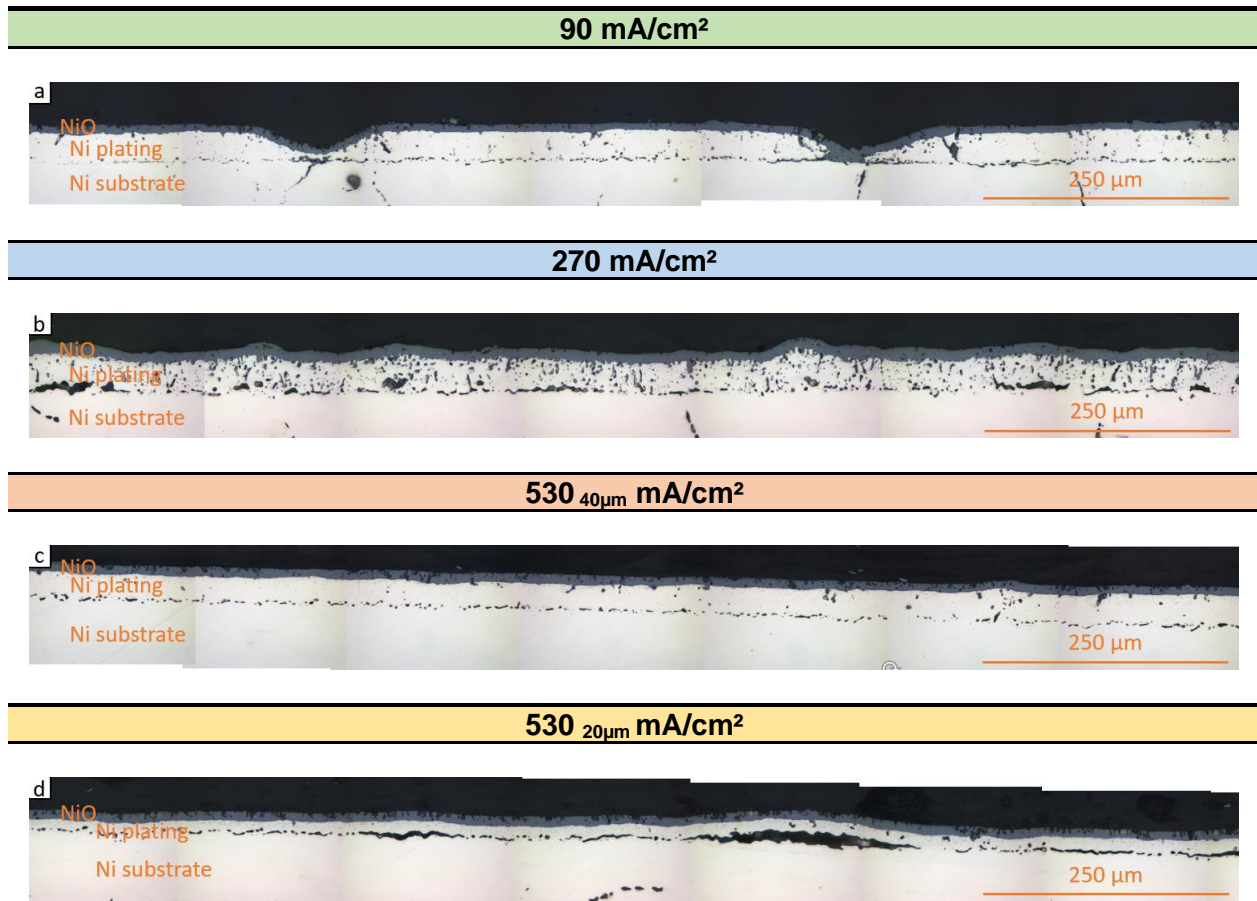


Figure V-18: Optical microscopy of cross-section images of Ni plating samples preoxidized at 1100°C under air for 1h.

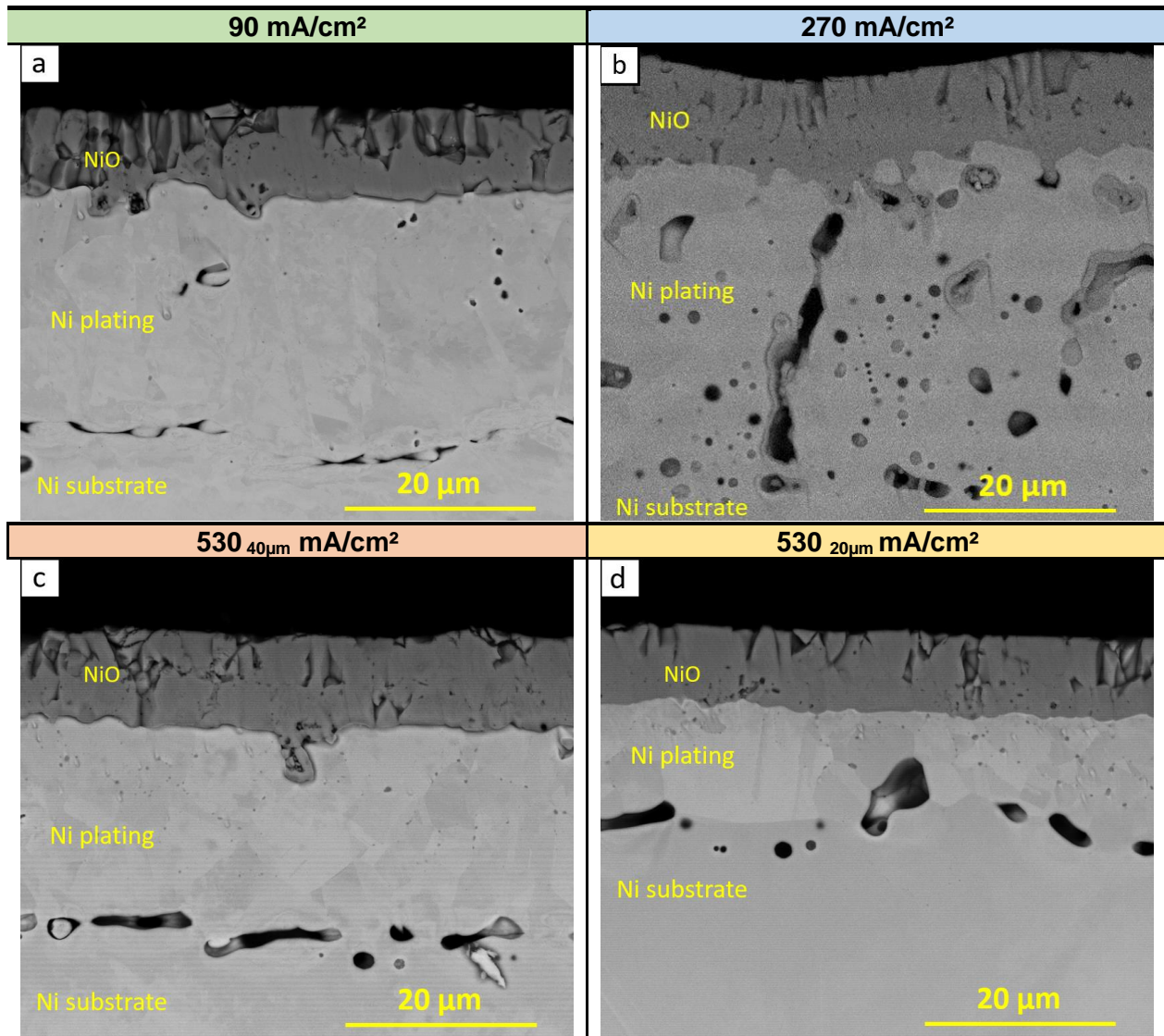


Figure IV-19: SEM (BSE mode) of cross-section images of Ni plating samples pre-oxidized at 1100 °C under air for 1 h.

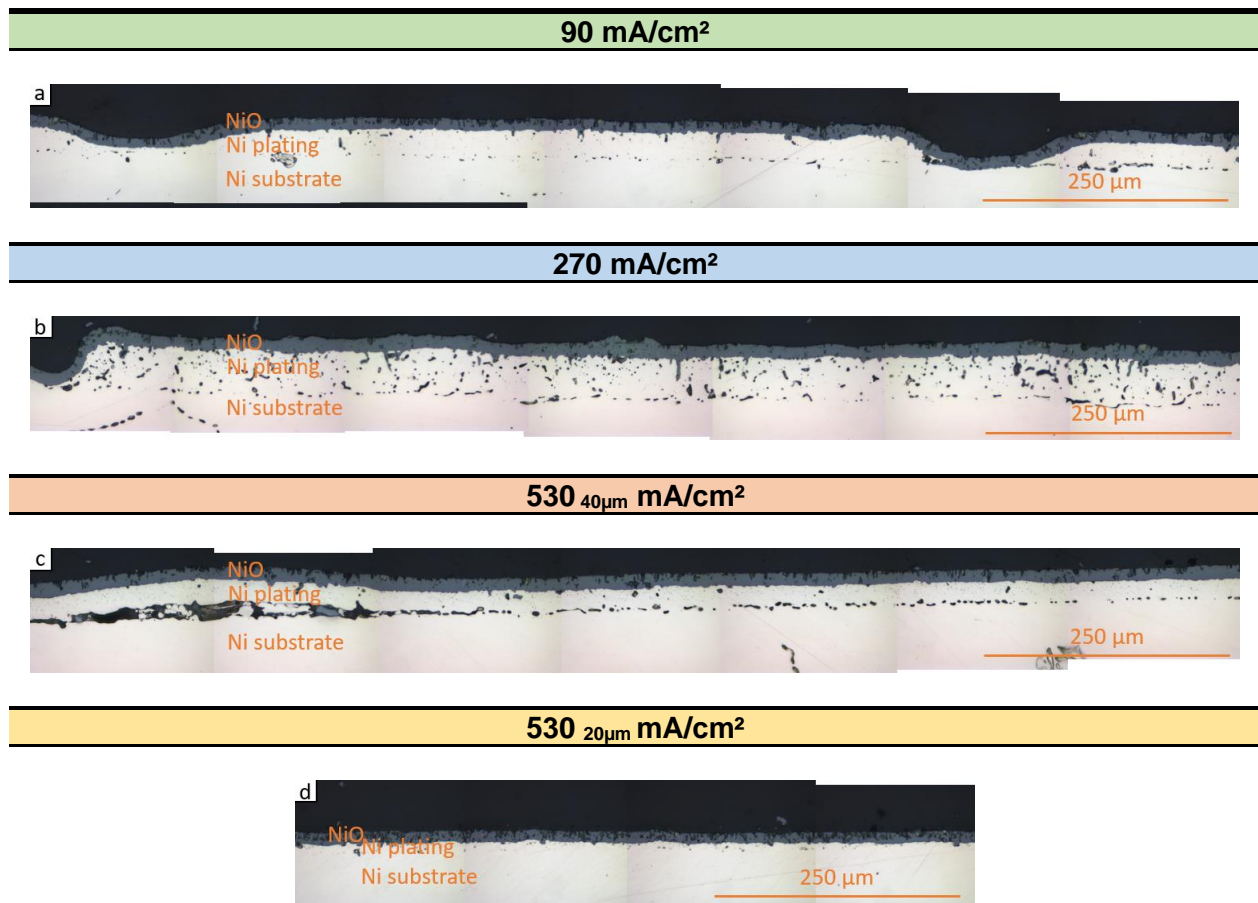


Figure V-20: Optical microscopy of cross-section images of Ni plating samples preoxidized at 1100°C under air for 2h.

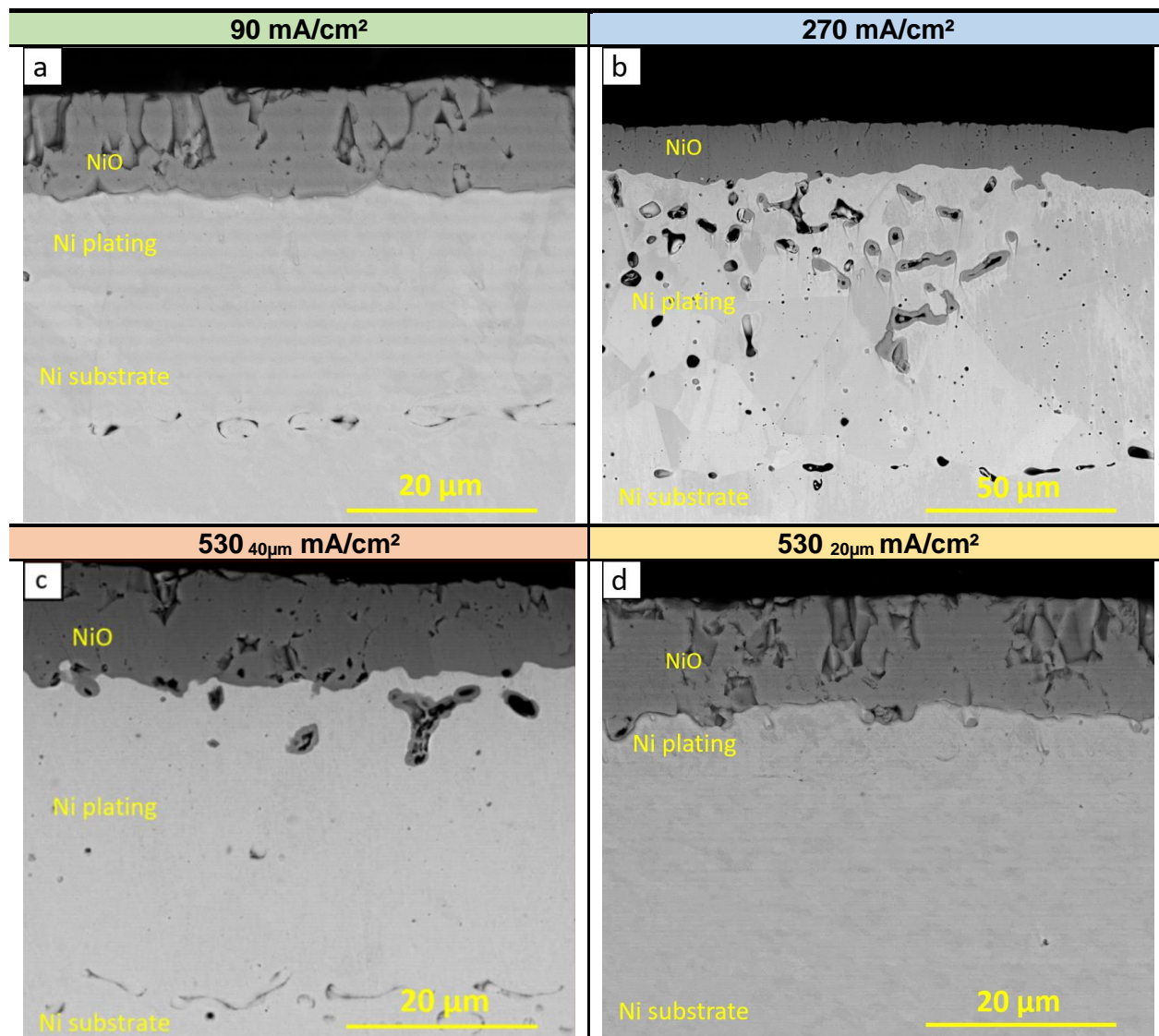


Figure IV-21: SEM (BSE mode) cross-section images of Ni plating samples pre-oxidized at 1100°C under air for 2 h.

Table IV-6: Summary table of the thicknesses of Ni plating and Ni oxide for different current densities and preoxidation times.

	Reference (Ni substrate)	Current density (mA/cm ²)	50	90	270	530 40µm	530 20µm
Ni plating	---	Ni thickness (µm)	5±1	39±2	45±2	42±3	22±2
Oxidation 1h	12±1	NiO thickness (µm)	---	10±1	10±1	11±2	9±1
	---	Ni thickness (µm)	---	28±2	33±4	24±1	10±4
Oxidation 2h	14±2	NiO thickness (µm)	---	11±1	14±2	12±1	14±1
	---	Ni thickness (µm)	---	25±2	49±2	20±2	8±1

II.A.4-Influence of the current density and preoxidation time on the aluminized layers

The microstructures of the preoxidized (1h or 2h) samples after reaction with Al at 700°C/24 h are shown in Figure IV-22. The compounds formed and the thicknesses of the different layers are summarized in Table IV-7.

- **Current density of 90 mA/cm²**

Two main areas can be observed in Figures IV-22.a & IV-22.b for respectively, 1 and 2h of preoxidation.

The first area on the left part of the images (Figure IV-22.a & 22.b) is similar to the ones obtained after aluminizing the preoxidized substrate (Chapter IV-1). Five main sublayers are displayed. The first at the top of the sample is the composite between the Al₃Ni intermetallic and the Al₂O₃ shells of the aluminum particles (label 1, Figure IV-22.a & 22.b). The second layer is composed of a cluster of Al₂O₃ and the intermetallic Al₃Ni (label 2, figure IV-22.a & 22.b). This alumina cluster layer is not continuous and the thickness is uneven. The third layer is very thin and consists of reduced Ni at the Al₃Ni/NiO or Al₂O₃/NiO interfaces. The fourth layer (label 3, figure IV-22.a & 22.b) is the residual nickel oxide layer. Finally, the fifth layer over the substrate is the nickel electrodeposit (label 5, Figure IV-22.a & 22.b) that was barely aluminized.

The second area can be observed on the right side of Figure IV-22.a and on the central part of Figure IV-19.b. These areas are made up of diffusion islands with a "volcano" appearance. In most cases, these islands are made up of 4 layers on the top and 5 layers on their side. Regarding the top, the first two layers are similar to those described on the left part, with the composite of Al₃Ni intermetallic and oxide shells of aluminum particles (label 1, Figure IV-22.a & 22.b), and the cluster layer of alumina (label 2, Figure IV-22.a & 22.b). The third layer is very irregular and consists of unreacted nickel oxide (label 3, Figure IV-22.a & 22.b). The nickel oxide residues are not systematically present on top of the diffusion islands. Whenever present, they form small clusters of a few microns with a core of nickel oxide and shells of reduced Ni. Finally, the fourth layer constitutes the majority of the diffusion island and is composed of an intermetallic NiAl (label 4, Figure IV-22.a & 22.b).

Aside the diffusion islands, five sublayers can again be observed. The top four follow the same sequence of the left area (the Al₃Ni layer, the layer of Al₂O₃ clusters, the thin layer of reduced nickel and the residual layer of nickel oxide). The sublayer closest to the substrate is now composed of the NiAl intermetallic compound according to the EDS analyses.

When comparing the left and the right areas after aluminizing the preoxidized Ni electroplates, it appears that the change in volume caused by the formation of the NiAl compound causes a deformation of the various layers present on the surface and results in the characteristic shape of "volcanoes". In addition, when the diffusion islands reach the substrate/electrodeposit interface, interfacial detachment occurs between the substrate and the nickel electrodeposit.

- **Current density of 270 mA/cm²**

The coatings obtained with a current density of 270 mA/cm² also exhibit two distinct zones: a first "homogeneous" zone where the aluminizing takes place at the surface and a second "diffusion island" zone where the aluminizing takes place mainly at the NiO/electrodeposit interface.

Regarding the homogeneous zone, from the surface to the bottom, one can observe a porous sublayer of Al_3Ni_2 intermetallic (label 1, figure IV-22.c & 22.d), a sublayer containing the alumina clusters (label 2, Figure IV-22.c & 22.d), a very thin layer of reduced Ni and finally the layer of residual NiO and the electrodeposit (label 3, Figure IV-22.c & 22.d).

Concerning the area with diffusion islands, the same observations can be made as on electrodeposits carried out at 90 mA/cm^2 except that Al_3Ni_2 forms instead of Al_3Ni .

With respect the 90 mA/cm^2 , it can also be noted that a greater proportion of diffusion islands and a greater thickness of the area affected by diffusion island are observed with approximately 36 and 46% of diffusion islands for, respectively, 1 and 2 h of preoxidation. In contrast, the extent of the diffusion islands barely reaches 22 and 25% in the 90 mA/cm^2 coatings.

- **Current density of $530_{40 \mu\text{m}} \text{ mA/cm}^2$**

As with the other electrodeposits, two aluminizing locations are observed: at the surface and under the NiO layer. With this current density, the coatings obtained are similar to those produced at 270 mA/cm^2 with a first layer made up of porous Al_3Ni_2 for a preoxidation time of 1h (label 1, figure IV-22.e) and of non-porous Al_3Ni with alumina shells for a preoxidation time of 2 h (label 1, figure IV-22.f). The second and third layer are respectively made up of the Al_2O_3 cluster and the NiO (label 2 & 3, figure IV-22.e & 22.f). Finally, the last layer consists of the intermetallic compound NiAl, obtained through the formation of the diffusion islands (label 4, figure IV-22.e & 22.f). Unlike the other aluminized electrodeposits, this coating is uniform over the entire surface of the samples.

In addition, it is important to note that the quantity of consumed NiO is the greatest for this aluminizing configuration (Table IV-7).

- **Current density of $530_{20 \mu\text{m}} \text{ mA/cm}^2$**

The last coating considered in this part was also carried out at 530 mA/cm^2 as above but with an average initial thickness of $20 \mu\text{m}$.

Aluminizing the samples preoxidized for 1h results in the coating with a microstructure similar to the ones previously observed for 270 and $530_{40 \mu\text{m}} \text{ mA/cm}^2$, with the first layer of Al_3Ni_2 (label 1, Figure IV-22.g), a layer of alumina cluster (label 2, Figure IV-22.g), a third thin and discontinuous layer of residual NiO (label 3, Figure IV-22.g) and a final sublayer of intermetallic compounds NiAl (label 4, Figure IV-22.g). The third and fourth layers are made of nickel oxide and nickel electrodeposits, respectively.

For the preoxidation time of 2h, the coating obtained resembles that obtained on the raw substrate for equivalent oxidation time (Figure IV-5.c), with a first layer of Al_3Ni intermetallic matrix and Al oxide shells (label 1, Figure IV-22.h). The central layer is composed of a cluster of oxides (label 2, Figure IV-22.h). The third and fourth layers are respectively composed of the residual NiO (label 3, Figure IV-22.h) and by the nickel electrodeposit (label 5, Figure IV-22.h).

Current density (mA/cm ²)	Preoxidation 1h + Aluminizing 700°C/24h	Spot	Preoxidation 2h + Aluminizing 700°C/24h		Al (at%)	Ni (at%)	
			Al (at%)	Ni (at%)			
90		1	74	26		72	28
		2	81	19		79	21
		3	7	93		21	79
		4	59	40		53	47
		5	13	87		17	86
270		1	65	35		60	40
		2	77	23		90	10
		3	14	86		15	85
		4	51	49		55	45
		5	10	90		7	93
530 _{40μm}		1	60	40		73	27
		2	78	22		82	18
		3	19	81		25	75
		4	59	41		56	44
		5	14	86		6	94

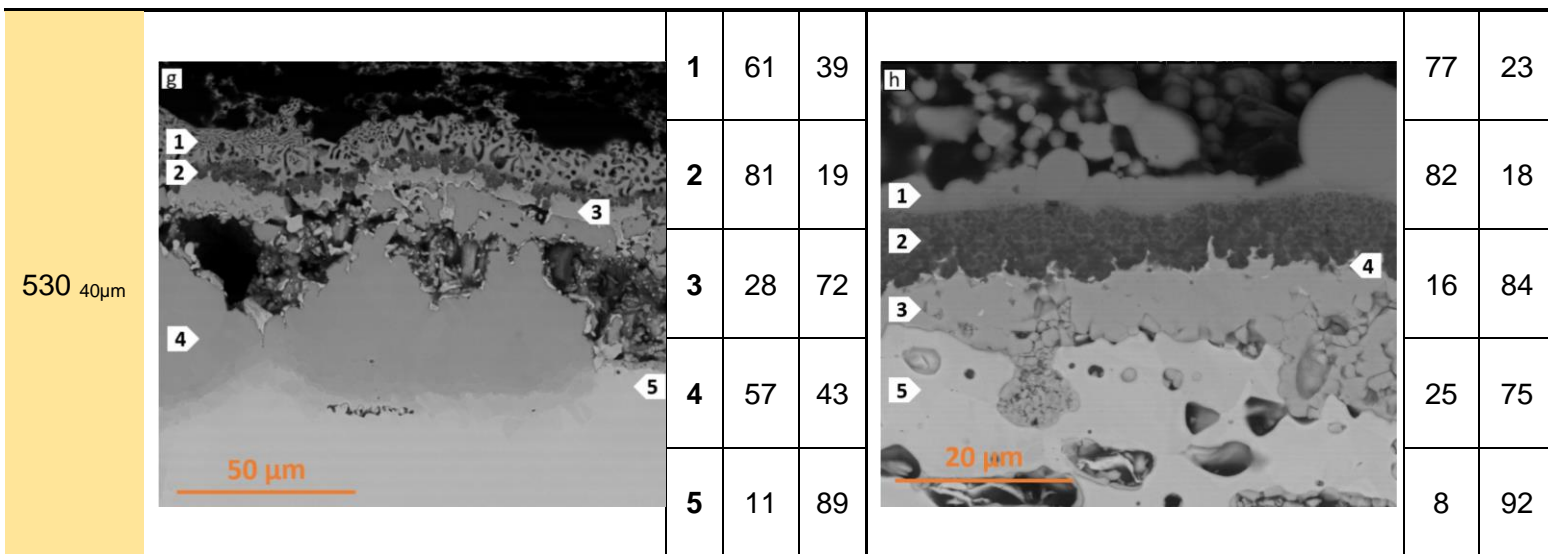


Figure IV-22: SEM (BSE mode) cross-sections of the samples pre-oxidized for 1h and 2h at 1100°C and subsequent slurry aluminizing at 700°C for 24h.

Table IV-7: Summary table of the different compounds and thicknesses of the different layers observed in the samples after the heat treatment (700°C for 24h).

		Oxidation 1h				Oxidation 2h			
90 mA/cm ²	Figure	19.a				19.b			
	Layer	1	2	3	4	1	2	3	4
	Compounds	Al ₃ Ni	Cluster of Al ₂ O ₃	NiO	NiAl	Al ₃ Ni	Cluster of Al ₂ O ₃	NiO	NiAl
	Thickness (μm)	5±2	4±3	7±4	4±7	2±2	3±2	6±2	5±9
270 mA/cm ²	Figure	19.c				19.d			
	Compounds	Al ₃ Ni ₂	Cluster of Al ₂ O ₃	NiO	NiAl	Al ₃ Ni ₂	Cluster of Al ₂ O ₃	NiO	NiAl
	Thickness (μm)	7±4	3±5	5±5	26±37	5±7	3±3	5±4	18±19
530 _{40μm} mA/cm ²	Figure	19.e				19.f			
	Compounds	Al ₃ Ni ₂	Cluster of Al ₂ O ₃	NiO	NiAl	Al ₃ Ni ₂	Cluster of Al ₂ O ₃	NiO	NiAl
	Thickness (μm)	9±6	8±4	2±2	48±16	18±5	6±2	2±2	54±11
530 _{20μm} mA/cm ²	Figure	19.g				19.h			
	Compounds	Al ₃ Ni ₂	Cluster of Al ₂ O ₃	NiO	NiAl	Al ₃ Ni	Cluster of Al ₂ O ₃	NiO	NiAl
	Thickness (μm)	14±3	4±1	5±2	68±11	15±3	8±2	5±3	8±8

II.B-Discussion

II.B.1-Preoxidation of the Ni plating

During the electrodeposit preoxidation step, many pores formed mainly at the electrodeposit/substrate interface, inside the electrodeposits for current density of 270 mA/cm², or close to the NiO/electrodeposit interface.

The formation of pores can be due to several phenomena: (i) the method of electroplating metals: those having a high melting point (Ni, Fe, Cr, etc.) lead to a high concentration of vacancies in the coatings under the action of temperature (during oxidation) [39]. These vacancies accumulate and coalesce to form micropores at the defective zones (grain boundaries, interface, etc.). In addition, other types of defects such as vacancies, dislocations, twin boundaries, etc. may also be involved in the formation of pores [39]; (ii) the weak bonding between the substrate and the Ni film, which can be induced by trapped hydrogen, by the substrate surface roughness or by the processing conditions of the coatings (solution, temperature, etc.) [43,55]. However, none of these theories can fully explain these differences between electrodeposits.

A factor that may explain the formation of pores in the Ni electrodeposit is the formation of hydrogen during the electrodeposition process. Two phenomena can be observed and have been studied so-called Hydrogen Evolution Reaction (HER). HER is described by reaction mechanism in several steps (Figure IV-23): (i) the first step, called the Volmer step, corresponds to the electro-adsorption of the hydrogen present in the solution (eq. 1); (ii) the second Heyrovsky step (eq. 2) corresponds to the desorption of hydrogen. This desorption is carried out by recombination between the adsorbed hydrogen and another hydrogen present in the solution. There is also Tafel desorption, but is extremely minor in the case of nickel in sulfuric acid (eq. 3) [57].

According to El Alami et al. [57] for low current densities, the rate of hydrogen surface coverage is low, the overall behavior is governed by the Volmer step (eq. 1). As the current density increases, the recovery rate increases, Heyrovsky desorption step that become predominant. This means, although the current density increases, the [H_{ads}] will increase to a threshold value (depend of the materials, solution, etc.) [58-59].



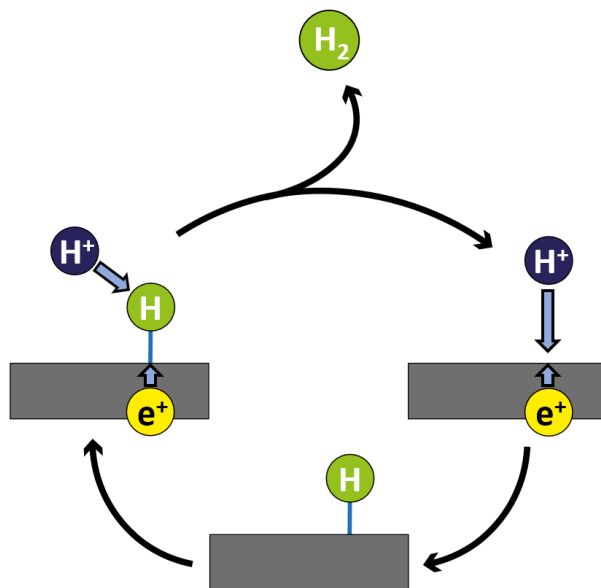


Figure IV-23: Schematic drawing of the Volmer-Heyrovsky mechanism of hydrogen evolution on the surface of an electrode in acidic solution [60].

For electrodeposits carried out at 90 mA/cm², depressions can be observed at the surface of the samples. This depression, with an average size of 72±28 μm, has the same order of magnitude than hydrogen bubbles formed by electrolysis in water [61]. The depression probably corresponds to the imprint left by a hydrogen bubble by a Volmer-Heyrovsky type mechanism. However, since the kinetics of the Heyrovsky reaction are slow at this current density, the residence time of a bubble on the surface sample is long enough to prevent the electrodeposit from forming in this area.

For electrodeposits made at 270 and 530 mA/cm², these depressions are not observable. This would tend to show that the residence time of the bubbles is lower and that the kinetics of the Heyrovsky reaction are faster. In addition, for electrodeposits carried out at 270 mA/cm², many small pores (a few micrometers) can be observed. These pores present in the nickel grains may correspond to the formation a hydrogen blister [62]. This tends to demonstrate the absorption of hydrogen within the electrodeposit. The difference between the electrodeposits carried out at 270 and 530 mA/cm² would hold while the reaction kinetics of Volmer and Heyrovsky have reached a plateau and the quantity of hydrogen absorbed depends on the electrodeposition time, which is respectively 23 and 10 min [58-59].

To conclude, the electrodeposits obtained with low current densities generated low stress in the layer but cause a greater amount of absorbed hydrogen.

II.B.2-Influence of the current density on the aluminothermic and aluminizing processes

During the aluminizing step, two types of mechanisms could be observed. The first one occurs with deposits made with “low” current densities (90 mA/cm²) and is similar to what was observed on the raw substrate (figure IV-5.d & 7.d). These coatings are composed of a first layer of Al₃Ni with Al₂O₃ shells, a second layer of Al₂O₃ cluster and a third layer made of unconsumed NiO. However, one key difference with respect the preoxidized substrate is the appearance of diffusion

islands at the NiO/Ni plating interface. These diffusion islands have a “volcano” shape and are present in relatively small quantities and induce only minor modifications in the mechanisms of formation of the aluminized coatings.

The diagrams displayed in Figure IV-24 gather the thicknesses of the different zones, the percentage of zones affected by the diffusion islands (Figure IV-24.a & 24.b respectively, for 1 and 2h of preoxidation), the quantity of NiO formed during the preoxidation step, and the amount of NiO consumed during the heat treatment (Figure IV-24.c & 24.d respectively, for 1h and 2h of preoxidation). The thicknesses of the intermetallic and Al₂O₃ zones differ only slightly between the coatings obtained on a raw substrate and those obtained on the 90 mA/cm² electrodeposits (Figure IV-24.a & 27.b).

For the samples preoxidized for 1h at 1100°C (raw substrate and Ni electrodeposit), the thickness of unreacted NiO from the aluminothermic reaction increases from ~20 to ~50% between the raw substrate and the electrodeposits (Figure IV-24.c). For pre-oxidation times of 1h and an electrodeposition current density of 90 mA/cm², it seems that the electrodeposit increases the permeability of the NiO layer towards aluminum. However, this observation cannot be extrapolated to longer (2h) preoxidation times because the thickness of NiO reacted is close to 50% for both the raw substrate and the electrodeposits (Figure IV-24.d).

The second mechanism is obtained for electrodeposits elaborated with current densities of 270 and 530 mA/cm² then preoxidized, and two types of aluminization can then occur. The first one is observed on both the preoxidized raw substrate and the preoxidized electrodeposits. It can be divided into three major stages: (i) the aluminothermic reaction between the solid aluminum particles and the nickel oxide provokes the reduction of the NiO, the formation of Al₂O₃ and a local rise in temperature; (ii) the temperature increase causes the melting of aluminum particles and the dissolution of previously formed nickel; (iii) the aluminothermic reaction between liquid aluminum and nickel oxide, accompanied by the formation and dissolution of the intermetallic Al₃Ni. The aluminothermic reaction keeps ongoing forming larger amounts of Al₃Ni and Al₂O₃. The intermetallic that forms on the surface is assumed to be viscous enough to trap the alumina shells of the aluminum particles. In addition, Al₂O₃ developed during the thermite reaction is trapped at the Al₃Ni/NiO interface. These phenomena will continue until a critical thickness of Al₂O₃ is reached that prevents the diffusion of aluminum, or until the system can no longer deliver enough free aluminum to sustain the thermite reaction.

The second type of aluminizing takes place at the NiO/Ni plating interface. A liquid phase rich in aluminum (Al and/or Al₃Ni) seeps through the defects of the nickel oxide layer (cracks, pores, etc.). This liquid infiltration induces the reduction of NiO and the formation of alumina along the defects (figure IV-22.b). Once molten Al reaches the Ni film, rapid aluminizing of the metallic nickel occurs, which causes the formation of a NiAl intermetallic zone. This aluminum enrichment of the Ni substrate provokes a significant change in volume inducing the formation of zones resembling volcanos [64-64]. For current densities close to 90 mA/cm², these “volcanos” are one far from the others and do not disturb the system very much. For higher current densities, these diffusion islands form in large quantities and are very close one to the others. This volume increase also induces an interfacial decohesion of the nickel electrodeposit from the substrate, as well as a lifting of the coating of several tens of microns (Figure IV-22.e & 22.f and Figure IV-22.a & IV-22.b).

The formation and number of diffusion islands seem to be closely related to the “quality” of the nickel oxide layer (amount of defects) and therefore to that of the nickel electrodeposit. Comparing

with the oxidation tests carried out on raw substrates, several phenomena can explain the increase in permeability of the NiO layers developed from Ni electrodeposits towards liquid aluminum. Graham et al. [65-68] demonstrated that the oxidation rate of Ni electrodeposits depends on the surface finish and of the Ni texture. Their results underlined the significant differences in the oxidation mechanisms that can occur at low temperatures and for short oxidation times. For an oxidation temperature of 600°C, the initial oxidation rate can be changed by a factor of four. In contrast, these differences are blurred for high oxidation temperatures or longer times. The surface finish and texture that were observed in the electrodeposits are therefore not sufficient to explain their different evolutions. Very likely, the hydrogen released upon the electroplating of nickel from a sulphamate bath may hinder the even deposition of the layer.

The hydrogen present in nickel films always results in a high tensile strength and a high rate of hydrogen into the substrate lattice [43]. The influence of heat treatment on nickel electrodeposits shows that for heat treatments of 1000°C/30 min, the tensile strength of the film decreases by a factor of four [69] which can be reflected by recrystallization phenomena (modification of the grain size, reduction in the number of defects, etc.) and due to the release of the hydrogen present in the deposit. Studies carried out on nickel electrodepositions have shown the release of hydrogen trapped during heat treatment [58,62]. Mass losses due to the evolution of hydrogen caused the formation of networks of cracks and the modification of thermal expansion properties. These phenomena can induce the formation of cracks in the nickel oxide layer leading to the formation of scattered islands. The greatest quantity of diffusion islands was obtained for high current densities, which can give credence to the hydrogen hypothesis. However, further studies should be done to confirm these hypotheses, e.g. evaluating the amount of trapped hydrogen in the electrodeposits obtained at different current densities and after the annealing treatment.

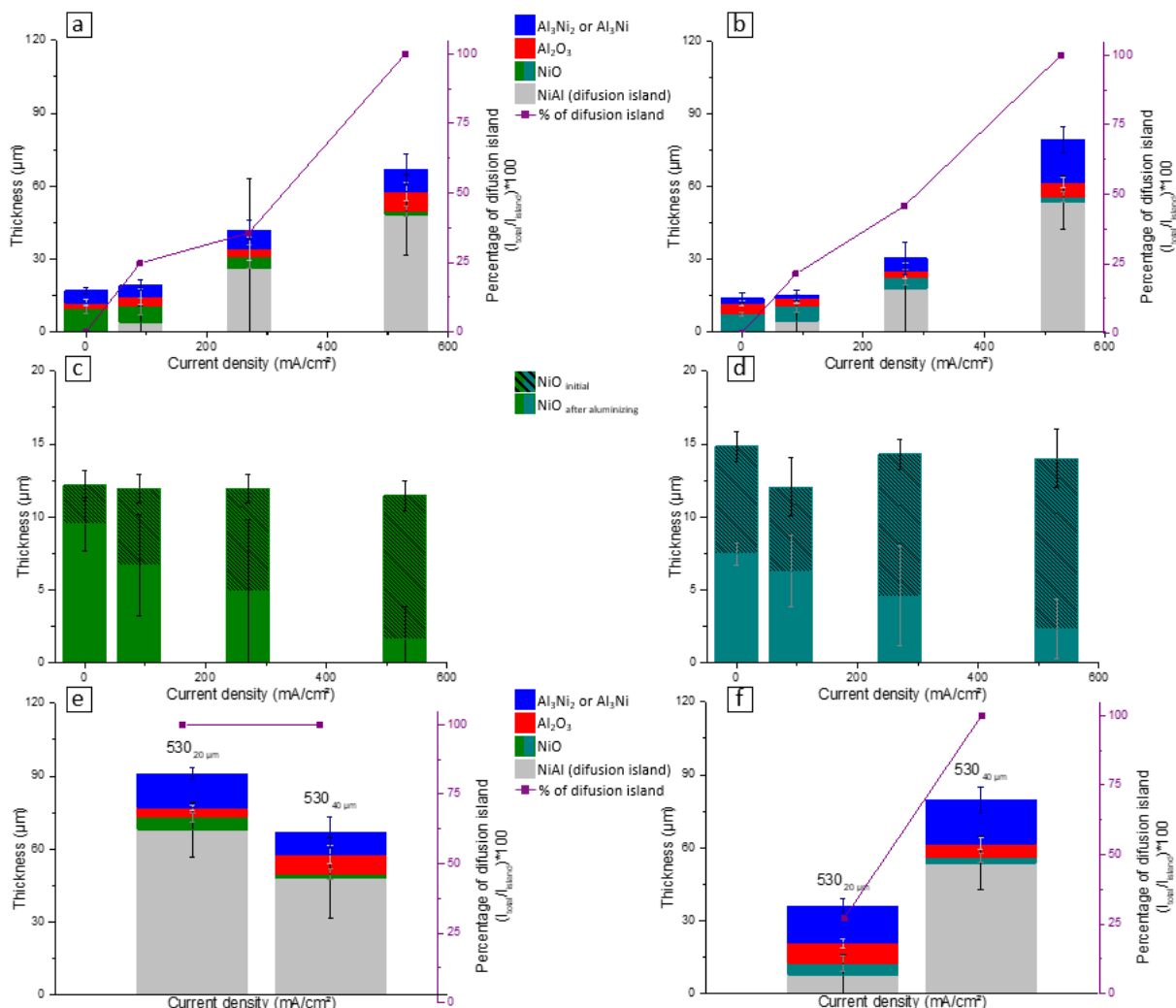


Figure V-24: Histograms of the thickness of the different sublayers formed after slurry aluminizing at 700°C/24h, (a) for a preoxidation time of 1h (a) and 2h (b) and the quantities of area affected by the formation of diffusion island. The thickness of the NiO formed during the preoxidation step and after the aluminizing for preoxidation time of 1h (c) and 2h (d). Detail of the different sublayers formed after slurry aluminizing at 700°C/24h the two different thickness of electrodeposits at 530 mA/cm² for preoxidation time of 1h (e) and 2h (f).

II.B.3-Influence of the electrodeposit thickness on the aluminothermic reactions and the aluminizing processes

Finally, in this last part, we will focus on the influence of the thickness of the electrodeposits (obtained at 530 mA/cm²) on the aluminothermic and aluminizing processes. Figures IV-20.e & 20.f show the differences in the thicknesses of the different zones observed as well as the percentage of coating affected by the formation of diffusion islands.

In the samples preoxidized for 1h at 1100°C (Figure IV.22.a), the whole surface (100%) is affected by the diffusion islands irrespective of the thickness (20 or 40 μm) of the electrodeposit. However, the thicknesses of NiO consumed and the derived formation of Al_2O_3 formed is less significant for 20 than for 40 μm while the thickness of the Al_xNi_y intermetallic sublayers is greater.

When the preoxidation time was extended to 2h, the differences between the initial thickness of the electrodeposits are more marked because only 27% of the surface was affected by the diffusion islands, less quantities of NiO consumed and Al₂O₃ formed and much thinner NiAl appeared after aluminizing the 20 μm electrodeposits in comparison with the 40 μm thick counterparts.

Increasing the thickness of the nickel electrodeposits will therefore tend to increase the concentration of defects in the nickel oxide layer and therefore the permeability of aluminum.

The difference in electrodeposition thicknesses is caused by longer electrodeposition times, according to Winand et al. [38]. Yet, for the BR type electrodeposits, the increased electrodeposition times is expected to lead to the formation of larger grains and to entrapment of electrolytes in the coatings. The release of the electrolyte and recrystallization at high temperature induce the formation of defects in the nickel oxide layer. In addition, the thinner oxide thickness for preoxidation times of 1 h compared to 2h would tend to minimize these effects.

In addition, we can hypothesize that the amount of hydrogen trapped in thin nickel electrodeposits would be less important than in thicker layers but such reduced amount would not be sufficient to induce changes in the electrodeposit and in the oxide layer at high temperature.

Finally, it is also possible that, for thin films, the potential differences in CTE between the substrate and the nickel electrodeposit would be minor than for the thick coatings, therefore allowing a more even aluminizing similar to the one observed in the preoxidized Ni substrate (part I of chapter IV).

To conclude, it seems likely that several complex phenomena come into play during the electroplating, preoxidation and aluminizing stages. Only one of the cited phenomena cannot explain all of these differences. Furthermore, very few studies have investigated these phenomena for nickel electroplating by Watt's bath. It therefore seems extremely difficult to theorize about these phenomena.

II.C-Conclusion

The formation of a potential self-regenerating coating by the aluminothermic route was tested on nickel substrates and on nickel electrodeposits.

For pure nickel substrates, the most promising results were obtained for preoxidation times of 2h and aluminizing treatments of 700°C/24h. These conditions lead to the formation of a composite coating consisting of an Al₃Ni layer composed of Al₃Ni micro-reservoirs and Al₂O₃ shell, then a second cluster layer of Al₂O₃ and finally a residual thickness of NiO.

In order to remove the residual NiO layer, nickel electrodeposits were elaborated on the Ni samples previously to preoxidation. These electrodeposits (carried out at high current densities) gave birth, through the applied preoxidation treatment, to NiO layers possessing increased permeability with respect to aluminum. This goal has been successfully achieved. However, the formation of electrodeposits leads to a high concentration of defects in the oxide layer which results in the formation of cracks and diffusion islands during the aluminizing. The aluminum therefore could pass through the nickel oxide to aluminize the substrate and a decohesion between the electrodeposit and the substrate was subsequently observed. The formation of the Al₃Ni layer and of the micro-reservoirs was no longer guaranteed.

It therefore appeared necessary to consume the entire nickel oxide layer in another way. One of the possibilities would be to carry out a preoxidation then reduction step in an Ar/H₂ atmosphere. This partly reduction in nickel oxide would allow a thin layer of nickel to form on the surface of the sample, thereby reducing the thickness of the nickel oxide layer. In another vein, the use of other electroplating baths like the sulphamate baths deserve further investigations to achieve a better homogeneity and possibly less decohesion between the electrodeposit and the substrate. This will be addressed in Chapter V.

References

[38]: R. Winand, Electrodeposition of metals and alloys – new results and perspectives, *Electrochimica Acta* 39 (1994) 1091–1105.

[https://doi.org/10.1016/0013-4686\(94\)E0023-S](https://doi.org/10.1016/0013-4686(94)E0023-S)

[39]: H.D. Merchant, Defect structure, morphology and properties of deposits, *The Minerals, Metals and Materials Society* 431 (1995) 1–159.

[40]: T. Watanabe, Nano plating – microstructure formation theory of plated films and a database of plated films, Elsevier (2004) 1–714.

ISBN: 9780080537252

[41]: H. Natter, M. Schmelzer, R. Hempelmann, Nanocrystalline nickel and nickel-copper alloys: Synthesis, characterization, and thermal stability, *Journal of Materials Research* 13 (1998) 1186–1197.

<https://doi.org/10.1557/JMR.1998.0169>

[42]: E. Thiele, R. Klemm, L. Hollang, C. Holste, N. Schell, H. Natter, R. Hempelmann, An approach to cyclic plasticity and deformation-induced structure changes of electrodeposited nickel, *Materials Science and Engineering: A* 390 (2005) 41–51.

<https://doi.org/10.1016/j.msea.2004.09.022>

[43]: M. Pushpavanam, K. Balakrishnan, Internal stress and hydrogen permeability of zinc-nickel alloy electrodeposits, *Transactions of the IMF* 74 (1996) 33–35.

<https://doi.org/10.1080/00202967.1996.11871087>

[44]: J.K. Dennis, T.E. Such, Deposition of nickel alloys, *Nickel and Chromium plating* (1993) 363–389.

<https://doi.org/10.1533/9781845698638.363>

[46]: M. Paunovic, M. Schlesinger, Fundamentals of electrochemical deposition, *The Electrochemical Society* (1998) John Wiley & Sons Inc.

ISBN: 978-0-471-71221-3

[47]: C.V. Thompson, Structure evolution during processing polycrystalline films, *Annual Review of Materials Science* 30 (2000) 159–190.

<https://doi.org/10.1146/annurev.matsci.30.1.159>

[45]: E. Budevski, G. Staikov, W.J. Lorenz, Electrochemical phase formation and growth. VCH verlagsgesellschaft, *Berichte der Bunsengesellschaft für physikalische Chemie* 101 (1996) 985–1082.

<https://doi.org/10.1002/bbbc.19971010719>

[52]: V. Kozlov, L. Peraldo Bicelli, Texture formation of electrodeposited fcc metals, *Materials Chemistry and Physics* 77 (2002) 289–293.

[https://doi.org/10.1016 / s0254-0584 \(02\) 00004-4](https://doi.org/10.1016 / s0254-0584 (02) 00004-4)

[53]: J.K. Dennis, T.E. Such, Metallurgical aspects of electrodeposition, Nickel and chromium plating (1993) 13–40.

<https://doi.org/10.1533/9781845698638.13>

[54]: J. Amblard, I. Epelboin, M. Froment, G. Maurin, Inhibition and nickel electrocrystallization, Journal of Applied Electrochemistry 9 (1979) 233–142.

<https://doi.org/10.1007/BF00616093>

[55]: J.K. Dennis, T.E. Such, Physical and mechanical properties of electrodeposits and methods of determination, Nickel and Chromium Plating (1993) 162–204.

<https://doi.org/10.1533/9781845698638.162>

[56]: D.E. Lozano, G.E. Totten, Y. Bedolla-Gill, M. Guerrero-Mata, M. Carpio, G.M. Martinez-Cazares, X-ray determination of compressive residual stresses in spring steel generated by high-speed water quenching, Materials 217 (2019) 1154.

<https://doi.org/10.3390/ma12071154>

[57]: H. El Alami, Influence de la déformation plastique sur la réactivité du nickel dans la Réaction d'Evolution de l'Hydrogène en milieu acide : approche cinétique et thermodynamique, PhD Thesis, Université de la Rochelle (2007).

<http://www.theses.fr/2007LAROS206>

[58]: J. Evans, The effect of nickel plating on hydrogen embrittlement of high strength steel, PhD Thesis, Cranfield Institute of Technology 1992).

<https://dspace.lib.cranfield.ac.uk/handle/1826/3238>

[59]: D. Mallick, N. Mary, V.S. Raja, B. Normand: Study of diffusible behavior of hydrogen in first generation advanced high strength steels, Metals 11 (2021) 782.

<https://doi.org/10.3390/met11050782>

[60]: C.G. Morales-Guio, L.A. Stern, X. Hu, Nanostructured hydrotreating catalysts for electrochemical hydrogen evolution, Chemical Society Review 43 (2014) 65545.

<https://doi.org/10.1039/C3CS60468C>

[61]: P. Chandran, S. Bakshi, D. Chatterjee, Study on the characteristics of hydrogen bubble formation and its transport during electrolysis of water, Chemical Engineering Science 138 (2015) 99–109.

<https://doi.org/10.1016/j.ces.2015.07.041>

[62]: M. Zamanzade, C. Müller, J.R. Velayarce, C. Motz, Susceptibility of different crystal orientations and grains boundaries of polycrystalline Ni to hydrogen blister formation, International Journal of Hydrogen Energy 44 (2019) 7706 7714–

<https://doi.org/10.1016/j.ijhydene.2019.01.263>

[63]: Y.S.Touloukian, R.K. Kirby, R.E. Taylor, P.D. Desai, Thermophysical properties of matter: the TPRC data series, A comprehensive compilation of data, vol. 12. IFI/Plenum, New York

<https://apps.dtic.mil/dtic/tr/fulltext/u2/a129115.pdf>

[64]: V. Tolpygo, D.R. Clarke, Surface rumpling of a (Ni, Pt)Al bond coat induced by cyclic oxidation, *Acta Materialia* 48 (2000) 3283–3293.

[https://doi.org/10.1016/S1359-6454\(00\)00156-7](https://doi.org/10.1016/S1359-6454(00)00156-7)

[65]: M.J. Graham, G.I. Sproule, D. Caplan, M. Cohen, The effect of surface preparation on the oxidation of nickel, *Journal of The Electrochemical Society* 119 (1972) 883.

[66]: M.J. Graham, R.J. Hussey, M. Cohen, Influence of oxide structure on the oxidation rate of nickel single crystals, *Journal of The Electrochemical Society* 120 (1973) 1523.

[67]: D. Caplan, M.J. Graham, M. Cohen, Effect of cold work on the oxidation of nickel at high temperature, *Journal of The Electrochemical Society* 119 (1972) 1205.

[68]: D. Caplan, R.J. Hussey, G.I. Sproule, M.J. Graham, Effect of carbon on cavity formation during the high-temperature oxidation of Ni, *Oxidation of Metals* 14 (1980) 279–299.

<https://doi.org/10.1007/BF00603786>

[69]: M. Pushpavanam, G. Varadarajan, S. Krishnamoorthy, R. Thangappan, B.A. Shenoi, H.V.K. Udupa, Occlusion plating with nickel, *Metal Finishing* 72 (1992) 46–52.

Chapter V: Synthesis of self-regenerating composite coating using electrocodeposition of Ni and preoxidized Al_3Ni_2 particles

The previous chapter focused on the use of thermite reactions to obtain self-regenerating coatings by slurry aluminizing either a preoxidized nickel substrate or a preoxidized nickel electrodeposit. Promising results were obtained in this way, in particular by annealing the Al slurry deposit at 700°C for 24h. This treatment resulted in a coating made of an Al_3Ni matrix containing a dispersion of Al_3Ni microspheres surrounded by an alumina shell. In addition, an Al_2O_3 diffusion barrier was synthesized in the same annealing step.

However, not all the NiO between the coating and the substrate was consumed. In an attempt to increase the permeability to Al of the NiO layer, Ni layers were then electrodeposited on the surface samples and subsequently oxidized to form the NiO layer. We demonstrated that this approach increased the permeability of Al through the NiO. However, no adequate compromise between the permeability and the formation of the composite structure between the microspheres, matrix and diffusion barrier could be found.

In this fifth (and final) chapter, the formation of self-regenerating coatings is investigated by electrodeposition. To do this, preoxidized intermetallic particles were incorporated into a nickel matrix and subsequently aluminized. One of the crucial issues is to incorporate a sufficient quantity of particles to get a beneficial effect but without damaging the diffusion coating by incorporating defects or trapping electrolytic solution. The originality of this approach stems from the numerous studies on the incorporation of nanometric ceramic, polymeric or metallic particles. However, very few works investigated the incorporation of micrometric composites and the influence of these particles under heat treatment.

Therefore, in this chapter, a first part will focus on the synthesis of intermetallic particles and on their preoxidation. In the second and third parts, the incorporation of the particles in Ni electrodeposits and the aluminizing of the composite coating are studied. Finally, the fourth part is devoted to preliminary isothermal oxidations tests with the aim of characterizing the self-regenerating character of these coatings.

Table of contents

I-Synthesis of intermetallic powders and preoxidation	169
II-Electro-codeposition of Ni and Al_3Ni_2 preoxidized particles.....	177
II.A-Surface morphology of the first layer.....	177
II.B-Electroplating and incorporation of $\text{Al}_3\text{Ni}_{2(\text{ox})}$ particles in a metallic Ni matrix	181
II.B.1-Influence of current density.....	182
II.B.2-Influence of heat treatment temperature.....	183
II.B.3-Influence of heat treatment time	186
III- Isothermal oxidation	189
III.A-Microstructure and composition	190
III.A.1-Aluminizing and isothermal oxidation of the coating carried out on the raw substrate	190
III.A.2-Aluminizing and isothermal oxidation of nickel plating	192
III.A.3-Aluminizing and isothermal oxidation of composite electrodeposits with “Ni flash”	193
III.A.4-Aluminizing and isothermal oxidation of composite electrodeposits without “Ni flash”	195
III.B-Oxidation kinetics.....	199
IV-Discussion	200
IV.A-Formation of the first layer of electrodeposited nickel (Ni flash)	200
IV.B-Effect of current density on the amount of preoxidized Al_3Ni_2 particles trapped in nickel electrodeposit matrix	200
IV.C-Effect of aluminizing temperature and time.....	201
IV.D-Isothermal oxidation	203
IV.D.1-Oxidation kinetics.....	203
IV.D.2-Evolution of the microstructure and compositions	204
V-Conclusions	207
References.....	208

I-Synthesis of intermetallic powders and preoxidation

In line with the coating concept of investigation, Al-rich intermetallic phases were envisaged to be incorporated in the composite coating. The choice was made on Al_3Ni_2 intermetallic powders for which no commercial product was found. The synthesis of the desired powder followed various steps including pack aluminizing, grinding, milling and sieving as follows.

- 1) Pack aluminizing. Nickel foils with a thickness of 250 μm and a purity of 99.98 wt. % (GoodFellow) were aluminized by pack-cementation. The nickel sheets were cut into 10 mm x 10 mm samples, placed in an alumina crucible by a number of 10, and then filled with 100 g of the reacting powder mixture. The powder mixture was made with a three-dimensional mixer (Turbula System Schatz type T2 F), and consisted of 56 g of Al_2O_3 , 40 g Al and 4 g NH_4Cl . The crucible was then closed and heated for 50h at 800°C under an Ar/5 % H_2 atmosphere. The crucible temperature of 800°C was chosen to produce an LTHA coating (Low-Temperature High-Activity), thus promoting the diffusion of aluminum and consequently the formation of the Al_3Ni_2 intermetallic phase.

After 50 hours at 800°C, the nickel samples were not completely aluminized. The thickness reached $616 \pm 6 \mu\text{m}$ (see Figure V-1). According to the EDS analyses (given further below), the aluminized samples are mainly composed of Al_3Ni_2 (Figure V-1, label 1) with a core made of γ -Ni slightly enriched in aluminum ($81 \pm 5 \mu\text{m}$) (Figure V-1, label 5). Between these two layers, the intermetallic compounds Al-rich β -NiAl (Figure V-1, label 2), Ni-rich β -NiAl (Figure V-1, label 3) and γ' - Ni_3Al (Figure V-1, label 4).

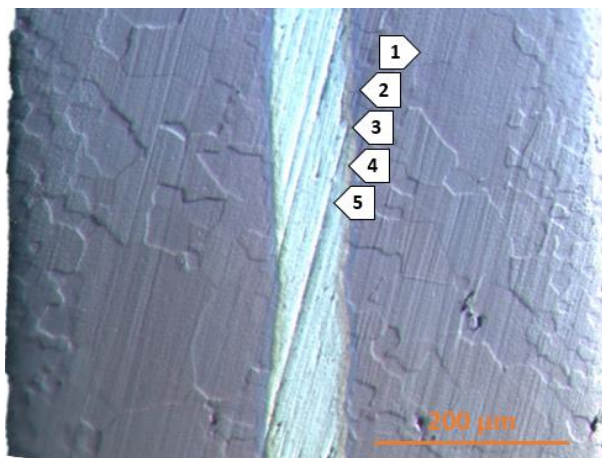


Figure V-1: Optical microscopy of the Ni samples after the pack-cementation (800°C/50h).

- 2) Grinding. The aluminized samples were then ground with a jar milling into a powder made of coarse particles (Figure V-2). The aluminized nickel sheets were placed by 3 in the jar with two balls and a few drops of ethanol (ball and crucible in WC). They were ground for 5 min at 30 Hz to obtain coarse particles (between 4 and 150 μm) while some fine particles (less than 1 μm) were also found.

After this step, the particles are rather coarse and present a high size dispersion (Figure V-3). A large majority of these particles are made of the single phase Al_3Ni_2 (Figure V-2.a). Other particles

- V. Synthesis of self-regenerating composite coating using electrocodeposition of Ni and preoxidized Al_3Ni_2 -

show several phases labeled from 2 to 5 on the SEM image (Figure V-2.b), respectively corresponding to Al_3Ni_2 , Al-rich $\beta\text{-NiAl}$, Ni-rich $\beta\text{-NiAl}$, $\gamma\text{-Ni}_3\text{Al}$ and $\gamma\text{-Ni}$.

In addition, due to the nature of the jar milling balls, small particles of WC are torn off during the process that can be observed under the SEM (Figure V-2.b, label 7) and in the X-ray patterns (Figure V-8).

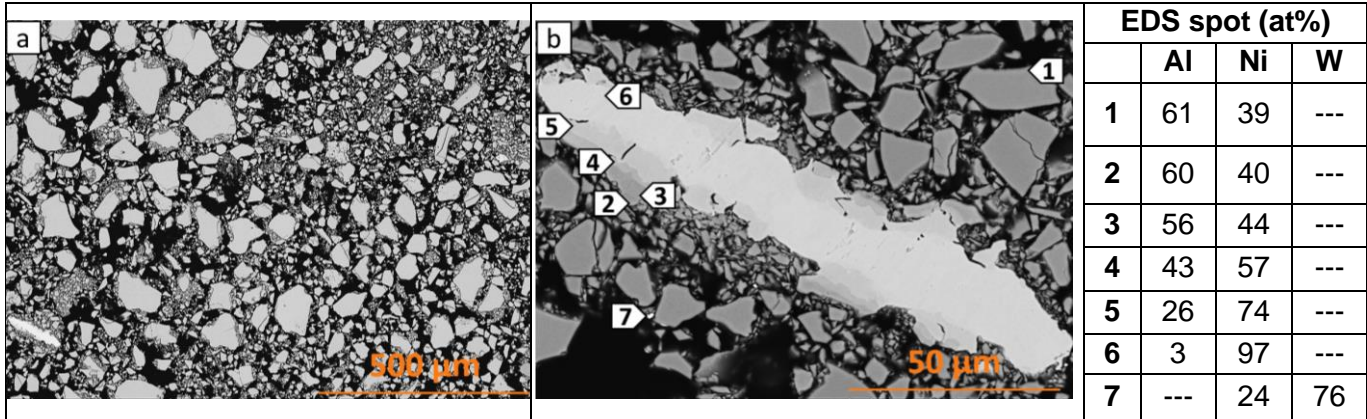


Figure V-2: SEM (BSE) cross-section images of the powders after the pack cementation (800°C/50h) and jar milling process (5 min at 30 Hz).

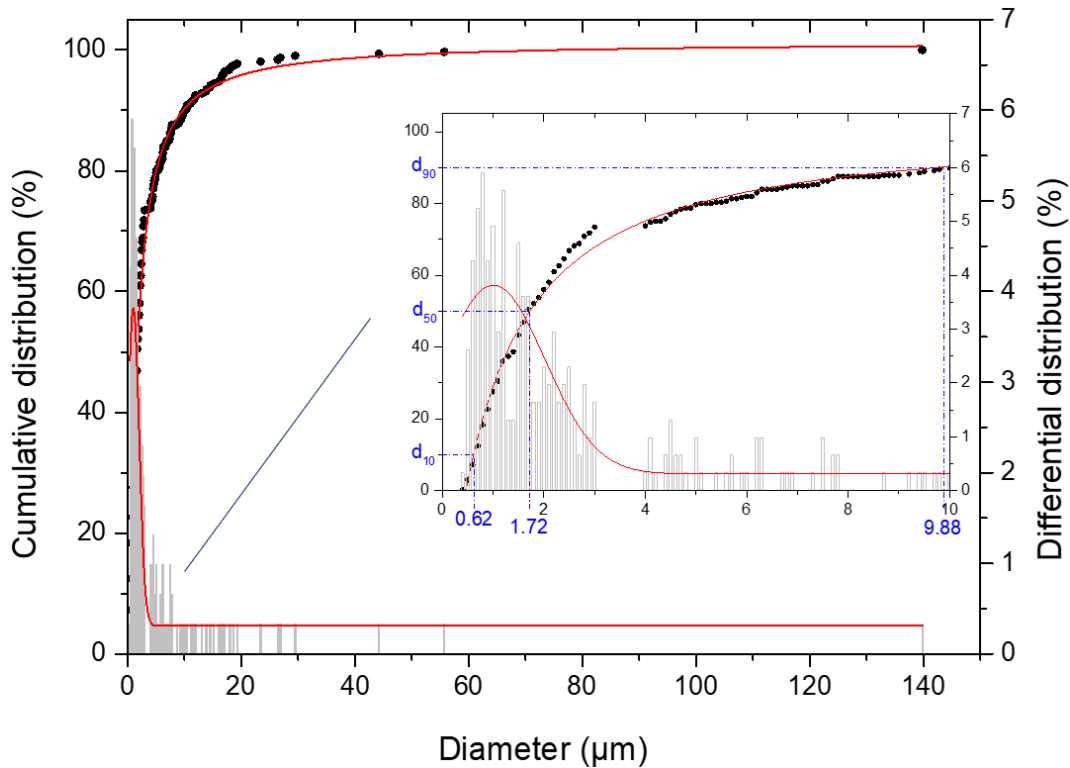


Figure IV-3: Size dispersion of the particles after the jar milling (5 min at 30 Hz).

- 3) Milling. To homogenize and further reduce the particles size, a planetary ball milling (P100 - Retsch) was used (Figure II-7). The powders previously obtained with the milling jar were placed at half of the volume of the crucible which was filled with zirconia balls of 2.15 mm diameter. The free spaces between the particles were then filled with 96% pure ethanol and the crucible was finally sealed. The crucible was then made to rotate at 500 rpm for 8 h. After this mechanical treatment, the particles and the balls were collected in a crystallizer and rinsed with ethanol. The crystallizer was then placed in a stove at 60°C to evaporate the whole remaining ethanol.
- 4) Sieving. The last step consisted of sorting the particles using several sieves positioned on a JEL 200 sieve machine. The sieves were built of 5 assembly sieves made up of 630 μm , 250 μm , 160 μm and 100 μm mesh. After the drying step, the particles are in the form of aggregates. The action of the vibrating table and manual scraping is necessary to break them up.

The SEM images of Figure V-4 show the particles right after crushing by the planetary ball mill and before being sieved. The morphology and size of the particles observed after the planetary ball milling are homogeneous (Figure V-4.b), except for the large rich in nickel particles (Figure V-4.a). In addition, due to the small particles size (less than a micron) these particles aggregate and appear as aggregates of around one hundred microns (Figure V-4.a). After sieving, these aggregates were disaggregated and large nickel-rich particles were removed (Figure V-5.a). This results in fine and quasi-spherical Al_3Ni_2 particles (Figure V-5.b and Figure V-6).

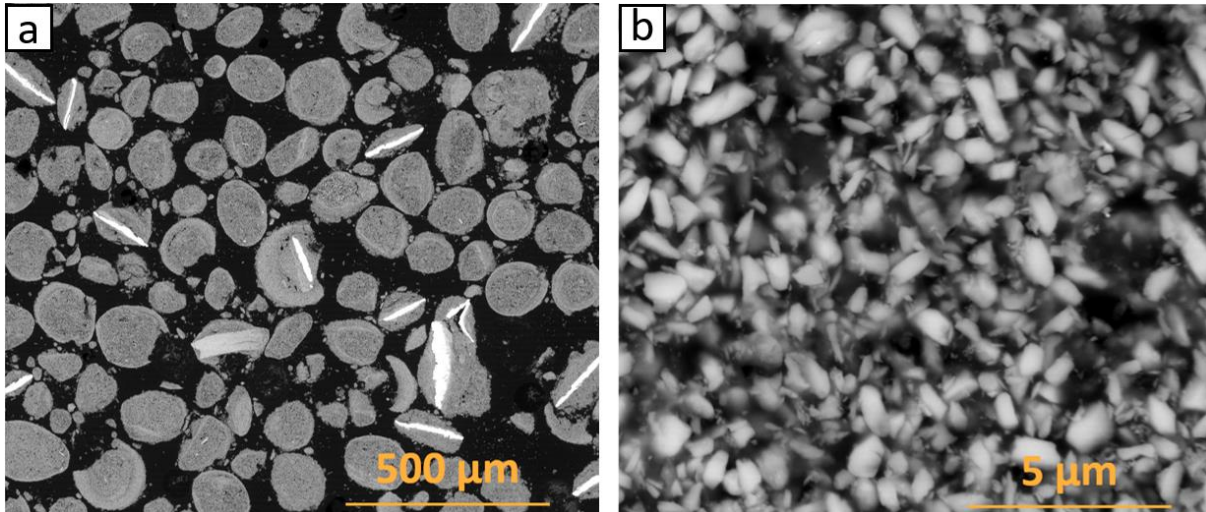


Figure V-4: SEM (BSE) cross-section images of the powders after the planetary ball milling (8h/500 rpm) with (a) magnification x500 and (b) magnification x20000.

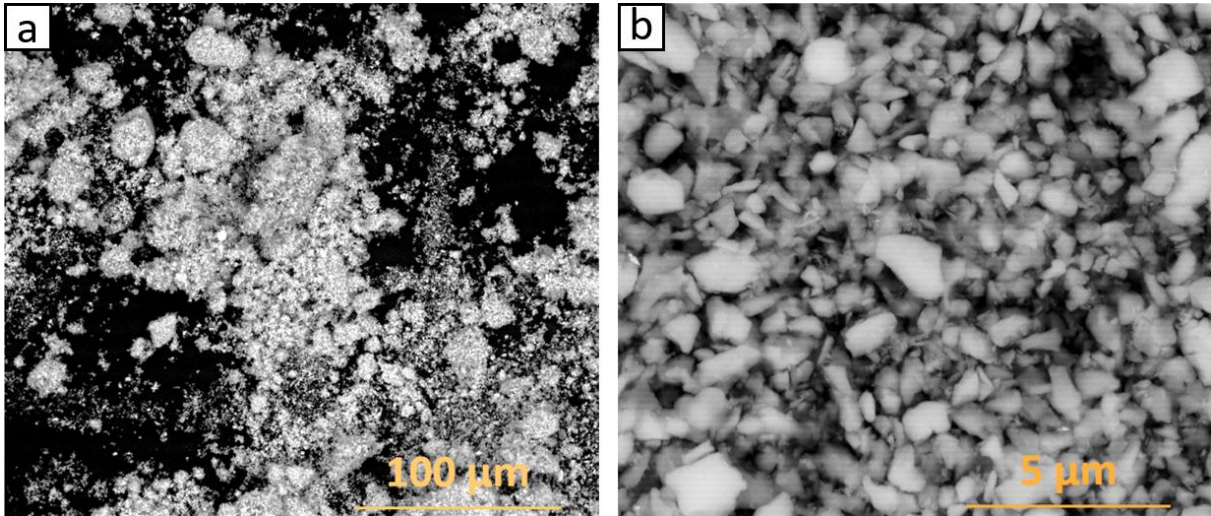


Figure V-5: SEM (BSE) cross-section images of the powders after the planetary ball milling retrieved after the 100 μm sieve with (a) magnification x500 and (b) magnification x20000.

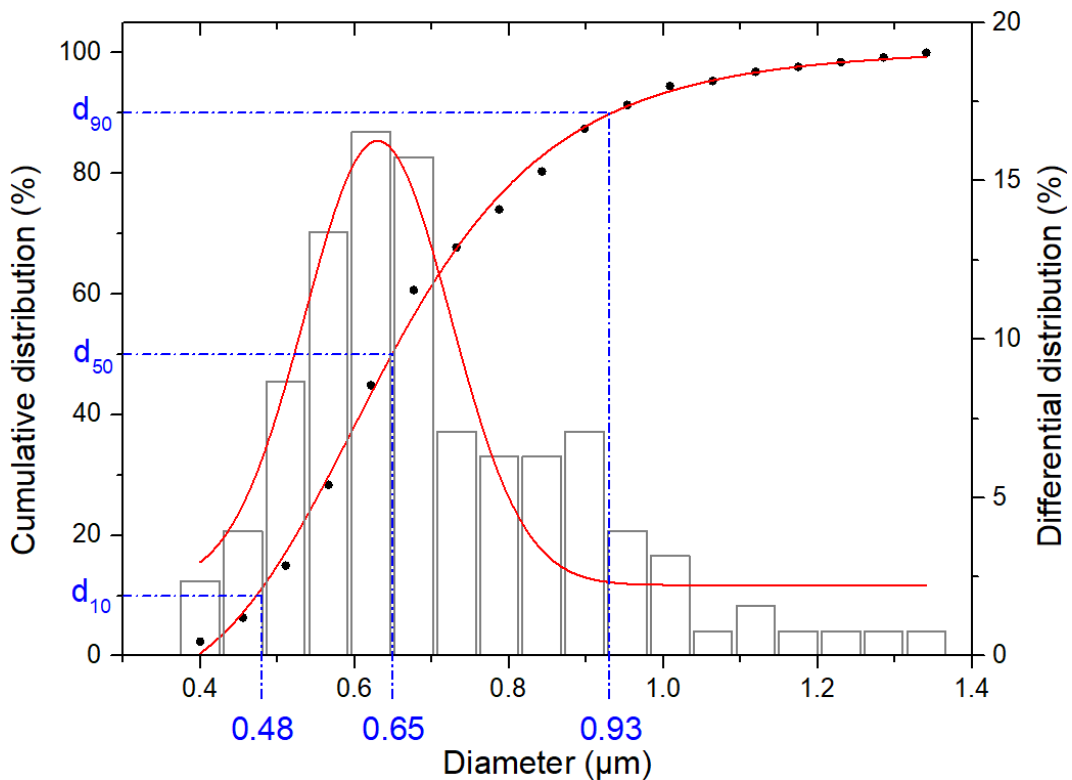


Figure V-6: Size dispersion of the particles after the planetary ball milling sorted with the 100 μm sieve.

The very last step consisted in the preoxidation of the particles to form an aluminum oxide shell while keeping a metallic core. For this, the particles were oxidized at 1100°C for 15 min under Ar. After the 15 min, the particles were quenched in laboratory air. It is important to note that the

applied temperature and time were the same as for the preoxidation of the Ni particles of the previous chapters. An Ar atmosphere was however used to selectively oxidize Al instead of Ni and form a thin alumina layer while maintaining a high amount of Al into the particles.

After the oxidation step, the particles show a quasi-spherical morphology (Figure V-7) with an $\text{Al}_3\text{Ni}_2/\beta\text{-NiAl}$ core and an aluminum oxide shell (Figure V-7 & V-8). The d_{50} of the preoxidized particles is $0.49\ \mu\text{m}$ (Figure V-9) with an oxide shell thickness of $0.06\ \mu\text{m}$ (Figure V-10).

The analyses carried out by Raman microspectroscopy are difficult to interpret when they are carried out on the preoxidized particles. However, when the particles are trapped in the electrodeposit, θ and $\alpha\text{-Al}_2\text{O}_3$ can be unambiguously identified (Figure V-18).

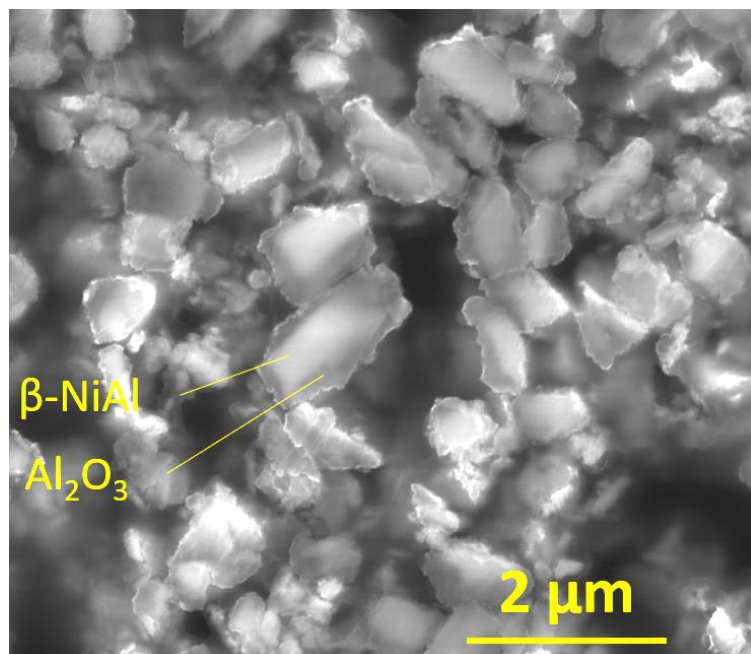


Figure V-7: SEM (BSE) cross-section images of the powders preoxidized at 1100°C for 15 min under Ar.

- V. Synthesis of self-regenerating composite coating using electrocodeposition of Ni and preoxidized Al_3Ni_2 -

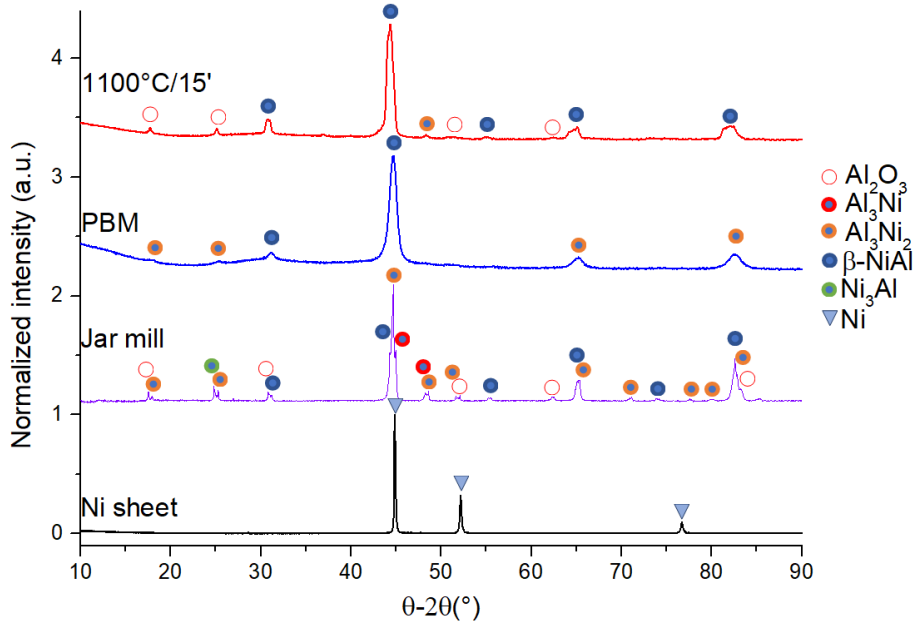


Figure V-8: X-ray patterns of the nickel sheets (black), the powder after the jar milling (purple), after the planetary ball milling (blue) and after the oxidation at 1100°C for 15 min (red).

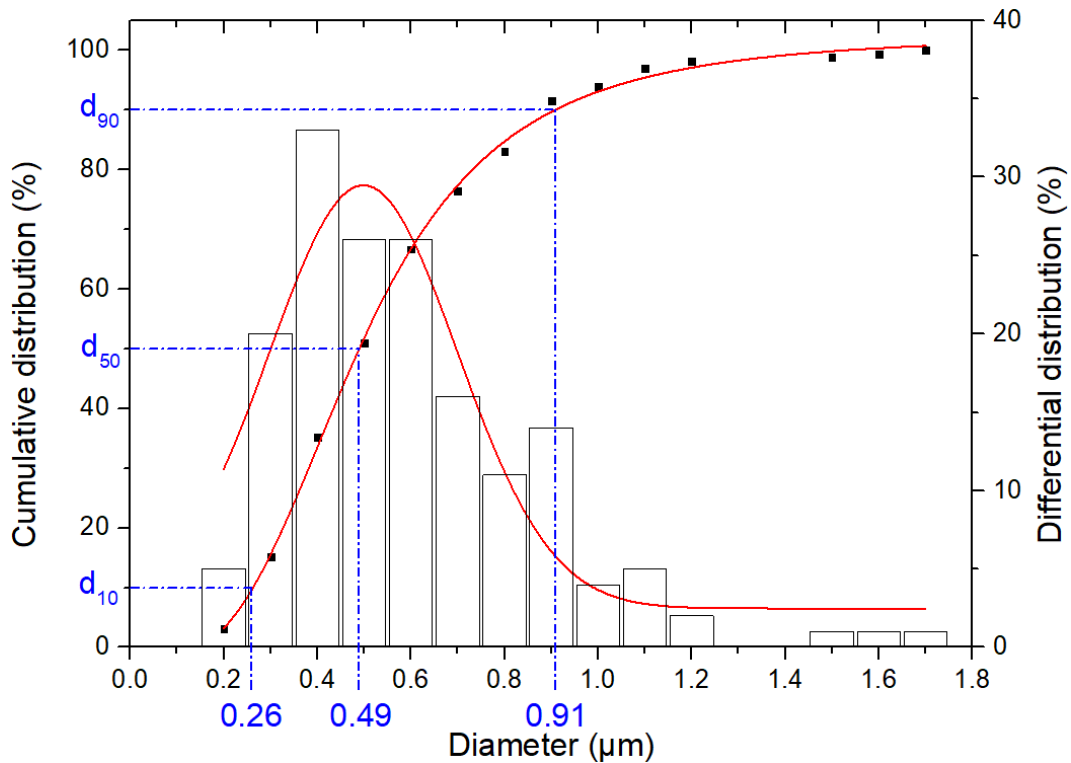


Figure V-9: Size dispersion of the particles of the powders preoxidized at 1100°C for 15 min under Ar.

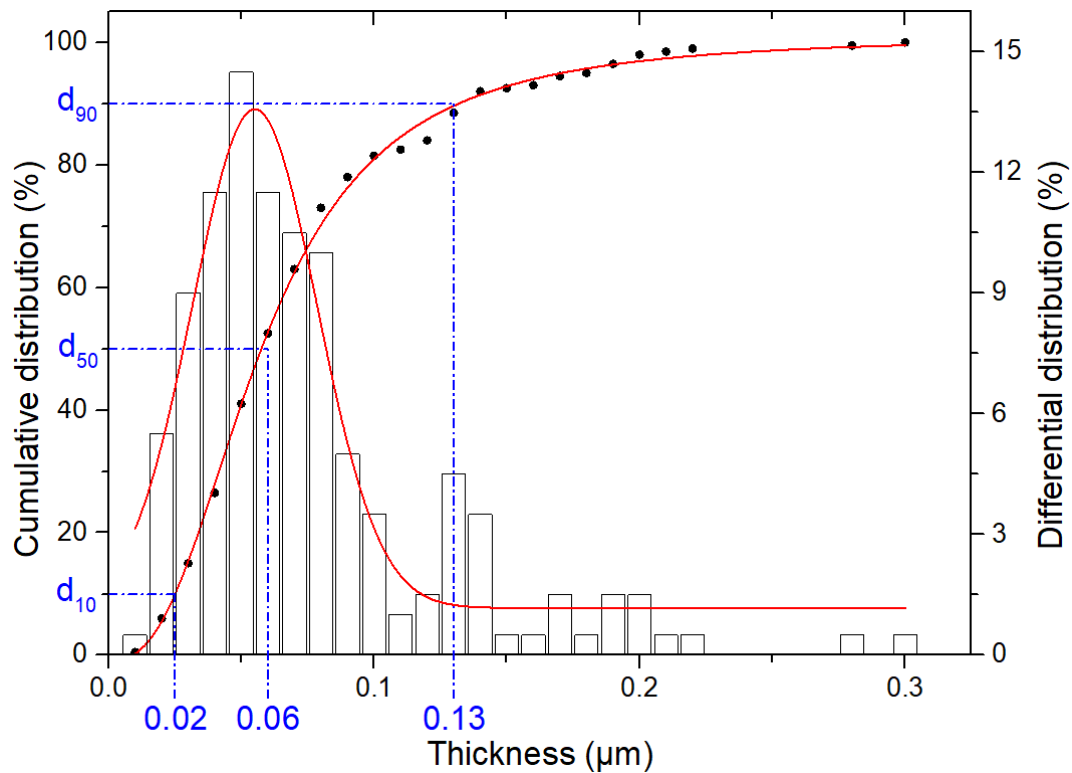


Figure V-10: Thickness of the oxide layer of the particles preoxidized at 1100°C for 15 min under Ar.

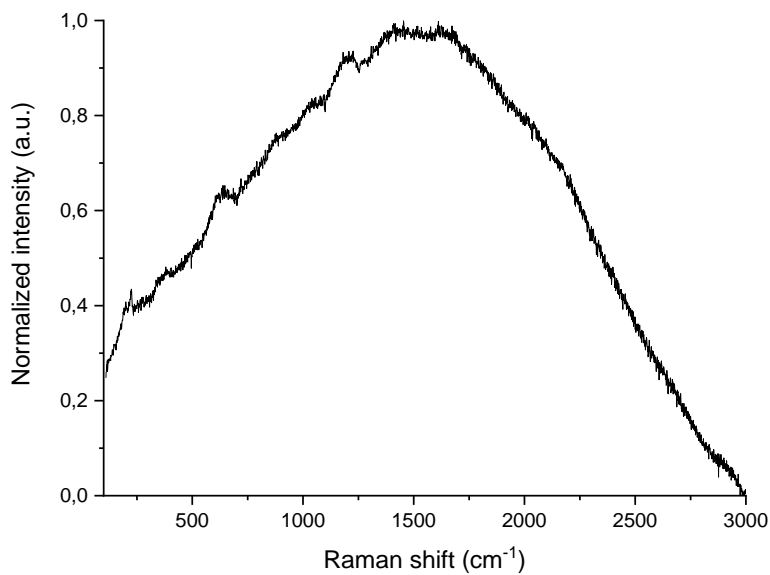


Figure IV-11: Raman spectrum of the preoxidized particles.

II-Electro-codeposition of Ni and Al_3Ni_2 preoxidized particles

This section investigates the incorporation of the synthesized and preoxidized Al_3Ni_2 intermetallic particles. For this, the Ni- $\text{Al}_3\text{Ni}_{2(\text{ox})}$ alloy material was prepared by the (direct current) DC electrocodeposition method on a Ni substrate. The samples were coated according to the procedure described in Figure V-12.

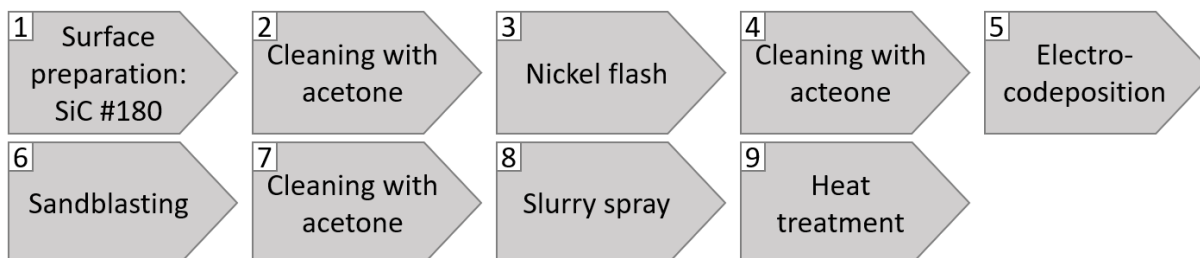


Figure V-12: Schematic representation of the different stage for obtaining coatings.

After the surface preparation, the substrates have been subjected to a nickel flash (also called “nickel strike”) electrodeposition process. Nickel strike baths are the same as that used for electrocodeposition bath but without the preoxidized particles (I.A.3-Chapter II). The purpose of nickel flash deposits is to improve the adhesion between the substrate and the composite layer. The use of nickel flash activates the surface as well as removes traces of oxides or pollution on the surface of the samples. Therefore, it allows to lay down an active thin pure Ni film ready-to electrodeposit [1].

The surfaces of the samples being extremely rough, the choice was made to use high current densities and significant deposit thicknesses ($\approx 10 \mu\text{m}$). The term of nickel flash therefore does not appear as the most suitable and we can rather talk about a “first layer”.

II.A-Surface morphology of the first layer

Figure V-13 shows the optical and SEM images of the surface and of the cross-section of the first layer made for current densities of 2 to 50 A/dm^2 . Table V-1 summarizes the current densities, deposition times and main observations. Note here that the deposition time was adjusted to get a 10 μm -thickness first layer.

Regarding the visual aspect, the first layer made at 2 A/dm^2 exhibits numerous polishing scratches as well as a shiny aspect (Figure V-13.a). Increasing the current density to 5 and 20 A/dm^2 results in few visible polishing scratches and a matt appearance (Figure V-13.d & 13.g). With the highest DC current of 50 A/dm^2 , the surface of the samples is again shiny, shows numerous polishing scratches and the edges are blackened (Figure V-13.j).

At higher magnifications, the surface of the electrodeposits displays three different microstructures: (i) a ridge-like microstructure for the electrodeposits made at 2 A/dm^2 (Figure V-13.b), (ii) pyramidal structures for the electrodeposits made at 5 and 20 A/dm^2 (Figure V-13.e & 13.h), and (iii) a nodular structure for the electrodeposit synthesized at 50 A/dm^2 (Figure V-13.k).

Finally, the grain microstructure of Ni electrodeposits is B.R. (“Basis Reproduction”, Chapter IV, Figure IV-15). The electrodeposits consist of fine grains close to the interface and coarser grains

towards the surface, with a greater grain size difference for electrodeposits of 5 and 20 A/dm^2 (Figure V-13.f & 13.i)

The X-ray diffraction patterns of the nickel flash obtained at 2, 5, 20, and 50 A/dm^2 are shown in Figure V-14. The XRD patterns of the Ni flash synthesized between 2 and 20 A/dm^2 show that the surface is textured following the (200) planes, which is in agreement with the literature whereas for low current densities, a strong [100] texture is observed ((200) \equiv (100) for a FCC structure) [2]. For a current density of 50 A/dm^2 , the texture shifts towards the (220) planes.

The changes in morphology can be attributed to the formation of different interfacial inhibitors, such as H_2 , H_{ads} or $\text{Ni}(\text{OH})_2$. In addition, the hydrogen reaction may change the electrochemical conditions leading to different surface morphologies, microstructure and texture [3].

- V. Synthesis of self-regenerating composite coating using electrocodeposition of Ni and preoxidized Al_3Ni_2 -

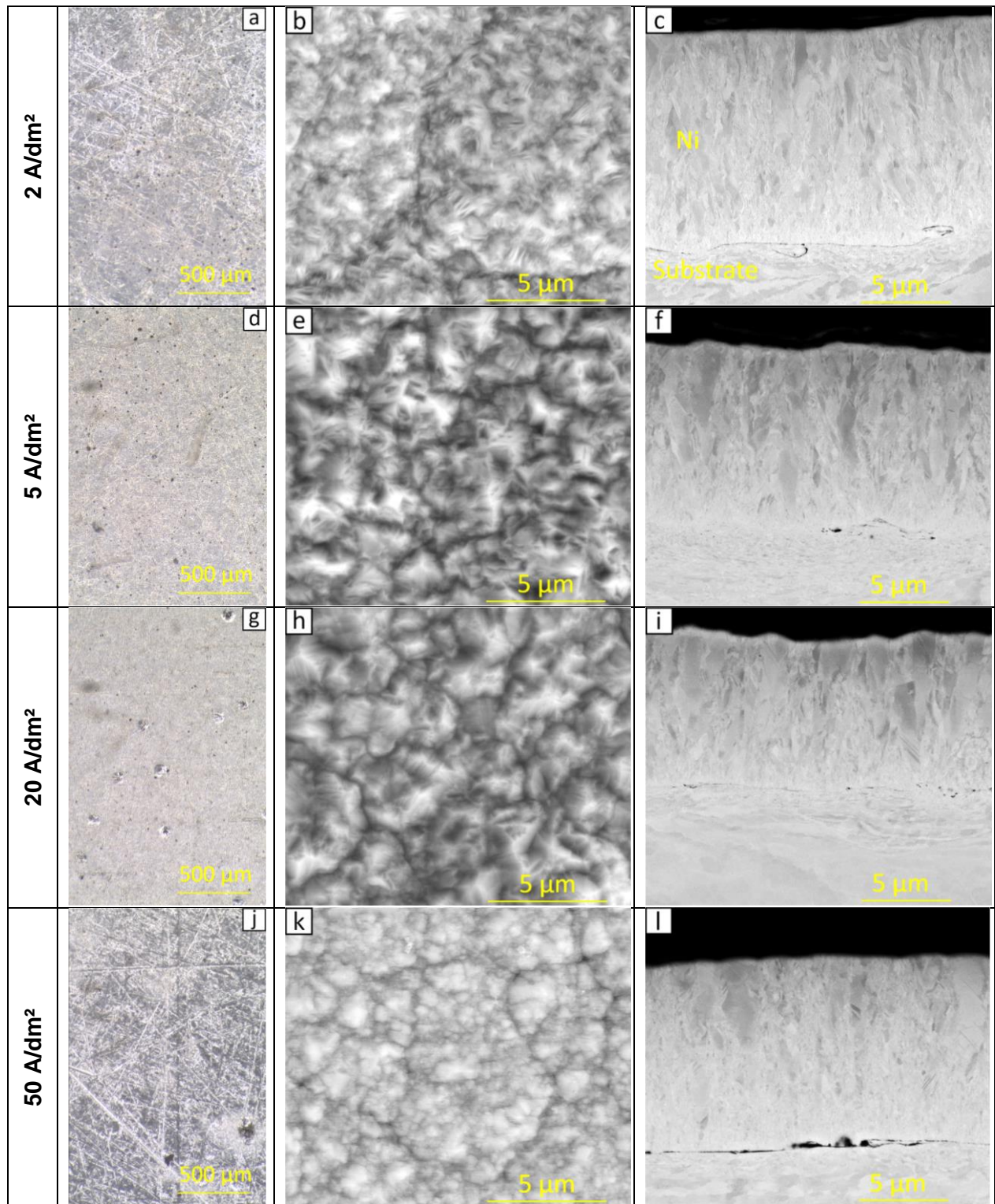


Figure V-13: OM, SEM images of surface (SE) and in cross-section (BSE) of the first layer of nickel for current densities of 2, 5, 20 and 50 A/dm².

Table V-1: Summary table of the thicknesses and visual qualities of the first layer for different current densities and times.

Current density (A/dm ²)	Time (min)	Thickness (μm)	Quality of the first layer (Ni flash)
2	60	12±1	Uniform deposition with shining surface and visible polishing scratches
5	20	10±1	Uniform deposition with low shining surface and low visible polishing scratches
20	5	9±1	Uniform deposition with shining surface and low visible polishing scratches
50	2	10±1	Non-uniform deposition with low shining surface, visible polishing scratches and burnt edge

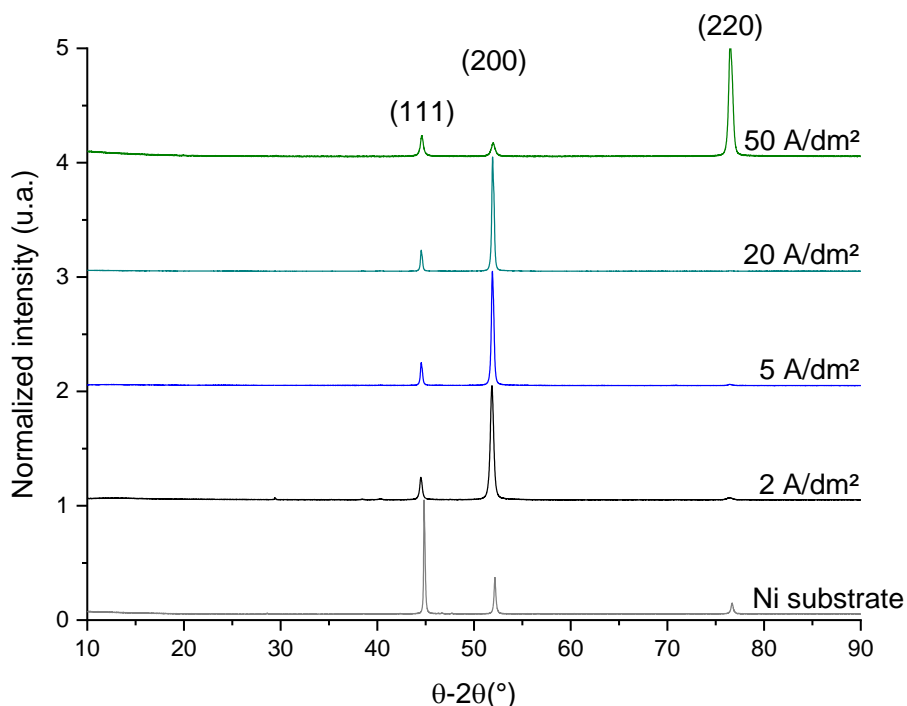


Figure V-14: XRD patterns of the surface of the electrodeposited Ni first layer with current density.

Following these results, it appears that the first Ni flash layers obtained with 5 and 20 A/dm² would be suitable as intermediate layers between the substrate and the subsequent thick electrodeposit. Therefore, further SEM analyses were conducted to underline the differences of both current densities (Figure V-15).

When the electrodeposits are carried out with 5 A/dm² and 20 A/dm², several defects can be observed. The most numerous defects are the polishing scratches randomly appearing on the surface of the samples. The second defect for both current densities is the presence of holes.

These holes do not seem to follow any specific pattern. The third and fourth types of defects are only observed for the electrodeposits made at 20 A/dm^2 . Coarse Ni particles can be observed on the surface of the samples, these large particles have an average size of $10 \pm 4 \mu\text{m}$ (Figure V-15.b). Finally, the last type of defects corresponds to spherical depressions of $73 \pm 34 \mu\text{m}$ (Figure V-15.b). These depressions are assumed to result from the formation of gaseous bubbles on the surface of the samples.

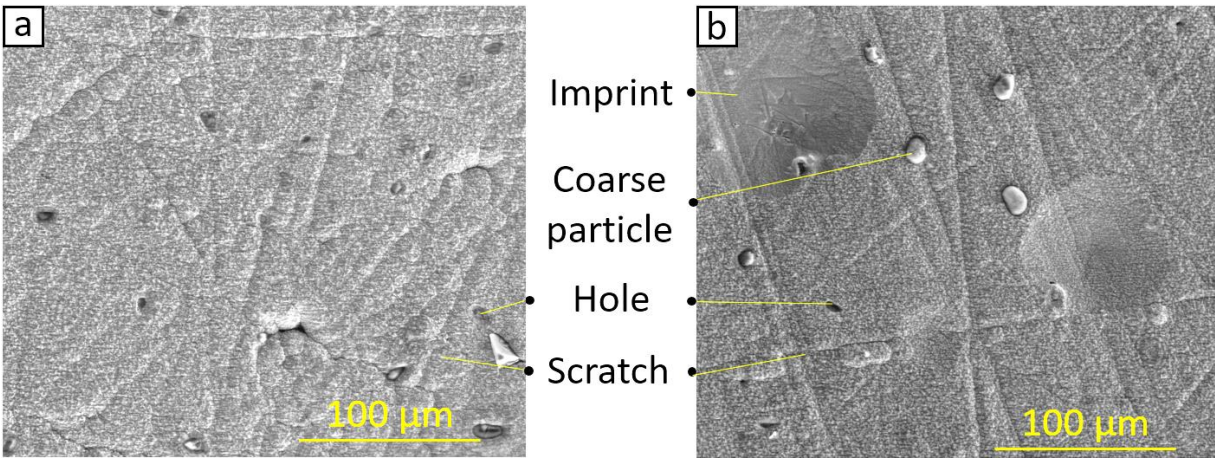


Figure V-15: SEM (SE) surface images of the Ni flash electrodeposit coated on the Ni substrate at (a) 5 A/dm^2 and (b) 20 A/dm^2 .

Since the occurrence of the defects is weaker with 5 A/dm^2 than with 20 A/dm^2 , the first layer electrodeposited with at 5 A/dm^2 was selected for the rest of the study.

In the next part, we will focus on the influence of current density to synthesize composite electrodeposits between Ni and $\text{Al}_3\text{Ni}_{2(\text{ox})}$ particles.

II.B-Electroplating and incorporation of $\text{Al}_3\text{Ni}_{2(\text{ox})}$ particles in a metallic Ni matrix

After studying the influence of current density to electrodeposit the first layer of Ni, we will now focus on the electrodeposition and trapping of $\text{Al}_3\text{Ni}_{2(\text{ox})}$. In a first part, the influence of the current density on the quantity of trapped particles will be studied and, in a second part, we will focus on the aluminizing treatments of composite electrodeposits.

After successfully trapping the preoxidized Al_3Ni_2 intermetallic particles, the electrodeposits will be aluminized. For this, two successive electrodepositions will be carried out. The first layer of Ni will be deposited at 5 A/dm^2 for 10 min with a nickel sulfamate bath and the second at 20 A/dm^2 during $10 \pm 1 \text{ min}$ in a solution of nickel sulfamate containing suspended preoxidized particles. The targeted thicknesses are respectively $10 \mu\text{m}$ and $50 \mu\text{m}$. This total thickness of $60 \mu\text{m}$ was retained because, for the slurry aluminizing route, it often corresponds to the aluminized thickness when spraying 10 mg/cm^2 of aluminum.

II.B.1-Influence of current density

Figure V-16 shows the volume percentage of trapped particles as a function of the current density. For a nickel sulfamate bath at 50°C (Table II-3 Chapter II), when current density increases the amount (volume percentage) of particles trapped increases from 10 to 17.5 % between 2 and 5 A/dm^2 and then stabilizes at 22 % for a current density of 20 A/dm^2 (Figure V-16).

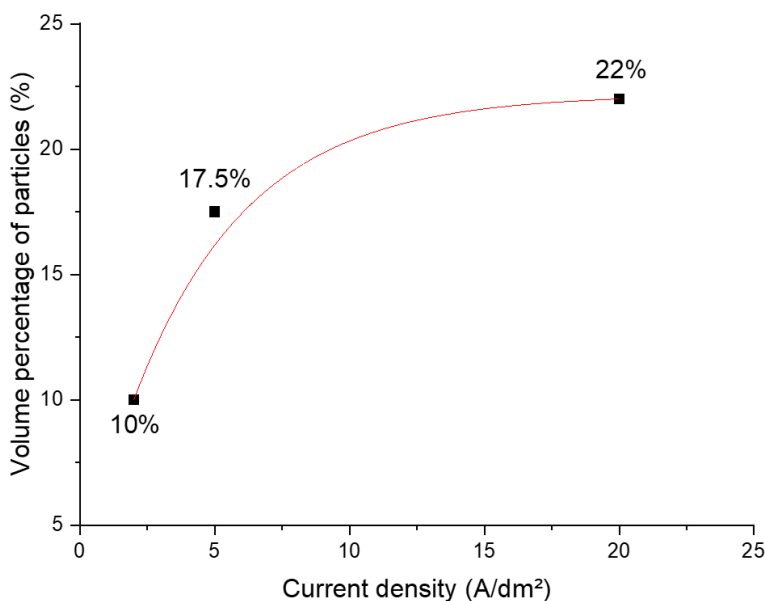


Figure V-16: Volume percentage of $\text{Al}_3\text{Ni}_{2\text{ox}}$ particles trapped in the Ni electrodeposit in function of current density.

Figure V-17 shows a cross-section of the samples after electrodeposition. The particles trapped in the coating are evenly distributed throughout its thickness (Figure V-17.a) except for some clustering of particles (Figure 17.b). One shall note that the particles appear to be stable in the electrodeposition bath since the metallic core and the oxide shell are still observed (Figure V-17.b). The Raman spectroscopy analysis of Figure V-18 allowed to unambiguously identify $\alpha\text{-Al}_2\text{O}_3$ and $\Theta\text{-Al}_2\text{O}_3$ on the shells of the particles. It is highly probable that several phases of aluminum oxide exist. Indeed, for similar oxidation temperatures, a first layer of $\Theta\text{-Al}_2\text{O}_3$ and a second layer of $\alpha\text{-Al}_2\text{O}_3$ have been identified for oxidations on Al_3Ni_2 intermetallic [4].

In addition, the EDS spots at the core of the particles revealed about 30 ± 4 at.% of Al. This concentration appears lower than expected compared with the theoretical value of Al_3Ni_2 (60 at.%). This result can be attributed to the fact that the volume analyzed by the EDS spots larger than the particle size and therefore includes the Ni from the matrix.

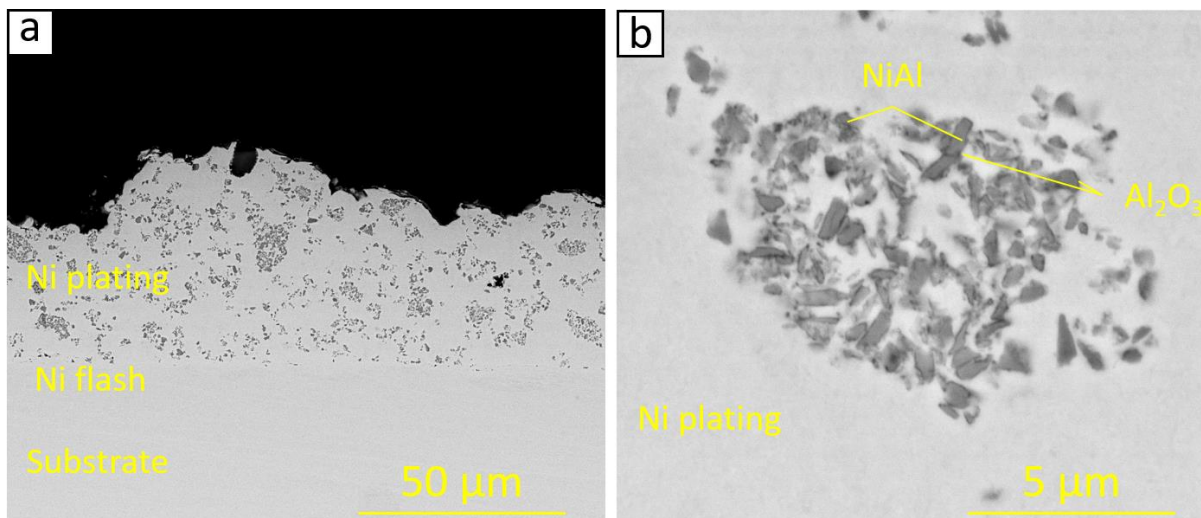


Figure V-17: SEM (BSE mode) cross-sections of the composite electrodeposit with a Ni matrix and preoxidized Al_3Ni_2 particles.

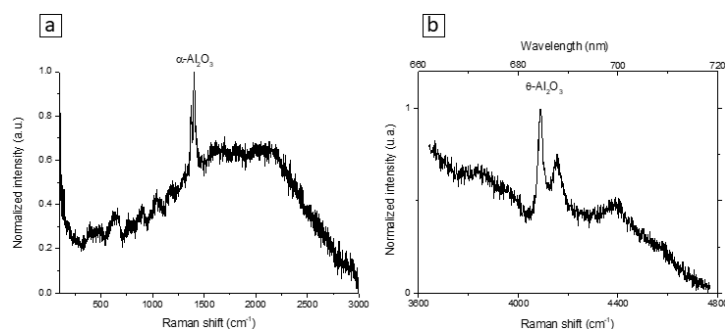


Figure V-18: Raman spectra on the shells of the particles trapped in the electrodeposit obtained at 20 A/dm^2 with (a) spectrum obtained for $\lambda=632 \text{ nm}$ and (b) $\lambda=532 \text{ nm}$ [5-6].

II.B.2-Influence of heat treatment temperature.

Once the electrodeposition of the composite ($\text{Ni}+\text{Al}_3\text{Ni}_2$) coatings achieved, the final step consists in aluminizing by slurry route. For this, “low” temperatures of 650 and 700°C were selected (Figure V-19.a label 1 & 2) based on previous investigations conducted in our research group on Ni-based substrates [7-9]. The high activity low temperature (HALT) aluminizing allows preferential diffusion of aluminum towards the substrate. This results in the formation of the intermetallic coating in the electroplated layer and preserves thus the structure of the coating produced by electrochemical means.

In addition, a short-term aluminizing was carried out at 1100°C (Figure V-19.a, label 3) to achieve a high-activity high temperature (HAHT) aluminizing allowing the preferential outward diffusion of nickel [7,10].

The heat treatments have been carried out in a TGA apparatus following the steps described in Figure V-19.

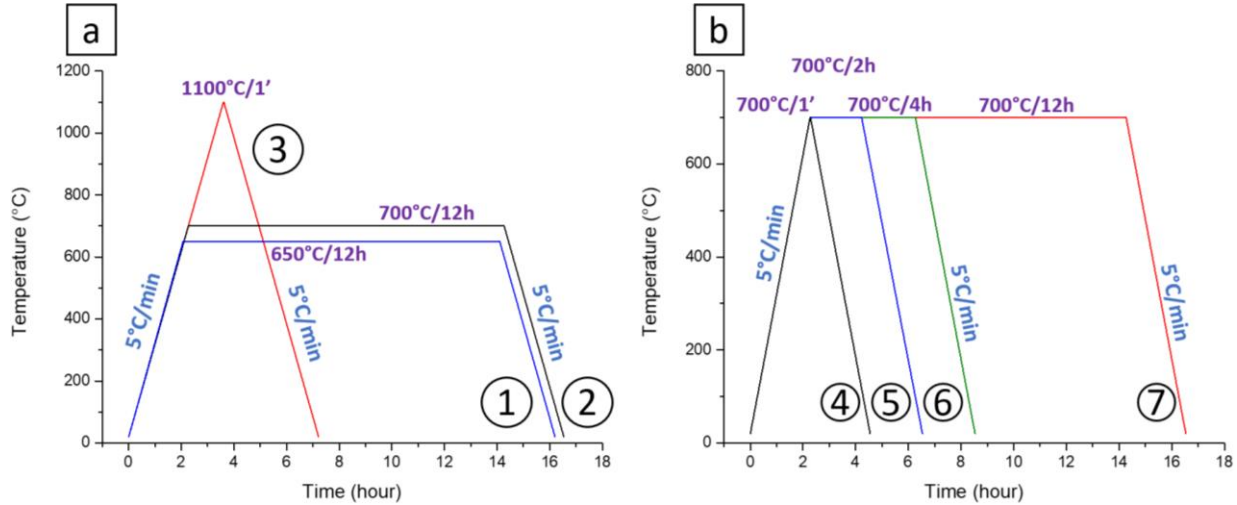


Figure V-19: Schematic drawing of the aluminizing heat treatments (a) for different temperatures and (b) for different times.

Figure V-20 and Figure V-21 respectively show the cross-sections of the aluminized samples at 650°C/12h (Figure V-20.a), 700°C/12h (Figure V-20.b) and 1100°C/1min (Figure V-20.c), the aluminum diffusion profiles of the coating (Figure V-20.a) as well as the thickness of the different layers observed (Figure V-20.b).

For these three heat treatments, the coatings obtained can be divided into four parts. The first part at the top of the coatings consists of a porous Al-rich β -NiAl intermetallic for low-temperature coatings (Figure V-20.a & 20.b) and a porous Ni-rich β -NiAl intermetallic for high-temperature treatment (Figure V-20.c). In addition, inclusions of aluminum oxide can be observed in this layer. This layer appears to come from the solidification of a previous liquid phase, according to its microstructure. The thicknesses of this porous layer are $10 \pm 4 \mu\text{m}$, $12 \pm 2 \mu\text{m}$ and $13 \pm 4 \mu\text{m}$ for respectively, the treatments of 650°C/12h, 700°C/12h, and 1100°C/1min (Figure V-20.b, label “melting layer”).

The second layer is the coating diffusion zone and shows a composite microstructure with the preoxidized Al_3Ni_2 particles in a matrix of β -NiAl and γ' -Ni₃Al intermetallic compounds. The intermetallic compound β -NiAl has a composition similar to the first layer, namely Al-rich β -NiAl for the aluminizing treatments at 650 and 700°C, and Ni-rich β -NiAl for the treatment of 1100°C/1min. The preoxidized particles appear to be homogeneously distributed for the heat treatment of 650°C (Figure V-20.a). For the 700°C treatment, the particles are aligned in lines perpendicular to the surface (Figure V-20.b). For the samples aluminized at 1100°C, the particles seem to be homogeneously distributed in the first two-thirds of this layer (Figure V-20.c). In the last third, no particles can be observed. In addition, the aluminum concentration is low in this part (Figure V-21.a). The composition of aluminum particles is given in Figure V-21.a.

The third layer is the interface between the aluminized part and the poorly-aluminized part. For the 650°C heat treatment (Figure V-20.a), this interface consisted of an oxide. For the two other treatments, this interface is mainly made up of voids and an interfacial decohesion appears for the samples treated at 700°C/12h (Figure V-20.b & 20.c). It can also be noted that, at high

- V. Synthesis of self-regenerating composite coating using electrocodeposition of Ni and preoxidized Al_3Ni_2 -

magnification, oxide particles can be observed on the upper part of the interface between the aluminized and poorly aluminized areas.

Finally, the last “poorly aluminized” layer below the interface is clearly distinguished for the $650^\circ\text{C}/12\text{h}$ treatment, with $10\pm 1\ \mu\text{m}$ of the electrocodeposited layer and $7\pm 1\ \mu\text{m}$ of the first layer of Ni, which have not been aluminized (Figure V-21.a). For the aluminizing treatments at higher temperatures (700 and 1100°C) (Figure V-20.c & 20.c), the interfaces between the electrodeposition and the first layer of Ni are less visible and it is difficult to differentiate these layers.

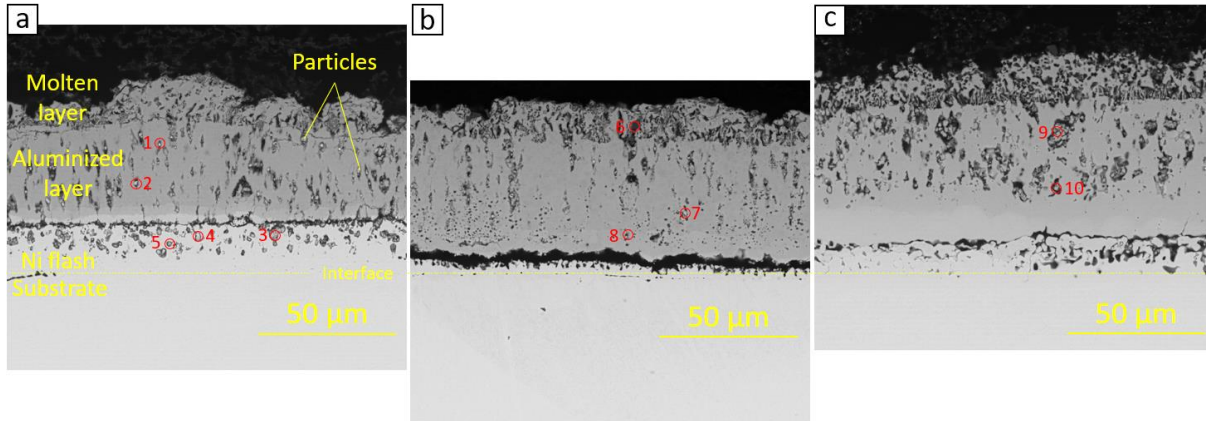


Figure V-20: SEM (BSE mode) cross-section of the aluminized composite coating with a heat treatment of (a) $650^\circ\text{C}/12\text{h}$, (b) $700^\circ\text{C}/12\text{h}$ and (c) $1100^\circ\text{C}/1\ \text{min}$.

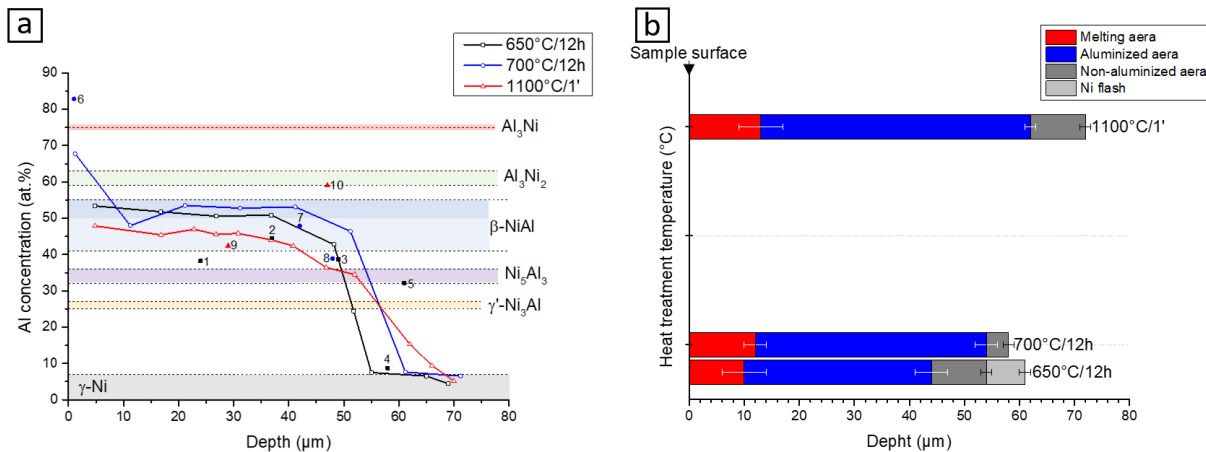


Figure V-21: (a) EDS diffusion profiles made in cross-section for the different heat treatments and (b) the thickness layers of the coatings.

Finally, Raman micro-spectroscopy analyses were carried out to identify the oxides present in the coating (Figure V-22).

In the non-aluminized layer (Figure V-22.a & 22.d), the peaks corresponding to the Θ and $\alpha\text{-Al}_2\text{O}_3$ can be observed for the aluminization treatments of 650°C . For 700 and 1100°C , the presence of $\alpha\text{-Al}_2\text{O}_3$ is predominant. Similar observations can be made at the interface level, with the presence

of Θ and $\alpha\text{-Al}_2\text{O}_3$ for aluminization treatments of 650 and 700°C (Figure V-22.b & 22.e). Finally, for the aluminized layer, contradictory spectra are obtained for the analyses carried out with the laser of 632 and 532 nm. Indeed, $\Theta\text{-Al}_2\text{O}_3$ is mainly observed for the $\lambda=632$ nm (Figure V-22.c) while for the $\lambda=532$ nm, only the $\alpha\text{-Al}_2\text{O}_3$ peaks are observable (Figure V-22.f). These contradictory spectra seem to indicate the presence of the two phases of aluminum oxide.

Finally, for the aluminization treatment of 700°C/12h, the peaks corresponding to SiO_2 could be identified (Figure V-22.c). These peaks are caused by the OPS polishing solution which remained trapped in the pores present between the particles and the coating.

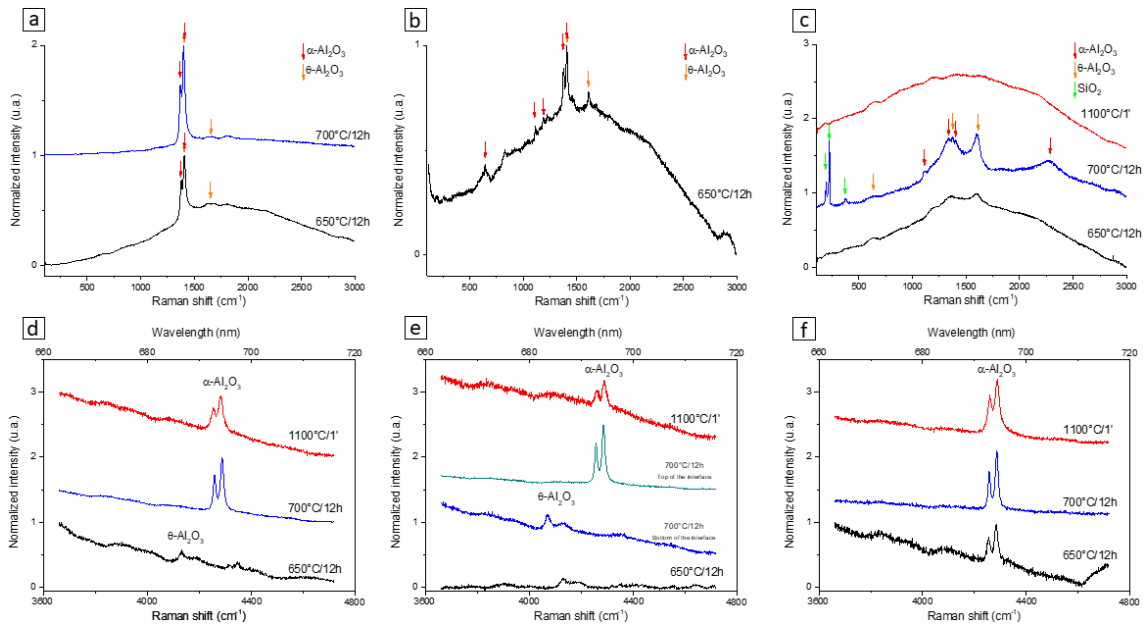


Figure V-22: Raman spectra ($\lambda=632$ nm for (a), (b) and (c) and $\lambda=532$ nm for (d), (e) and (f)) on the cross-sections of the samples after the aluminization process, with (a and d) in the particles on the non-aluminized layer, (b and e) interface layer and (c and f) in the particles on the aluminized layer [5-6, 11-12].

II.B.3-Influence of heat treatment time

In the previous part, three heat treatment temperatures were conducted at 650, 700 and 1100°C. The temperature of 700°C was selected to continue the investigations and study the influence of heat treatment time on the development of the composite coating.

The microstructures of the coating after reaction with Al at 700°C during 1 min, 2, 4 and 12h are shown in Figure V-23. The diffusion profiles and the thicknesses of the layers are presented in Figure V-24. For the heat treatments of 1 min (Figure V-23.a), 2h (Figure V-23.b) and 4h (Figure V-23.c), the microstructure, composition and coating thickness obtained are quite similar and comparable to what was obtained at 650°C/12h (Figure 20.a). Indeed, a first porous layer due to the solidification of a liquid phase can be observed at the surface of the coating. This layer is rich in Al, with a content greater than 56 at. % of Al (Figure V-24.a). The second layer consists of Al-

- V. Synthesis of self-regenerating composite coating using electrocodeposition of Ni and preoxidized Al_3Ni_2 -

rich $\beta\text{-NiAl}$ and $\text{Al}_3\text{Ni}_{2(\text{ox})}$ particles whose thicknesses range between 25 and 33 μm (Figure V-24.b). Underneath, the non-aluminized composite electroplating is about 7 ± 1 μm thick and the Ni flash layer over the substrate kept its thickness (10 ± 1 μm) (Figure V-24.b). It is interesting to note that the longer the aluminizing time at 700°C , the more porous becomes the interface between the aluminized and non-aluminized layers (Figure V-23).

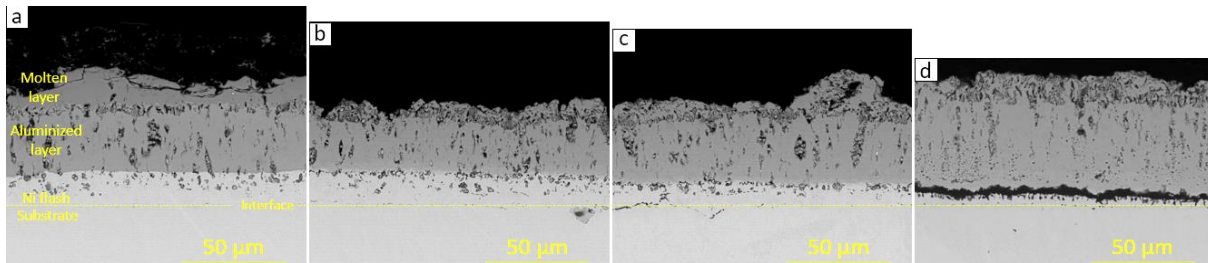


Figure V-23: SEM (BSE mode) cross-section of the aluminized composite coating with a heat treatment of 700°C during (a) 1 min, (b) 2h, (c) 4h and (d) 12h.

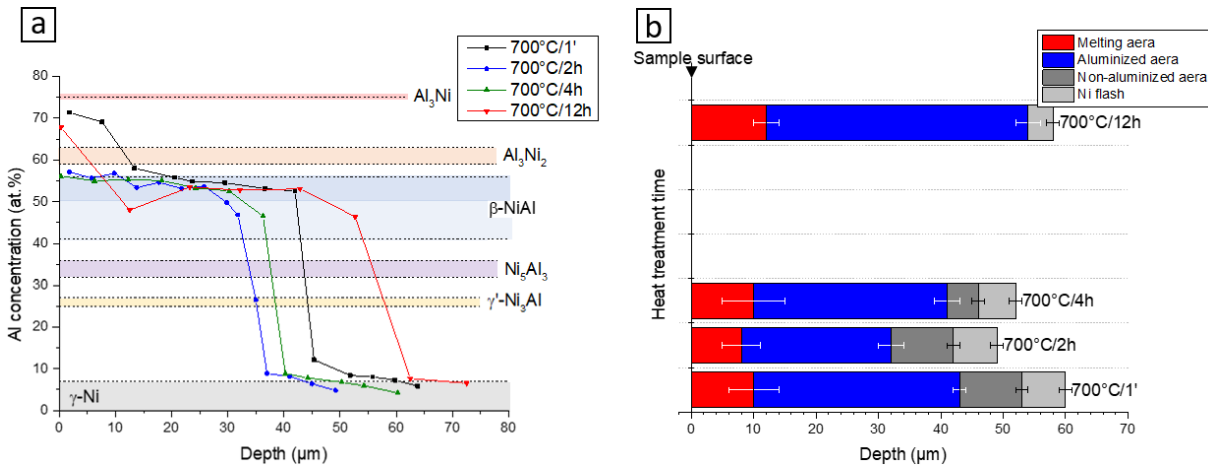


Figure V-24: (a) EDS diffusion profiles made in cross-section for the different heat treatments at 700°C and (b) the thickness layers of the coatings.

The analyses of Raman spectroscopy shown in Figure V-25 for the different aluminizing times indicate the formation different phases of aluminum oxide.

In the non-aluminized layer (Figure V-25.a & 25.d), peaks corresponding to the $\alpha\text{-Al}_2\text{O}_3$ can be observed for the heat treatments of 12h at 700°C . For shorter times, the analyses carried out with a 532 nm laser (Figure V-25.d) show the presence of $\alpha\text{-Al}_2\text{O}_3$ and for the analyses carried out with the 632 nm laser (Figure V-25.a), these peaks of $\alpha\text{-Al}_2\text{O}_3$ are not observed. This strongly suggests the main presence of $\alpha\text{-Al}_2\text{O}_3$ for times greater than 12h and the presence of several phases of aluminum oxide for shorter times. At the interface of the samples treated at $700^\circ\text{C}/12\text{h}$ (Figure V-25.b), the Θ and $\alpha\text{-Al}_2\text{O}_3$ are observed (Figure V-25.e).

Finally, in the aluminized layer (Figure V-25.c & 25.f), the presence of the $\Theta\text{-Al}_2\text{O}_3$ seems to predominant for the different processing times, although for analyses with the 532 nm laser, $\alpha\text{-Al}_2\text{O}_3$ is also observed (Figure V-25.f). In addition, for the heat treatments of 12h, the $\alpha\text{-Al}_2\text{O}_3$

peaks begin to appear (Figure V-25.c) and some traces of SiO_2 due to the polishing OPS solution are also visible. It therefore seems that the aluminized area requires greater aluminizing time to allow the transformation of Θ in $\alpha\text{-Al}_2\text{O}_3$. than the non-aluminized layer, for which a majority of $\alpha\text{-Al}_2\text{O}_3$. Since the oxidation temperature is the same, this difference can only be attributed to the greater content of oxygen in the aluminized area according to Garriga-Majo et al. [13]

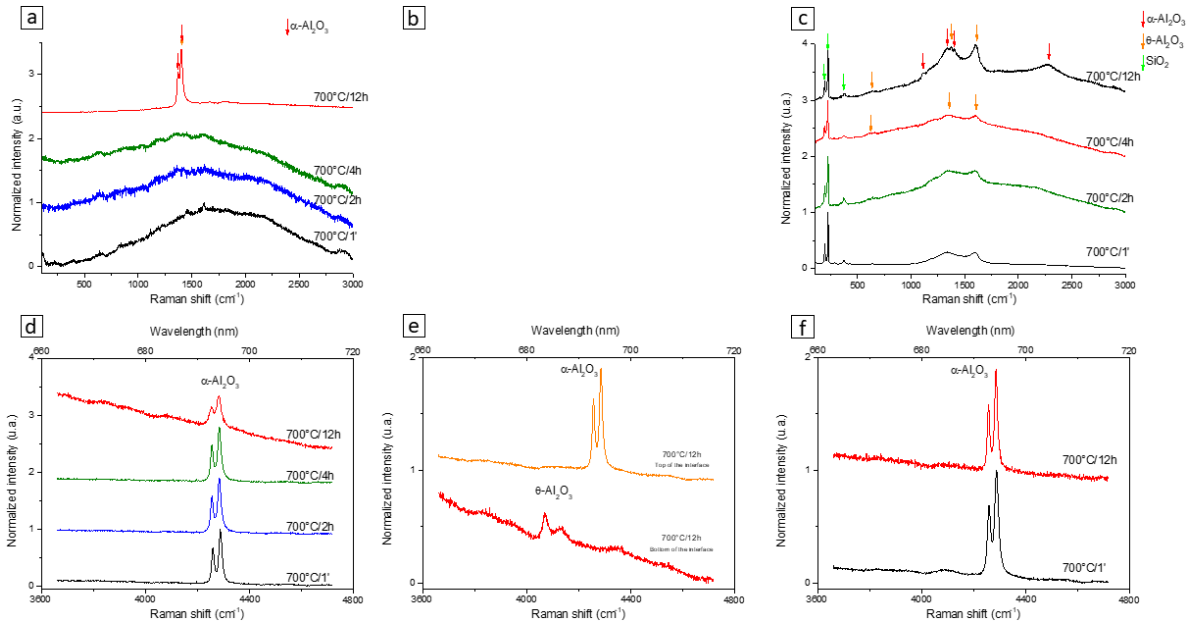


Figure V-25: Raman spectra ($\lambda=632$ nm for (a), (b) and (c) and $\lambda=532$ nm for (d), (e) and (f)) on the cross-sections of the samples after the aluminization process, with (a and d) in the particles on the non-aluminized layer, (b and e) interface layer and (c and f) in the particles on the aluminized layer [5-6, 11-12].

III- Isothermal oxidation

This section deals with the characterization of the self-regenerating nature of the obtained composite coatings. For this, preliminary isothermal oxidation tests of various nickel aluminide coatings prepared from four coatings and two aluminizing treatments were carried out in air at 1000°C for 48 h. Therefore, these oxidation tests were not intended to finely characterize the oxidation behavior of the coatings but to demonstrate (or not) the self-regenerating nature of the coatings.

Aluminizing on a raw nickel substrate and on a nickel electrodeposit have been used as references. These two coatings have been formed following an aluminizing treatment of $700^\circ\text{C}/2\text{h}$ or $700^\circ\text{C}/2\text{h}+1100^\circ\text{C}/1\text{min}$ (designated thereafter as “ $1100^\circ\text{C}/1\text{min}$ ”) (Figure V-26). The nickel plating has been deposited from a bath of nickel sulfamate and with a current density of $20 \text{ A}/\text{dm}^2$.

The two composite coatings tested were a coating consisting of the first flash layer of electrodeposited Ni and a second $\text{Ni}/\text{Al}_3\text{Ni}_{2(\text{ox})}$ composite layer. For the second coating, only the composite $\text{Ni}/\text{Al}_3\text{Ni}_{2(\text{ox})}$ layer has been coated, i.e. with no electrodeposited flash of Ni. The coatings tested are summarized in Table V-2.

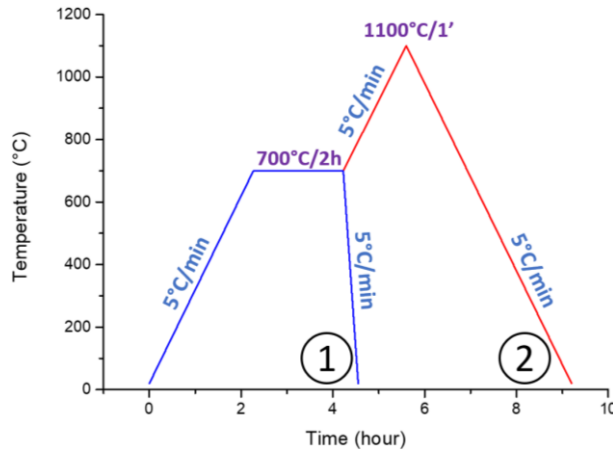


Figure V-26: Schematic drawing of the aluminizing treatments of $700^\circ\text{C}/2\text{h}$ and $700^\circ\text{C}/2\text{h}+1100^\circ\text{C}/1\text{min}$.

Table V-2: Summary table of the coatings tested in isothermal oxidation ($1000^\circ\text{C}/48\text{h}$ in air).

Substrate	First Ni layer	$\text{Al}_3\text{Ni}_{2(\text{ox})}+\text{Ni}$	Aluminization treatment
Ni	---	---	$700^\circ\text{C}/2\text{h}$
	---	---	$700^\circ\text{C}/2\text{h} + 1100^\circ\text{C}/1 \text{ min}$
	$50 \mu\text{m}$	---	$700^\circ\text{C}/2\text{h}$
	$50 \mu\text{m}$	---	$700^\circ\text{C}/2\text{h} + 1100^\circ\text{C}/1 \text{ min}$
	$10 \mu\text{m}$	$50 \mu\text{m}$	$700^\circ\text{C}/2\text{h}$
	$10 \mu\text{m}$	$50 \mu\text{m}$	$700^\circ\text{C}/2\text{h} + 1100^\circ\text{C}/1 \text{ min}$
	---	$50 \mu\text{m}$	$700^\circ\text{C}/2\text{h}$
	---	$50 \mu\text{m}$	$700^\circ\text{C}/2\text{h} + 1100^\circ\text{C}/1 \text{ min}$

III.A-Microstructure and composition

III.A.1-Aluminizing and isothermal oxidation of the coating carried out on the raw substrate

Aluminizing of the raw substrates requires a few preparation steps to achieve the diffusion coating like the ones shown in Figure V-27.

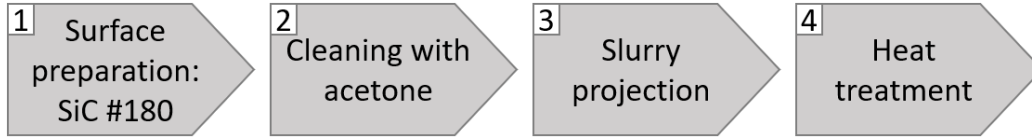


Figure V-27: Schematic representation of the different steps for obtaining an Al-diffusion coating on a raw substrate (Ni).

Figure V-28 shows the cross-sections of the coating made after the aluminizing treatment of $700^\circ\text{C}/2\text{h}$ (Figure V-28.a) and $1100^\circ\text{C}/1\text{ min}$ (Figure V-28.b). In addition, the EDS concentration profiles are plotted later in the manuscript in Figure V-39.a for the heat treatment of $700^\circ\text{C}/2\text{h}$ and Figure V-39.b for the heat treatment of $1100^\circ\text{C}/1\text{ min}$.

Three main layers can be observed in Figure V-28.a & V-28.b for, respectively, $700^\circ\text{C}/2\text{h}$ and $1100^\circ\text{C}/1\text{min}$ aluminizing heat treatment. The first layer of about $21\pm 1\ \mu\text{m}$ at the top of the coating consists of a multitude of micrometric grains with a composition of Al-rich $\beta\text{-NiAl}$ for the treatment of $700^\circ\text{C}/2\text{h}$ (Figure 28.a & V-39), in line with the pioneer work of Pedraza et al. on the slurry aluminizing of pure Ni substrate [14]. In contrast, the grain size obtained with the $1100^\circ\text{C}/1\text{min}$ treatment is similar to the thickness ($16\pm 2\ \mu\text{m}$) of the Ni-rich $\beta\text{-NiAl}$ upper layer (Figure 28.b & V-40.a). The second main coating layer is made up of a $2\pm 1\ \mu\text{m}$ thick Ni-rich $\beta\text{-NiAl}$ intermetallic compounds for the $700^\circ\text{C}/2\text{h}$ treatment (Figure V-28.a & V-39.a) and of a $18\pm 1\ \mu\text{m}$ thick layer with a composition close to the Ni_5Al_3 intermetallic compound (Figure V-28.b & V-40.a) although this phase is supposedly thermodynamically unstable above 700°C [15]. The last sublayers right above the substrate are similar in thickness ($\sim 5\ \mu\text{m}$) (Figure V-28) and composition (Ni_3Al) for both coatings (Figure V-39.a & V-40.a). In addition, one can note the presence of a few round pores in this layer (Figure V-28.b).

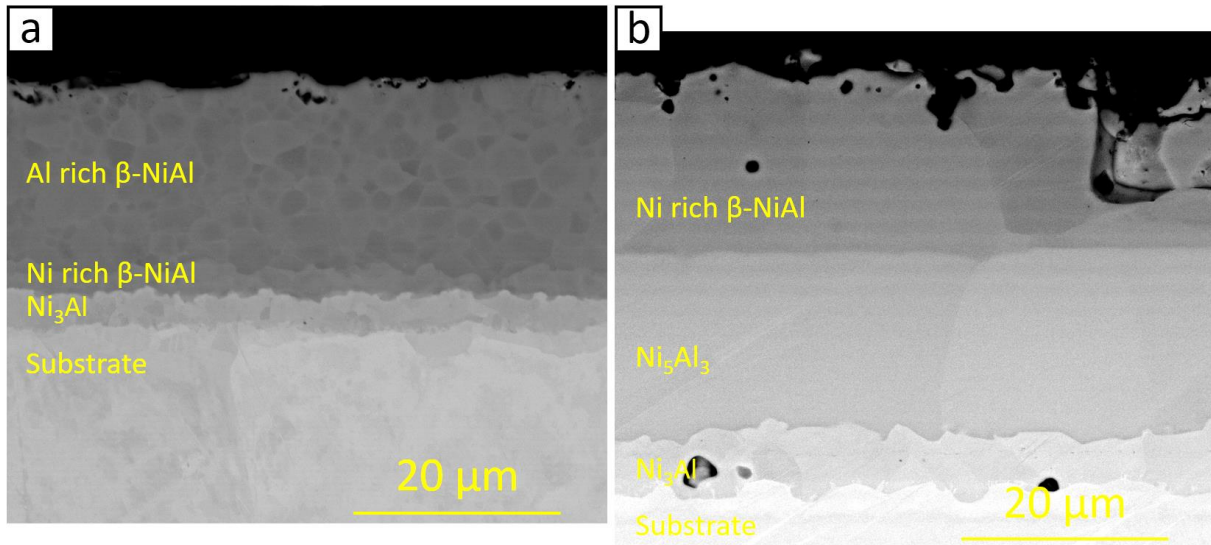


Figure V-28: SEM (BSE) mode cross-section of the aluminized substrate with heat treatment of (a) 700°C/2h and (b) 1100°C/1min.

Following the aluminizing step, the samples were oxidized at 1000°C for 48h. The two main coating layers shown in Figure V-29 have the same composition ($\text{Ni}_5\text{Al}_3 + \text{Ni}_3\text{Al}$ on top and $\text{Ni}_3\text{Al} + \text{Ni}(\text{Al})$ at the bottom, Figures V-39.b & V-40.b) but the thicknesses are slightly greater ($30 \pm 3 \mu\text{m}$ and $19 \pm 2 \mu\text{m}$ vs. $13 \pm 3 \mu\text{m}$ and $20 \pm 3 \mu\text{m}$) with the additional step at 1100°C/1min in line with a fostered interdiffusion. It is also important to note that following the oxidation tests, a thin layer of α - Al_2O_3 developed on the surface of the coatings (Figure V-41.a & V-42.a). However, for the sake of contrasting conditions in the backscattered electron mode, this $1 \pm 0.7 \mu\text{m}$ oxide layer cannot be observed in Figure V-29.

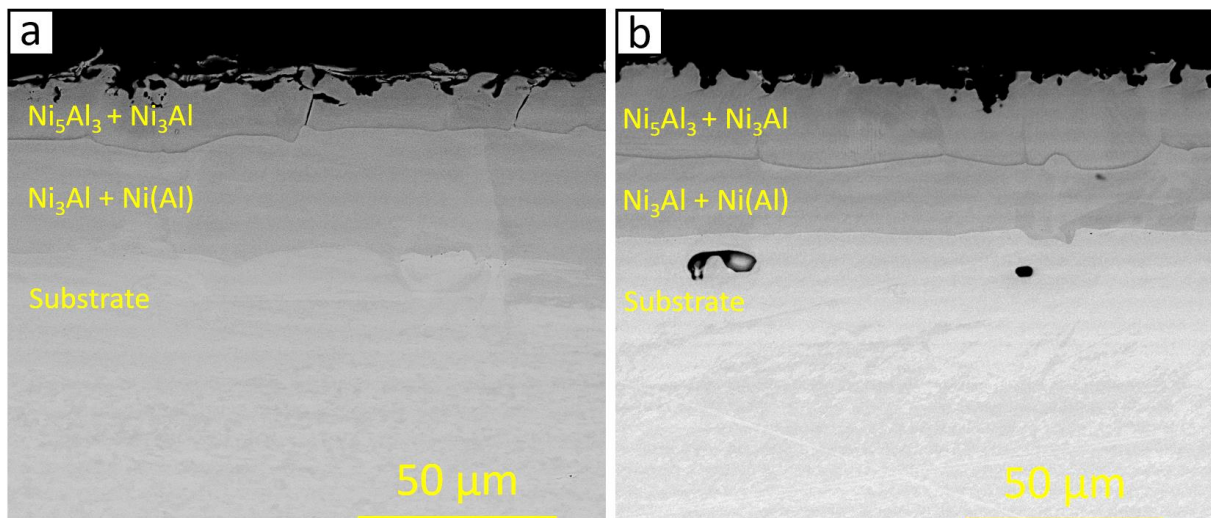


Figure V-29: SEM (BSE) cross-section of the aluminized substrate ((a) 700°C/2h and (b) 1100°C/1min) after isothermal oxidation of 1000°C/48h in synthetic air.

III.A.2-Aluminizing and isothermal oxidation of nickel plating

The second reference coating is the diffusion coating obtained on nickel electrodeposits. The different preparation steps are summarized and given in Figure V-30.

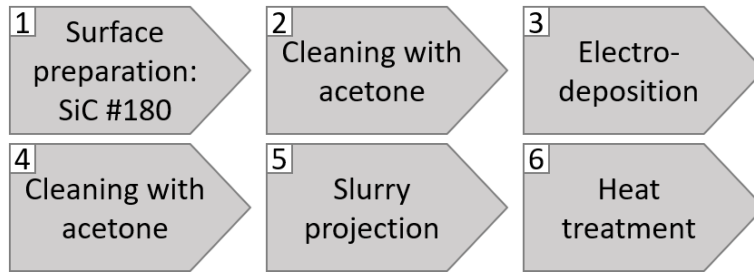


Figure V-30: Schematic representation of the different steps for obtaining an Al diffusion coating on a nickel electroplated layer.

The coatings obtained on the Ni plating are made up of several heterogeneous layers (Figure V-31).

For the coating of $700^\circ\text{C}/2\text{h}$, the first layer of $31\pm 3\ \mu\text{m}$ consists of Ni-rich $\beta\text{-NiAl}$ intermetallic and displays many defects with a bubble shape escaping from the layer (Figure V-31.a & V-39.a). Other smaller pores and cracks are also present. In addition, areas with a lower concentration of aluminum (light contrast) can be observed at the bottom of this layer. At the aluminized and non-aluminized layers, a porous interface with aluminum oxide crystals on the edges of the interface appear at higher magnifications (Figure V-31.a).

The second coating layer seems to correspond to the non-aluminized nickel plating (Figure V-31.a). This $21\pm 3\ \mu\text{m}$ thick layer is porous and the aluminum concentration does not exceed 7 at. % (Figure V-39). Finally, the interface between the coating and the substrate is also porous.

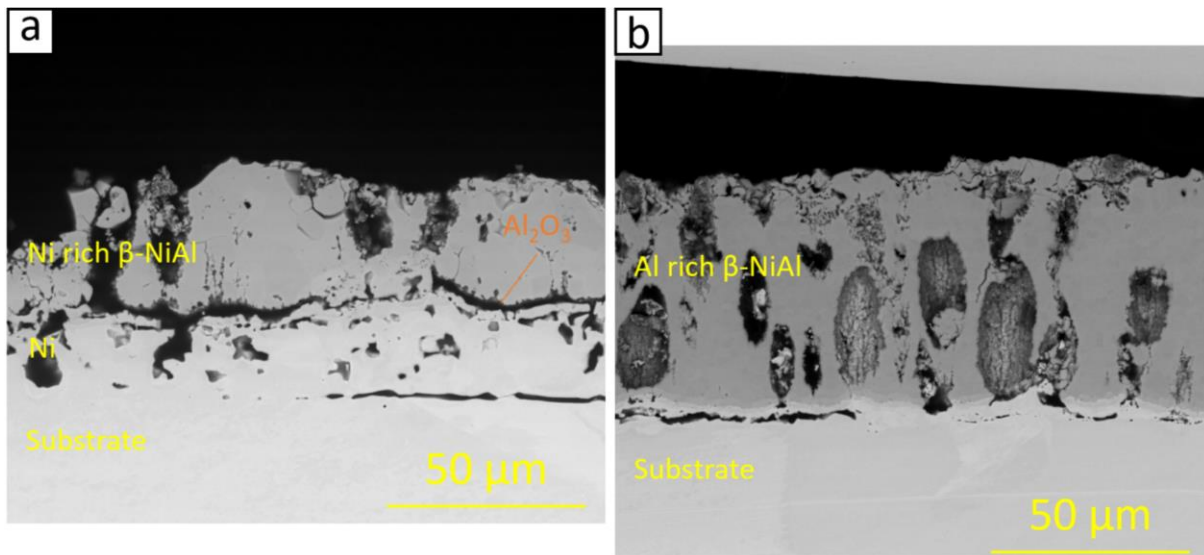


Figure V-31: SEM (BSE) mode cross-section of the aluminized Ni plating substrate with heat treatment of (a) $700^\circ\text{C}/2\text{h}$ and (b) $1100^\circ\text{C}/1\text{min}$.

When adding the second aluminizing step of $1100^\circ\text{C}/1\text{min}$, the coating consists of 1 main layer and three very thin layers (Figure V-31.b). The first layer is the thickest, with an average thickness of $62\pm 5\ \mu\text{m}$, and consists of Al-rich $\beta\text{-NiAl}$ as well as pores (Figure V-40.a). The pores also take the form of « bubbles » running perpendicular to the surface as if they tried to raise the surface. The three consecutive thin layers towards the substrate are composed of Ni-rich $\beta\text{-NiAl}$, $\gamma\text{-Ni}_3\text{Al}$, and $\gamma\text{-Ni}(\text{Al})$. Finally, a porous interface can again be observed between the $\gamma\text{-Ni}(\text{Al})$ layer and the substrate (Figure V-31.b).

After the oxidation, the aluminide coating becomes surrounded by oxides (Figure V-32). On the surface of the coatings, $\alpha\text{-Al}_2\text{O}_3$ with a thickness of $6\pm 2\ \mu\text{m}$ can be observed (Figure V-32, V-41.a & V-42.a). Below, the composition of the $700^\circ\text{C}/2\text{h}$ aluminide coating is that of $\gamma\text{-Ni}_3\text{Al}$ (Figure V-32.a) and equivalent to the compound Ni_5Al_3 for the treatment of $1100^\circ\text{C}/1\text{min}$ (Figure V-32.b). Within the aluminized layer, many grains of $\alpha\text{-Al}_2\text{O}_3$ can be observed (Figure V-41.b & V-42.b).

Between the aluminized layer and the non-aluminized layer, a sequence of $\alpha\text{-Al}_2\text{O}_3$, NiAl_2O_4 and NiO grow following the increasing gradient of Ni towards the electrodeposit (Figure V-32, V-41.c & V-42.c). In addition, some pores develop in the NiO area of the coatings formed with the addition aluminizing step of $1100^\circ\text{C}/1\ \text{min}$ (Figure V-32.b).

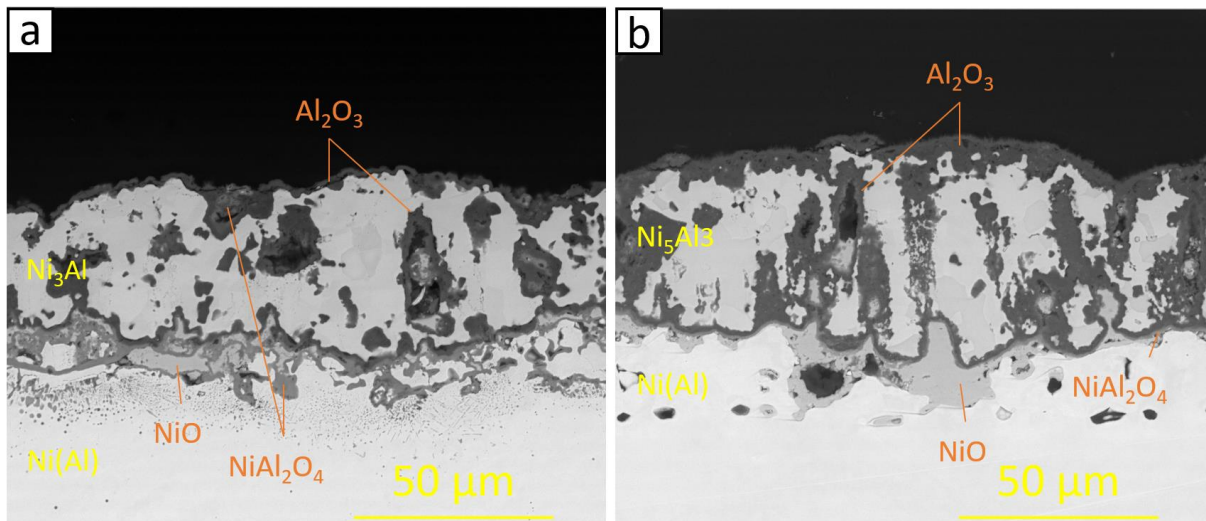


Figure V-32: SEM (BSE) cross-section of the aluminized Ni plating ((a) $700^\circ\text{C}/2\text{h}$ and (b) $1100^\circ\text{C}/1'$) after isothermal oxidation of $1000^\circ\text{C}/48\text{h}$ in synthetic air.

III.A.3-Aluminizing and isothermal oxidation of composite electrodeposits with “Ni flash”

The coatings studied in this part are similar to those discussed in part V-II, i.e. a first electrodeposit of pure Ni at $5\ \text{A}/\text{dm}^2$ followed by a second composite $\text{Ni}+\text{Al}_3\text{Ni}_{2(\text{ox})}$ coating at $20\ \text{A}/\text{dm}^2$. The different steps for the synthesis of this coating are detailed in Figure V-33.

- V. Synthesis of self-regenerating composite coating using electrocodeposition of Ni and preoxidized Al_3Ni_2 -

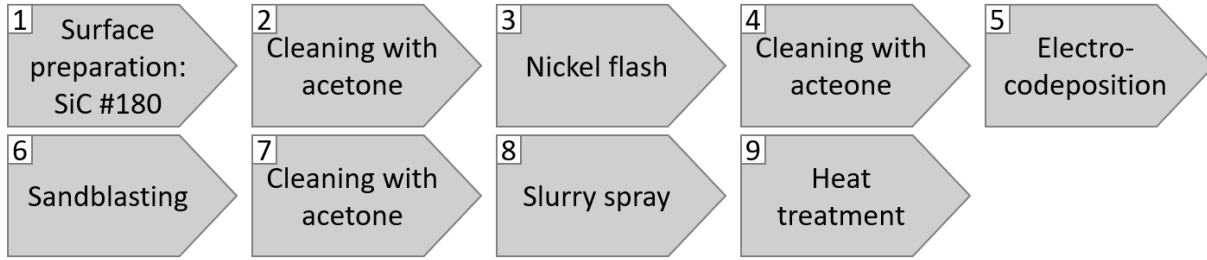


Figure V-33: Schematic representation of the different step for obtaining a composite diffusion coating (with a first layer of Ni).

For the aluminizing treatment of $700^\circ\text{C}/2\text{h}$, the first layer of $28\pm 2\ \mu\text{m}$ is composed of Ni-rich $\beta\text{-NiAl}$ and preoxidized Al_3Ni_2 particles (Figure V-34.a & V-39.a). In addition, pores vertically aligned appear. The Ni(Al) sublayer corresponding to the Ni electrodeposit has an average thickness of $21\pm 2\ \mu\text{m}$ and ends with an interface containing pores (Figure V-34.a). Between the two main coating layers, several very thin layers form but the EDS spot analyses are too large to unambiguously identify any particular intermetallic compound.

Increasing the aluminizing treatment to $1100^\circ\text{C}/1\ \text{min}$ results in a $34\pm 5\ \mu\text{m}$ thick Ni-rich $\beta\text{-NiAl}$ external sublayer (Figure V-34.b & V-40.a) over a particle and pore-free zone with a Ni_5Al_3 composition. Below, a porous interface can be observed (Figure V-34.b). Next comes, the Ni(Al) composite electrodeposit with many pores (Figure V-34.b).

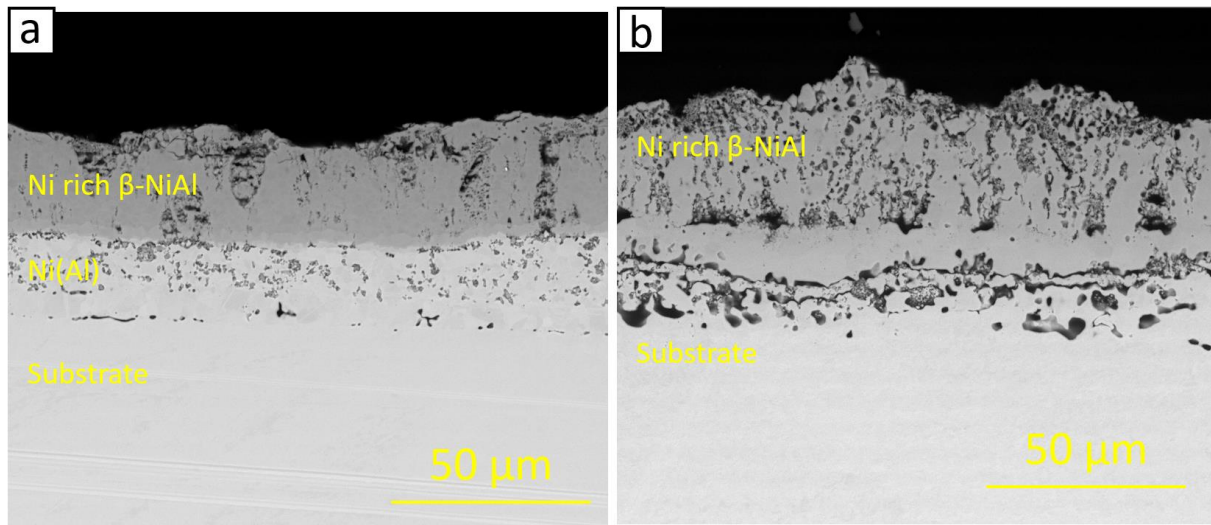


Figure V-34: SEM (BSE) mode cross-section of the aluminized $\text{Ni}/\text{Al}_3\text{Ni}_{2(\text{ox})}$ composite electrodeposit with heat treatment of (a) $700^\circ\text{C}/2\text{h}$ and (b) $1100^\circ\text{C}/1\ \text{min}$ (with a first layer of Ni).

After oxidation at $1100^\circ\text{C}/48\text{h}$ in air, the cross-sections of both coatings are quite similar with an aluminized layer covered with an $\alpha\text{-Al}_2\text{O}_3$ oxide scale (Figure V-33, Figures V-41.a & V-42.a). The aluminized layer has a composition close to the Ni_5Al_3 compound (Figure V-39.b & V-40.b) and contains many grains of $\alpha\text{-Al}_2\text{O}_3$ (Figure V-41.b & V-42.b). This layer has an average thickness of $30\pm 10\ \mu\text{m}$ for the heat treatment of $700^\circ\text{C}/2\text{h}$ (Figure V-39.b) and $19\pm 8\ \mu\text{m}$ for the heat treatment of $1100^\circ\text{C}/1\text{min}$ (Figure V-40.b). A thin layer of $\alpha\text{-Al}_2\text{O}_3$ and NiAl_2O_4 spinel (Figure V-41.c & V-

42.c) grows underneath at the interface with the Ni(Al) layer that contains numerous clusters of α - Al_2O_3 , spinel NiO and a few pores (Figure V-35.b).

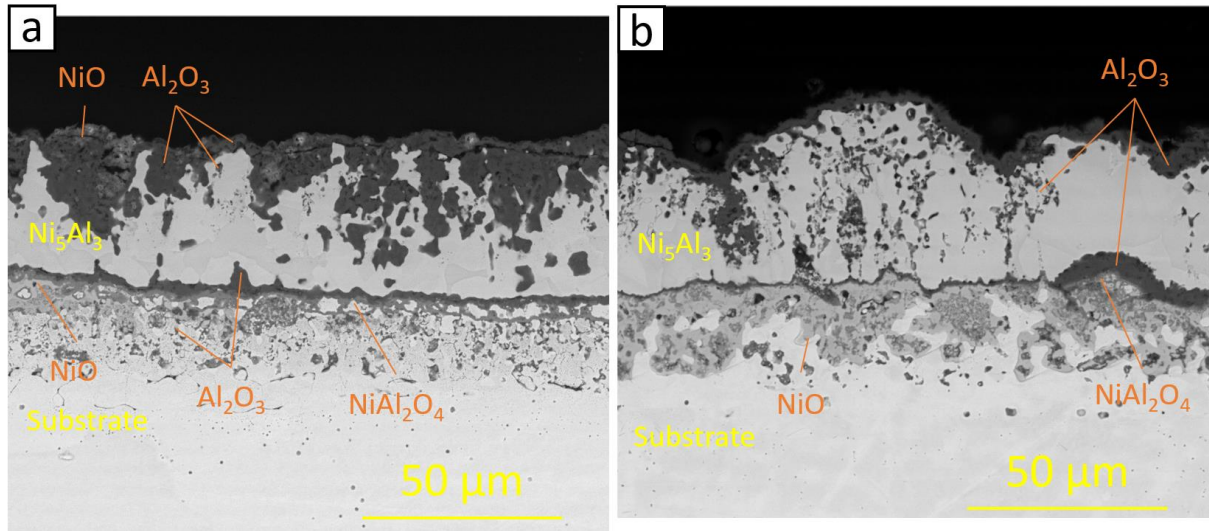


Figure V-35: SEM (BSE) cross-section of the aluminized $\text{Ni}/\text{Al}_3\text{Ni}_{2(\text{ox})}$ composite electrodeposit ((a) $700^\circ\text{C}/2\text{h}$ and (b) $1100^\circ\text{C}/1\text{min}$) after isothermal oxidation of $1000^\circ\text{C}/48\text{h}$ in synthetic air (with a first layer of Ni).

III.A.4-Aluminizing and isothermal oxidation of composite electrodeposits without “Ni flash”

The last coating studied corresponds to the composite $\text{Ni}+\text{Al}_3\text{Ni}_{2\text{ox}}$ electroplating, i.e. without the initial Ni flash electrodeposit (Figure V-36).

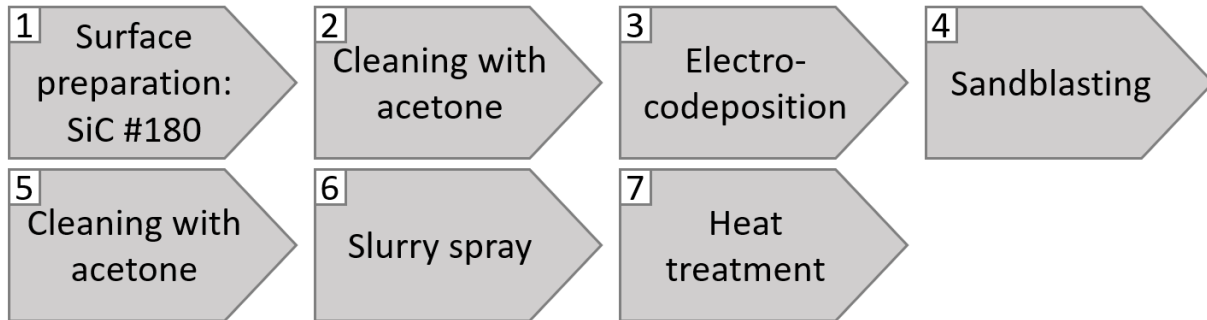


Figure V-36: Schematic representation of the different step for obtaining a composite diffusion coating.

The coatings obtained with an aluminizing heat treatment of $700^\circ\text{C}/2\text{h}$ and $1100^\circ\text{C}/1\text{min}$ exhibit two distinct zones: a first heavily "aluminized" zone on top of a second "less-aluminized" of Ni(Al) (Figure V-37). The first aluminized layer consists of an Al-rich β -NiAl intermetallic compound for the aluminizing treatment of $700^\circ\text{C}/2\text{h}$ (Figure V-39.a) while a Ni-rich β -NiAl and Ni_5Al_3 formed when the aluminizing was increased to $1100^\circ\text{C}/1\text{min}$ (Figure V-40.a). In addition, the Al-rich area contains many pores unlike the Ni-rich area (Figure V-37.b). The average thickness of these layers is $29\pm 4\ \mu\text{m}$ and $39\pm 2\ \mu\text{m}$ for respectively, the aluminizing treatments of $700^\circ\text{C}/2\text{h}$ and

1100°C/1min. The second layers over the substrate is much less aluminized and Al incorporates into the Ni matrix (substrate) as Ni(Al). It is interesting to remark that the preoxidized particles can be readily observed for the 700°C/2h and 1100°C/1min aluminizing treatments (Figures V-37.a & 37.b) but the latter also display some pores.

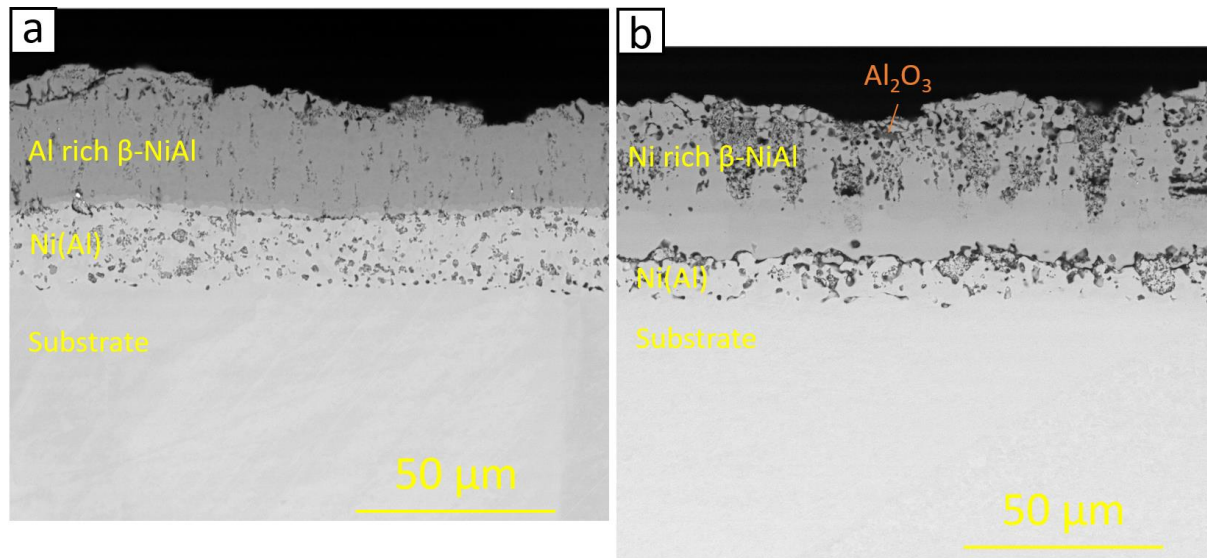


Figure V-37: SEM (BSE) mode cross-section of the aluminized $\text{Ni}/\text{Al}_3\text{Ni}_{2(\text{ox})}$ composite electrodeposit with heat treatment of (a) 700°C/2h and (b) 1100°C/1 min (no Ni flash layer over the Ni substrate).

After the isothermal oxidation, some minor changes occur in the coatings (figure V-36) and relate just to some thickening ($34 \pm 4 \mu\text{m}$) and greater oxidation of the trapped particles to result in Al_2O_3 in a Ni-rich β -NiAl matrix (Figure V-38.a & 41.b). The α - Al_2O_3 scale is just $2 \pm 1 \mu\text{m}$ thick and homogeneously covers the coating (Figure V-41.a). Another Al_2O_3 oxide layer develops between the Al-rich and the Al-poor layers of the coating, that could act as a diffusion barrier (Figure V-41.c). It is also interesting to remark that the $\text{Al}_3\text{Ni}_{2(\text{ox})}$ particles in the less-aluminized area are oxidized further like in the upper coating layer (Figure V-38.a). This suggests that either the coatings are permeable to the external oxygen or that the oxygen of the oxidized particles reacts further to produce more bulky oxides (e.g. NiAl_2O_4) or both but the bulky oxides have not been observed by Raman spectroscopy.

For the samples aluminized at 1100°C/1min, the α - Al_2O_3 present on the top of the coating is thicker than at 700°C/2h because the average thickness is of $12 \pm 6 \mu\text{m}$ (Figure V-38.b & 42.a). The layer below has a composition similar to the samples aluminized at 700°C/2h. In addition, numerous oxide particles can be observed in the first part of this layer, which would confirm the above hypothesis, i.e. the coatings would be permeable to oxygen. The potential α - Al_2O_3 diffusion barrier is again observed between the heavily and the poorly aluminized areas (Figure V-42.b). One can also note that the grain boundaries of the less-aluminized zone are oxidized (Figure V-38.b) forming Al_2O_3 (Figure V-42.c).

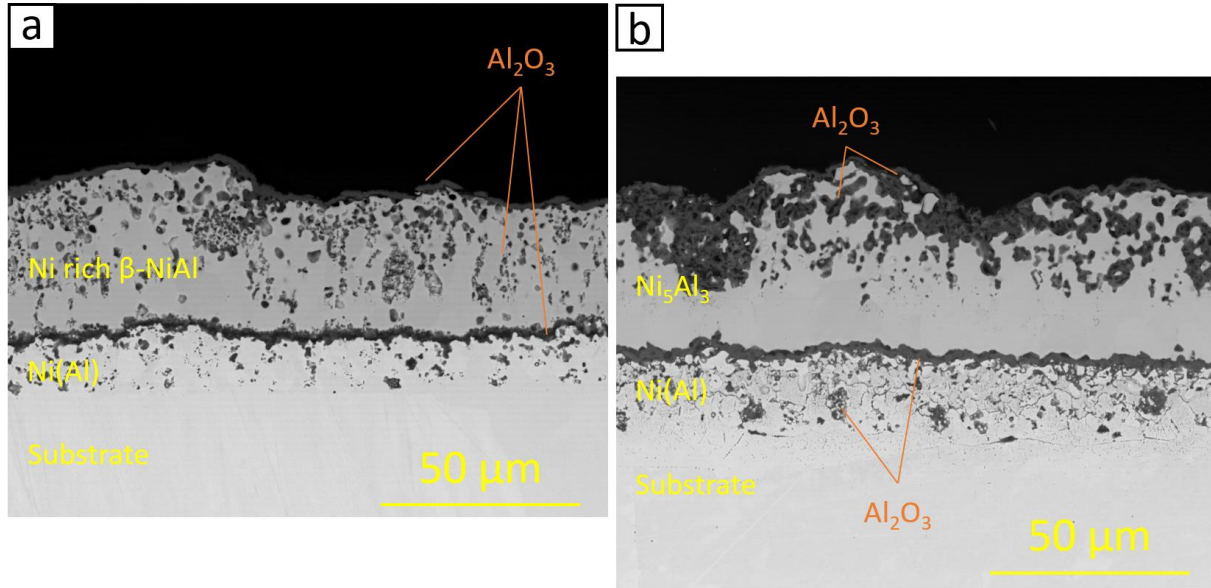


Figure V-38: SEM (BSE) cross-section of the aluminized Ni/ $Al_3Ni_{2(ox)}$ composite electrodeposit ((a) 700°C/2h and (b) 1100°C/1min) after isothermal oxidation of 1000°C/48h in synthetic air.

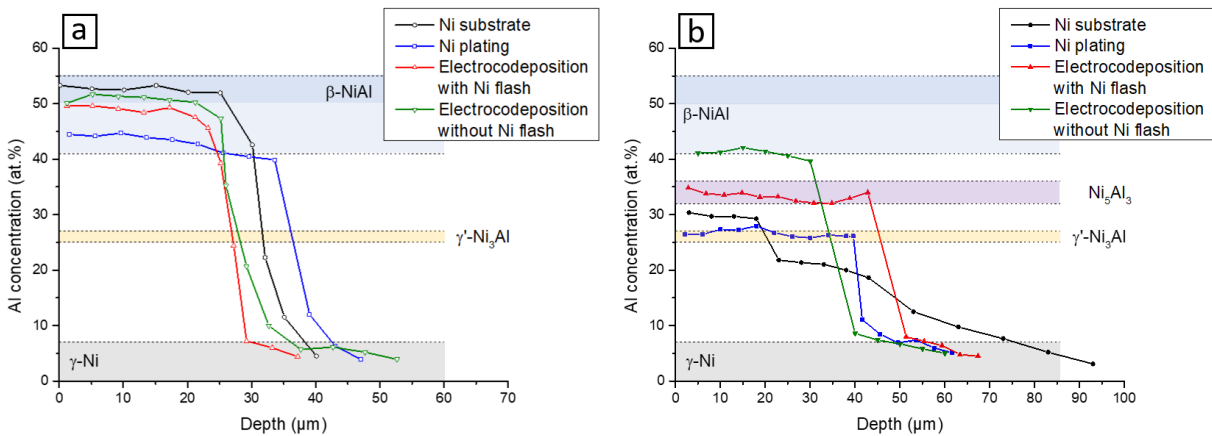


Figure V-39: EDS diffusion profiles made in the cross-sections for the different coatings after (a) the aluminizing treatment of 700°C/2h and (b) the isothermal oxidation at 1000°C/48h.

- V. Synthesis of self-regenerating composite coating using electrocodeposition of Ni and preoxidized Al_3Ni_2 -

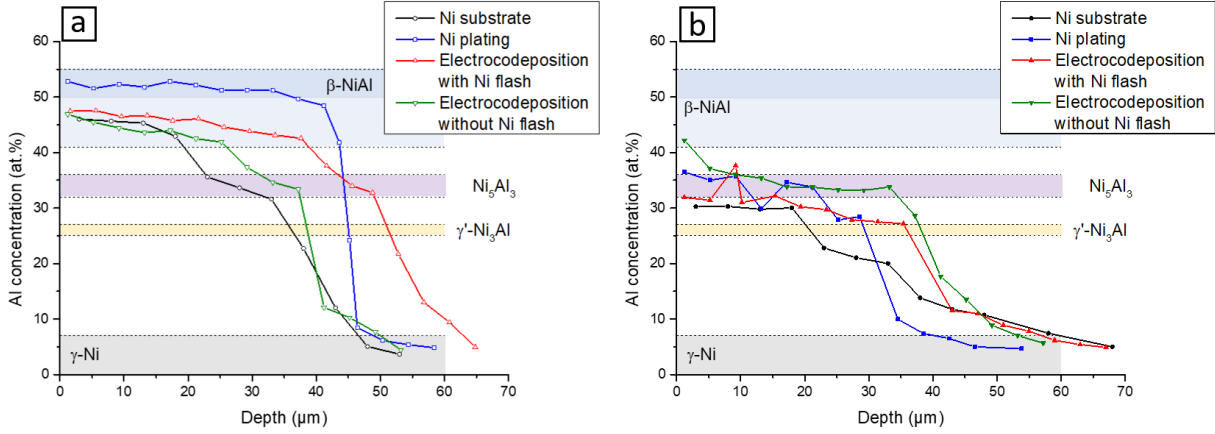


Figure V-40: EDS diffusion profiles made in the cross-sections for the different coatings after (a) the aluminizing treatment of 1100°C/1min and (b) the isothermal oxidation at 1000°C/48h.

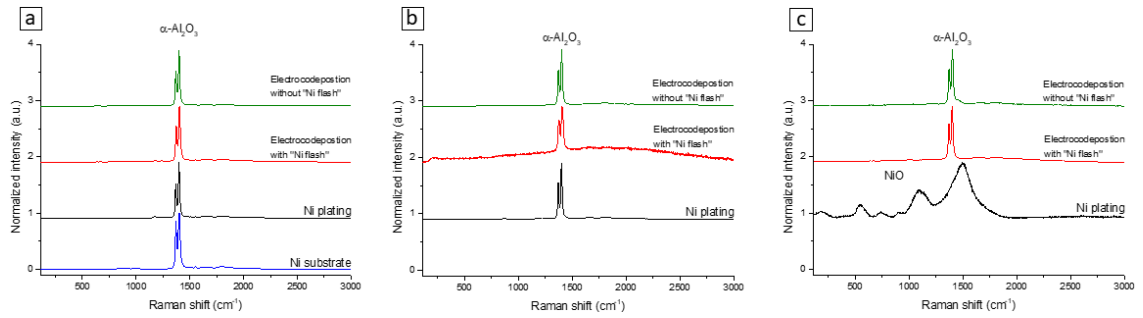


Figure V-41: Raman spectra of samples carried out at 700°C/2h after oxidation, with (a) the oxide layer on the surface, (b) the oxide present in the aluminized layer and (c) the oxide present in the less-aluminized layer [5, 11].

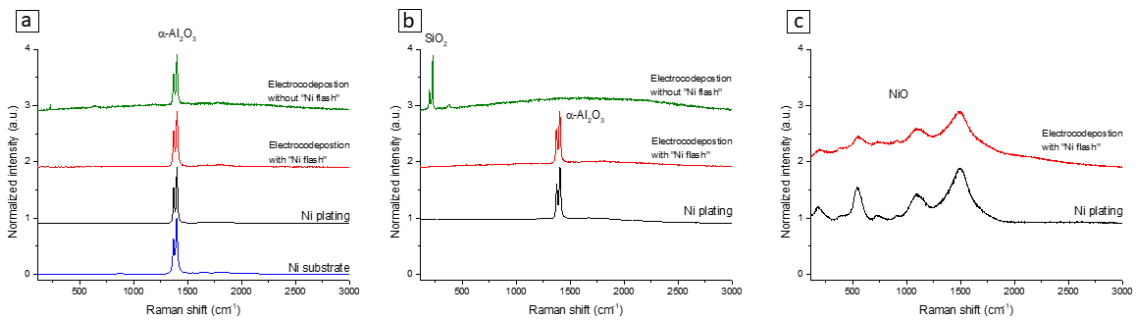


Figure V-42: Raman spectra of samples carried out at 1100°C/1min after oxidation, with (a) the oxide layer on the surface, (b) the oxide present in the aluminized layer and (c) the oxide present in the less-aluminized layer [5, 11].

III.B-Oxidation kinetics

Figure V-43 shows the mass gain per surface unit against the isothermal (1000°C) oxidation time (48h) of the different coatings. These curves can be divided into two parts. The first part is characterized by a rapid mass gain, referring to the formation and growth of an oxide. The second part is characteristic of a quasi-stationary regime and characterized by a slow mass gain. During this step, the transformations of the aluminum oxide phase $\gamma \rightarrow \Theta \rightarrow \alpha-Al_2O_3$ have been proposed by many authors under similar oxidizing conditions [16-17].

For the simple aluminized raw nickel substrates, the mass gains are quite low. These mass gains are less than 0.24 mg/cm² for the aluminizing treatments of 700°C/2h and 0.36 mg/cm² for the treatments of 1100°C/1min (Figure V-43). These values are in line with other studies on the oxidation of different aluminide coatings on pure Ni [8,18-19]. For the oxidation of the other coatings with the electrodeposited layers, the mass gains are much greater than for the pure aluminized substrate, in particular when the aluminizing treatment is extended from 700°C/2h to 1100°C/1min as they pass from 3.9 to 6.1 mg/cm² (Figure V-43).

For the composite electrodeposited coating with the first Ni flash layer, the mass gain is very important for treatment of 700°C/2h with 5.9 mg/cm². For the 1100°C/1min treatment, the mass gain is initially faster but tends to slow down with time to reach 5.6 mg/cm².

Finally, for the last composite coating without “nickel flash”, the mass gains are very close between the two treatments with 2.4 mg/cm². In addition, higher mass gains occur during the first oxidation stages of the 1100°C/1min aluminized samples.

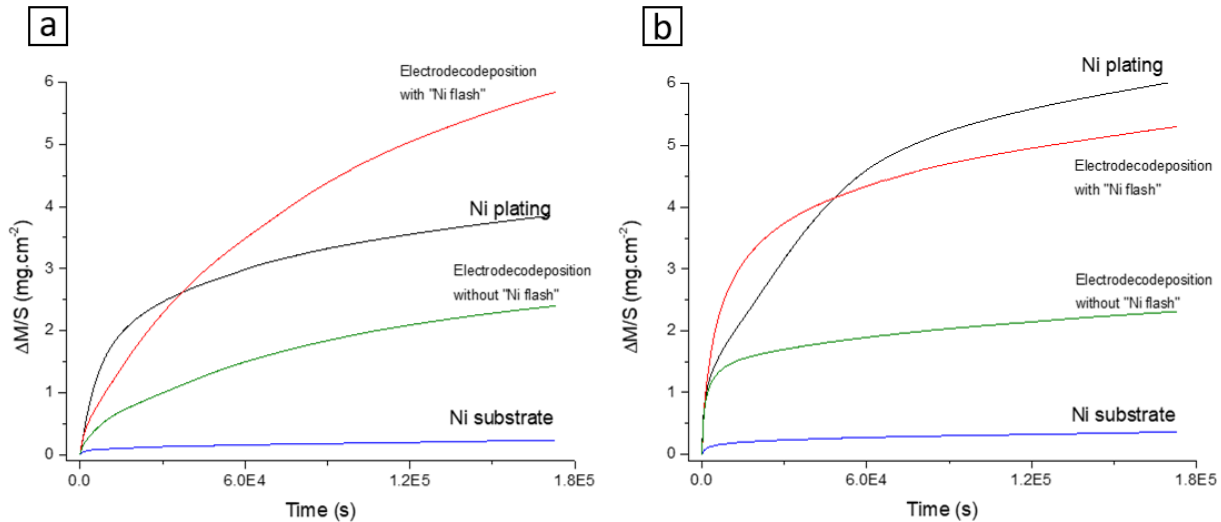


Figure V-43: TGA curves of the coatings isothermally oxidized at 1000°C/48h with (a) the coatings aluminized at 700°C/2h and (b) with the extension to 1100°C/1min.

IV-Discussion

IV.A-Formation of the first layer of electrodeposited nickel (Ni flash)

To characterize the quality of the nickel electrodeposits, only basic inspections were carried out. Indeed, we were mostly interested in the covering power of the electrodeposit as well as in the presence or absence of a marked interface between the electrodeposits and the substrate.

For current densities of 2 and 50 A/dm², the covering power of the electrodeposits is low. Indeed, numerous polishing scratches are observed unlike in the electrodeposits obtained at 5 and 20 A/dm². For the low current densities, Ni²⁺ ions preferentially adsorb at the most prominent defects (ridges, polishing scratches, etc.). This causes an increase in the difference in thickness between the most prominent and the deeper areas, resulting in a rough surface [20]. In addition, for low overvoltage, the surface roughness increases [21]. For current densities of 5 and 20 A/dm², it seems that the low surface roughness is also linked with overvoltage. When the overvoltage is high, the roughness decreases [21]. Finally, for the current density of 50 A/dm², the low covering power must be linked with the hydrogen adsorption at the surface of the samples.

The texture of Ni plating has been studied by many authors. For “low” current density, the texture of the electrodeposits largely depends on the processing conditions (current density, pH, temperature, additives, etc.) [22]. According to many authors, a texture following the [100] is observed for sulfamate Ni plating [23-26]. For very low current densities, a [110] plane will preferably be observed [27-28]. In addition, when a strong inhibition by adsorbed hydrogen takes place, an orientation in the direction (220) is often observed, which may explain the low covering power for the current density of 50 A/dm².

All these results can also be extrapolated to the interface. In fact, the lower surface roughness and the less visible interface can be observed for the Ni plating synthesized at 5 A/dm². As for the samples which have a high surface roughness, it also has a visible and porous interface.

For these reasons, a current density of 5 A/dm² was selected to synthesize the first layer of electroplated nickel. In addition, this conclusion is consistent with the work of Kale & al. which demonstrates a better adhesion and corrosion resistance for a system with a first layer of Ni made at 5A/dm² and a second layer of Zn-Ni [1].

IV.B-Effect of current density on the amount of preoxidized Al_3Ni_2 particles trapped in nickel electrodeposit matrix

The electrodeposition conditions (stirring, layout of the electrodes, etc.) make it possible to synthesize a nickel composite electrodeposit with a high concentration of $Al_3Ni_{2(ox)}$ particles. Our studies on the incorporation of alumina particles into nickel electrodeposits have shown that the amount of trapped particles is large for low current densities, unlike for high current densities. In addition, two evolution behaviors can be observed. The first is a rapid decrease in the number of trapped particles as a function of the current density and the second is a plateau. The distinctions between the two behaviors take place around 5A/dm². According to several authors [1,29-38], the amount of incorporated alumina increases with the decrease of plating current density and increased bath loading. Such authors proposed that increasing the number of effective collisions between the particles and the cathode surface per unit volume of the deposited matrix will increase the amount incorporated into the coating. Therefore, using low current density or high particles

concentration in the bath, a large amount of particles can be trapped. However, in our case, for an equivalent size and quantity of particles, these results seem contradictory with what should be observed. As a matter of fact, the study of Bakhit et al. on the incorporation of silicon carbide in a nickel/cobalt electrodeposit [39] reported results similar to ours. Indeed, an increase in the current density allows the trapping of a greater quantity of particles. A rapid increase in the quantity of trapped particles and then a quasi-stationary state can be observed up to 3 A/dm^2 . Beyond this value, a rapid decrease in the concentration of particles can be observed. It is therefore possible that the same phenomena occur for preoxidized Al_3Ni_2 particles.

A current density of 20 A/dm^2 was chosen for the rest of the experiments. This value permits to synthesize a composite coating containing 20% vol. particles in a Ni matrix.

IV.C-Effect of aluminizing temperature and time

After selecting the parameters and synthesizing the composite electrodeposits, aluminizing by slurry route was carried out to synthesize the self-regenerating coatings. Various parameters such as aluminizing temperature and time were considered.

The mechanism governing the aluminizing of the substrate at low temperatures is the diffusivity of Al. Indeed, it is accepted that below an aluminizing temperature of 950°C , a High-Activity Low-Temperature aluminizing (HALT) takes place [40-41].

The mechanisms and different stages of slurry aluminizing have been studied. When the temperatures rise, the aluminum particles react with the substrate by solid/solid diffusion and a small diffusion island can be observed after treatment of $600^\circ\text{C}/1\text{h}$ [7]. When the temperature reaches 650°C , the self-propagating high temperature (SHS) reactions occur [42] where molten Al dissolves Ni and produces a highly exothermic reaction and the immediate aluminizing of the Ni substrate [14,43]. Therefore, after 1h at 650°C , $35\mu\text{m}$ of the substrate are already aluminized. This would be in line with the slurry aluminizing mechanisms put down in our group [7,14,43] and at the Dechema Institute [42] a few years ago. The first step is defined by wetting, dissolution and formation of a zone of molten aluminum on the surface of the sample. The second step is defined by a majority diffusion of aluminum towards the substrate and a weak diffusion of the nickel towards the aluminum. The intermetallics formed during this step range from the nickel to aluminum-rich phase ($\gamma\text{-Ni} \rightarrow \gamma'\text{-Ni}_3\text{Al} \rightarrow \beta\text{-NiAl} \rightarrow \text{Al}_3\text{Ni}_2 \rightarrow \text{Al}_3\text{Ni}$). During this step, an aluminized zone of several tens of microns will form. During the last phase at a higher temperature ($T > 950^\circ\text{C}$), the Ni will preferentially diffuse towards the surface to form the desired phase of $\beta\text{-NiAl}$ ($\text{Al}_3\text{Ni}_2 \rightarrow \beta\text{-NiAl}$).

The mechanisms of slurry aluminizing of the coatings at $650^\circ\text{C}/12\text{h}$ and $700^\circ\text{C}/1\text{min}$, 2, 4 and 12h are thus similar. Indeed, a first porous layer is formed on the surface. This porous zone is characteristic of a bath of molten aluminum [43]. This molten Al bath will dissolve a thin layer of nickel on the surface and the dissolved nickel will enrich the molten bath (Figure V-44.b) [7,42]. For longer aluminizing times, the amount of Al available on the surface will increase (due to the melting of Al particles) and diffusion of Al onto the electrodeposits will quickly occur forming a layer of Al_3Ni_2 intermetallic compound (Figure V-44.c), then $\beta\text{-NiAl}$. This layer will quickly grow until it reaches a thickness of $30 \mu\text{m}$. In addition, during this time, nickel will diffuse on the surface and induce the solidification of the molten aluminum bath and the formation of the Al_3Ni and Al_3Ni_2 phases (Figure V-44.c). For treatments of $700^\circ\text{C}/1\text{min}$, these different steps have already occurred (Figure V-22.a). For longer aluminizing times, a slight thickening of the aluminized zone and a

modification of the aluminized/non-aluminized areas interface appears to occur (Figure V-22 & V-23.a).

In addition, the phases of the aluminum oxide differ between the different layers. In the aluminized areas, the $\Theta\text{-Al}_2\text{O}_3$ is majorly observed at 650°C and 700°C while the peaks of $\alpha\text{-Al}_2\text{O}_3$ are detected after 12h at 700°C, for the two laser wavelengths employed in the Raman analyses. In the non-aluminized area, the rapid transformation at low temperature of the $\Theta \rightarrow \alpha\text{-Al}_2\text{O}_3$ suggests a low partial pressure of oxygen in this layer, in contrast to the aluminized zone. Networks of defect such as micro-porosities and trapped gas in the aluminized layer may explain these differences in Po_2 . Indeed, part of the trapped gas can be released during the heat treatment and will keep a high Po_2 in the system. This theory seems consistent with the oxidation tests. Indeed, during the oxidation of the two-layers electrodeposited coatings, significant oxidation of the sub-surface of the coating is observed. This internal oxidation could be explained by a network of defects in the aluminized layer. In addition, nickel oxide and spinels form in the non-aluminized layer. According to the Ellingham diagram (thermodynamic and non-kinetic value) the formation of NiO is possible for Po_2 around 10^{-17} and 10^{-11} bar for respectively, 700 and 1000°C. It is therefore probable that the trapped gas in the coating maintains a Po_2 between these two values.

In addition, interfacial oxidation occurs around $\text{Al}_3\text{Ni}_{2(\text{ox})}$ particles (Figure V-44.d). The formation of this aluminum oxide continues all along with the interface and for aluminizing treatment of 700°C/12h, interfacial detachment can be observed (Figure V-45.e). For lower temperature (650°C/12h), no detachment occurs but an $\alpha\text{-Al}_2\text{O}_3$ can be observed.

For the treatment of 1100°C/1min, the first stages of aluminizing are identical. The major differences will occur when the furnace temperature exceeds 950°C. Indeed, at these temperatures, the coating formation mechanisms will go from High to Low-activity (LAHT) following the outward Ni diffusion [40]. Moreover, this diffusion of Ni is clearly observed for the samples aluminized at 1100°C/1min. Indeed, at the bottom of the aluminized layer, a greater Ni concentration and no pores are observed. The lack of pores is caused by the diffusion of Ni which will provide a surplus of atoms allowing gaps and pores to be filled. In addition, at the interface of the aluminized/non-aluminized areas, an interfacial detachment occurs. Finally, at the layers of the first nickel electrodeposit, pores form throughout the thickness of this layer.

For all the aluminizing temperatures, the coatings are porous and the finer particles appear to dissolve. The porosity of the coating appears to be caused by the nature of the electrodeposits in relation to their fabrication mode. As such, when sufficient thermal energy (e.g. aluminizing temperature) is provided, the defects coalesce and form pores. Regarding the $\text{Al}_3\text{Ni}_{2\text{ox}}$ particles, it seems that only the finest particles have been completely dissolved. If we compare the area of the aluminized and less-aluminized electrodeposits, a large amount of particles can be observed in the less-aluminized area (Figure V-19.a). This clearly implies that, despite the oxide shell exchanges take place between the core of the particles and the external matrix. In addition, this total dissolution of the particles could be prevented by using larger particles or by applying longer preoxidation times and therefore forming thicker oxide scales.

To conclude, these three aluminizing treatments generate quite similar results. Nevertheless, it seems that the treatment of 700°C/12h leads to a lower porosity around the preoxidized Al_3Ni_2 particles. An excessive interfacial oxidation can occur during the oxidation step the formation of a thick oxide layer, which will locally decrease the Al content and allow no exchange between the particles and the coatings. For these reasons, a temperature of 700°C was selected for further

investigations. For the aluminizing time, the treatment of $700^\circ\text{C}/2\text{h}$ was chosen. Indeed, with the extension to $1100^\circ\text{C}/1\text{min}$, a thick residual layer of molten Al bath remains on the surface. For longer times (4 and 12h), cracks appear at the interface that can cause interfacial detachment.

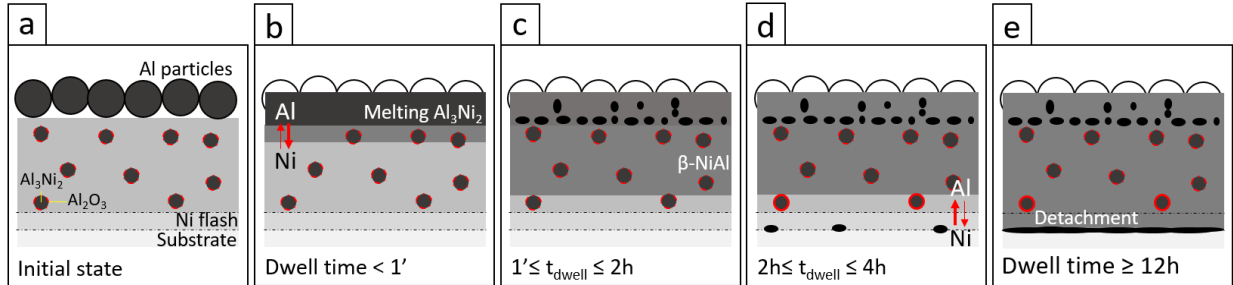


Figure V-44: Schematic drawing of the aluminizing process between the composite coating and Al particles heated at 700°C .

IV.D-Isothermal oxidation

IV.D.1-Oxidation kinetics

During this study, preliminary short isothermal oxidation tests (48h) were carried out in air at 1000°C to confirm or refute the self-regenerating nature of the composite coatings.

The thermogravimetric measurements of the coatings were given in the previous Figure V-43. All the samples had been coated by applying $10\text{ mg}\cdot\text{cm}^{-2}$ of slurry and subsequently annealed. For all samples, the mass increases with the oxidation time. The lowest mass gain is obtained with the aluminized pure Ni substrate. and the typical value to compare with other coatings and with other studies is the parabolic rate constant, K_p . The parabolic rate constant is calculated using the linear part of the curves $\Delta m/A=f(t^{1/2})$ (Figure V-45) as described in detail in the work of B. Pieraggi [44]. This value gives a good estimate of the oxidation rate and of the type of oxide formed on the surface of the coating [44]. Therefore, the lower the values of k_p , the slower the oxidation kinetics, which is thus attributed to a slowly growing (protective) oxide. In addition, it is important to consider that the longer the oxidation times, the greater the accuracy of the k_p values because issues like surface roughness, etc. particularly affecting the initial oxidation stages become negligible. However, our approach will allow to make a direct comparison with other equivalent systems and with other studies. The values of k_p are given in Table V-3.

For the coatings carried out on the raw substrate, the values of k_p obtained for the two aluminizing treatments are close. In addition, these values are similar to those obtained for other studies on $\beta\text{-NiAl}$ diffusion coatings elaborated through slurry route ($\approx 2.10^{-9}$ and $7.10^{-9}\text{ g}^2\cdot\text{cm}^{-4}\cdot\text{s}^{-1}$) for isothermal oxidation at 1000°C [8,45].

The oxidation of the different aluminized nickel electrodeposits largely differs from that of the simple aluminide coatings on the Ni substrate. This greater difference in oxidation kinetics can be explained by three factors, (i) the difference in composition, (ii) the difference in microstructure, and (iii) the presence of internal defects. The microstructure and the composition of the coatings obtained on the Ni electrodeposits are quite similar to those obtained on a raw substrate. Therefore, the main factor that can explain these differences is the presence of defects. Indeed, porosities of several microns are observed in the aluminized layer. In addition, interfacial oxidation and detachment of the oxide scale occur. Finally, for the aluminized composite $\text{Ni}+\text{Al}_3\text{Ni}_{2\text{ox}}$

coatings, the values of k_p are far from to two orders of magnitude with respect the values of Ni electrodeposits.

The k_p values show higher oxidation rates for the electrodeposits and the composite coatings. This suggests the formation of less protective oxides such as spinels and nickel oxide, which has been shown for Ni plating and the two-layer electro-codeposits. The formation of such oxides occurs in several areas of the coatings and not just at the surface like in the simple diffusion coatings. Therefore, the mass gain is greater and results in greater k_p values. In essence, the physical meaning of the parabolic rate constant accounting for solid state diffusion cannot really apply to these very uneven situations.

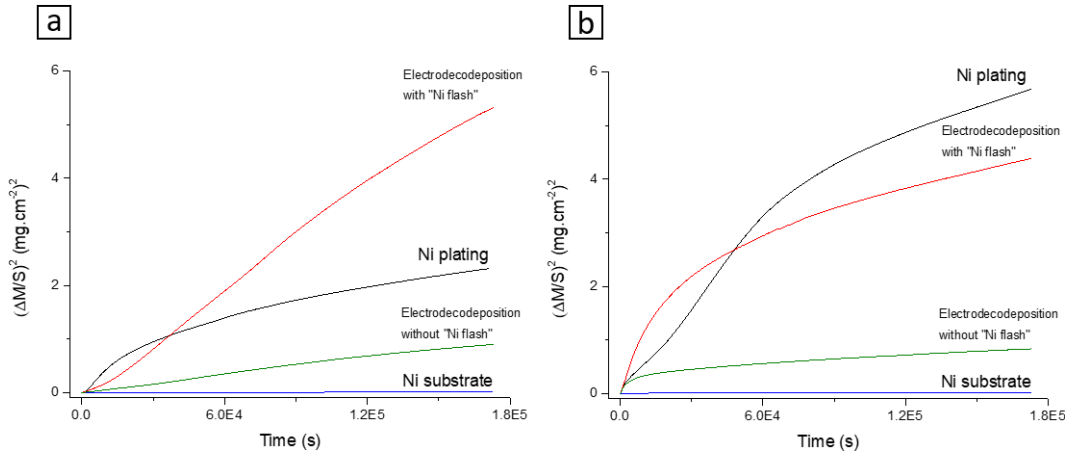


Figure V-45: $(\Delta/mS)^2$ vs time curves for the aluminized samples for (a) 700°C/2h and (b) 1100°C/1min.

Table V-3: Parabolic rate constants of the different Al diffusion coatings after 1000°C/48h in air.

Heat treatment	700°C/2h	1100°C/1min	Oxidation time	48h	100h
Coatings	k_p ($g^2.cm^{-4}.s^{-1}$)		Reference coatings	k_p ($g^2.cm^{-4}.s^{-1}$)	
Ni substrate	4E-8	8E-8	Slurry [45]	2E-9	4.7E-13
Ni plating	8E-6	2E-5	Slurry [8]	7E-9	2.4E-12
Electrocodeposition with "Ni flash"	3E-5	1E-5	Pack-Cementation [8]	8E-10	6.1E-14
Electrocodeposition without "Ni flash"	5E-6	2E-6			

IV.D.2-Evolution of the microstructure and compositions

The diffusion coatings obtained on the raw substrate exhibit a similar morphology before and after oxidation. Almost the entire aluminized layer is made of an Al-rich β -NiAl expected to evolve upon oxidation. First, due to contact with oxygen, the aluminum on the surface of the coating will be oxidized, which will slightly deplete its content close to the surface. Second, the structure of these

coatings together with the difference in composition between the coating and the substrate will induce a compositional driving force to foster interdiffusion. The Al present in the coating will diffuse towards the substrate and the nickel present in the substrate will diffuse towards the surface of the sample. These interdiffusion phenomena can be observed in Figure V-39 and Figure V-40. Indeed, at the end of the aluminizing treatments of $700^\circ\text{C}/2\text{h}$, a concentration of 5 at. % of Al can be detected to a depth of about $40\ \mu\text{m}$. At the end of the oxidation treatment, a concentration of 5 at. % of Al can be detected up to about $94\ \mu\text{m}$ depth.

In addition, the gradual depletion of Al will cause several phase changes. For instance, at 1100°C the $\beta\text{-NiAl}$ phase is stable up to about 37 at. % of Al and then transforms into $\gamma'\text{-Ni}_3\text{Al}$ [15]. These phase changes will induce changes in volume and changes in microstructure. Close to the surface, a typical plate-like martensitic transformation microstructure can be observed and confirmed by the $\text{L}_{10}\text{-Ni}_3\text{Al}$ XRD peaks. This martensitic structure has been extensively studied and precisely forms when the Al content is around 36-37 at.% [45-50]. Below, a layer of an undefined phase can be observed. In this layer, the Al concentration gradually decreases to levels below 9 at. % leading to the $\gamma\text{-Ni}$ phase with Al dissolved.

On the aluminized nickel electrodeposits, the oxidation induced much greater modifications. This can be attributed to the fact that the coatings contain many defects (pores, cavities, cracks, etc.) after aluminizing. The imprints of bubbles formed during the aluminizing step (Figure V-32) could come from trapped foreign species such as hydrogen and/or species coming from the electrodeposition bath. During the aluminizing treatment, the temperature very likely exceeded the value necessary to get gaseous species, which tended to escape from the coating. The defects generated by these “gas pockets” appear smaller close to the surface than those observed deeper in the coating, which could confirm that these gaseous species were indeed able to escape. Deeper in the coating, the “gas pockets” tended to coalesce and to escape but remained trapped in the shape of elongated bubbles. During the oxidation step, these defects play a significant role by facilitating the penetration of oxygen into the coating.

In fact, during the oxidation step, significant internal oxidation takes place in the coating, with a major formation of $\alpha\text{-Al}_2\text{O}_3$ and of NiO at the coating/substrate interface. This strong oxidation induces internal stresses which can lead to an interfacial detachment of the coating from the substrate. In addition, this significant oxidation explains the important mass gain during the oxidation of this type of coating.

The oxidation of electrocodeposited coatings (Ni flash + composite) has similarities to simple Ni electrodeposits. Due to the high quantity of defects of the electrocodeposited layer, a thick layer of Al_2O_3 forms on the surface, in the coating and at the interface non-aluminized layer/aluminized layer. In addition, in the non-aluminized layer, a network of aluminum oxide, spinel and nickel oxide are observed. The formation of the aluminum oxide in this layer is probably due to the preoxidation of the particles trapped in this layer. Indeed, the diffusion barrier formed by the oxides at the interface is too thick and aluminum oxide could also have been observed for the coatings carried out on the Ni plating. These observations tend to demonstrate that interdiffusion between $\text{Al}_3\text{Ni}_{2(\text{ox})}$ particles and the nickel matrix takes place.

However, to obtain a functional self-regenerating coating too many defects are present in the coating. To reduce the presence of defects, it was decided to carry out an oxidation test on composite coatings without the first flash layer of Ni because it oxidizes extremely quickly and introduces many defects that affect oxidation.

The tests carried out on the composite coatings without “Ni flash” after aluminization are only composed of few pores and no interfacial detachment compared to the previous. These observations are confirmed after oxidation. Indeed, the observations made on the coating and in particular for the treatments of 700°C/2h appear really interesting to us. This coating is homogeneous and has a very high aluminum concentration.

For comparison with the simple aluminide coating made on a raw substrate whose surface aluminum oxide is just about 1 μm thick, the Al_2O_3 scale is barely thicker (2 ± 1 and 12 ± 4 μm respectively for the 700°C/2h and 1100°C/1min aluminizing times). After oxidation, the outermost 20 μm of the simple diffusion coating contain 30 at% of Al while for the self-regenerating coating the Al content is higher (41 at%) over the entire aluminized area ($\approx 30\mu\text{m}$). In this concentration range, the β -NiAl intermetallic compounds are stable. This means that after 48 hours of exposure to 1000°C in air, there is no phase change. Therefore, no change in volume and no internal stresses induced by the phase changes. In addition, a concentration of 5 at. % of Al is observed up to about 94 μm for the simple coatings while for the composite coatings this concentration is reached at 60 μm due to the Al_2O_3 diffusion barrier. Finally, the preoxidized particles in the non-aluminized area have fully oxidized.

This high concentration of aluminum in the coating appears to be induced by the combined action of the $\text{Al}_3\text{Ni}_{2(\text{ox})}$ particles and the alumina diffusion barrier. Unfortunately, due to the total oxidation of the particles, it is not possible to quantify the amount of aluminum released by the particles. It is therefore not possible to quantify the effect of preoxidized particles and the effect of the diffusion barrier. Nevertheless, it would seem that the composite coatings synthesized at 700°C/2h, have only a low self-regenerating character and that the large quantity of aluminum in the coating after the oxidation test is due to the oxidation of the interface. Indeed, after 48h of oxidation, all of the $\text{Al}_3\text{Ni}_{2(\text{ox})}$ particles are oxidized, which suggests that the coating matrix is permeable to oxygen.

For the aluminizing treatments of 700°C/2h + 1100°C/1min, the observations are less promising. This is because a significant portion of the surface of the coatings has oxidized. In addition, strong intergranular oxidation can be observed in the non-aluminized area. This greater oxidation can be caused by a greater diffusion of oxygen through the defect network [51-52]. This network of defects could also explain the greater diffusion of aluminum in the substrate (Figure V-39.b & 40.b).

V-Conclusions

The synthesis, preoxidation, and incorporation of preoxidized Al_3Ni_2 nanometric particles into a nickel matrix by electrodeposition have been investigated in this work. The preoxidation treatment of the particles in Ar and air produced a thin layer of aluminum oxide on the surface, thus forming particles with an $\text{Al}_3\text{Ni}_2/\beta\text{-NiAl}$ core and an Al_2O_3 shell. During the electrochemical step and the synthesis of composite coating, the concentration of particles trapped in the coating increased with the current density forming a composite coating containing 20 vol% of preoxidized particles homogeneously distributed.

These 50 μm composite coatings were aluminized at 700°C to form a HALT diffusion coating. The coating obtained for an aluminizing treatment of 700°C/2h is made of a first layer of Al-rich $\beta\text{-NiAl}$ (30 μm) and of a second layer of less-aluminized electrodeposit (Ni(Al)). For longer processing times or higher temperatures, interfacial decohesion occurred.

The self-regenerating nature of the coatings was estimated through isothermal oxidation experiments (1000°C/48h) and the obtained results revealed promising. Indeed, after 48h of oxidation at 1000°C, the aluminum content is of 40 at. % in the first 30 microns of the coating whereas, for a simple diffusion coating, the aluminum content is approximately equal to 30 at. % in the first 20 μm

Nevertheless, long-term oxidation is needed to evaluate the long-term effect on the composite coating and the alumina diffusion barrier on the durability of the systems. After 48h of oxidation, the amount of Al has not yet reached critical values. Additionally, cyclic oxidation assays can also be conducted to assess the effect of particles, diffusion barrier, and the delayed $\beta\text{-NiAl} \rightarrow \gamma\text{-Ni}_3\text{Al}$ transformation.

References

[1]: V. N. Kale, S. Kumaraguru, G. Saravanan, A. Syed Jalaluddeen, P. Rajkumar, R. Subadevi, M. Sivakumar, R.M. Gnanamuthu, Influence of nickel strike as adhesive layer on electrodeposited Zn-Co-Ni alloy and their performance in metal-finishing, *Materials Today: Proceedings* 40 (2021) 248–253.

<https://doi.org/10.1016/j.matpr.2020.11.157>

[2]: C.S. Lin, P.C. Hsu, K.C. Peng, L. Chang, C.H. Chen, Annealing behavior of nickel electrodeposited from sulfamate bath at different temperatures, *Materials Transactions* 42 (2001) 316–322.

<https://doi.org/10.2320/matertrans.42.316>

[3]: L. Feng, Y.Y. Ren, Y.H. Zhang, S. Wang, L. Li, direct correlations among the grain size, texture, and indentation behavior of nanocrystalline nickel coatings, *Metals* 9 (2019) 188.

<https://doi.org/10.3390/met9020188>

[4]: X. Wang, X. Peng, X. Tan, F. Wang, *The reactive element effect of ceria particle dispersion on alumina growth: A model based on microstructural observations*, *Scientific Reports* 6 (2016) 29593.

<https://doi.org/10.1038/srep29593>

[5]: S. Hakkar, S. Achache, F. Sanchette, Z. Mekhalif, N. Kamoun, A. Boumaza, Characterization by Raman spectroscopy of the oxide scales grown on the PM2000 at high-temperatures, *Journal of Molecular and Engineering Materials* 7 (2019).

<https://doi.org/10.1142/S2251237319500035>

[6]: A.B. Kulinkin, S.P. Feofilov, R.I. Zakharchenya, Luminescence of impurity 3d and 4f metals ions in different crystalline forms of Al₂O₃, *Physics of the Solid State* 42 (2000) 857–600.

<https://doi.org/10.1134/1.1131301>

[7]: G. Bonnet, M. Mollard, B. Rannou, J. Balmain, F. Pedraza, X. Montero, M. Galetz, M. Schütze, Initial aluminizing steps of pure nickel from Al micro-particles, *Defect and Diffusion Forum* 323-325 (2012) 381–386.

<https://doi.org/10.4028/www.scientific.net/ddf.323-325.381>

[8]: M. Mollard, B. Rannou, B. Bouchaud, J. Balmain, G. Bonnet, F. Pedraza, *Comparative degradation of nickel aluminized by slurry and by pack cementation under isothermal conditions*, *Corrosion Science* 66 (2013) 118–124.

<https://doi.org/10.1016/j.corsci.2012.09.009>

[9]: F. Pedraza, M. Mollard, B. Rannou, B. Bouchaud, J. Balmain, G. Bonnet, *Oxidation resistance of thermal barrier coatings based on hollow alumina particles*, *Oxidation of Metals* 85 (2016) 231–244.

<https://doi.org/10.1007/s11085-015-9570-3>

[10] X. Montero, M.C. Galetz, M. Schütze, *Low activity aluminide coatings for superalloys using a slurry process free of halide activators and chromates*, Surface & Coatings Technology 222 (2013) 9–14.

<https://doi.org/10.1016/j.surfcoat.2013.01.033>

[11]: A.S. Jbara, Z. Othaman, M.A. Saeed, Structural, morphologies and optical investigations of Θ -Al₂O₃ ultrafine powder, Journal of Alloys and Compounds 718 (2017) 1–6.

<https://doi.org/10.1016/j.jallcom.2017.05.085>

[12]: J. Hruby, S. Vavreckova, L. Masaryk, P. Neugebauer, Deposition of tetracoordinate Co(II) complex with chalcone ligands on graphene, Molecules 25 (2020) 5021.

<https://doi.org/10.1063/1.3543838>

[13]: D.P. Garriga-Majo, B.A. Shollock, D.S. McPhail, R.J. Chater, J.F. Walker, Novel Strategies for Evaluating the Degradation of Protective Coatings on Superalloys, International Journal of Inorganic Materials 1 (1999) 325–336.

[https://doi.org/10.1016/S1466-6049\(99\)00047-1](https://doi.org/10.1016/S1466-6049(99)00047-1)

[14]: F. Pedraza, M. Mollard, B. Rannou, J. Balmain, B. Bouchaud, G. Bonnet, Potential thermal barrier coating systems from Al microparticles. Mechanisms of coating formation on pure nickel, Materials Chemistry and Physics 134 (2012) 700–705.

<https://doi.org/10.1016/j.matchemphys.2012.03.053>

[15]: H. Okamoto, Al-Ni (aluminum-nickel), Journal of Phase Equilibria and Diffusion 25 (2004).

<https://doi.org/10.1007/s11669-004-0163-0>

[16]: M.W. Brumm, H.J. Grabke, The oxidation behaviour of NiAl – I. Phase transformations in the alumina scale during oxidation of NiAl and NiAl-Cr, Alloys Corrosion Science 33 (1992) 1677–1690.

[https://doi.org/10.1016/0010-938X\(92\)90002-K](https://doi.org/10.1016/0010-938X(92)90002-K)

[17]: K. Shivarni, S. Firouzi, A. Rashidghamat, Microstructures and cyclic oxidation behavior of Pt-free and low-Pt NiAl coatings on the Ni-base superalloy Rene-80, Corrosion Science 55 (2012) 378–384.

<https://doi.org/10.1016/j.corsci.2011.10.037>

[18]: B. Rannou, B. Bouchaud, J. Balmain, G. Bonnet, F. Pedraza, Comparative isothermal oxidation behaviour of new aluminide coatings from slurries containing Al particles and conventional out-of-pack aluminide coatings, Oxidation of Metals 81 (2014) 139-149.

<https://doi.org/10.1007/s11085-013-9427-6>

[20]: T. Watanabe, Nano plating – microstructure formation theory of plated films and a database of plated films, Elsevier (2004) 1–714.

ISBN: 9780080537252

[21]: R. Winand, Electrodeposition of metals and alloys – new results and perspectives, *Electrochimica Acta* 39 (1994) 1091–1105.

[https://doi.org/10.1016/0013-4686\(94\)E0023-S](https://doi.org/10.1016/0013-4686(94)E0023-S)

[22]: C. Bergenstorf Nielsen, A. Horsewell, M.J.L. Østergård, On texture formation of nickel electrodeposits, *Journal of Applied Electrochemistry* 27 (1997) 839–848.

<https://doi.org/10.1023/A:1018429013660>

[23]: Y. Tsuru, M. Nomura, F.R. Foulkes, Effects of boric acid on hydrogen evolution and internal stress in films deposited from a nickel sulfamate bath, *Journal of Applied Electrochemistry* 32 (2002) 629–634.

<https://doi.org/10.1023/A:1020130205866>

[24]: F. Ebrahimi, Z. Ahmed, The effect of substrate on the microstructure and tensile properties of electrodeposited nanocrystalline nickel, *Materials Characterization* 48 (2003) 373–379.

[https://doi.org/10.1016/S1044-5803\(02\)00305-4](https://doi.org/10.1016/S1044-5803(02)00305-4)

[25]: A.A. Rasmussen, P. Møller, M. Somers, Microstructure and thermal stability of nickel layers electrodeposited from an additive-free sulphamate-based electrolyte, *Surface and Coatings Technology* 200 (2006) 6037–6046.

<https://doi.org/10.1016/j.surfcoat.2005.09.019>

[26]: H. Zhao, L. Liu, J. Zhu, Y. Tang, W. Hu, Microstructure and corrosion behavior of electrodeposited nickel prepared from a sulphamate bath, *Materials Letters* 61 (2007) 1605–1608.

<https://doi.org/10.1016/j.matlet.2006.07.178>

[27]: T. Fritz, W. Mokwa, U. Schnakenberg, material characterization of electroplated nickel structures for microsystem technology, *Electrochimica Acta* 47 (2001) 55–60.

[https://doi.org/10.1016/S0013-4686\(01\)00576-X](https://doi.org/10.1016/S0013-4686(01)00576-X)

[28]: S.H. Goods, J.J. Kelly, A.A. Telin, J.R. Michael, R.M. Watson, Electrodeposition of Ni from low-temperature sulfamate electrolytes, II. Properties and structures of electrodeposits, *Journal of the Electrochemical Society* 153 (2006) 31–62.

<https://doi.org/10.1149/1.2181447>

[29]: K. Barmak, S.W. Banovic, C.M. Petronis, D.F. Susan, A.R. Marder, Structure of electrodeposited graded composite coatings of Ni-Al-Al₂O₃, *Journal of Microscopy* 185 (1997) 265–274.

<https://doi.org/10.1046/j.1365-2818.1997.d01-606.x>

[30]: N. Merk, X.M. Ding, B. Ilschner, Detailed microstructural study of electroplated metal matrix composites for gradient hard coatings, Federal Institute of Technology of Lausanne, Switzerland (1994) 377–382.

[31]: V. Greco, W.J.P. Baldauf, Electrodeposition of Ni-Al₂O₃, Ni-TiO₂ and Cr-TiO₂ dispersion hardened alloys, *Plating* 55 (1968) 250–257.

[32]: M.R. Scanlon, R.R. Oberle, P.C. Searson, R.C. Cammarata, Mechanical properties and deformation behavior of materials having ultra-fine microstructures, Kluwer Academic Publishers, Boston, MA (1993) 315–321.

[33]: M. Pushpavanam, K. Balakrishnan, L.R. Sharma, Characteristics of Ni-Al₂O₃ electrodeposited composites, Key Engineering Materials 20-28 (1998) 1343–1354.

<https://doi.org/10.4028/www.scientific.net/KEM.20-28.1343>

[34]: Y.S. Chang, J.Y. Lee, Wear-resistant nickel composite coating from bright nickel baths with suspended very low concentration alumina, Materials Chemistry and Physics 20 (1988) 309–321.

[https://doi.org/10.1016/0254-0584\(88\)90071-5](https://doi.org/10.1016/0254-0584(88)90071-5)

[35]: M. Verelst, J.P. Bonino, A. Rousset, Electroforming of metal matrix composite: dispersoid grain size dependence of thermostructural and mechanical properties, Materials Science and Engineering: A 135 (1991) 51–57.

[https://doi.org/10.1016/0921-5093\(91\)90536-V](https://doi.org/10.1016/0921-5093(91)90536-V)

[36]: P.R. Webb, N.L. Robertson, Electrolytic codeposition of Ni-γ Al₂O₃ thin films, Journal of the Electrochemical Society 141 (1994) 669–673.

<https://doi.org/10.1149/1.2054789>

[37]: F.K. Sautter, Electrodeposition of dispersion-hardened nickel-Al₂O₃ alloys, Journal of the Electrochemical society 110 (1963) 557–560.

<https://doi.org/10.1149/1.2425813/meta>

[38]: S.W. Banovic, K. Barmak, A.R. Marder, Characterization of single and discretely-stepped electro-composite coating of nickel-alumina, Journal of Materials Science 34 (1993) 3203–3211.

<https://doi.org/10.1023/a:100463392368>

[39]: B. Bakhit, A. Akbari, Effect of particle size and co-deposition technique on hardness and corrosion properties of Ni-Co/SiC composite coatings, Surface & Coatings Technology 206 (2012) 4964–4975.

<https://doi.org/10.1016/j.surfcoat.2012.05.122>

[40]: G.W. Goward, D.H. Boone, *Mechanisms of formation of diffusion aluminide coatings on nickel-base superalloys*, Oxidation of Metals 3 (1971) 475–495.

<https://doi.org/10.1007/BF00604047>

[41]: J.M. Brossard, B. Panicaud, J. Balmain, G. Bonnet, *Modeling of aluminized coating growth on nickel*, Acta Materialia 55 (2007) 6586–6595.

<https://doi.org/10.1016/j.actamat.2007.08.025>

[42]: M.C. Galetz, X. Montero, M. Mollard, M. Günthner, F. Pedraza, M. Schütze, The role of combustion synthesis in the formation of slurry aluminization, Intermetallics 44 (2014) 8–17.

<https://doi.org/10.1016/j.intermet.2013.08.002>

[44]: B. Pieraggi, Calculations of parabolic reaction rate constants, *Oxidation of Metals* 27 (1987) 177–185.

<https://doi.org/10.1007/BF00667057>

[45]: T. Kepa, G. Bonnet, F. Pedraza, Oxidation behavior of ultrafast slurry aluminized nickel, *Surface & Coatings Technology* 424 (2021) 127667.

<https://doi.org/10.1016/j.surfcoat.2021.127667>

[46]: S. Rosen, J.A. Goebel, Crystal structure of nickel-rich nickel aluminium and martensitic nickel aluminium, *Transaction of the Metallurgical Society of AIME* 242 (1968) 722-4.

[47]: J.L. Smialek, Martensite in NiAl oxidation-resistant coatings, *Metallurgical Transactions* 2 (1971) 913–915.

<https://doi.org/10.1007/BF02662758>

[48]: J.L. Smialek, R.F. Hehemann, Transformation temperatures of martensite in β -phase nickel aluminide, *Metallurgical Transactions* 4 (1973) 1571–1575.

<https://doi.org/10.1007/BF02668010>

[49]: Y. Zhang, J.A. Haynes, B.A. Pint, I.G. Wright, W.Y. Lee, Martensitic transformation in CVD NiAl and (Ni,Pt)Al bond coatings, *Surface and Coatings Technology* 163-164 (2003) 19–24.

[https://doi.org/10.1016/S0257-8972\(02\)00585-6](https://doi.org/10.1016/S0257-8972(02)00585-6)

[50]: S.V. Kositsyn, A.I. Valiullin, N.V. Kataeva, I.I. Kositsyna, Investigation of microcrystalline NiAl-based alloys with high-temperature thermoelastic martensitic transformation: I. Resistometry of the Ni-Al and Ni-Al-X (X=Co, Si, or Cr) alloys, *The Physics of Metals and Metallography* 102 (2006) 391–405.

<https://doi.org/10.1134/s0031918x06100073>

[51]: A.H. Heuer, Oxygen and aluminum diffusion in α -Al₂O₃: How much do we really understand, *Journal of the European Ceramic Society* 28 (2008) 1495–1507.

<https://doi.org/10.1016/j.jeurceramsoc.2007.12.020>

[52]: S. Perusin, D. Monceau, E. Andrieu, Investigations of the diffusion of oxygen in nickel at 1000°C by SIMS analysis, *Journal of the Electrochemical Society* 152 (2005) 390–937.

<https://doi.org/10.1149/1.2116787>

Conclusion and perspectives

I-Summary and conclusion

One of the main shortcomings of diffusion coatings is the difference in concentration between the coating and the substrate. These differences in concentration generate driving forces of aluminum and nickel in, and one of the possible ways to overcome this interdiffusion is to synthesize diffusion barrier. However, diffusion barrier weakens the interface between the coating and the substrate, increasing the weight and the manufacturing costs. Therefore, the main objective of this work was to synthesize a self-regenerated nickel aluminide diffusion coating

One of the ways to synthesize a self-regenerating coating is to synthesize a nickel aluminide coating with microreservoirs composed of an Al-rich Ni_xAl_y and an Al_2O_3 oxide shell. For this, two procedures have been explored, (i) the first consists in preoxidizing a nickel substrate to form a thin layer of NiO and during the aluminization process an aluminothermic reaction between Al and NiO will form in-situ Al_2O_3 . This method can allow the simultaneous formation of the coating and the microreservoirs. (ii) The second method consists in incorporating preoxidized Al_3Ni_2 microparticles in a nickel electrodeposits before carrying out an aluminization.

- **Aluminothermic way**

For the first method, the first step is to study reactivity between preoxidized nickel particles and aluminum particles by DSC. Secondly, the results obtained were extrapolated to nickel substrate and preoxidized nickel electrodeposits.

To study the reactivity, 3 particles configurations, 2 heating rates, 2 particles size and 4 preoxidation times were tested. It was observed during the heating 3 exothermic peaks and an endothermic peak. At around 620°C, the first stage of the aluminothermic reaction between the NiO shells and the aluminum particles takes place. Then at around 660°C, the aluminum melts. This melting will stop the thermite reaction up to 700°C, where the second step of the aluminothermic reaction between the NiO and liquid Al takes place. This aluminothermic reaction causes reduction of NiO and oxidation of Al. These steps are then followed by the formation of the intermetallic compound Ni_xAl_y and the transformation of $\gamma-Al_2O_3$ into $\alpha-Al_2O_3$ above 1000°C.

Regarding the microstructure, it has been identified that the size, the preoxidation time, the heating rate and the arrangement of the particles are predominant parameters. In the case of mixing the powders between the small preoxidized nickel particles and the aluminum particles, a composite structure between Ni_3Al intermetallic compound and Al_2O_3 was observed. This structure made up of metallic particles and alumina shell interpenetrated are influence by the heating rated and the size of nickel particles. In fact, for rapid heating rates or coarse particles, the structure become porous and a smaller quantity of alumina has been observed on the edges of the intermetallic particles.

For the two-layer layouts, the heating rates play an opposing role. When the nickel particles are above the aluminum particles, the fast heating rates bring about the formation of compact composite structures unlike the opposed configurations. In all 3 layouts (layout A: mixture of preoxidized aluminum and nickel particles, layout B: preoxidized nickel particles above the aluminum particles and layout C: preoxidized nickel particles below the aluminum particles), the fine preoxidized particles provide a promising structure consisting of intermetallic grains and

aluminum oxide grains boundaries and/or shells. These grains can act as a reservoir for self-regenerating coatings and aluminum oxide can act as thin and discontinuous diffusion barrier. The results were therefore extrapolated to a preoxidized raw nickel substrate coated with Al powder. From a calorimetric point of view, the results obtained for fast heating rates are similar to those obtained in the case of powder mixing. For slower heating rates, the energies released are extremely low. This difference is probably caused by the difference in the amount of material and the difference in porosity between the particles and the raw substrate.

In addition, the thermal treatments made it possible to highlight the various exothermic reactions. When the crucibles have been heated to 700°C/2h, the different stages of the aluminothermic reaction lead to the formation of a multilayer system, with a first layer Al₃Ni intermetallic and a thick layer of Al₂O₃ which blocks the diffusion of Al. Residual NiO can be still observed. Yet despite this dense layer of alumina, the aluminum succeeds in infiltrating through defects present in the nickel oxide layer and aluminizing the substrate. This aluminization caused the formation of diffusion islands and the lifting of the NiO layer. As the temperature rises to 1080°C, the entire NiO layers have been reduced and a thick aluminized area of about one hundred microns has been observed. The structure of the coating obtained after a treatment of 700°C/2h could make it possible to form a self-regenerating coating. However, it appears necessary to reduce the entire NiO layer. For this, it was decided to study the influence of the preoxidation time and therefore of the thicknesses in order to obtain coatings without residual NiO.

The tests were carried out on pure Ni substrates, preoxidized and subsequently aluminized under TGA. For a preoxidized nickel substrate at 1100°C/2h, the most interesting results are obtained by aluminizing at 700°C/24h. The coating obtained consists of a first composite layer between Al₃Ni matrix and microspheres composed of an Al₃Ni core and an Al₂O₃ shell. A second layer of Al₃Ni and Al₂O₃ cluster. Finally, a layer of reduced nickel and NiO are observed. The synthesis of the composite layer between Al₃Ni and alumina shells was made possible by the formation of the diffusion barrier. Indeed, the layer of alumina prevents the aluminum from diffusing deeper into the substrate, the intermetallic will then form outwards and trapping the aluminum particles oxidizing shells.

In addition, due to the mechanisms of formation of the nickel oxide layer, the longer the preoxidation times, the greater the amount of defects in the NiO layers. These defects are preferential diffusion paths for Al, which allows a large amount of NiO to be reduced. However, the longer the preoxidation time, the greater the amount of NiO to be reduced. It therefore seems complicated to reduce the entire NiO layer with this method.

It was therefore decided to synthesize electrodeposits of Ni on the substrate. These electrodeposits were synthesized at high-current densities, resulting in electrodeposits and nickel oxide after preoxidation with a high-concentration of defects. This increase in defects allows an increase in the reduced Ni, however, this leads to obtaining a heterogeneous coating. These heterogeneous coatings, made up of diffusion islands, led to a decohesion of the coating. In addition, the formation of the composite layer between, a, intermetallic matrix and particles consisting of an alumina shell is no longer guaranteed. Indeed, to obtain this layer it is necessary that part of aluminum be blocked by the alumina diffusion barrier. However, by increasing the amount of defects in the oxide layer, this barrier has not been homogeneously formed and a large amount of Al reacts with the substrate. This method did not make it possible to obtain self-regenerating coating without nickel oxide.

- **Electrochemical way**

In this way, preoxidized Al_3Ni_2 intermetallic particles have been incorporated in a nickel plating. This makes it possible to incorporate microreservoirs of a precise size and composition in the coating. The micrometric particles of Al_3Ni_2 were synthesized by pack cementation and preoxidized to form a thin shell of Al_2O_3 . It has been observed that during the electrochemical step and the synthesis of composite coating, the concentration of particles trapped in the coating increased with the current density forming a composite coating containing 20% vol. of preoxidized particles homogeneously distributed. 50 μm composite coatings were subsequently aluminized at 700°C to form low-activity coatings. It was found an optimal time of 2h of heat treatment, where about 30 μm of coating are made of Al-rich $\beta\text{-NiAl}$ and preoxidized microparticles, and, the other 20 μm is slightly enriched with Al. For longer times, an interfacial decohesion was observable. These coatings were subsequently oxidized at $1000^\circ\text{C}/48\text{h}$.

The oxidation of this coating appears promising. In fact, after 48h of oxidation at 1000°C in air, the Al concentration is about 40 at. % in the first 30 μm of the coating. In contrast, the Al concentration is about 30 at. % in the first 20 μm in a "classic" diffusion coating. In addition, a thin layer of alumina which acts as a diffusion barrier is formed between the aluminized and non-aluminized layers of the coating. It appears that the high concentration of aluminum that remains in the coating after the oxidation treatment is caused by the action of the diffusion barrier and not by the direct action of the particles. However, in view of the results obtained on a simple nickel electrodeposits coating, no alumina diffusion barrier is formed. It is therefore highly likely that this thin layer of alumina will form due to the incorporation of the particles into the coating.

II-Perspectives

This PhD thesis corresponds to a pioneering study on the synthesis of self-regenerating aluminide coatings on nickel substrates and therefore, not all the different hypothesis of investigation that were set at the beginning of the study have been answered. In some other cases, the initial path of investigation had to be detoured according to the results obtained in view of selecting a potential self-regenerating coating within the limits of duration of this thesis (3 years). This necessarily opens new avenues of investigation among which, some key perspectives in the short term can be proposed in the following.

In the study of the thermite reactions, some of the unanswered questions are:

- Which the actual physical state (liquid/solid) of the alumina formed during the thermite reaction and can this affect the derived intermetallic formation by absorbing/releasing heat locally?
- How does the reaction and diffusion front form and advance? And what are the temperatures reached at the interface?
- As the Al percolate through the NiO layer to form the diffusion islands, is the Al in a liquid or solid state? And what are these defects in the NiO (network of pores, grain boundaries, etc.)?
- Will larger defects in the NiO layer completely reduce the nickel oxide layer?

To answer these questions, several experiments can be imagined:

- Thermodynamic and kinetics simulation can be carried out and will allow a better understanding of the aluminothermic reaction between Al/NiO/Ni systems.
- More detailed analyses on the NiO layer (eg. TEM, SEM with FIB, etc.) can reveal the defects through which the Al infiltrates NiO. In addition, other in-situ analyses (e.g. SEM and Raman spectroscopy with hot stages) can help to determine the different stages involved in this Al infiltration.
- Real-time monitoring tests using methods such as a thermal and SEM images of the reaction could help to better understand the sequence of coating formation at the different evolving interfaces. For this, a cross-section of a preoxidized sample with an Al deposit can be heated in a heating stage in an enclosure and imaged under the SEM.
- To reduce the thickness of the NiO layer without reducing the preoxidation time or temperature. It can be tested to preoxidize the sample, then to reduce the NiO formed by a reducing gas such as H₂. A thin layer of nickel will form on the top of the NiO layer and the aluminizing step should allow to grow a first layer of NiAl and the formation of an alumina diffusion barrier. Another possible solution is a light polishing of the NiO to reduce the thickness and increase the defects concentration.
- In addition, higher temperatures and shorter oxidation times can be tested.

When a Ni plating is synthesized and preoxidized:

- What is the role of hydrogen in the synthesis, oxidation and aluminization stages?
- Is this method viable to achieve homogeneous coatings on Ni-based superalloys?

To answer these questions:

- TDS (thermodesorption spectroscopy) analyses can be carried out to quantify the amount of trapped hydrogen in the electrodeposit before and after the preoxidation step as well as after the aluminization step.
- Finally, in recent years several porous electrodeposits and porous bulk produced by 3D printing have been developing. It will be interesting to preoxidize and aluminize then. These complex structures could make it possible to form composite coatings with alumina inclusions.

Regarding the synthesis of electrochemically self-regenerating coatings:

- One of the main questions are the influence of the size, composition and oxide thickness of the microparticles.
- In addition, the results obtained in oxidation were found to be satisfactory, but how the manner Al is supplied from the microparticles to the matrix (if really occurring) could be not clearly defined. Thus, the way the microparticles will evolve with time and temperature under constant pressure should be investigated, in particular by extending the duration of the isothermal tests to assess the critical Al content in these systems. In the same vein, one key point is the study of the adhesion of the coating to the different substrates (Ni-based alloys) under high temperature oxidizing cycles since the induced thermal stresses might concentrate at the coating/substrate interface especially if the latter is still made by a continuous oxide (i.e. incomplete reduction of NiO or excessively thick interfacial Al_2O_3).

To answer these questions, several tests can be set up such as the synthesis of different particle sizes, Al and Ni compositions, and different preoxidation times. These differences will make it possible to observe the interactions between the particles and the coating, as well as to quantify the interdiffusion phenomena during the aluminization and oxidation stages. In particular, very local analyses by e.g. EPMA (electron probe microanalyses) and EDS coupled to a TEM might reveal convenient.

In addition, the great flexibility of this method can allow a great adaptability in synthesizable coatings. Indeed, each parameter such as thickness and composition of the electrodeposits, the size and composition of the particles and the thickness of the oxide shell can be modified independently of the others. This makes it possible to adapt the coating to the targeted applications. For example, for high-temperature corrosion, preoxidizing Al_xCr_y or $\text{Ni}_x\text{Al}_y\text{Cr}_z$ particles can be trapped in the Ni plating. Subsequently, a slurry aluminization of Al and Cr particles would form a Cr-rich self-regenerating coating for very harsh corrosive environments such as waste recovery and biomass plants.

Annexes

Annex 1

Theoretically, the basis of x-ray diffraction is that the penetration (and therefore the intensity) can reach different values depending on the material studied. Thus, the intensity is related to the linear absorption coefficient by the following relation:

$$I(x) = I_0 \cdot e^{-\mu \cdot x} \quad (\text{eq.1})$$

Penetration is also calculated by the relation:

$$p = \frac{1}{\mu} \cdot \ln\left(\frac{I_0}{I}\right) \cdot \frac{\sin(\omega) \cdot \sin(2\theta - \omega)}{\sin(\omega) + \sin(2\theta - \omega)} \quad (\text{eq.2})$$

With ω the angle of incidence and 2θ the experimental position of the considered peak.

In our study, the assembly is symmetrical, therefore $\omega = \theta$. Which give:

$$p = \frac{1}{\mu} \cdot \ln\left(\frac{I_0}{I}\right) \cdot \frac{\sin(\theta)}{2} \quad (\text{eq.3})$$

It is considered that only the crystallographic planes located at a depth p , such that the total path of the X-rays in the samples verifies $\frac{I_0}{I} = \frac{1}{10}$ participate significantly in the 2θ peak considered. So $\ln\left(\frac{I_0}{I}\right) = \ln(10) = 2.3$.

Then $\mu_m = \frac{\mu}{\rho}$ with μ_m the mass absorption coefficient and ρ the density of the coating. Since μ and μ_m depend on the energy of the photons, it is necessary to consider the energy associated with the wavelength of X-rays. In our case $\lambda \equiv \lambda_{K\alpha}(Cu) \rightarrow E \sim 8 \text{ KeV}$ and then:

Ni : $\mu_m = 49.52 \text{ cm}^2 \cdot \text{g}^{-1}$	$\rho = 8.902 \text{ g} \cdot \text{cm}^{-3}$	$\Rightarrow \mu = 440.827 \text{ cm}^{-1}$
M = 58.70 g		
W : $\mu_m = 170.5 \text{ cm}^2 \cdot \text{g}^{-1}$	$\rho = 19.3 \text{ g} \cdot \text{cm}^{-3}$	$\Rightarrow \mu = 3290.65 \text{ cm}^{-1}$
M = 183.85 g		

For a Ni samples of M_x molar mass then:

$$\mu_m(x) = [x M(Ni) \mu_m(Ni)] \times \frac{1}{M_x}$$

$$\text{and } \mu(x) = \rho_x \times \mu_m(x)$$

Where $\rho_x \equiv$ Density of Ni

For a Ni_xAl_y compound of M_{xy} molar mass then:

$$\mu_m(x, y) = [x M(Ni) \mu_m(Ni) + y M(Al) \mu_m(Al)] \times \frac{1}{M_{xy}}$$

$$\text{and } \mu(x, y) = \rho_{xy} \times \mu_m(x, y)$$

Where $\rho_{xy} \equiv$ Density of Ni_xAl_y

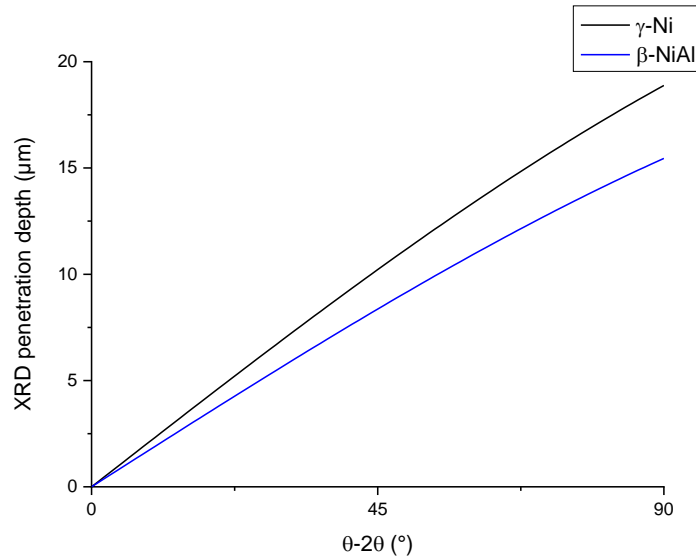


Figure 1: γ -Ni and β -NiAl penetration depth for the $K_{\alpha 1}$ copper for symmetrical mounting

Table 1: Summary table of the X penetration depth for the different plan and peaks

γ -Ni	Plane	Penetration depth	β -NiAl	Planes	Penetration depth
2θ	(hkl)	μm	2θ	(hkl)	μm
44.5	(111)	10.1	31.1	(100)	5.8
51.8	(200)	11.7	44.5	(110)	8.3
76.4	(220)	16.5	55.3	(111)	10.1
			64.7	(200)	11.7
			73.5	(210)	13
			82	(211)	14.3

Synthèse et comportement à haute température des revêtements auto-régénérants

La sélection des matériaux utilisés dans les parties chaudes des moteurs aéronautiques ou dans les centrales de production d'énergie sont devenu un enjeu crucial au vu des impératifs écologiques et économiques. L'un des composants critiques de ces systèmes sont les aubes de turbine dont leur tenue mécanique est assurée par la nature des substrats employés (aciers et superalliages à base nickel). Cependant, leur tenue environnementale nécessite l'application de revêtements protecteurs source d'Al capables de former de barrières d'oxyde (Al_2O_3) imperméables à l'attaque externe par oxydation et corrosion aux hautes températures. L'épuisement de l'Al pour former l'oxyde et par interdiffusion avec le substrat conduit inexorablement à la perte de protection. Ainsi, des structures spécifiques de revêtement telles les barrières de diffusion peuvent alors être mise en place pour augmenter la durée des vies des aubes au détriment de leurs propriétés mécaniques et de coûts élevés de fabrication et environnementaux. Durant cette étude, des nouvelles voies originales de synthèse des revêtements de diffusion d'aluminium « autorégénérants » ont été étudiées. Ces revêtements disposent d'une structure composite, avec une matrice de phases intermétallique (Ni_xAl_y) renforcée par des microréservoirs constitués d'un cœur (Ni_xAl_y) et une paroi en Al_2O_3 au travers laquelle l'Al du cœur peut ravitailler la matrice et maintenir une concentration globale en Al suffisamment élevée dans la matrice capable de former la couche externe protectrice d' Al_2O_3 .

Nos études démontrent que les réactions aluminothermiques entre du NiO et l'Al permettent de former un tel revêtement autorégénérant avec une barrière de diffusion à l'interface substrat/revêtement lorsque le Ni est initialement pré-oxydé à 1100°C pendant 2h. Néanmoins, aucun compromis n'a été trouvé pour former des revêtements sans NiO résiduel qui pourrait compromettre l'adhérence du revêtement au substrat. En revanche, une voie électrochimique permet d'incorporer de microparticules d' Al_3Ni_2 dans des électrodépôts de Ni. A la suite d'un traitement d'aluminisation par barbotine, les microparticules préoxydées s'incorporent de manière homogène dans un revêtement de β -NiAl. Après traitement d'oxydation isotherme à 1000°C durant 48h, ce revêtement par voie électrodéposition + aluminisation présente une teneur en aluminium supérieure à 40 at%, ce qui est supérieur à un revêtement de diffusion absent de microréservoirs démontrant ainsi le caractère autorégénérant des nouveaux revêtements.

Mots-clés : Revêtements auto-régénérants ; aluminothermie ; électrodéposition ; aluminisation barbotine ; NiAl- Al_2O_3 .

Synthesis and high-temperature behavior of self-restoring coatings

The selection of materials used in the hot parts of aeronautical turbines or in power plants has become a crucial issue in view of ecological and economic imperative. Turbine blades are amongst the most critical components. Their mechanical resistance is ensured by the substrate itself (steels and Ni alloys and superalloys). However, their low environmental resistance requires the application of protective coatings delivering Al to form oxide barriers blocking the external oxidative and corrosive attack. Upon exposure at high temperatures, Al depletes from the coating by oxidation to grow the oxide scale and by interdiffusion with the substrate's elements resulting in the loss of protection. Some specific coating structures like the diffusion barriers have been investigated in the past but the overall mechanical properties are lowered and the fabrication and environmental costs are high. Therefore, a pioneering and original investigation has been conducted to synthesize "self-regenerating" aluminum diffusion coatings. These coatings are characterized by a composite structure whereby the matrix made of Ni_xAl_y intermetallic phases is strengthened with microreservoirs made of Ni_xAl_y core and an Al_2O_3 shell through which Al diffuses out to maintain the adequate Al concentration in the matrix, hence to stabilize the external protective Al_2O_3 scale.

Our studies demonstrate that the aluminothermic reactions between NiO and Al lead to the formation of such a self-regenerating coating with an interdiffusion barrier at the coating/substrate interface whenever Ni is preoxidized at 1100°C for 2h beforehand. However, all the coatings sintered through this method possess residual NiO, which may compromise their adherence to the substrate. In contrast, the use of electrochemical methods allows to incorporate Al_3Ni_2 microparticles in the Ni electrodeposits. With a subsequent slurry aluminizing treatment, the preoxidized particles incorporate homogeneously in a β -NiAl coating matrix. After exposure at 1100°C for 48h in air, the Al content in the self-regenerating coatings is greater than 40 at% as opposed to the micro-reservoirs-free aluminide coating allowing to demonstrate the self-regenerating property of these new coatings.

Keywords: Self-regenerating coatings; aluminothermic reactions; electrodeposition; slurry aluminizing; NiAl- Al_2O_3 .